

Towards experimental characterization of nanoparticle charging in plasmas

Citation for published version (APA):

Staps, T. J. A. (2022). *Towards experimental characterization of nanoparticle charging in plasmas*. [Phd Thesis 1 (Research TU/e / Graduation TU/e), Applied Physics and Science Education]. Eindhoven University of Technology.

Document status and date:

Published: 08/02/2022

Document Version:

Publisher's PDF, also known as Version of Record (includes final page, issue and volume numbers)

Please check the document version of this publication:

- A submitted manuscript is the version of the article upon submission and before peer-review. There can be important differences between the submitted version and the official published version of record. People interested in the research are advised to contact the author for the final version of the publication, or visit the DOI to the publisher's website.
- The final author version and the galley proof are versions of the publication after peer review.
- The final published version features the final layout of the paper including the volume, issue and page numbers.

[Link to publication](#)

General rights

Copyright and moral rights for the publications made accessible in the public portal are retained by the authors and/or other copyright owners and it is a condition of accessing publications that users recognise and abide by the legal requirements associated with these rights.

- Users may download and print one copy of any publication from the public portal for the purpose of private study or research.
- You may not further distribute the material or use it for any profit-making activity or commercial gain
- You may freely distribute the URL identifying the publication in the public portal.

If the publication is distributed under the terms of Article 25fa of the Dutch Copyright Act, indicated by the "Taverne" license above, please follow below link for the End User Agreement:

www.tue.nl/taverne

Take down policy

If you believe that this document breaches copyright please contact us at:

openaccess@tue.nl

providing details and we will investigate your claim.

Towards experimental characterization of nanoparticle charging in plasmas

PROEFSCHRIFT

ter verkrijging van de graad van doctor aan de Technische Universiteit Eindhoven,
op gezag van de rector magnificus prof.dr.ir. F.P.T. Baaijens,
voor een commissie aangewezen door het College voor Promoties,
in het openbaar te verdedigen op dinsdag 8 februari 2022 om 16:00 uur

door

Timmy Jacobus Adrianus Staps

geboren te Tilburg

Dit proefschrift is goedgekeurd door de promotoren en de samenstelling van de promotiecommissie is als volgt:

voorzitter: prof.dr.ir. E. J. E. Cottaar
promotoren: dr.ir. J. Beckers
 prof.dr.ir. G. M. W. Kroesen
leden: prof.dr. U. Kortshagen (University of Minnesota)
 prof.dr. M. Creatore
 prof.dr. E. Kovačević (Université d'Orléans)

Het onderzoek dat in dit proefschrift wordt beschreven is uitgevoerd in overeenstemming met de TU/e Gedragscode Wetenschapsbeoefening.

Towards experimental characterization of nanoparticle charging in plasmas

Timmy Jacobus Adrianus Staps

The front cover shows a cloud of nanoparticles confined in a gas discharge generated under low pressure. The back cover depicts a cloud of nanoparticles in the spatial afterglow of a gas discharge generated at atmospheric pressure.

Preparation. L^AT_EX documentation system in OverLeaf.

Printing. Print Service Ede / proefschriftenprinten.nl

Cover photos. dr.ir. Bart Platier

ISBN. 978-90-386-5439-3

A catalogue record is available from the Eindhoven University of Technology Library.

Financial support. This project is co-funded by PPS-contribution Research and Innovation of the Ministry of Economic Affairs and Climate Policy (The Netherlands), and Prodrive Technologies B.V.

ORCID.  Open Researcher and Contributor ID: 0000-0002-9859-2942

Copyright. © Tim Staps, 2021

Holland High Tech
Global Challenges, Smart Solutions

 **PRODRIVE**
TECHNOLOGIES

*To my beloved wife, Gaby,
and our beautiful daughter, Faye.*

Contents

1	Introduction	1
1.1	Air pollution	1
1.2	Ultrafine particle (UFP) sensing	3
1.3	Knowledge gaps in the physics of dusty plasmas	6
1.4	Research questions	7
1.5	Objectives and structure	8
1.6	Bibliography	12
2	Theory of plasma-induced charging of dust grains	19
2.1	Concepts in the physical ecosystem	20
2.2	Collisionless regime	21
2.3	Collision-enhanced regime	24
2.4	Hydrodynamic regime	26
2.5	Weighted contributions to the total ion current	26
2.6	Implications of the dust charge	28
2.7	Bibliography	29
3	Experimental setups	31
3.1	Setup for experiments under low pressure conditions	31
3.1.1	Microwave cavities with integrated discharge electrodes	32
3.1.2	Vacuum vessel, gas supply and pumping system	38
3.1.3	RF power supply	40
3.1.4	Optics	42
3.2	Setup for experiments under atmospheric pressure conditions	44
3.2.1	Integrated design of the plasma jet and microwave cavity	44
3.2.2	Vessel, gas supply and pumping system	47
3.2.3	RF power supply	49
3.2.4	Optics	52

3.3	Bibliography	54
4	Effect of spatial electron density profiles on MCRS	55
4.1	Introduction	56
4.2	Microwave cavity resonance spectroscopy	57
4.2.1	Refractive index of plasmas	57
4.2.2	Principles of MCRS	58
4.3	Experiment	59
4.3.1	Devices and interconnections	59
4.3.2	Methodology	62
4.4	Numerical model	65
4.4.1	Drift-diffusion equations and boundary conditions	65
4.4.2	Plasma species and reactions	66
4.4.3	Solutions of the numerical model in PLASIMO software	67
4.5	Results and discussion	71
4.5.1	Typical electron density evolution during and after a pulsed discharge	71
4.5.2	Profile correction	72
4.5.3	Comparison of uniform and profile-corrected electron densities	73
4.6	Conclusion	75
4.7	Bibliography	76
5	Elastic electron collisions in dusty plasmas	81
5.1	Introduction	81
5.2	Methods	83
5.2.1	Experiment	83
5.2.2	Microwave Cavity Resonance Spectroscopy	85
5.2.3	Theoretical analysis	88
5.3	Results	91
5.3.1	Dust formation process	91
5.3.2	Electron plasma frequency	92
5.3.3	Effective collision frequency	92
5.4	Discussion	93
5.5	Implications	95
5.6	Conclusion	96
5.7	Bibliography	97
6	Dust charge density of nanoparticles in dusty plasma	103
6.1	Introduction	104
6.2	Methods	105
6.3	Results	108
6.4	Discussion	111
6.5	Conclusion	113
6.6	Appendix	113
6.6.1	Extinction	114

6.6.2	Microwave cavity with integrated discharge electrodes and dust collection system	115
6.6.3	Stability of dust and plasma parameters	119
6.6.4	Calculation of electric-field-weighted volume ratio	121
6.6.5	SEM micrographs of collected nanoparticles	122
6.6.6	Model description	124
6.6.7	Model solution for Si- and C-like nanoparticles	126
6.6.8	Derivation of charging timescale	132
6.7	Bibliography	134
7	Characterization of afterglow electron dynamics	141
7.1	Introduction	142
7.2	Experiment	143
7.3	Results and discussion	147
7.4	Conclusion	149
7.5	Bibliography	150
8	Effect of dust formation on the spatial afterglow of an atmospheric pressure plasma jet	153
8.1	Introduction	153
8.2	Experiment	155
8.3	Results	160
8.4	Discussion	162
8.4.1	Electron depletion	163
8.4.2	Analysis of decay timescales	164
8.5	Conclusion	166
8.6	Appendix	168
8.6.1	Laser light scattering experiments on dust grains in the afterglow	168
8.6.2	Microwave-electric-field-weighted volume ratio	168
8.7	Bibliography	171
9	Laser-induced photodetachment of negative oxygen ions	177
9.1	Introduction	177
9.2	Experiment	179
9.3	Results	182
9.3.1	Time-resolved cavity response	182
9.3.2	Argon discharge afterglow	184
9.3.3	Laser-induced photodetachment	186
9.3.4	Decay of photodetached electrons	188
9.4	Discussion	189
9.4.1	Identification of anion species	189
9.4.2	Detachment processes from negative atomic oxygen ion	190
9.4.3	Decay of the photodetached electron density	191
9.4.4	Electron energy relaxation	193
9.5	Conclusion	194
9.6	Appendix	195

9.6.1	Electric-field-weighted volume ratio	195
9.6.2	Calculation of the photodetached electron density	196
9.6.3	Beam cross section	198
9.6.4	Temperature-correction of resonance frequency	199
9.6.5	Theoretical analysis of collision frequency	201
9.6.6	Timescale of first-order reaction	204
9.7	Bibliography	205
10	Conclusion	211
10.1	General conclusions	211
10.2	Research question I	212
10.3	Research question II	213
10.4	Research question III	214
11	Outlook and recommendations	215
11.1	Outlook for future research	215
11.2	Recommendations for applications	217
	Summary	219
	Acknowledgments	221
	Scientific contributions	225
11.3	Journal publications	225
11.4	Oral contributions	226
11.5	Poster contributions	226
	Curriculum Vitae	229

Introduction

1.1 Air pollution

The earth's atmosphere transitioned from a mixture of hot gases and solids to one that facilitates the greenhouse effect [1] and the development of oxygen-based life [2, 3]. However, for this life, the atmosphere is becoming increasingly hostile due to human activities increasing the concentration of molecular constituents such as carbon dioxide (CO_2), nitrogen dioxide (NO_2), sulfur dioxide (SO_2), and particulate matter (PM) including dust grains. Dust originates from natural sources, such as sea salt and desert dust, as well as from anthropogenic activities, such as burning fossil fuels and using car brakes. The dust formed by anthropogenic sources most often contains hazardous constituents, which is the main reason that dust forms one of the greatest risks to human health [4].

Exposure to dust particles mainly proceeds by inhalation of the ambient air containing such particles, and becomes increasingly dangerous with decreasing dust size (denoted by the dust grain radius a_d). To give an impression of the relative size of such particles, the size of the various categories of particulate matter (PM) are indicated with respect to a human hair and a sand grain in Fig. 1.1, showing PM_{10} , $\text{PM}_{2.5}$, and $\text{PM}_{0.1}$. The largest dust grains belong to the category PM_{10} (including all dust grains with a size $a_d \leq 10 \mu\text{m}$) and are effectively captured by the human lungs [5, 6]. Fine particles, categorized as $\text{PM}_{2.5}$, include all dust grains with radii $a_d \leq 2.5 \mu\text{m}$. Particles in this category have an increased negative impact on the human body, because these grains are deposited deeper into the lungs. Ultrafine particles (UFP), termed $\text{PM}_{0.1}$, are the smallest kind and constitute dust grains in the nanometer size range with $a_d \leq 0.1 \mu\text{m}$. Ultrafine particles possess the ability to enter deeply into human lungs [7, 8, 9], and penetrate into the blood stream by diffusion through the alveolar membrane [10]. Hence, they may end up causing harm in various parts of the body [11]. Nevertheless, the interaction of ultrafine particles with the body and possible health-related effects are still largely unexplored [12, 13].

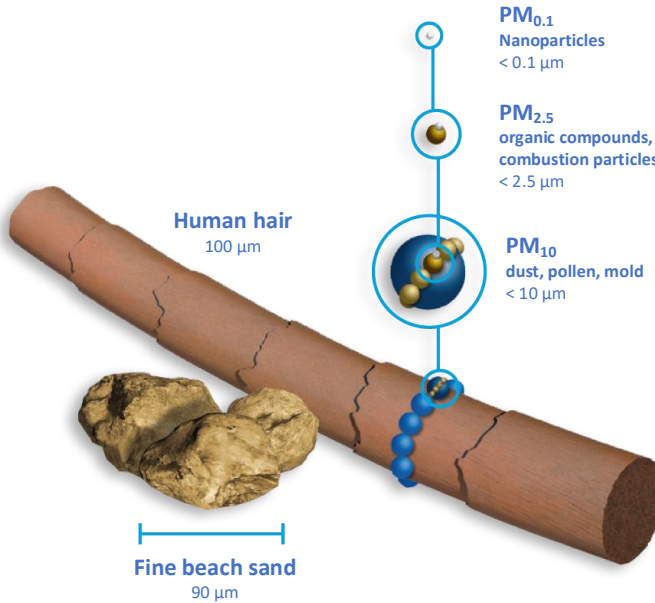


Figure 1.1: The relative size of particulate matter (PM) with respect to a sand grain and human hair. $\text{PM}_{2.5}$ and PM_{10} constitute dust particles that are typically in the micrometer size range, whereas $\text{PM}_{0.1}$ or ultrafine particles (UFP) are the smallest kind of particulate matter in the nanometer size range. Adapted figure based on the source file: <https://www.pikpng.com/transpng/hJmToi/>.

The effects of particulate matter in general have already been related to cardiovascular and respiratory diseases [14, 15, 16, 17, 18], neurotoxicity [19], epigenetic modifications [20], and cancer metastasis [21]. This resulted in the definition of exposure guidelines for $\text{PM}_{2.5}$ and PM_{10} [22] based on the total surface area or mass concentration. However, exposure limits based on surface area and mass concentration do not account for the presence (of large quantities) of ultrafine particles, although they constitute the largest PM-related health risk. The fact that ultrafine particles do not contribute to such measures is visualized in Fig. 1.2, for a fictional particle size distribution, in terms of the number concentration, surface area and mass concentration. It can be inferred that a billion ultrafine particles with $a_d = 0.010 \mu\text{m}$ have the same mass as a single particle with $a_d = 10 \mu\text{m}$ (assuming the same material), and only a thousand times larger surface area. This shows that the number concentration of ultrafine particles constitutes a better exposure measure, but nevertheless recommendations for $\text{PM}_{0.1}$ are not provided due to insufficient epidemiological evidence regarding the health impact of ultrafine particles [22], and due to the lack of a suitable measurement technique. As a consequence, it is concluded that ultrafine particles are effectively not accounted for by the current exposure limits for $\text{PM}_{2.5}$ and PM_{10} , and that exposure limits connected to these PM-levels underestimate the actual health risks.

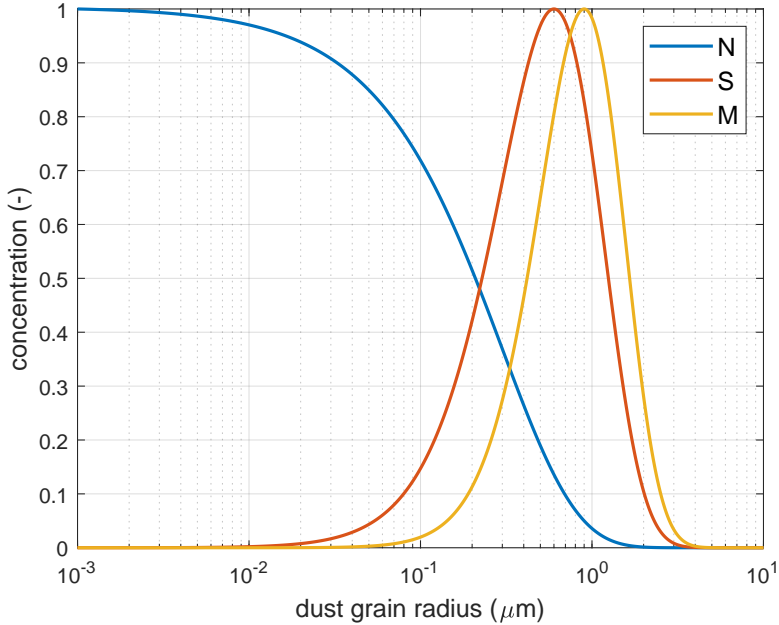


Figure 1.2: Particle size distributions in terms of the number concentration (N), surface area concentration (S), and mass concentration (M). A fictional exponential distribution was assumed for the number concentration, $N = \exp(-a_d/0.3 \mu\text{m})$, whereas $S = Na_d^2$ and $M = Na_d^3$. This shows that, although the number concentration of $\text{PM}_{0.1}$ particles with $a_d \leq 0.1 \mu\text{m}$ is largest, the surface area and mass concentration are dominated by the larger particles with size $\sim 1 \mu\text{m}$.

1.2 Ultrafine particle (UFP) sensing

Ultrafine particles or nanoparticles are very difficult to detect because these particles are smaller than the wavelength (termed λ) of visible light. Most techniques for measuring the total particle mass or surface area, for which the exposure is regulated in most countries, are based on the interaction of dust grains with laser light. According to the Mie theory [23], the amount of light scattered or absorbed by a solid dust grain decreases strongly with the dust radius. This implies that ultrafine particles scatter or absorb only a tiny fraction of the incoming light with respect to larger dust grains such as those in the category of $\text{PM}_{2.5}$. As a consequence, this leads to a dramatic decrease of the signal-to-noise ratio for light-based detection of nanoparticles. Hence, in contrast to $\text{PM}_{2.5}$ and PM_{10} , most of the current techniques for measuring the dust grain size and concentration are ineffective in the nanometer regime [24].

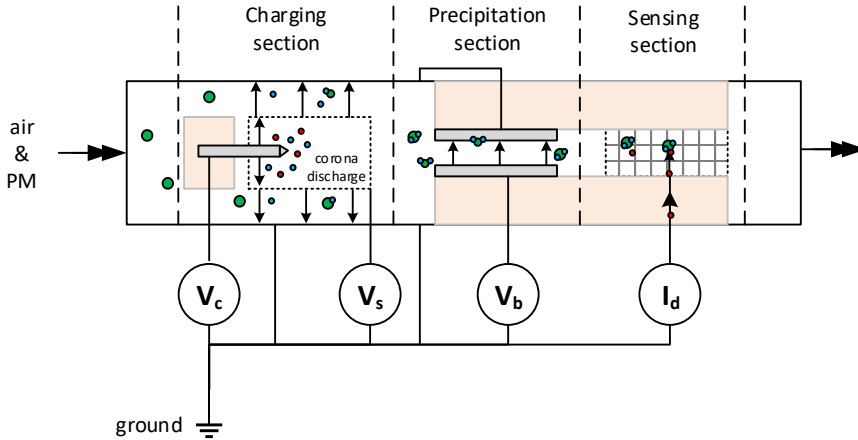


Figure 1.3: Ultrafine particle sensor (UFPS) as described by Marra *et al* [25, 26]. Atmospheric air and particulate matter (PM) enters the sensor from the left (gas flow direction indicated by double-headed arrows), and pass an ion-rich region resulting in the electrical charging of the dust grains (green) in the *charging section*. The ion concentration is produced by a direct-current *corona discharge* containing ions (blue) and electrons (red), after which the ions are extracted by the electric field (single head arrows) between the corona needle (corona discharge voltage V_c), the screen electrode (screen voltage V_s), and the grounded sensor housing (ground). The positively charged dust grains (dust: green, with attached ions: blue) are carried by the gas flow towards the *precipitation section*, where an electric field (due to a bias voltage V_b) is applied to remove a part of the dust particle size distribution. Because this selection process occurs on the basis of the charge to mass ratio, the smallest particles are precipitated. The non-precipitated part of the dust particle cloud enters the Faraday cage and is neutralized by the sensor current I_d in the *sensing section*, from which the total amount of charge is derived.

The most promising technique to detect ultrafine particles is based on the detection of the charge that they acquired from an ionized gas, also called a gas discharge or plasma [25, 26]. A schematic overview of such an ultrafine particle sensor is depicted in Fig. 1.3. In such a device, ambient air containing dust particles (green in fig 1.3) is guided into a region close to a gas discharge (i.e., a plasma), which effectively charges the dust particles by attaching electrons (red in Fig. 1.3) and/or ions (blue in Fig. 1.3) to their surface in the *charging section*. These free electrons and ions are naturally present in such a gas discharge which is also the reason that the dust grains become electrically charged (as will be explained later in this thesis). After being carried by the gas flow to the *precipitation section*, the charged nanoparticles are deflected by an electric field due to the potential difference between the bias voltage V_b applied to the bottom electrode and the grounded electrode on top. Based on the ratio between their mass and their electric charge, a collection of ultrafine particles becomes separated

from dust grains larger in size. The charged nanoparticles that are able to transit the deflection stage are deposited in a conductive mesh constituting a Faraday cage located in the *sensing section*, where they transfer their charge to an electrical circuit inducing the dust sensor current I_d . The average size and number concentration of the collected ultrafine particles is obtained by precisely measuring the electric current I_d for varying the bias electric field strengths (i.e., by varying V_b). Consequently, the main strengths of this measurement principle are that the number concentration can be measured instead of the surface area or mass concentration, and that the measurement signal (the total amount of charge carried by all dust grains) scales linearly with the dust grain size according to Fuchs charging theory [27].

The relative simplicity of the technique brings several difficulties in terms of the charging of nanoparticles, sustaining stable atmospheric pressure discharge conditions in ambient air, and the translation of the measurements into useful numbers. These difficulties include, but are not limited to:

- Contamination of the electrode surfaces. Due to the presence of organosilicon molecules in the air, for extended periods of plasma operation, the gas discharge facilitates the formation of dust grains and molecular contaminants which are subsequently deposited on the discharge electrodes. The thin layer of organosilicon material forms an electrical insulation for the direct-current (DC) discharge. Subsequently, an increasing DC corona voltage (V_c) is required to generate the discharge and maintain the ion concentration for dust charging, which is limited by breakdown in the electrical circuit (~ 10 kV). As a consequence, electrode contamination limits the lifetime of the device.
- Unstable charging due to fluctuating gas conditions. The ion concentration is the key parameter that should be kept constant for stably charging the ultrafine particles, because it is directly responsible for the dust charging process. Upon longer operation times, the ion concentration becomes unstable due to the contamination of the electrode surface, and varying gas conditions. The increasingly higher corona voltage results in breakdown of the thin layer, and irregular release of molecular and particulate contaminants into the discharge volume leading to short-term fluctuations in the ion concentration. The air conditions change on a longer timescale due to variations in, for instance, the gas temperature, the relative humidity (amount of water vapor), and altitude with respect to the sea level (gas density). These fluctuations in the gas conditions lead to decreased performance of the device.
- The decharging of dust by interaction with neutral gas (in the spatial plasma afterglow). The ultrafine particles charged in the charging section are transported to subsequent stages, where they are deflected and measured. However, during their transport, the charged ultrafine particles can interact with the neutral gas species such as oxygen. Oxygen, as an example, can easily form a negative ion by capturing an electron from the discharge due to its strong electron affinity. In the spatial afterglow, the negative ions can form a source of electrons causing the neutralization of the (originally positively) charged dust grains. The

neutralization of the dust charge negatively affects the interpretation of the device's signals.

In order to enable further development of charge-based ultrafine particle sensing techniques, these engineering challenges are translated into fundamental questions regarding the interaction between gas discharges and ultrafine particles.

1.3 Knowledge gaps in the physics of dusty plasmas

In the previous section, the concept of ultrafine particle sensing and the related engineering challenges have been treated. In this section, the engineering challenges are related to the basic knowledge in the field of dusty plasmas in order to identify gaps in our understanding of the physics of dusty and dust-forming plasmas. These knowledge gaps need to be filled in order to further develop plasma-based ultrafine particle sensing techniques.

The formation of thin layers of dust grains and molecular contaminants on the electrode surfaces, related to the first engineering challenge in Section 1.2, resembles a fundamental process in dusty plasmas. In dust-forming plasmas (without the external injection of dust grains), a reactive gas is added to a (noble) carrier gas in order to promote the formation of nano- to micrometer-sized dust grains through three well-characterized phases: nucleation, coagulation, and accretion [28]. This process has been studied in a wide variety of gas mixtures including acetylene, silane, methane, and fluorocarbon as precursor (reactive component) [29, 30, 31, 32]. In case of organosilicon precursors, only a handful of experimental studies focused on dust formation under low pressure conditions [33, 34, 35, 36]. Under atmospheric pressure conditions, many studies have used organosilicon precursors for the deposition of thin layers [37, 38, 39, 40, 41, 42], but studies on the formation processes of dust grains in the discharge bulk and spatial afterglow have only become recently to the attention [43, 44]. An important deficit in the previously stated literature is the lack of knowledge of the electron dynamics in organosilicon-containing dust-forming discharges. Consequently, there is a gap in the understanding of dust formation in case of organosilicon precursors under low and atmospheric pressure, and dust formation in general under atmospheric pressure conditions, specifically in terms of the electron dynamics.

The charging of dust grains in contact with plasma is another fundamental process in low and atmospheric pressure dust-containing discharges, related to the second engineering challenge in Section 1.2. The charge of nanoparticles immersed in, or in contact with, a gas discharge originates from the difference in the mobility of electrons and ions resulting in most cases in a permanent negative charge on the nanoparticles, at least in the plasma bulk. Much research has been devoted to micrometer-sized dust grains (or microparticles in short) charged by low pressure discharges in the plasma bulk [45, 46], levitated in the plasma sheath [47, 48], and the discharging of dust grains in the spatial afterglow [49, 50]. The situation for nanosized dust grains charged by low pressure discharges is very different, with only a few works focusing on experimental measurement of the dust charge [51, 52, 53, 54]. Under atmospheric

pressure conditions, the charge of nanosized dust grains is relatively well studied in the spatial afterglow [55, 56, 57, 58, 59], but the dust charge in the bulk is often not accessible. Therefore, low pressure dusty plasmas constitute an ideal model system for dust charge measurements, because the dust particles are confined in the discharge volume and a solid theoretical framework is available for predicting the dust charge.

Charge measurements of nanoparticles at atmospheric pressure are routinely performed using commercial devices such as the scanning mobility particle sizer (SMPS), the differential mobility analyzer (DMA), the condensation particle counter (CPC), or combinations of the former. These experimental methods are based on extracting charged nanoparticles from the plasma and measuring their charge distribution downstream. However, the interaction of nanoparticles charged negatively by the plasma bulk with the afterglow often causes neutralization or even charge reversal [56, 57, 59, 58], which implies that the charge depends heavily on the transport time. This is because there is ample time for the interaction of ions with charged nanoparticles, while the electrons are quickly lost due to recombination, attachment and losses to the walls of the device. The interaction of positive ions and (charged) nanoparticles is relatively well understood experimentally and theoretically under atmospheric pressure conditions. However, the effect of negative ions is often not considered, although the formation and behavior of negative ions is important for atmospheric pressure plasma sources in general [60, 61], and may affect the charge distribution of the dust grains under consideration. The limited knowledge of the negative ion dynamics in the spatial afterglow of atmospheric pressure discharges represents the third gap, related to the third engineering challenge in Section 1.2.

1.4 Research questions

The gaps in the knowledge of dusty and dust-forming plasmas are defined in the previous section. Related to these gaps in knowledge, this section outlines three research questions which aim to contribute to an increased understanding of the physical mechanisms that play a fundamental role in the complex physical ecosystem inside UFP sensing devices.

The formation of dust grains in gas discharges containing hexamethyldisiloxane (HMDSO)—a common organosilicon precursor—is investigated under low and atmospheric pressure conditions. The focus is specifically on the effect of dust formation on the electron dynamics in order to be able to use its evolution as a monitor for dust growth and dust charging. This gives rise to the first question:

Research question I: how do dust grains affect the plasma properties in organosilicon-containing gas discharges?

The second research question arises from limitations in the experimental validation of the charging theory with respect to nanoparticles. We limit the conditions to a low pressure environment, which constitutes an idealized (steady-state) model system

compared to more complicated situations at higher (e.g. atmospheric) gas pressure, or in the spatial (or temporal) afterglow. The focus is on experimental determination of the nanoparticle charge in the plasma bulk. This gives rise to the second question:

Research question II: how well does the theoretical framework predict the charge of nanometer-sized dust grains immersed in a low pressure plasma?

The third research question is related to the dynamics of negative ions in the spatial afterglow of an atmospheric pressure discharge. The focus is on experimental detection of negative ions in the spatial afterglow of an atmospheric pressure discharge, which potentially have an important and underexposed effect on the dust charge distribution in that region. This raises the third question:

Research question III: how do negative ions behave in the spatial afterglow of atmospheric pressure plasmas?

The work presented in this thesis is outlined in the subsequent section by two research lines. The first research line bundles parts of the research questions that are related to low pressure discharges, addressing the following:

- The formation of dust in organosilicon-containing discharges at low pressure, which can be directly compared to the well studied growth processes using different reactive gas mixtures such as acetylene, methane, or silane.
- The measurement of the dust charge under low pressure conditions, which forms an ideal model system in which the plasma-induced currents are collisionless.

The second research line combines the parts of the research questions which are concerned with the spatial afterglow of an atmospheric pressure plasma:

- The effect of dust formation on the electron dynamics in the spatial afterglow of an atmospheric pressure discharge.
- The dynamics of negative ions in the spatial afterglow of an atmospheric pressure discharge.

1.5 Objectives and structure

This work is devoted to studying the fundamental research questions outlined in the previous section, which concern the fundamental process of dust formation and (de)charging in dust-forming plasmas. This dissertation is divided in four major parts, which represent the general items providing the background for understanding the work

presented by the research lines, the first research line, the second research line, and the closing and concluding chapters. A mind-map of this thesis is shown in Fig. 1.4.

First, the general items are presented:

- Chapter 2 provides an extensive overview of the literature concerning the charging of dust grains by plasma-induced fluxes of charged particles.
- Chapter 3 presents the experimental setups used to conduct experiments at low and at atmospheric pressure.

Second, research line I focuses on results obtained from the experiments conducted on low pressure pristine and organosilicon-containing discharges:

- Chapter 4 concerns a critical evaluation of the effect of spatial plasma profiles on the plasma diagnostic technique microwave cavity resonance spectroscopy (MCRS) in pristine argon. This technique is used in subsequent chapters to study dusty plasmas which exhibit a stronger inhomogeneous character than pristine plasmas.
- Chapter 5 studies the evolution of the electron density and the electron collision frequency with neutral gas particles during the formation process that is typical for dust-forming plasmas at low pressure. Specifically, this study highlights the importance of the electron collisionality in dusty plasmas.
- Chapter 6 provides experimental results on the dust charge of nanoparticles immersed in a dusty plasma and a comparison to the theoretical predictions. Laser-induced photodetachment liberates the electrons from the surface of the dust particles, whereas MCRS effectively measures the photodetached electrons during the phases of liberation and recharging of the dust particles.

Third, research line II presents the experiments performed in the spatial afterglow of atmospheric pressure pristine and organosilicon-containing discharges:

- Chapter 7 proves the feasibility of characterizing the electron behavior in the spatial afterglow of a radio-frequency excited discharge at atmospheric pressure. Measurements of the electron dynamics are provided by applying microwave cavity resonance spectroscopy (MCRS) under atmospheric pressure conditions, in which the electrons collide frequently with the neutral gas particles as opposed to low pressure discharge where such electron-neutral collisions can usually be neglected.
- Chapter 8 assesses the effect of dust charging on the conditions in the spatial plasma afterglow by adding a reactive component (i.e., HMDSO) to the discharge gas. This reactive mixture promotes the formation of nanoscale dust particles, which are charged by the plasma fluxes. The effect of dust charging is explored by determination of the electron density and collision frequency by MCRS.
- Chapter 9 applies laser-induced photodetachment in the spatial afterglow of the same reactor with argon as discharge gas, which results in the creation of negative

oxygen ions by the interaction of the afterglow electrons with the argon-oxygen atmosphere. Photodetachment converts the negative ions into neutral particles and free electrons that are detected with MCRS. This experiment demonstrates that laser-induced photodetachment in concert with MCRS provides a valuable technique to study the spatial afterglow of reactive gas discharges, which could be further exploited in case of dust-forming discharges.

Fourth, this thesis is completed by the closing chapters:

- Chapter 10 concludes this thesis by relating the main results to the research questions initially defined.
- Chapter 11 provides an outlook and recommendations for future research on dust-forming discharges and the development of ultrafine particle sensing technologies.
- The final chapters representing the back matter provide a summary of the main results and conclusions, the acknowledgments, a list of scientific contributions, and the curriculum vitae of the author.

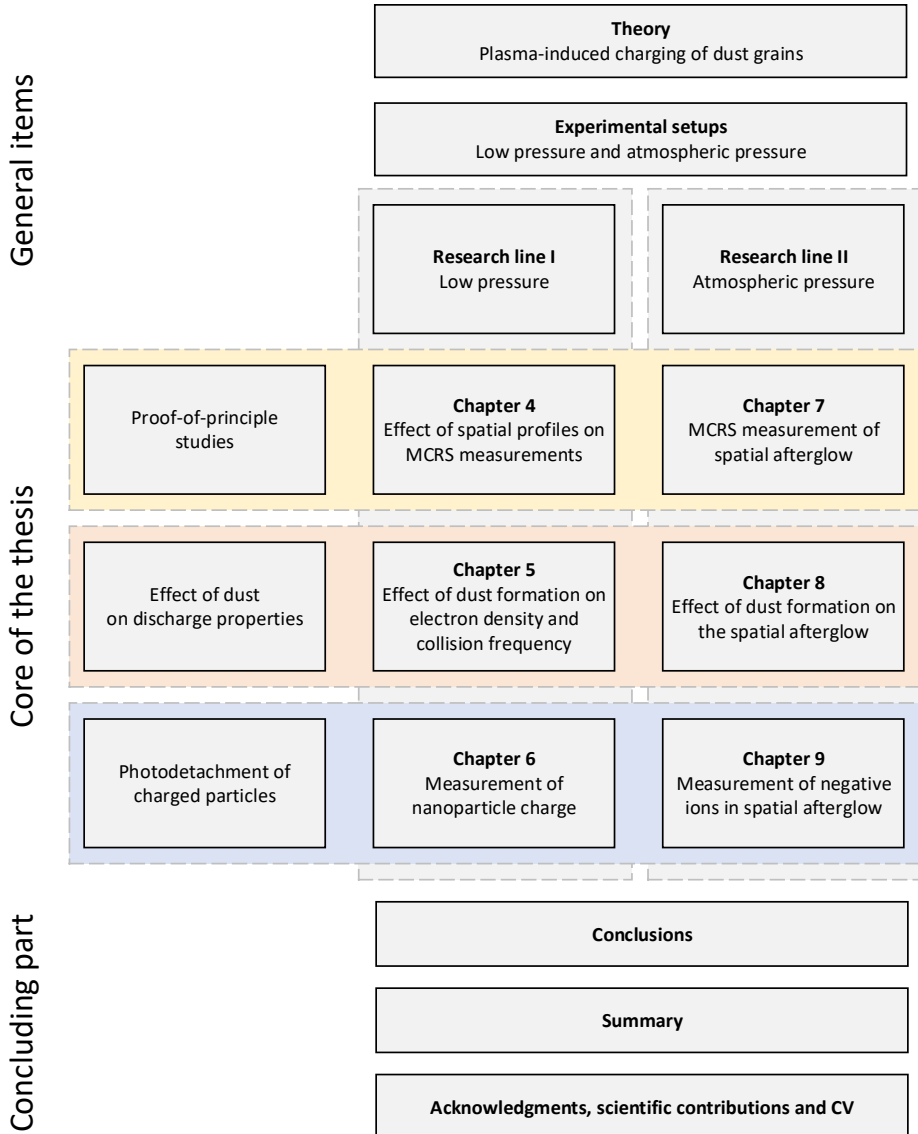


Figure 1.4: Overview of the research framework with four major parts: the general items, research line I, research line II, and the concluding part. The two research lines (vertically) each contain three main result chapters.

1.6 Bibliography

- [1] S. A. Montzka, E. J. Dlugokencky, and J. H. Butler. Non-CO₂ greenhouse gases and climate change. *Nature*, 476(7358):43–50, 2011.
- [2] Timothy W. Lyons, Christopher T. Reinhard, and Noah J. Planavsky. The rise of oxygen in Earth’s early ocean and atmosphere. *Nature*, 506(7488):307–315, 2014.
- [3] Kazumi Ozaki and Christopher T Reinhard. The future lifespan of Earth’s oxygenated atmosphere. *Nature Geoscience*, 14(3):138–142, 2021.
- [4] World Health Organisation. Ambient (outdoor) air pollution, 2021.
- [5] Sung Ok Kwon, Seok Ho Hong, Young Ji Han, So Hyeon Bak, Junghyun Kim, Mi Kyeong Lee, Stephanie J. London, Woo Jin Kim, and Sun Young Kim. Long-term exposure to PM₁₀ and NO₂ in relation to lung function and imaging phenotypes in a COPD cohort. *Respiratory Research*, 21(1):1–11, 2020.
- [6] Laura Paulin and Nadia Hansel. Particulate air pollution and impaired lung function. *F1000Research*, 5(0):1–9, 2016.
- [7] Robert Sturm. Local lung deposition of ultrafine particles in healthy adults: Experimental results and theoretical predictions. *Annals of Translational Medicine*, 4(21):1–9, 2016.
- [8] Yulia Olsen, Dorina Gabriela Karottki, Ditte Marie Jensen, Gabriel Bekö, Birthe Uldahl Kjeldsen, Geo Clausen, Lars Georg Hersoug, Gitte Juel Holst, Aneta Wierzbicka, Torben Sigsgaard, Allan Linneberg, Peter Møller, and Steffen Loft. Vascular and lung function related to ultrafine and fine particles exposure assessed by personal and indoor monitoring: A cross-sectional study. *Environmental Health: A Global Access Science Source*, 13(1):1–10, 2014.
- [9] Winfried Möller, Kathrin Felten, Knut Sommerer, Gerhard Scheuch, Gabriele Meyer, Peter Meyer, Karl Häussinger, and Wolfgang G. Kreyling. Deposition, retention, and translocation of ultrafine particles from the central airways and lung periphery. *American Journal of Respiratory and Critical Care Medicine*, 177(4):426–432, 2008.
- [10] Nazanin R. Yacobi, Noah Malmstadt, Farnoosh Fazlollahi, Lucas DeMaio, Ronald Marchelletta, Sarah F. Hamm-Alvarez, Zea Borok, Kwang Jin Kim, and Edward D. Crandall. Mechanisms of alveolar epithelial translocation of a defined population of nanoparticles. *American Journal of Respiratory Cell and Molecular Biology*, 42(5):604–614, 2010.
- [11] Annette Peters, Bellina Veronesi, Lilian Calderón-Garcidueñas, Peter Gehr, Lung Chi Chen, Marianne Geiser, William Reed, Barbara Rothen-Rutishauser, Samuel Schürch, and Holger Schulz. Translocation and potential neurological effects of fine and ultrafine particles a critical update. *Particle and Fibre Toxicology*, 3:1–13, 2006.

-
- [12] Dean E. Schraufnagel. The health effects of ultrafine particles. *Experimental and Molecular Medicine*, 52(3):311–317, 2020.
- [13] Simone Ohlwein, Ron Kappeler, Meltem Kutlar Joss, Nino Künzli, and Barbara Hoffmann. Health effects of ultrafine particles: a systematic literature review update of epidemiological evidence. *International Journal of Public Health*, 64(4):547–559, 2019.
- [14] Vivian C. Pun, Fatemeh Kazemiparkouhi, Justin Manjourides, and Helen H. Suh. Long-Term PM_{2.5} Exposure and Respiratory, Cancer, and Cardiovascular Mortality in Older US Adults. *American Journal of Epidemiology*, 186(8):961–969, 2017.
- [15] Junling Zhao, Miao Li, Zhihua Wang, Jinkun Chen, Jianping Zhao, Yongjian Xu, Xiang Wei, Jianmao Wang, and Jungang Xie. Role of PM_{2.5} in the development and progression of COPD and its mechanisms. *Respiratory Research*, 20(1):1–13, 2019.
- [16] A. Zwozdziak, I. Sówka, E. Willak-Janc, J. Zwozdziak, K. Kwiecińska, and W. Balińska-Miśkiewicz. Influence of PM₁ and PM_{2.5} on lung function parameters in healthy schoolchildren—a panel study. *Environmental Science and Pollution Research*, 23(23):23892–23901, 2016.
- [17] Yu Fei Xing, Yue Hua Xu, Min Hua Shi, and Yi Xin Lian. The impact of PM_{2.5} on the human respiratory system. *Journal of Thoracic Disease*, 8(1):E69–E74, 2016.
- [18] Mark R. Miller, Catherine A. Shaw, and Jeremy P. Langrish. From particles to patients: Oxidative stress and the cardiovascular effects of air pollution. *Future Cardiology*, 8(4):577–602, 2012.
- [19] Hongying Wei, Yan Feng, Fan Liang, Wei Cheng, Xiaomeng Wu, Ren Zhou, and Yan Wang. Role of oxidative stress and DNA hydroxymethylation in the neurotoxicity of fine particulate matter. *Toxicology*, 380:94–103, 2017.
- [20] Anushi Shukla, Neha Bunkar, Rajat Kumar, Arpit Bhargava, Rajnarayan Tiwari, Koel Chaudhury, Irina Y. Goryacheva, and Pradyumna K. Mishra. Air pollution associated epigenetic modifications: Transgenerational inheritance and underlying molecular mechanisms. *Science of the Total Environment*, 656:760–777, 2019.
- [21] Rui Gao and Nan Sang. Quasi-ultrafine particles promote cell metastasis via HMGB1-mediated cancer cell adhesion. *Environmental Pollution*, 256:113390, 2020.
- [22] World Health Organization. Occupational Team. and Environmental Health. WHO Air quality guidelines for particulate matter, ozone, nitrogen dioxide and sulfur dioxide: global update 2005: summary of risk assessment. Technical report, World Health Organization, 2006.

- [23] Gustav Mie. Beiträge zur Optik trüber Medien speziell kolloidaler Goldlösungen (contributions to the optics of diffuse media, especially colloid metal solutions). *Annalen der Physik*, 25:377–445, 1908.
- [24] Hyouk Soo Kwon, Min Hyung Ryu, and Christopher Carlsten. Ultrafine particles: unique physicochemical properties relevant to health and disease. *Experimental and Molecular Medicine*, 52(3):318–328, 2020.
- [25] Johan Marra, Matthias Voetz, and H. J. Kiesling. Monitor for detecting and assessing exposure to airborne nanoparticles. *Journal of Nanoparticle Research*, 12(1):21–37, 2010.
- [26] J Marra. Using the Aerasense NanoTracer for simultaneously obtaining several ultrafine particle exposure metrics. *Journal of Physics: Conference Series*, 304:012010, 2011.
- [27] N. A. Fuchs. On the stationary charge distribution on aerosol particles in a bipolar ionic atmosphere. *Geofisica Pura e Applicata*, 56(1):185–193, 1963.
- [28] L. Boufendi and A. Bouchoule. Particle nucleation and growth in a low-pressure argon-silane discharge. *Plasma Sources Science and Technology*, 3(3):262–267, 1994.
- [29] Y. A. Ussenov, E. von Wahl, Zahra Marvi, T. S. Ramazanov, and H. Kersten. Langmuir probe measurements in nanodust containing argon-acetylene plasmas. *Vacuum*, 166(April):15–25, 2019.
- [30] W. W. Stoffels, E. Stoffels, G. M.W. Kroesen, and F. J. De Hoog. Electron density fluctuations in a dusty Ar/SiH₄ rf discharge. *Journal of Applied Physics*, 78(8):4867–4872, 1995.
- [31] J. Beckers and G. M W Kroesen. Gas temperature dependence of coagulation onset times for nanoparticles in low pressure hydrocarbon plasmas. *Applied Physics Letters*, 103(12):123106, 2013.
- [32] M. Haverlag, G. M.W. Kroesen, T. H.J. Bisschops, and F. J. de Hoog. Measurement of electron densities by a microwave cavity method in 13.56-MHz RF plasmas of Ar, CF₄, C₂F₆, and CHF₃. *Plasma Chemistry and Plasma Processing*, 11(3):357–370, 1991.
- [33] B. Despax, K. Makasheva, and H. Caquineau. Cyclic powder formation during pulsed injection of hexamethyldisiloxane in an axially asymmetric radiofrequency argon discharge. *Journal of Applied Physics*, 112(9):093302, 2012.
- [34] B. Despax, F. Gaboriau, H. Caquineau, and K. Makasheva. Influence of the temporal variations of plasma composition on the cyclic formation of dust in hexamethyldisiloxane-argon radiofrequency discharges: Analysis by time-resolved mass spectrometry. *AIP Advances*, 6(10), 2016.

-
- [35] V. Garofano, L. Stafford, B. Despax, R. Clergereaux, and K. Makasheva. Cyclic evolution of the electron temperature and density in dusty low-pressure radio frequency plasmas with pulsed injection of hexamethyldisiloxane. *Applied Physics Letters*, 107(18):183104, 2015.
- [36] V. Garofano, L. Stafford, J. Gorka, F. Gaboriau, B. Despax, J. Boulon, C. Joblin, K. Demyk, and K. Makasheva. Experimental study of nanoparticle formation dynamics in HMDSO-Ar asymmetric capacitively-coupled radiofrequency plasma with application to deposition of nanocomposite layers. *Nanotechnology Materials and Devices Conference, NMDC 2016 - Conference Proceedings*, pages 1–2, 2016.
- [37] Rino Morent, Nathalie De Geyter, Tinneke Jacobs, Sandra Van Vlierberghe, Peter Dubruel, Christophe Leys, and Etienne Schacht. Plasma-polymerization of HMDSO using an atmospheric pressure dielectric barrier discharge. *Plasma Processes and Polymers*, 6(SUPPL. 1):537–542, 2009.
- [38] Yu Chun Lin and Meng Jiy Wang. Fabrication of hydrophobic/hydrophilic HMDSO films by atmospheric pressure plasma jet deposition. *Japanese Journal of Applied Physics*, 58(SA):3–8, 2019.
- [39] Rüdiger Reuter, Katja Rügner, Dirk Ellerweg, Teresa De Los Arcos, Achim Von Keudell, and Jan Benedikt. The role of oxygen and surface reactions in the deposition of silicon oxide like films from HMDSO at atmospheric pressure. *Plasma Processes and Polymers*, 9(11-12):1116–1124, 2012.
- [40] Uwe Lommatzsch and Jörg Ihde. Plasma polymerization of HMDSO with an atmospheric pressure plasma jet for corrosion protection of aluminum and low-adhesion surfaces. *Plasma Processes and Polymers*, 6(10):642–648, 2009.
- [41] R. Reuter, D. Ellerweg, A. Von Keudell, and J. Benedikt. Surface reactions as carbon removal mechanism in deposition of silicon dioxide films at atmospheric pressure. *Applied Physics Letters*, 98(11):3–5, 2011.
- [42] Iryna Kuchakova, Maria Daniela Ionita, Eusebiu Rosini Ionita, Andrada Lazea-Stoyanova, Simona Brajnicov, Bogdana Mitu, Gheorghe Dinescu, Mike De Vrieze, Uroš Cvelbar, Andrea Zille, Christophe Leys, and Anton Yu Nikiforov. Atmospheric pressure plasma deposition of organosilicon thin films by direct current and radio-frequency plasma jets. *Materials*, 13(6), 2020.
- [43] Xiaoshuang Chen and Christopher J. Hogan. Nanoparticle dynamics in the spatial afterglows of nonthermal plasma synthesis reactors. *Chemical Engineering Journal*, 411(October 2020):128383, 2021.
- [44] Eric Husmann, Elijah Thimsen, and Xiaoshuang Chen. Particle charge distributions in the effluent of a flow-through atmospheric pressure low temperature plasma. *Plasma Sources Science and Technology*, 30(7), 2021.
- [45] Manis Chaudhuri, Sergey A. Khrapak, and Gregor E. Morfill. Experimental determination of particle charge in highly collisional plasma. *AIP Conference Proceedings*, 1397(November):263–264, 2011.

- [46] S. Ratynskaia, S. Khrapak, A. Zobnin, M. H. Thoma, M. Kretschmer, A. Usachev, V. Yaroshenko, R. A. Quinn, G. E. Morfill, O. Petrov, and V. Fortov. Experimental determination of dust-particle charge in a discharge plasma at elevated pressures. *Physical Review Letters*, 93(8):8–11, 2004.
- [47] J. Beckers, T. Ockenga, M. Wolter, W. W. Stoffels, J. Van Dijk, H. Kersten, and G. M. W. Kroesen. Microparticles in a collisional rf plasma sheath under hypergravity conditions as probes for the electric field strength and the particle charge. *Physical Review Letters*, 106(11):115002, 2011.
- [48] P. Meijaard, T. J.A. Staps, and J. Beckers. Step-wise excitation for the determination of the resonance frequency of a microparticle confined in a low pressure plasma. *Physics of Plasmas*, 28(8), 2021.
- [49] B. Van Minderhout, J. C.A. Van Huijstee, B. Platier, T. Peijnenburg, P. Blom, G. M.W. Kroesen, and J. Beckers. Charge control of micro-particles in a shielded plasma afterglow. *Plasma Sources Science and Technology*, 29(6):065005, 2020.
- [50] Judith van Huijstee, Boy van Minderhout, Robert M. H. Rempelberg, Paul Blom, Ton Peijnenburg, and Job Beckers. Plasma assisted particle contamination control: plasma charging dependence on particle morphology. *Proceedings SPIE*, 11611(February):116113A, 2021.
- [51] Benjamin Tadsen, Franko Greiner, Sebastian Groth, and Alexander Piel. Self-excited dust-acoustic waves in an electron-depleted nanodusty plasma. *Physics of Plasmas*, 22(11):113701, 2015.
- [52] E. Stoffels, W. W. Stoffels, G. M. W. Kroesen, and F. J. de Hoog. Dust formation and charging in an Ar/SiH₄ radio-frequency discharge. *Journal of Vacuum Science & Technology A: Vacuum, Surfaces, and Films*, 14(2):556–561, 1996.
- [53] M. A. Smith, J. Goodrich, H. U. Rahman, and U. Mohideen. Measurement of grain charge in dusty plasma Coulomb crystals. *IEEE Transactions on Plasma Science*, 29(2 I):216–220, 2001.
- [54] Tonuj Deka, A. Boruah, S. K. Sharma, and H. Bailung. Observation of self-excited dust acoustic wave in dusty plasma with nanometer size dust grains. *Physics of Plasmas*, 24(9):093706, 2017.
- [55] Nabil H. Abuyazid, Xiaoshuang Chen, Davide Mariotti, Paul Maguire, Christopher J. Hogan, and R. Mohan Sankaran. Understanding the depletion of electrons in dusty plasmas at atmospheric pressure. *Plasma Sources Science and Technology*, 29(7), 2020.
- [56] Sukrant Dhawan, Abhay Vidwans, Girish Sharma, Nabil Hilmy Abuyazid, R. Mohan Sankaran, and Pratim Biswas. Enhancing charging and capture efficiency of aerosol nanoparticles using an atmospheric-pressure, flow-through RF plasma with a downstream DC bias. *Aerosol Science and Technology*, 54(11):1249–1254, 2020.

- [57] Shuji Matsusaka. Control of particle charge by atmospheric pressure plasma jet (APPJ): A review. *Advanced Powder Technology*, 30(12):2851–2858, 2019.
- [58] Vikram Suresh, Li Li, Joshua Redmond Go Felipe, and Ranganathan Gopalakrishnan. Modeling nanoparticle charge distribution in the afterglow of non-thermal plasmas and comparison with measurements. *Journal of Physics D: Applied Physics*, 54(27):275205, 2021.
- [59] Ranganathan Gopalakrishnan, Peter H. McMurry, and Christopher J. Hogan. The bipolar diffusion charging of nanoparticles: A review and development of approaches for non-spherical particles. *Aerosol Science and Technology*, 49(12):1181–1194, 2015.
- [60] Peter Bruggeman, Felipe Iza, Daniël Lauwers, and Yolanda Aranda Gonzalvo. Mass spectrometry study of positive and negative ions in a capacitively coupled atmospheric pressure RF excited glow discharge in He–water mixtures. *Journal of Physics D: Applied Physics*, 43(1):012003, 2010.
- [61] K. Sekimoto and M. Takayama. Dependence of negative ion formation on inhomogeneous electric field strength in atmospheric pressure negative corona discharge. *European Physical Journal D*, 50(3):297–305, 2008.

Theory of plasma-induced charging of dust grains

Preface. The charge acquired by dust grains immersed in a plasma environment forms a central topic throughout the work presented in this thesis. Therefore, this chapter describes the theoretical frameworks used to predict the dust charge. Section 2.1 defines important concepts in the field of plasma physics, which are encountered several times throughout this thesis. The collisionless orbital-motion-limited (OML) theory is often used for the prediction of the charge obtained by dust grains, larger than a few nm in size, immersed in low pressure discharges as described in Section 2.2. The dust charge depends directly on the floating potential of the dust grain, which is governed by the balance between the electron and ion current. This theoretical framework, however, becomes invalid at neutral gas pressures exceeding about 10 Pa. For these higher pressures, collisions between ions and neutral gas particles play an important role in the dust charging process, since they affect the ion current towards a dust grain. This led to the development of the collision-enhanced theory described in Section 2.3. At even more elevated pressures, the problem tends towards the hydrodynamic limit, since the mean free path of the ions becomes so small that the ion current can be treated as a continuum. The charging theory in the hydrodynamic or continuum limit is described in Section 2.4. In Section 2.5, the framework for combining the ion current contributions by the three regimes into a single expression is defined based on the work by Gatti and Kortshagen [1]. The fact that dust grains are electrically charged by a plasma leads to many implications such as the confinement of dust in low pressure discharges, and the formation of dust crystals. Also, this charge limits the aggregation of unipolarly charged dust grains. The implications of the dust charge are treated in Section 2.6.

2.1 Concepts in the physical ecosystem

A number of concepts in the field of plasma physics are often encountered in the description of the charging theory. Two concepts are outlined briefly.

The Debye length λ_D serves as a measure for the ability of the plasma to shield electric disturbances in the form of a length scale. If an electric field is applied to the plasma, the electrons and ions can only be separated by a distance approximated by the Debye length. Hence, in case of a charged dust grain, the Debye length is a measure for the size of the sheath surrounding the dust grain, which draws electrons from the quasi-neutral plasma environment.

The Debye length is defined as follows, where $s = e, i$ for the electrons and ions, respectively:

$$\lambda_{Ds} = \sqrt{\frac{\varepsilon_0 k_B T_s}{n_s q_s^2}}. \quad (2.1)$$

Here, the vacuum permittivity is denoted by ε_0 , the Boltzmann constant by k_B , the species temperature by T_s , the species density by n_s , and the species charge by q_s . Since the plasma comprises a system of multiple species, the linearized Debye length is defined to account for each of these:

$$\lambda_{DL} = \left(\sum_s \frac{1}{\lambda_{Ds}^2} \right)^{-1/2}. \quad (2.2)$$

Because the ions are much less mobile than the electrons, they dictate the Debye length in low temperature plasmas. Since the plasma is a three-dimensional system, generally speaking, the concept of the Debye length is also used in the definition of the Debye sphere, e.g., surrounding a spherical dust grain, and the Debye radius.

The mean free path denoted by l_s is used to describe the (average) distance that one of the colliding species can travel without encountering its collision partner. The species involved in the plasmas considered in this work are neutrals, electrons, positive ions, negative ions, and dust grains. These species encounter each other by collisions, which results, for instance, in the transfer of momentum or in the production of electron-ion pairs by ionization. For low temperature plasmas, the thermal energy of the neutral gas species is close to the room temperature such that they can be considered as a fixed background species. This leads to the following expression for the mean free path:

$$l_s = \frac{1}{n_g \sigma_{sn}}, \quad (2.3)$$

with the neutral gas density denoted by n_g , and the cross section for a collision by σ_{sn} .

In general, we use the term low pressure to describe conditions in which the mean free path is much larger than the other length scales considered, such as the Debye length or the radius of a dust grain. At sufficiently high neutral gas pressure, the mean free path becomes smaller than the Debye length and the plasma can be considered as a fluid or a continuous medium.

2.2 Collisionless regime

The orbital-motion-limited (OML) theory of dust charging, originally developed by Mott-Smith and Langmuir [2], considers a dust grain immersed in a quasi-neutral plasma environment. Surrounded by electrons and ions, an initially neutral dust grain first receives a net electron flux—due to the much higher mobility of electrons compared to ions—charging its surface negatively. Consequently, the low-energy part of the electron cloud is repelled, and ions are attracted towards the grain’s surface by the (negative) floating potential. Finally, the ion flux cancels the electron flux in steady state, which results in a permanent negative dust charge for dust grains exceeding a size of about 5 nm. This theoretical framework has received a considerable amount of attention in the form of theoretical studies concerning its validity, limitations and improvements [3, 4, 5, 6, 7, 8].

The OML theory concerns three important assumptions based on the dust grain radius a_d , the Debye length λ_D , and the mean free path l :

- The electron and ion fluxes are collisionless, i.e. the species do not collide with neutrals inside the Debye sphere surrounding the dust grain.
- The radius of the dust grain is much smaller than the Debye length.
- The electron energy is distributed according to a Maxwellian distribution.

In essence, the first two conditions imply that $l \gg \lambda_D \gg a_d$, which applies to many low pressure discharges in which dust grains are formed or injected.

The electrical currents constituted by the electron and ion flux towards any surface in contact with plasma are in balance in a steady state situation:

$$\frac{dI}{dt} = I_e + I_i = 0. \quad (2.4)$$

Assuming a Maxwellian energy distribution for the electrons, the electron density n_e as a function of radial distance x from the dust grain surface can be described as follows:

$$n_e(x) = n_e(\infty) \exp\left(\frac{eV(x)}{k_B T_e}\right). \quad (2.5)$$

Here, the electron density in the plasma bulk is denoted by $n_e(\infty)$, the elementary charge by e , the Boltzmann constant by k_B , the potential by V , and the electron temperature by T_e . The electron flux Γ_e can be defined as the product of the electron density, at the dust grain’s surface equal to $n_e(a_d)$, and the thermal velocity \bar{v}_e , leading to the result obtained by Allen [9]:

$$\Gamma_e(a_d) = \frac{1}{4} n_e(a_d) \bar{v}_e = \frac{1}{4} n_e(\infty) \exp\left(\frac{eV(a_d)}{k_B T_e}\right) \sqrt{\frac{8k_B T_e}{\pi m_e}}. \quad (2.6)$$

Hence, the electron current follows by realizing that the total electron current to the surface is the product of dust surface area $A_d = 4\pi a_d^2$, the electron flux Γ_e , and the charge $-e$ carried by a single electron:

$$I_e(a_d) = -e\pi a_d^2 \Gamma_e(a_d). \quad (2.7)$$

The ion current is derived using the ion flux for (singly charged) positive ions, which experience no collisions during their movement towards the grain's surface. This implies that the ion flux Γ_i follows from the thermal ion velocity \bar{v}_i , and the Coulomb force field that attracts ions towards the negatively charged dust grain, as obtained by Allen [9]:

$$\Gamma_i(x) = \frac{1}{4}n_i(\infty) \left(1 - \frac{eV(x)}{k_B T_i}\right) \sqrt{\frac{8k_B T_i}{\pi m_i}}, \quad (2.8)$$

with the ion density denoted by n_i (in the bulk equal to $n_i(\infty)$), the ion temperature by T_i , and the ion mass by m_i , which results in the ion current:

$$I_i(a_d) = e\pi a_d^2 \Gamma_i(a_d). \quad (2.9)$$

Balancing the electron and ion current, the surface potential can be calculated self-consistently in steady state, i.e. $dI/dt = 0$. This means that the following expression can be solved for a certain background gas:

$$\exp\left(\frac{eV_d}{k_B T_e}\right) \sqrt{\frac{T_e}{m_e}} = \left(1 - \frac{eV_d}{k_B T_i}\right) \sqrt{\frac{T_i}{m_i}}, \quad (2.10)$$

with $V_d = V(a_d)$. Please note that the dust grain surface area A_d is cancelled from the equation, as well as the species densities n_e and n_i by assumption of quasi-neutrality (which is not a necessary condition for solving the equation). The surface charge follows by considering the dust grain as a spherical capacitor with a capacitance $C_d = 4\pi\epsilon_0 a_d$ so that the surface charge q_d is

$$q_d = C_d V_d = 4\pi\epsilon_0 a_d V_d. \quad (2.11)$$

The left- and right-hand side Eqn. (2.10) are depicted as a function of the grain's potential V_d in Fig. 2.1, where the intersection of the curves denotes the floating potential of the dust grain in steady state equal to $V_d^{\text{OML}} = -2.76$ V, or $q_d^{\text{OML}} \approx -193$ elementary charges by definition of Eqn. (2.11), for typical low pressure conditions (see the caption of Fig. 2.1). It can be seen from the figure that the electron current increases exponentially with the potential V_d , which forms a linear curve on the logarithmic scale. However, the ion current follows a linear decay as a function of V_d , and tends towards the thermal ion flux $1/4n_i\bar{v}_i$ for $V_d \rightarrow 0$. This is because the ions are repelled if the potential $V_d > 0$.

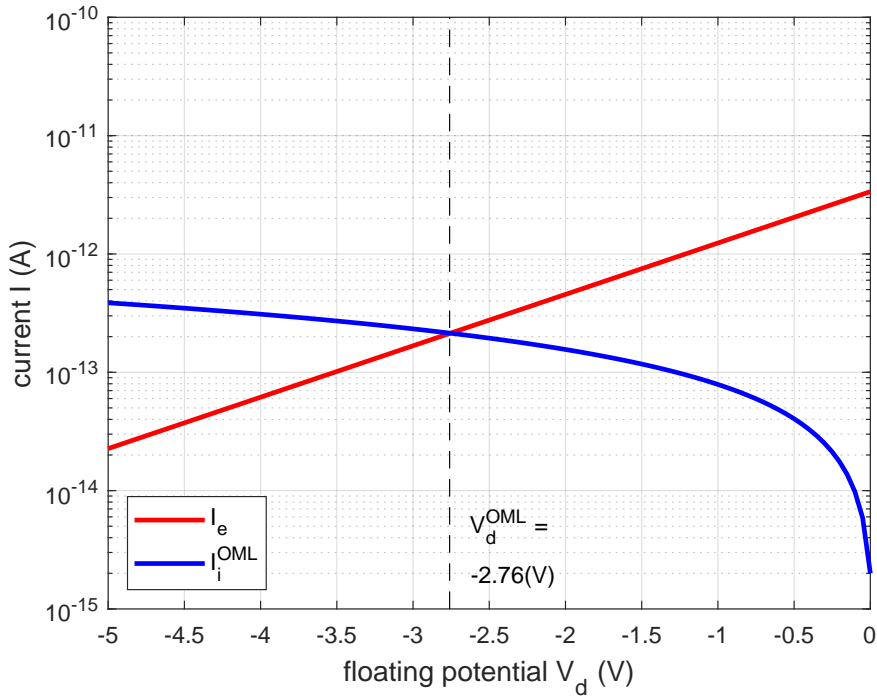


Figure 2.1: For the collisionless (OML) regime, the electron (red) and ion (blue) current are visualized as a function of the dust floating potential V_d . The intersection of the curves provides the floating potential of the dust grain in steady state: $V_d^{\text{OML}} = -2.76$ V. The following values were used: $T_e = 1$ eV, $T_i = 0.026$ eV (i.e. equal to 300 K), and $m_i = 40$ u for argon gas.

2.3 Collision-enhanced regime

The effect of ion-neutral collisions, part of which lead to charge-exchange and momentum transfer, becomes important with increasing density of the neutral gas species. Several decades ago, it was proposed by Bernstein and Rabinowitz [10] that ions trapped in the sheath could influence the potential function near a Langmuir probe. This has resulted in many studies investigating the effect of ion-neutral collisions in order to explain discrepancies between experimental results and the OML theory [11, 12, 1, 13, 14, 15, 16, 17].

Ion-neutral collisions can result in charge-exchange between a neutral gas particle, considered to be at rest, and an energetic ion accelerated from the quasi-neutral bulk by the sheath around the dust grain. In principle, in a neutral gas containing, e.g., only argon, this implies that an energetic ion is converted into a thermal ion. The resulting effect is that the ion is trapped in the potential field surrounding the dust grain, and that the ion current towards the dust surface is increased. This is because ions that would have followed a momentum transfer orbit—i.e. passing the dust grain surface without collection due to the combination of their energy and angular momentum—now have an increased chance to be confined by the potential field, and subsequently, collected by the (negatively charged) dust grain. The effect of ion-neutral collisions becomes already important for cases where the ion mean free path l_i (see Eqn. (2.3)) is larger than the (linearized) Debye length λ_{DL} (see Eqn. (2.2)) [17].

The theoretical framework for the collision-enhanced ion current is initiated by the consideration that ions are captured by the dust grain, if their kinetic energy is insufficient to overcome the attracting potential due to the Coulomb field, which is captured by the condition [12]:

$$E_i + U(R_0) = 0, \quad (2.12)$$

where the Yukawa potential is often used as an approximation for the potential:

$$U(x) = eV_d \frac{a_d}{x} \exp\left(-\frac{x - a_d}{\lambda_{DL}}\right). \quad (2.13)$$

This leads to the definition of the so-called capture radius R_0 (based on the linearized Yukawa potential), which dictates the imaginary sphere within which ions are captured, as follows [1, 18, 12, 19]:

$$R_0 = \frac{e|V_d|a_d \left(1 + \frac{a_d}{\lambda_{DL}}\right)}{E_i + e|V_d|\frac{a_d}{\lambda_{DL}}}. \quad (2.14)$$

Here, λ_{DL} denotes the linearized Debye length, and E_i represents the ion kinetic energy. Using the capture radius, the OML ion current is adapted by considering the surface area constituted by the capture sphere, i.e. $4\pi R_0^2$, instead of the dust surface, and the probability of ions undergoing a charge-exchange collision represented by the ratio R_0/l_i with l_i the ion mean free path. These amendments results in the collision-enhanced (CE) ion current [12, 19]:

$$I_i^{CE} = e\pi R_0^2 n_i \bar{v}_i \frac{R_0}{l_i}. \quad (2.15)$$

From here onwards, we follow the definition of the collision-enhanced ion current by Gatti and Kortshagen [1]:

$$I_i^{\text{CE}} = e\pi(\alpha R_0)^2 n_i \bar{v}_i. \quad (2.16)$$

Here, the factor $\alpha = 1.22$ is due to the Maxwellian energy distribution of the ion energy. In conclusion, it can be seen that the collision-enhanced current constitutes the thermal ion current that enters the capture sphere with radius R_0 .

Fig. 2.2 shows the electron current (OML) and the collision-enhanced ion current I_i^{CE} as a function of the potential. It can be seen that the ion current is increased significantly with respect to the OML ion current. As a consequence, the floating potential of the dust grain V_d^{CE} in steady state is much less negative resulting in a lower (negative) dust charge due to ion-neutral collisions.

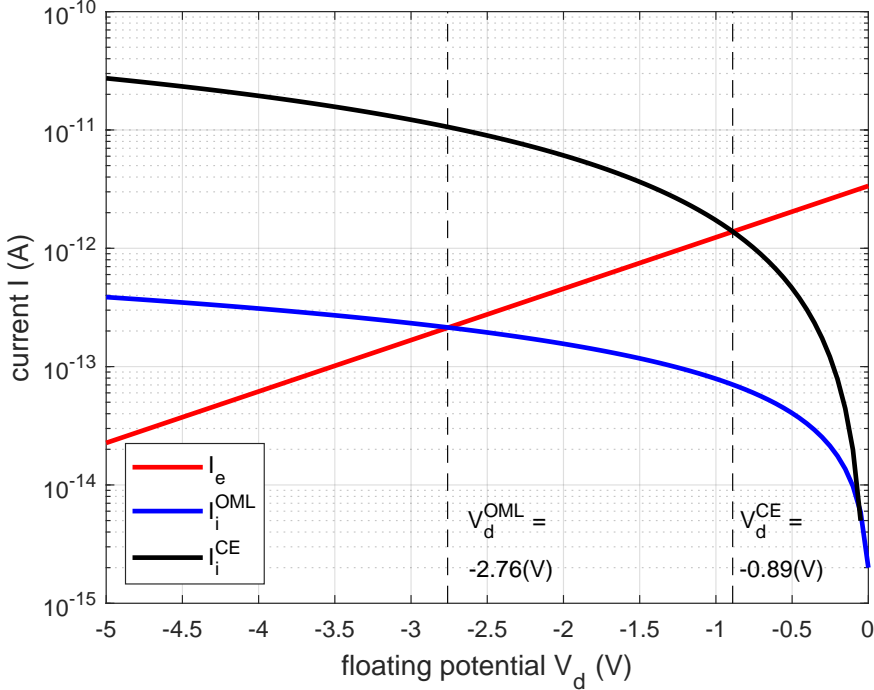


Figure 2.2: For the collision-enhanced (CE) regime, the electron (red) and ion (black) current are depicted as a function of the potential V_d . The intersection of the curves provides the floating potential of the dust grain in steady state: $V_d^{\text{CE}} = -0.89$ V. The following values were used: $T_e = 1$ eV, $T_i = 0.026$ eV (i.e., equal to 300 K), $\lambda_{\text{DL}} \approx 38$ μm , $E_i = 3/2k_B T_i$, and $a_d = 100$ nm.

2.4 Hydrodynamic regime

The ion current tends towards the continuum solution in case the ion mean free path l_i becomes smaller than the Debye length λ_D . In this case, ions experience multiple collisions in the sheath, and the flux can be described by the drift term of the drift-diffusion equation [20]:

$$\Gamma_i^{\text{HYD}} = -\mu_i n_i \nabla V, \quad (2.17)$$

where μ_i denotes the ion mobility coefficient, ∇ the gradient operator, μ_i the electrical mobility of the ion, and V the potential function. The continuum, or hydrodynamic, ion current follows by approximating the electric field $\nabla V \approx V_d/a_d$, and using $A_d = 4\pi a_d^2$, such that:

$$I_i^{\text{HYD}} = -e4\pi a_d \mu_i n_i V_d. \quad (2.18)$$

Please note that if $V_d < 0$ (so a negatively charged dust grain), the ion current towards the dust grain is positive. This result is the same as that obtained by Gatti and Kortshagen [1].

Fig. 2.3 plots the electron current (OML: I_e) and the hydrodynamic ion current I_i^{HYD} as a function of the grain's potential V_d . The floating potential, at which the currents are in balance, has shifted to more negative values compared to the OML solution.

2.5 Weighted contributions to the total ion current

The definition of the total ion current I_i is based on the approach by Gatti and Kortshagen [1], which comprises the sum of the ion currents by the different regimes weighted by their respective probability P :

$$I_i = P_0 I_i^{\text{OML}} + P_1 I_i^{\text{CE}} + P_2 I_i^{\text{HYD}}. \quad (2.19)$$

The probability of each current term is defined on the basis of the capture radius Knudsen number $\text{Kn}_{R_0} = l_i/(2\alpha R_0)$. This leads to the following probability for the collisionless regime P_0 :

$$P_0 = \exp\left(-\frac{1}{\text{Kn}_{R_0}}\right), \quad (2.20)$$

for the collision-enhanced regime P_1 ,

$$P_1 = \frac{1}{\text{Kn}_{R_0}} \exp\left(-\frac{1}{\text{Kn}_{R_0}}\right), \quad (2.21)$$

and for the hydrodynamic regime P_2 ,

$$P_2 = 1 - (P_0 + P_1). \quad (2.22)$$

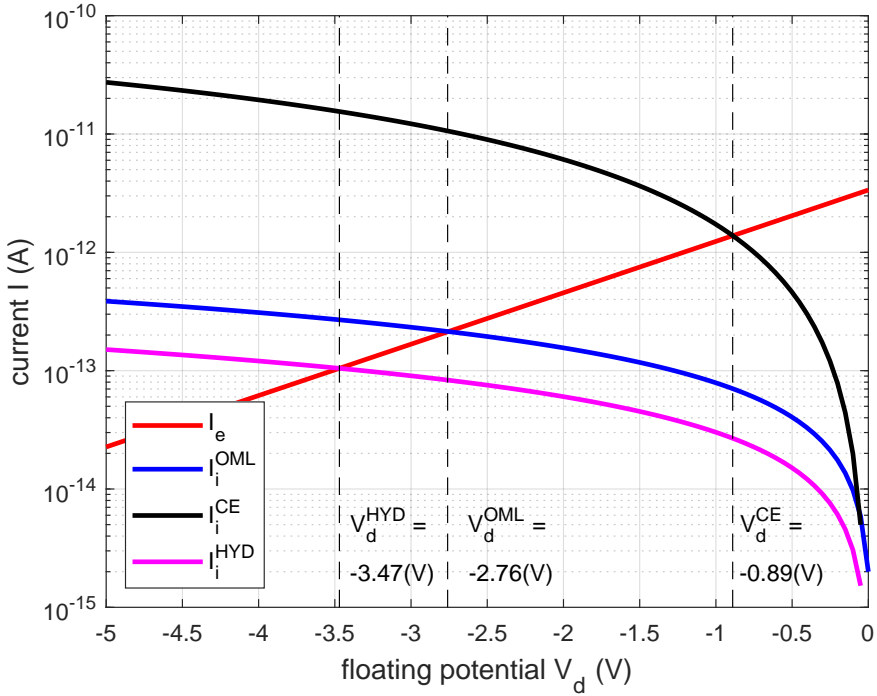


Figure 2.3: For the hydrodynamic (HYD) or continuum regime, the electron (red) and ion (magenta) current are shown as a function of the potential V_d . The intersection of the curves provides the floating potential of the dust grain in steady state: $V_d^{\text{HYD}} = -3.47$ V. The following values were used: $T_e = 1$ eV, $\mu_i = 1.5 \times 10^{-4} \text{ m}^2 \text{ V}^{-1} \text{ s}^{-1}$ (for a reduced electric field $E/n_g \approx 0$, and $n_g = 2.5 \times 10^{25} \text{ m}^{-3}$ at atmospheric pressure), and $a_d = 100$ nm.

2.6 Implications of the dust charge

The dust charge governs the interactions between (charged) dust grains, and the interactions between the dust grains and the plasma species. Due to the fundamental character of the charge, there are several implications that are useful to note in view of the work presented in this thesis:

- Forces between, and acting on, charged dust grains: the Coulomb force is one of the dominant forces acting on a dust grain in contact with a plasma. It determines whether a dust grain can be confined in the plasma bulk (applies mostly to nanoparticles), or levitated in the plasma sheath (applies mostly to microparticles) [21, 22, 23]. Furthermore, the ion drag force is governed by the momentum transfer and collection of ions by the dust grain (quite similar to the fluxes discussed in this chapter), and depends strongly on the dust charge. In fact, it governs the location of nanosized dust grains in the plasma bulk together with the Coulomb force. In case of levitating multiple particles in the sheath, e.g., the dust charge affects the inter-particle spacing [24] due to the Coulomb force.
- Growth in dust-forming plasma: the coagulation of charged protoparticles that clump together to form larger dust grains is initially inhibited by the mutual repulsion, but changes to the ratio of thermal energy and repulsive potential may promote or slow down this growth process. During subsequent growth phases, the dust charge determines the ion flux for further growth [25].
- Electron depletion: the permanent negative charging of dust grains, in case of immersion in an initially quasi-neutral environment (i.e. $n_e \approx n_i$) forms a significant loss channel for the free electrons in the plasma. At least in low pressure dust-forming plasmas, the electron density is severely depleted when dust grains reach sizes exceeding ~ 50 nm. This can be easily understood by considering that a number of $n_d q_d$ elementary charges are permanently retained on the dust surface, where $n_d \sim 1 \times 10^{14} \text{ m}^{-3}$ and the charge $\sim 10e$, typically. Comparing $n_d q_d$ to a typical electron density $n_e \sim 1 \times 10^{15} \text{ m}^{-3}$, it can be seen that the number of electrons quickly diminishes due to the charging process. This effect is actually used in Chapter 5 and 8 as a monitoring signal for the dust growth process, and its impact on the electron energy (distribution function).

2.7 Bibliography

- [1] Marco Gatti and Uwe Kortshagen. Analytical model of particle charging in plasmas over a wide range of collisionality. *Physical Review E*, 78(4):046402, 2008.
- [2] H. M. Mott-Smith and Irving Langmuir. The theory of collectors in gaseous discharges. *Physical Review*, 28(4):727–763, 1926.
- [3] Martin Lampe. Limits of validity for orbital-motion-limited theory for a small floating collector. *Journal of Plasma Physics*, 65(03):171–180, 2001.
- [4] Xian Zhu Tang and Gian Luca Delzanno. Orbital-motion-limited theory of dust charging and plasma response. *Physics of Plasmas*, 21(12):123708, 2014.
- [5] Zahida Ehsan, Nodar L. Tsintsadze, and S. Poedts. A modified orbital motion limited (OML) theory. (c):0–3, 2011.
- [6] Gian Luca Delzanno and Xian Zhu Tang. Comparison of dust charging between orbital-motion-limited theory and particle-in-cell simulations. *Physics of Plasmas*, 22(11):113703, 2015.
- [7] J. E. Allen, B. M. Annaratone, and U. de Angelis. On the orbital motion limited theory for a small body at floating potential in a Maxwellian plasma. *Journal of Plasma Physics*, 63(4):299–309, 2000.
- [8] R. V. Kennedy and J. E. Allen. The floating potential of spherical probes and dust grains. II: Orbital motion theory. *Journal of Plasma Physics*, 69(6):485–506, 2003.
- [9] J E Allen. Probe theory - the orbital motion approach. *Physica Scripta*, 45(5):497–503, 1992.
- [10] Ira B. Bernstein and Irving N. Rabinowitz. Theory of Electrostatic Probes in a Low-Density Plasma. *Physics of Fluids*, 2(2):112, 1959.
- [11] S. Ratynskaia, S. Khrapak, A. Zobnin, M. H. Thoma, M. Kretschmer, A. Usachev, V. Yaroshenko, R. A. Quinn, G. E. Morfill, O. Petrov, and V. Fortov. Experimental determination of dust-particle charge in a discharge plasma at elevated pressures. *Physical Review Letters*, 93(8):8–11, 2004.
- [12] S. A. Khrapak, S. V. Ratynskaia, M. H. Thoma, A. V. Zobnin, A. D. Usachev, V. V. Yaroshenko, M. Kretschmer, H. Höfner, G. E. Morfill, O. F. Petrov, and V. E. Fortov. Grain charge in the bulk of gas discharges. *AIP Conference Proceedings*, 799:177–180, 2005.
- [13] A. V. Zobnin, A. P. Nefedov, V. A. Sinel'shchikov, and V. E. Fortov. On the charge of dust particles in a low-pressure gas discharge plasma. *Journal of Experimental and Theoretical Physics*, 91(3):483–487, 2000.

- [14] Martin Lampe, Valeriy Gavrishchaka, Gurudas Ganguli, and Glenn Joyce. Effect of trapped ions on shielding of a charged spherical object in a plasma. *Physical Review Letters*, 86(23):5278–5281, 2001.
- [15] A. V. Zobnin, A. D. Usachev, O. F. Petrov, and V. E. Fortov. Ion current on a small spherical attractive probe in a weakly ionized plasma with ion-neutral collisions (kinetic approach). *Physics of Plasmas*, 15(4), 2008.
- [16] S. A. Khrapak, G. E. Morfill, A. G. Khrapak, and L. G. D’Yachkov. Charging properties of a dust grain in collisional plasmas. *Physics of Plasmas*, 13(5), 2006.
- [17] Alexander Piel and Christian Schmidt. Dust charging and charge fluctuations in a weakly collisional radio-frequency sheath at low pressure. *Physics of Plasmas*, 22(5), 2015.
- [18] F. Galli. *Charge and Energy Interactions between Nanoparticles and Low Pressure Plasmas*. PhD thesis, 2010.
- [19] Márton Lampe, Rajiv Goswami, Zoltan Sternovsky, Scott Robertson, Valeriy Gavrishchaka, Gurudas Ganguli, and Glenn Joyce. Trapped ion effect on shielding, current flow, and charging of a small object in a plasma. *Physics of Plasmas*, 10(5 I):1500–1513, 2003.
- [20] Leonardo Patacchini and Ian H. Hutchinson. Continuum-plasma solution surrounding nonemitting spherical bodies. *Physics of Plasmas*, 16(6):062101, 2009.
- [21] T. Nitter. Levitation of dust in rf and dc glow discharges. *Plasma Sources Science and Technology*, 5(1):93–111, 1996.
- [22] J. Beckers, T. Ockenga, M. Wolter, W. W. Stoffels, J. Van Dijk, H. Kersten, and G. M. W. Kroesen. Microparticles in a collisional rf plasma sheath under hypergravity conditions as probes for the electric field strength and the particle charge. *Physical Review Letters*, 106(11):115002, 2011.
- [23] J. Beckers, D. J M Trienekens, and G. M W Kroesen. Revealing an intermediate region between the collisional radiofrequency plasma bulk and its sheath. *Physical Review E - Statistical, Nonlinear, and Soft Matter Physics*, 91(3), 2015.
- [24] Althea Wilson and Babak Shotorban. Effects of collision-enhanced charging on dust crystal. *Physics of Plasmas*, 28(3), 2021.
- [25] I. Pilch, L. Caillault, T. Minea, U. Helmersson, A. A. Tal, I. A. Abrikosov, E. P. Münger, and N. Brenning. Nanoparticle growth by collection of ions: Orbital motion limited theory and collision-enhanced collection. *Journal of Physics D: Applied Physics*, 49(39):395208, 2016.

Experimental setups

This chapter describes the experimental setups used to conduct experiments under low and atmospheric pressure conditions. Section 3.1 presents the low pressure setup where gas discharges were created and probed under vacuum. Section 3.2 describes the atmospheric pressure discharge reactor. For each section, the auxiliary systems are also described as used for the supply and removal of gas flows, supply of radio-frequency power, and the optical systems including lasers.

3.1 Setup for experiments under low pressure conditions

Experiments under low pressure conditions were performed by creating gas discharges inside a microwave cavity in a large vacuum vessel. In this section, the general components of the system are explained in the following order. In Section 3.1.1, the three different microwave cavity designs—used to obtain the results outlined in Chapter 4, 5, and 6—are explained in more detail indicating the various components and considerations for the designs. In Section 3.1.2, the vacuum vessel, gas supply and pumping system are explained in detail for different experiments concerning pristine discharges as well as dust-forming discharges. In Section 3.1.3, the supply of radio-frequency power is discussed in more detail. In Section 3.1.4, the optical systems are treated concerning the laser light scattering and extinction setup, and the laser setup for photodetachment experiments.

3.1.1 Microwave cavities with integrated discharge electrodes

The electron density and effective collision frequency results at low pressure have been obtained using three different microwave cavity designs with integrated discharge electrodes. However, the basic design for each cavity was similar. A microwave cavity comprises a cylindrical metal pillbox in which microwaves are injected at a frequency close to the resonance frequency of one of the resonant modes. The cavity is electromagnetically closed for microwave radiation in the range of 1 – 10 GHz, which corresponds to a wavelength range that is on the order of the diameter of the cavity. The electric fields associated with the resonant mode are perturbed by the presence of electrons created by the gas discharge such that the resonance frequency (and perhaps the quality factor) shifts proportionally with the number of electrons present (and perhaps their momentum transfer collision frequency). A detailed description of the physics underlying the microwave cavity measurement technique is outlined in each result chapter, i.e. Chapter 4, 5, and 6.

Cavity design I

The first cavity design, which is used for the experiments described in Chapter 4, is a basic cylindrical cavity made from aluminum, and was based on a design used earlier by Van de Wetering [1]. This design is depicted in Fig. 3.1 with the corresponding dimensions. An important difference compared to earlier work is that it did not include a shower head, but allowed neutral gas to enter through openings in the cylindrical wall. These openings were initially used for microwave interferometry measurements, and to make camera images of the plasma to estimate the size of the sheath regions in the axial direction. The size of the cavity was mainly determined by the large amount of resonant modes that could be excited starting close to 1 GHz for the fundamental modes, which provided the option to perform measurements with multiple higher harmonics.

This cavity consists of a top and bottom disk that encapsulate a hollow cylinder forming the microwave cavity itself (1). The discharge (2) was created by applying RF power to the electrode (3) located on top of the cavity's bottom disk with an insulating disk (4) in between. The cylindrical walls of the cavity and the top disk were grounded, thereby forming the grounded electrode. A SMA connector (5) was mounted on the outside of the cavity on the bottom disk, which protruded the insulating disk and connected the RF transmission line with the RF-powered electrode. As such, an asymmetric capacitively coupled discharge was created inside the microwave cavity. Using screw threads and nuts, the top and bottom disk were pulled towards each other in a fixed position so that the metal components made electrical contact with minimum electrical resistance. A microwave antenna (6) was mounted on the top flange for the injection of microwaves, which consists of a standard SMA connector—standard threaded antenna connector for high frequency applications—to which a copper wire is soldered. The copper wire was positioned in an iterative fashion so that the resonant mode was excited properly. Proper excitation in this case meant that the amount of attenuation of the injected microwave power at the resonance frequency was at least –20 dB, i.e. a factor 100.

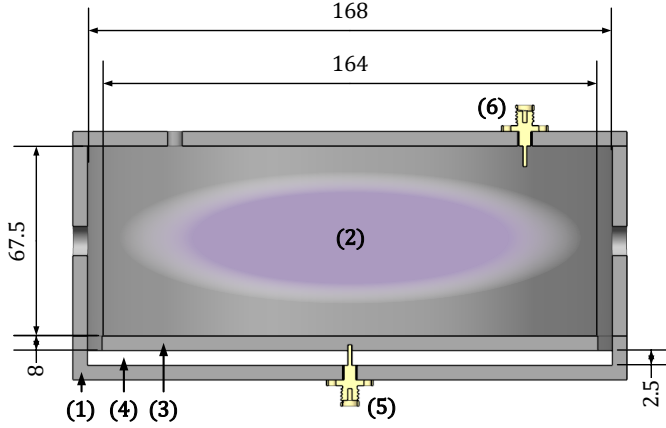


Figure 3.1: Cavity design I: microwave cavity and discharge electrodes as used in Chapter 4. The cavity (1) consists of separate top and bottom disks, and a cylindrical base. A gas discharge (2) is ignited and sustained by RF power applied to the RF electrode (3) located at the bottom of the cavity, and insulated from the grounded cavity by a dielectric disk (4). A SMA connector (5) is used to transfer RF power to the RF electrode, and the microwave antenna (6) allows coupling of the microwaves into the cavity. This figure has been published by Staps *et al* [2].

Cavity design II

The second cavity design, as used for the experiments in Chapter 5, was significantly smaller than cavity design I, as can be seen from Fig. 3.2. This resulted in an increase of the attainable power density (power per unit volume) of about a factor 10, and resulted in higher resonance frequencies and, for a given plasma density, larger diagnostic signals. Another change with respect to the first cavity design is that the microwave antenna (4) was located in the cylindrical side wall of the cavity (2), and that the RF electrode (5), insulating disk (6) and RF connector (7) were located below the top disk of the cavity (1). The microwave antenna was located in the cylindrical wall, because the RF electrode was located on top, and the bottom of the cavity was not accessible due to the placement of the cavity at the bottom of the vessel. The bottom disk (3) was completely solid in this design. The cavity had an interior diameter of 66 mm and height of 40 mm, and contained two thin slits with a width of 2 mm over the full height of the cavity. In addition, a viewing window was integrated in the design by fixing a steel mesh on the inside of the cylindrical wall with screws, which allowed to view the cavity's interior volume over an angle of about 60 degrees and half of the cavity's interior height. The slits allowed laser light to be transmitted through the volume, as explained in the Methods section in Chapter 5.

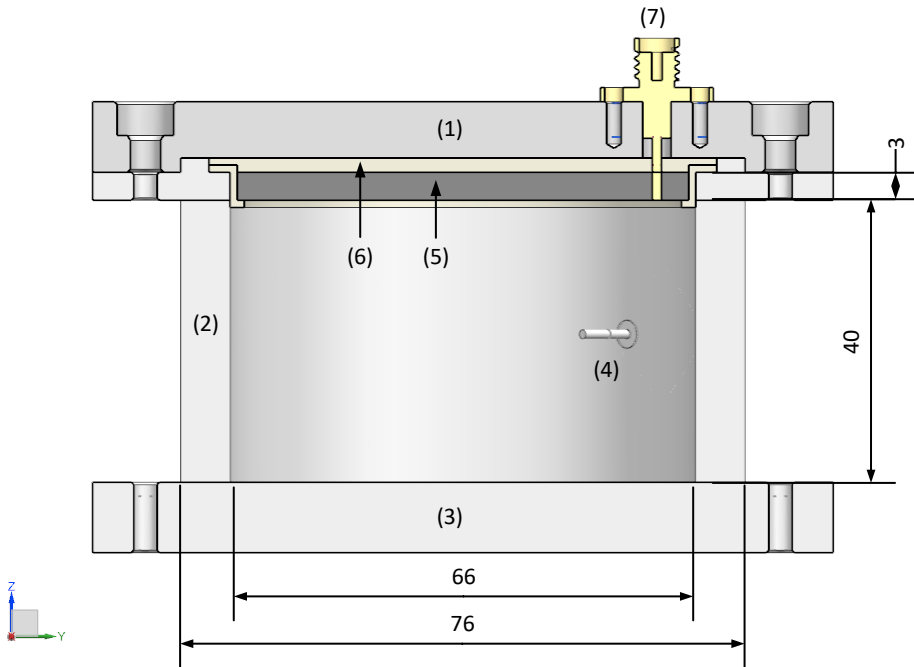


Figure 3.2: Cavity design II: microwave cavity and discharge electrodes used for the experiments presented in Chapter 5. The cavity comprises a disk on top (1), cylindrical base (2) and a solid bottom electrode (3) which are held in a fixed position with respect to each other. A microwave antenna (4) is used to excite resonant modes. The RF-powered electrode (5) is insulated from the grounded cavity by a dielectric disk (6), and powered by the RF transmission line through the SMA connector (7) on top.

Cavity design III

The third cavity design is an improved and extended version of the second cavity design concerning its application for visualizing a dusty plasma and collecting in-situ grown dust particles for ex-situ analysis, and is depicted in Fig. 3.3. The microwave cavity discharge chamber has the same dimensions as the second cavity, comprising a top disk (1) with a KF16 flange for mounting inside the vacuum vessel, and a cylindrical side wall (2). However, there are a few noteworthy improvements.

The first improvement concerns the bottom disk, which is made from a stainless steel mesh (3) allowing dust particles to fall through for subsequent collection.

The second improvement is that the top flange consists of an RF-powered shower head (4) with multiple small holes (spacing of 5 mm in a rectangular array and hole diameter of 0.5 mm), which was electrically insulated from the grounded cavity by a perforated dielectric disk (5). This allowed for a homogeneous gas flow (and neutral drag force) into the cavity volume, whereas the gas entered through diffusion in the case of cavity design I and II.

This cavity also contained two slits in the side wall, but, as a third improvement, the viewing window (6, stainless steel perforated mesh) was spatially extended so that a 160° view across the full axial height of the cavity interior could be captured on the camera images.

The fourth improvement concerned the desire to collect dust grains, formed by the discharge, for ex-situ analysis using, e.g., scanning electron microscopy (SEM) and/or energy-dispersive X-ray spectroscopy (EDX) in order to gain information about the size and composition of the dust grains. As indicated in Fig. 3.3, this improvement led to the addition of an interchangeable holder (9) with locations for seven SEM stubs (10), onto which dust particles could be collected at different spatial locations. An actively actuated cover (8) could be translated in the $-Z$ -direction (as indicated in Fig. 3.3) so that the hole pattern was aligned with the SEM stubs when looking in the $-X$ -direction (as indicated in Fig. 3.3).

A more detailed view of the cover and SEM stub holder can be seen in Fig. 3.4, which shows a view of the X-Y plane by looking into the $-X$ -direction, effectively showing the hole pattern as seen by the plasma. This figure shows the electric actuator (1), which comprises a linear motor with two positions in which the lever (2) was fully extended (base position) or fully retracted (powered position). The cover (3) contained multiple holes (4) with a diameter of 13 mm. If the cover was in the base position, as depicted by (a) in Fig. 3.4, the holes in the cover (4) were aligned with the holes (9) in the SEM stub holder located in between the SEM stubs. In this position, the dust particles were not able to reach the SEM stub surfaces, but were transported towards the pumping system directly. If the electric actuator was powered, as depicted by (b) in Fig. 3.4, the cover was pulled towards the actuator such that the hole pattern of the cover exposed the SEM stub surfaces. When the gas discharge was terminated by shutting down the RF power, the dust particles could fall downwards (in the $-X$ -direction) due to gravity. Subsequently, a part of the dust particles fell onto the SEM substrates (6) and was thereby collected at different spatial locations depending on their initial location in the dusty plasma.

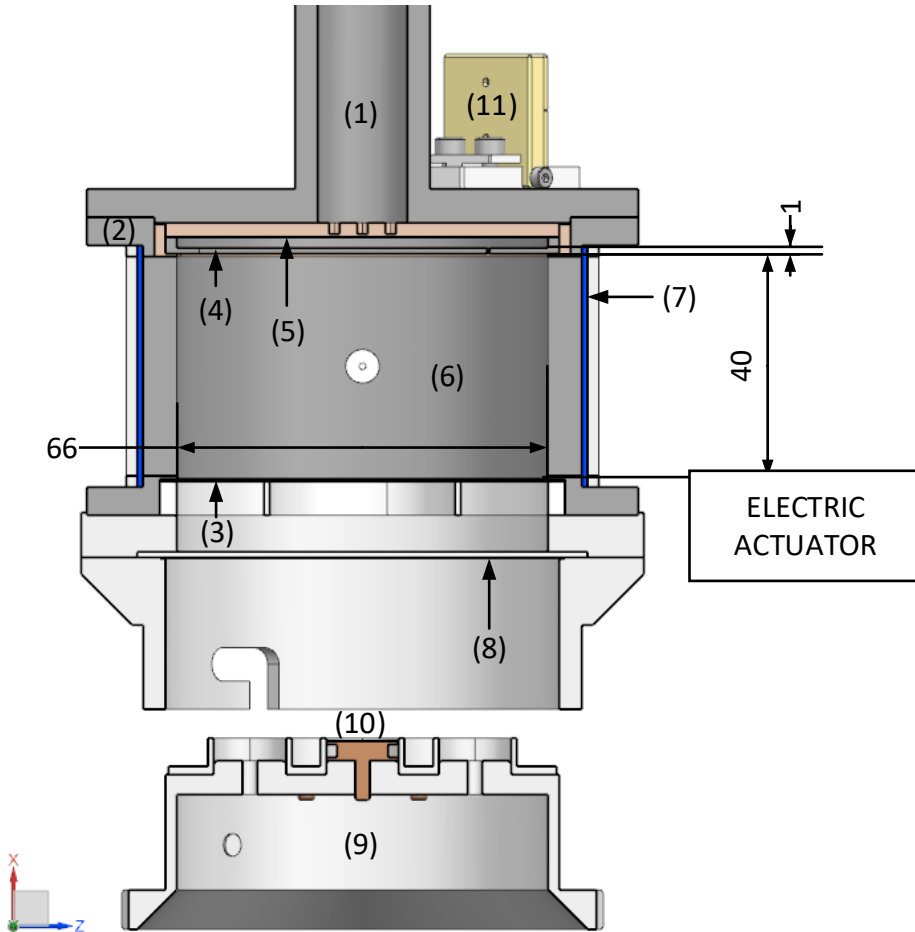


Figure 3.3: Cavity design III: microwave cavity and discharge electrodes used for the experiments presented in Chapter 6. The cavity comprises a top disk (1) with gas inlet, which was fixed to a cylindrical base (2) containing a bottom mesh grid as grounded electrode (3), and an RF-powered shower head-type electrode (4) on top insulated from the grounded cavity by a dielectric perforated disk (5). The cavity side wall contains a viewing mesh (6) on one of the sides and two slits (7) for laser beams to be transmitted through the volume. An actively powered shutter plate (8) with a specific hole pattern can be actuated to expose the SEM substrates (10) mounted on the SEM stub holder (9) at the operator's request. This figure has been published by Staps *et al* [3].

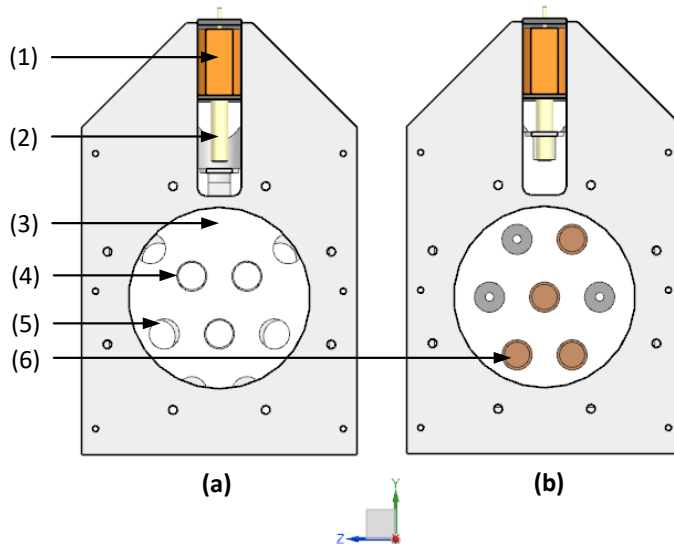


Figure 3.4: SEM stub holder and actuation scheme for collecting dust particles on operator's request (see Chapter 6). Both figure panels contain a cross sectional view of the cover and SEM stub holder in the Y-Z plane looking into the -X-direction, which shows the patterns as seen by the plasma. In numerical order, the numbers indicate the actuator (1) with lever (2), which pulls on the cover (3) with holes (4) when actively powered. This cover is aligned with the holes (5) in the stub holder in the base position, and exposes the SEM substrates (6) when the actuator was powered. (a) This cross sectional view shows the base position. (b) This cross sectional view shows the powered position, when the SEM substrates are exposed to the plasma volume for the deposition of dust grains. This figure has been published by Staps *et al* [3].

3.1.2 Vacuum vessel, gas supply and pumping system

A schematic overview of the systems for the creation and sustenance of the vacuum is depicted in Fig. 3.5, which shows the vacuum vessel including the used cavity, the gas supply lines, and the pumping system. The vacuum vessel had an interior diameter of 600 mm and an interior height of 400 mm. Using ISO-K flanges and EPDM seals, the base pressure was $\sim 1 \times 10^{-6}$ mbar, while experiments were performed at an operating pressure of $\sim 1 \times 10^{-1}$ mbar. This means that the purity of the gases introduced ($\geq 99.999\%$) determined the impurity level of the gas composition.

Before the start of an experiment or after maintenance was done to the setup, a vacuum was created by evacuating the air out of the vessel using two pumps. First, an initial vacuum was created at a pressure in the range 0.01 – 0.1 mbar using a dry scroll pump (Kashiyama NeoDry 30E). Below 0.1 mbar, a turbo-molecular pump (Pfeiffer TPH 240, water-cooled) was started to gain a further reduction of the base pressure to 1×10^{-6} mbar. The combination of the turbo-molecular and scroll pump was continuously running during experiments as well as during idle periods to maintain the purity in the vessel. In case maintenance had to be performed, e.g., cleaning the cavity or replacing SEM substrates, the vessel was aerated to atmospheric pressure using nitrogen. Afterwards, the vacuum pumps were ran for at least two days in order to obtain again the base pressure before new experiments were performed.

Neutral gas was supplied to the vessel using two supply lines, of which one was used for the plasma gas flow (argon), and a second line for the dust precursor gas flow (HMDSO). The top flange of the vacuum vessel was chosen for the injection of the gas, because this facilitated the use of different types of cavities (see Section 3.1.1) without an integrated shower head. For the experiments in this thesis, the gas entered the discharge gap by diffusion and advection through openings in the cavity walls (i.e. laser slits and meshed viewing ports). However, it should be noted that the cavity design depicted in the figure has an integrated shower head (cavity design III used in Chapter 6), and this allows for a homogeneous introduction of the gas flow in future experiments.

At the start of an experiment, an argon flow was introduced using a mass flow controller (Brooks SLA 5850, ≤ 300 sccm) supplying argon with a purity of 99.999%, although the setup provides the option to use helium. During the experiments, the argon flow rate was set to 20 sccm, the automated valve (V1) was opened, the shutter valve (V6) was closed completely, and the butterfly valve (V5) was fully open. This resulted in an operating pressure of 5.4×10^{-2} mbar, which was monitored using a Pfeiffer full range pressure gauge (PG). For dust growth experiments, the second step was the introduction of the precursor hexamethyldisiloxane (HMDSO, Sigma-Aldrich, purity 99.5%), which is in the liquid phase at room temperature, and put into a small container before a series of experiments. After filling the container, the valves (V3 and V4) were opened completely to remove the ambient air captured during the insertion of the liquid. Thereafter, the valve was closed and an equilibrium was established between condensation and evaporation at the liquid-gas interface leading to an equilibrium vapor pressure during idle periods of the setup. By opening the automated valve (V3) and tuning the manual micrometer spindle valve (V4), HMDSO vapor was injected into the vessel as a gaseous precursor at a controlled rate.

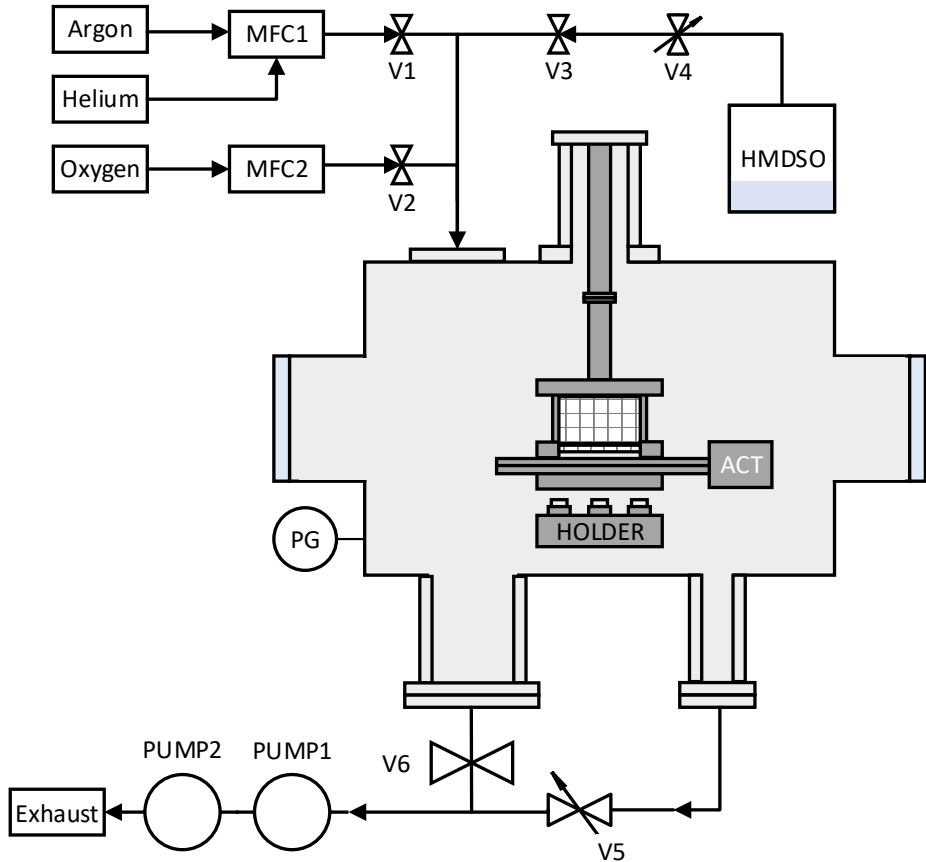


Figure 3.5: Gas supply and pumping system for the low pressure setup. A large vacuum vessel—including quartz viewing windows and vacuum feedthroughs for the RF power, microwaves, and gas lines—contained the microwave cavities with discharge electrodes described in Section 3.1.1. The schematic of the cavity is based on cavity design III. For each cavity design, the discharge was created using the RF power supply described in Section 3.1.3. Gas was injected at the top of the vessel using various combinations of noble (i.e. argon) and reactive gases (i.e. HMDSO), which could be controlled in terms of their flow rates using the mass flow controllers (MFCs). The gas lines could be opened or closed automatically using pneumatic valves (V1-V3) controlled by the computer, which allowed for accurate timing of the injection of reactive gases such as HMDSO for time-controlled dust growth. The pressure inside the vessel was monitored by the pressure gauge (PG) and controlled, for a given inflow of gas, by adapting the flow resistance through the valves (V5 and V6), for a constant pumping speed of pump 1 and 2.

The manual valve (V4) was adjusted such that the desired HMDSO partial pressure was added to the existing partial pressure caused by the argon flow, where the partial HMDSO pressure was typically around 1.3×10^{-2} mbar (e.g., during the experiments covered in Chapter 5).

The experimental setup covers additional possibilities for studies targeting dust growth, which have not been pursued in this thesis, but are nevertheless worthy of consideration. First, it should be noted that this type of precursor injection allows for any type of reactive gases, which are liquid at room temperature, to be used in the setup. Second, the possibility of introducing oxygen exists using the second mass flow controller (MFC2 and V2, Brooks SLA 5850, ≤ 30 sccm, purity 99.999%). Oxygen was not used in this work during the low pressure experiments, but could be valuable to investigate the effect of oxygen on the material composition of the dust particles formed in the discharge. This is because HMDSO contains only a single oxygen atom compared to two silicon atoms, which could limit the formation of silicon dioxide-like particles. Third, the shower head integrated in the cavity currently in place allows for a homogeneous introduction of the gas flow, which exerts a direct neutral drag force on the dust cloud. This could be valuable in studies to actively replenish the volume by the removal of dust particles, radicals and other products, prior to subsequent pulses.

3.1.3 RF power supply

Radio-frequency (RF) voltage excitation, using the system indicated in Fig. 3.6, was applied to the powered electrode of the discharge gap for the creation of gas discharges. This input was generated using a low voltage signal generator (0 – 5 V) at a frequency $f_{\text{RF}} = 13.56$ MHz, which was amplified by an RF amplifier (Amplifier Research Model 100A250B, 0.01 – 250 MHz, ≤ 100 W CW) with an output impedance of 50Ω . Using a matching circuit with an L-type design, the plasma impedance was matched close to 50Ω for optimum power transfer to the load.

To monitor the RF voltage and power, two probes were used for electrical characterization of the transmission line. A first power sensor (Amplifier Research Model PM2002) was integrated in the transmission line between the RF amplifier and the matching circuit to monitor the amount of reflected and transmitted power. This power sensor thus observed the total amount of power absorbed by the matching circuit in combination with the plasma load, and did see a load impedance of nearly 50Ω if the circuit was properly matched. A second power sensor (Impedans OctivPoly 1.0) was installed between the matching circuit and the plasma load, of which the signals were digitally acquired with $10 \mu\text{s}$ time resolution using a computer (PC). This was done in order to avoid measurement of the effect of the matching circuit components on the phase angle and dissipated power. Moreover, this position allowed for digital acquisition of these signals, e.g., the phase angle of the third harmonic, which are sensitive to changes in the plasma due to dust formation.

The experiments in Chapter 5 and 6 were performed using continuous wave (CW) excitation of the discharge, while the experiments in Chapter 4 were performed using pulsed RF discharges. A pulse delay generator was used to trigger the RF signal generator which then provided an RF output for a limited period of time. This allowed the synchronization of the RF pulses with other signal acquisition systems

such as those used for microwave measurements, and the second RF power sensor in time-resolved measurement mode.

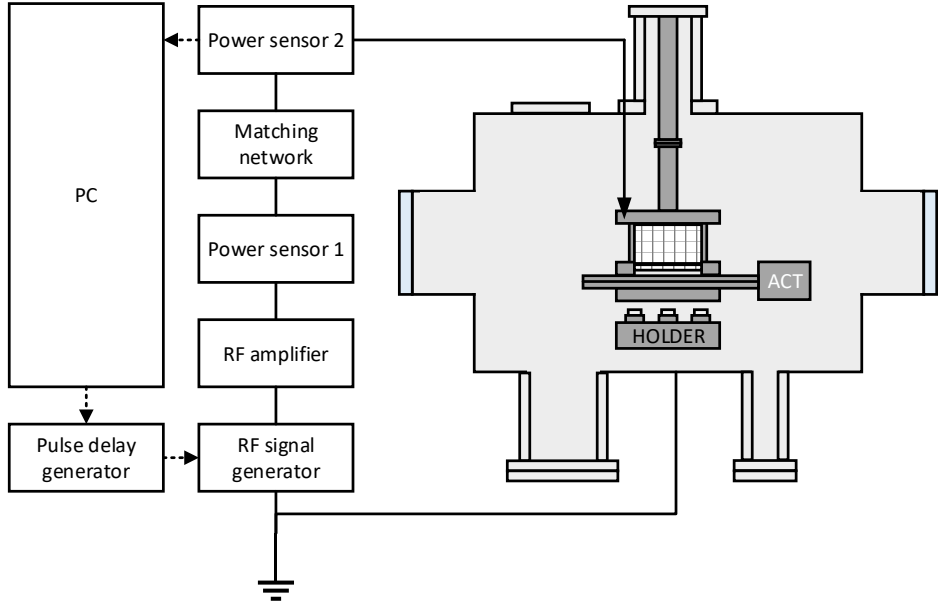


Figure 3.6: Power supply for RF discharges in the low pressure setup. The 13.56 MHz (RF) low-voltage signal from the generator was amplified and sent to the RF-powered electrode, which was integrated in the microwave cavity. An L-type matching network ensured that the power transfer into the load was close to optimal, and the reflected and absorbed RF power were monitored using two power sensors. The computer was used to digitally acquire the signals from the second power sensor. For pulsed operation of the discharge, a pulse delay generator triggered the RF signal generator which then generated the RF output for a limited period of time. This triggering signal was also sent to other devices, such as the microwave system, in order to synchronize the discharges with diagnostic measurements.

3.1.4 Optics

The optical systems used for the low pressure setup are shown in Fig. 3.7, which include a laser light scattering setup (532 nm path), photodetachment setup (266 nm path), and a high speed camera for imaging.

Laser light scattering experiments were performed using a green laser (532 nm, Nd:YAG, continuous, ≤ 500 mW) for the visualization of the dust particle cloud. The Nd:YAG laser was mounted onto a XYZ-stage in order to accurately determine the initial location of the beam. The mirrors, M1 and M2, used to reflect and steer the laser beam were obtained from Thorlabs: type NB1-K13, Nd:YAG mirrors, suitable for 532 nm and 1064 nm laser light, and with a reflectance $\geq 98\%$. The laser light was reflected by a first mirror (M1) and transmitted through two apertures (A1 and A2) that were used to align the beam at the target height. The target height was set initially to the axial center between the upper (RF) and lower (ground) electrode of the discharge gap. The second mirror (M2) was used in combination with the first mirror to steer the beam through the slits in the cavity.

A set of two lenses (L1 and L2) was used to shape the laser beam with circular cross section into a planar sheet with a thickness equal to the beam diameter. This was done by diverging the beam using a concave cylindrical lens (L1), and thereafter converging the beam by a convex cylindrical lens (L2). Hereafter, the beam propagated through the vacuum window (quartz, transmission efficiency $\geq 85\%$) and the beam splitter (BS1) located inside the vacuum, which transmitted $\geq 99.5\%$ of the laser light. The beam splitter was oriented such that the green laser sheet and ultraviolet laser beam were actually merged and, therefore, the laser beams coincided spatially.

After passing the cavity slits, the dust cloud (if present), the second vacuum window and the second beam splitter (BS2) (oriented to function as an actual beam splitter), the green laser light was captured by a photodiode (PD, Thorlabs DET10A). By comparing the intensity before and after dust was grown, an extinction ratio could be determined in order to estimate the dust density for a given dust size.

Part of the laser light was scattered by dust particles in case the dust density and/or dust size was sufficient. This scattered light was filtered using a narrow band-pass filter (BPF, central wavelength 532 nm, full-width-at-half-maximum 3 nm) and captured using a high speed camera (Photron Mini UX100), typically at a frame rate of 50 – 1000 fps.

Photodetachment was induced using a pulsed ultraviolet (UV) laser (Quantel, 266 nm, pulsed Nd:YAG laser, pulse length 8 ns) that targeted the axial center between the electrodes. A first mirror (M3) and second mirror (M4) were used to steer the laser through the cavity. These mirrors (Thorlabs NB1-K04) were designed for use with 266 nm pulsed laser light with a reflectance $\geq 99.0\%$, and a sufficient damage threshold. A set of two cylindrical lenses was used to reduce the beam diameter to about 1 mm so that it was smaller than the width of the cavity slits (2 mm). This ensured that the laser beam could enter and leave the cavity without reflections. Subsequently, the beam propagated through the vacuum window and was reflected by the third UV mirror (M5) and the beam splitter (BS1). After passing the cavity, the UV laser pulse was reflected by the second beam splitter (BS2) so that the light was captured by the laser power sensor (LPS). This power sensor (Ophir PE50-DIF-C

pyroelectric sensor with an Ophir Starbright meter) monitored each laser pulse to provide the laser pulse frequency (verification of the laser setting), and an average and standard deviation of the laser pulse energy. The signal was determined by a moving average filter with a duration of 1 s, and digitally acquired on a computer.

It should be noted that the complete optical system was integrated in metal enclosures that were fitted to the vacuum windows. This ensured that the laser light was not able to escape from the enclosures for personnel safety. On the other hand, stray light was not able to enter the enclosures and cause distortion of, e.g., the camera images and the laser diagnostics.

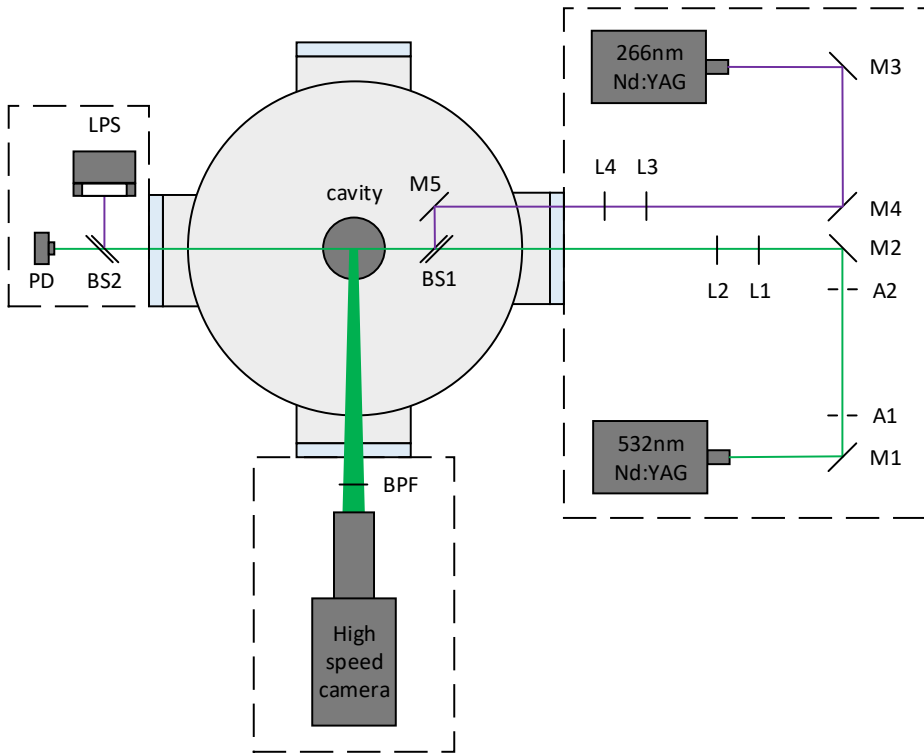


Figure 3.7: Optical system for the low pressure setup comprising a green (continuous wave, CW) laser for laser light scattering and extinction measurements, and a pulsed ultraviolet laser for photodetachment. The green laser (532 nm) propagated from the Nd:YAG output through the cavity towards the photodiode (PD), and a part of the light was scattered and captured by the high-speed camera. The pulsed ultraviolet laser beam (266 nm) propagated from the right into the vessel, and was reflected through the cavity via two beam splitters (BS) towards the laser power sensor (LPS).

3.2 Setup for experiments under atmospheric pressure conditions

The setup used for atmospheric pressure discharge experiments—presented in Chapter 7, 8, and 9—is discussed in this section. In Section 3.2.1, the integrated design of the plasma jet and microwave cavity are explained in detail. In Section 3.2.2, the gas supply and pumping system are considered with respect to ambient air removal and gas supply during experiments at atmospheric pressure under controlled conditions. In Section 3.2.3, we note specific items of the radio-frequency power supply, including matching and the in-house design of the power probe for accurately monitoring the electrical characteristics. In Section 3.2.4, this section is concluded with an overview of the 532 nm laser setup for dust particle visualization and extinction measurements, and the pulsed 355 nm laser setup used for laser-induced photodetachment of negative ions, and possibly charged nanoparticles.

3.2.1 Integrated design of the plasma jet and microwave cavity

The central component of the atmospheric pressure setup was the vacuum flange with integrated plasma jet and mounted microwave cavity. The plasma jet design was based on the plasma reactor geometry used by Van der Schans *et al* [4]. However, the excitation for the production of gas discharges in this work was done by RF excitation instead of by high-voltage pulses so that the physical mechanisms of, e.g., electron heating were comparable to those governing the low pressure discharges. This required a complete re-design of the jet to account for different requirements for stable discharge operation and microwave measurements.

Fig. 3.8 shows the integrated design of the plasma jet and microwave cavity. The base was an ISO160-K flange (1) which fitted to a standard cubic vacuum vessel with an ISO160-K opening. The top flange (1) contains two KF25 flanges (2 and 3) for connecting internal elements with the microwave cabling, temperature sensor and gas inlet for the background gas. In the middle of the flange, a printed circuit board (4) can be seen that was specifically tailored to the setup for monitoring the RF voltage, current and power. The micrometer spindle (5) was used to alter the distance of the microwave cavity (6) with respect to the plasma jet, while the cavity and jet were present inside the controlled atmosphere in the vacuum vessel.

A backplate (7) connected the microwave cavity to the base flange through four leaf springs (8, of which two are indicated by the arrows) that counteracted the force exerted on the cavity by the micrometer spindle's extension (9). Two springs (10) pulled the back of the cavity towards the top flange, while the spindle pushed the cavity downwards. The connection through the four leaf springs ensured that, when moving the cavity along the X-axis (opposite to the gravitational direction), the cavity could only be translated in the normal direction with respect to the leaf springs' flat surfaces. This is because the leaf springs are, by approximation, infinitely stiff in the directions parallel to their flat surface, and have a finite stiffness in the direction perpendicular to their surface. Consequently, this implied that the radial center of the cavity was always aligned with the radial center of the plasma jet, and that cylindrical

symmetry could be applied in the interpretation of the experimental results.

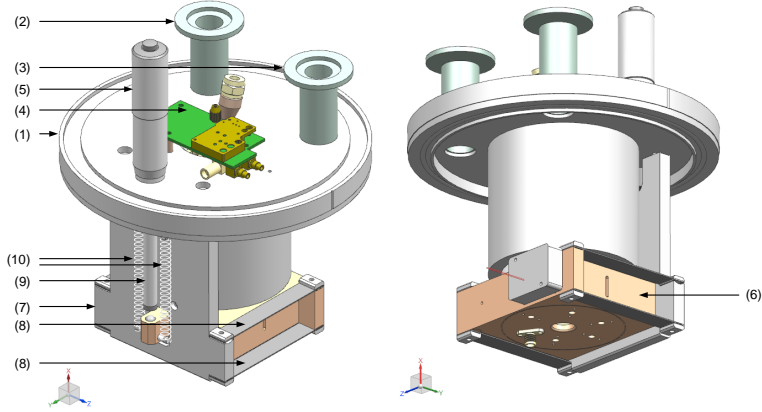


Figure 3.8: Design of the plasma jet and microwave cavity integrated on a standard vacuum flange (1). Two KF25 connections (2 and 3) were used, of which the first flange was used for connecting the microwave antenna and temperature sensor to systems outside the vessel, and the second flange allowed the background gas to be fed into the vessel. The electronic circuit for monitoring the RF voltage, current and power was integrated on a printed circuit board (4) mounted on top of the flange, which was connected to the RF-powered and grounded electrode. A micrometer spindle (5) was used to externally translate the microwave cavity (6) in the X-direction in order to define the distance of the cavity with respect to the gas discharge geometry. A backplate (7) connected the top flange and the cavity through leaf springs (8), while the spindle extension (9) pushed the cavity downwards and the springs (10) pulled the cavity upwards, allowing for accurate ($\sim 5 \mu\text{m}$) control of the cavity-jet distance.

Fig. 3.9 depicts a cross sectional view of the plasma jet and microwave cavity design in the X-Z plane. From top to bottom, it can be seen that the gas inlet (1) for the discharge gap is located outside of the vessel, which was connected to the different gas lines described in Section 3.2.2. This gas flows towards the mixing chamber (2), where six channels (3) are located that connect the mixing chamber to the capacitively coupled discharge gap. It should be noted that only two diagonally oriented channels (3) are visible in the cross section, and the other channels are located under an angle of 60° with respect to each other. This was done such that the gas injection was more homogeneously applied at the beginning of the discharge gap. The gas was driven through the annular gap between the RF needle (4) and the dielectric quartz tube (5). At the end of the tube (6), the gas flow and plasma species (if a gas discharge was generated) entered the volume probed by the microwave cavity (7), which is termed the spatial afterglow.

The gas discharge comprised a capacitively coupled geometry, where the powered electrode (4) was in contact with the discharge, and the grounded cylindrical electrode (8) was covered on the inside by a dielectric quartz tube (5). The grounded electrode

covered the RF needle almost completely over the axial axis, except for a small part that extended above the top flange, which ensured that the geometry approximated that of an ideal capacitor with a precisely defined capacitance. However, the grounded electrode had a capacitance with respect to the outside world, which is termed the parasitic capacitance of the electrical circuitry. This capacitance can cause variations in the absorbed power by forming an alternative path for the RF current, which thus depends on the location of, e.g., cables. To mitigate the effect of undefined components on the parasitic capacitance, an aluminum hollow cylinder (9) was integrated in the design, which defined the parasitic capacitance at a specific value such that the matching conditions for the discharge were properly defined regardless of other (conductive) elements.

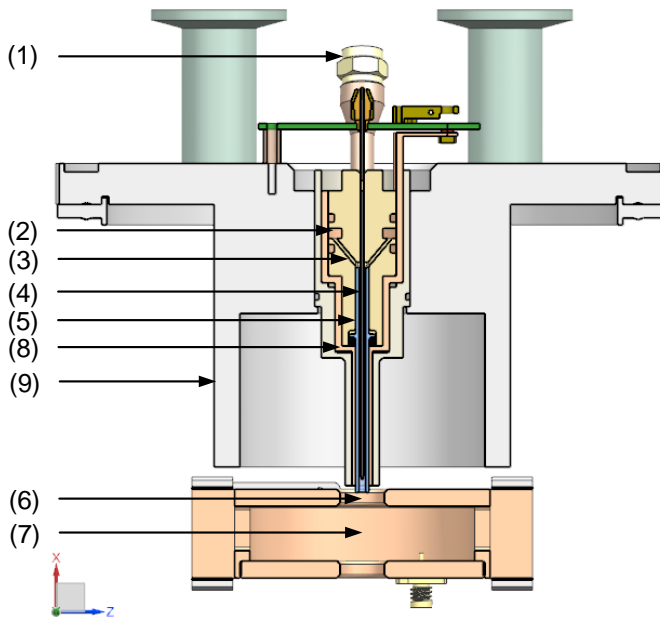


Figure 3.9: A cross sectional view of the integrated design comprising the plasma jet and microwave cavity in the X-Z plane. A gas inlet (1) introduced the gas mixture into the mixing chamber (2), which was connected to the discharge gap through six channels (3). The RF needle (4) and dielectric tube (5) formed the gap through which the gas could flow, which left the gap at the tube exit (6) and entered the cavity measurement volume (7). A grounded electrode (8) formed, together with the RF-powered electrode (4) and dielectric tube (5), a capacitively coupled dielectric barrier discharge geometry. The large hollow cylinder (9) defined the parasitic capacitance so that the electrical characteristics of the discharge geometry were not perturbed by external (conductive) elements such as cabling for the temperature sensor and microwave signals.

3.2.2 Vessel, gas supply and pumping system

The atmospheric pressure experiments are conducted at standard pressure, i.e. $p \approx 1000$ mbar, and near room temperature, i.e. $T = 20 - 25^\circ$. The first experimental results described in Chapter 7 were obtained in a situation where the plasma jet effluent interacted with the ambient air. The ambient air contains, besides nitrogen and oxygen, a fluctuating amount of water vapor. Variations in the composition of the background gas undermined the reproducibility on the longer term and complicated the chemistry. To avoid these effects, the plasma jet and microwave cavity were integrated in a vacuum vessel from which the ambient air species could be replaced by a background gas with a controlled composition.

Fig. 3.10 shows the gas supply and exhaust system used for the atmospheric pressure experiments. On the top of the figure, it can be seen that there are four different gas lines. MFC1 and MFC4 were connected to the gas flow introduced in the plasma jet's discharge gap, whereas MFC2 and MFC3 were used to provide the background gas flow through a port in the top flange. The background gas could, after entering the port, freely flow through the vessel's volume and the microwave cavity volume. Both gas flows left the vessel through a port at the bottom connected to the central exhaust system of the laboratory through three parallel pipelines.

The exhaust system was designed so that a pre-experiment vacuum could be created to remove ambient air prior to experiments, and a controlled atmosphere could be maintained during an experiment. Prior to experiments for which a controlled background gas was desired, the manually-controlled valve (V4) connected to the scroll pump (PUMP) was opened in order to create a vacuum inside the vessel and other gas supply lines up to the mass flow controllers, while V5 was closed. A vacuum with a base pressure of ~ 0.1 mbar was created to evacuate the ambient air species. Afterwards, the vacuum was disconnected from the vessel by closing V4 (vacuum valve with diameter 40 mm), and the volume was filled with a known gas (i.e. helium for the experiments described in Chapter 7 and 8, and an argon-oxygen mixture for the experiments described in Chapter 9) using MFC3 (and, in some cases, MFC2) until the pressure gauge (PG) indicated ≥ 1000 mbar. This resulted in a purity level in the vessel of about 99.99%. For safety, a pressure-relief valve (V6) was installed that automatically opened up if $p > 1100$ mbar, and an emergency button was installed that could close the valves V1, V2 and V3 in case of emergency. When atmospheric pressure was reached, the valve V5 was opened, the discharge gas flow was installed, and the combination of background and discharge gas continuously flew through the system and left via the exhaust.

In the first set of experiments, described in Chapter 7, a helium gas flow (purity 99.999%) was introduced into the discharge gap using a mass flow controller and automated valve (MFC1 and V1, Brooks SLA 5820, ≤ 3000 sccm). Meanwhile, the effluent entered the ambient air (relative humidity 30 – 65%) downstream of the gap. During this experiment, there were no vacuum windows on the sides of the vessel so that the ambient air could freely enter the volume. In addition, only the exhaust valve (V5) was opened so that a continuous suction was applied to the volume which ensured the continuous removal of the gases introduced and any plasma-generated species such as ozone (hazardous to human health at high concentration).

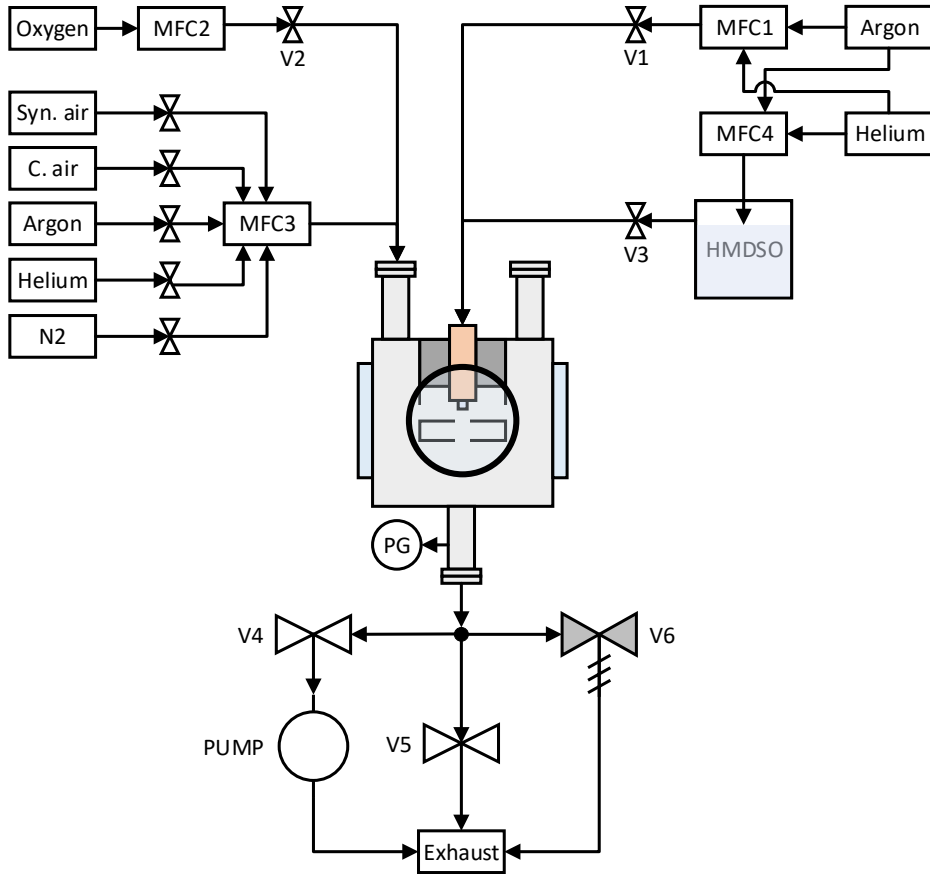


Figure 3.10: Gas supply and exhaust system for the atmospheric pressure setup. Four gas supply lines connected to mass flow controllers (MFC1 to MFC4) were used to supply the discharge gap (discharge gas flow) and vessel volume (background gas flow) with the desired mixture of gases at controlled flow rates. The plasma jet and microwave cavity were integrated in a vacuum vessel to enable experiments in a controlled atmosphere, and pre-experiment removal of ambient air. The pumping system is located at the bottom of the vessel. The operator has the choice of connecting the vacuum system for air removal prior to experiments. During experiments, the vessel volume is directly connected with the central exhaust system in order to conduct experiments at atmospheric pressure with continuous renewal of the gas and removal of plasma-produced species. The abbreviations denote synthetic air (Syn. air, 80% N₂ and 20% O₂) and compressed air (C. air, de-humidified and pressurized ambient air).

In the second set of experiments, described in Chapter 8, a reactive gas component called hexamethyldisiloxane (HMDSO) was added to the pristine helium flow through the discharge gap in order to promote the formation of dust grains. Before the experiments were carried out, a vacuum was created to remove the ambient air, and the vessel and other gas pipelines were filled with pristine helium (purity 99.999%). As opposed to the low pressure experiments, a bubbler system was used to add HMDSO vapor to the helium carrier flow. Helium was driven through the HMDSO fluid layer using a mass flow controller (MFC4, ≤ 100 sccm) which actively mixed the helium gas with the HMDSO vapor. By opening valve V3, the helium-HMDSO mixture entered the pipeline connected to MFC1, where the helium-HMDSO mixture was diluted by adding pristine helium gas (MFC1 and V1, Brooks SLA 5820, ≤ 3000 sccm). The diluted mixture entered the discharge gap afterwards for subsequent processing in the plasma. Meanwhile, a continuous background flow was introduced into the vessel using MFC3 with pristine helium, which reduced the complexity of the gas mixture compared to ambient air.

In the third set of experiments, described in Chapter 9, the background gas contained a mixture of argon and oxygen. Again, the vessel was cleaned from ambient air prior to the experiments using the vacuum system. Thereafter, the vessel and gas supply lines were filled with a mixture of argon (MFC3, 2000 sccm, purity 99.999%) and oxygen (MFC2 and V2, 150 sccm, purity 99.999%) as the background gas, which was continuously applied also during the experiments. The discharge gas comprised pure argon gas (MFC1 and V1, 3000 sccm, purity 99.999%), which interacted in the region downstream of the discharge gap with oxygen.

3.2.3 RF power supply

The radio-frequency (RF) power supply used for the atmospheric pressure setup is schematically depicted in Fig. 3.11, indicating the main electrical components, and a schematic view of the plasma jet. An RF signal generator created sinusoidal waves at a frequency of 13.56 MHz with a voltage of 3 – 5 V depending on the desired RF power. This signal was amplified by the RF amplifier (Amplifier Research Model 75A250, 0.01 – 250 MHz, ≤ 75 W CW) and sent to the matching coil. Together with the capacitive discharge gap, the inductance of the coil formed an LC-circuit with a resonance frequency that could be tuned by changing the inductance. The mechanical construction of the coil was such that the distance between the turns of the spring-like wounded coil could be manually changed.

It should be noted that only a variable inductor was necessary to tune the system impedance, because the discharge gap contained a dielectric barrier avoiding conduction current. However, the stray capacitance can be troublesome—as mentioned earlier in this chapter—because the system (due to atmospheric pressure) was open to external perturbations to the capacitance due to, for example, cabling. The stray capacitance was therefore defined by including a large aluminum cylinder surrounding the plasma jet, as can be seen in Fig. 3.9.

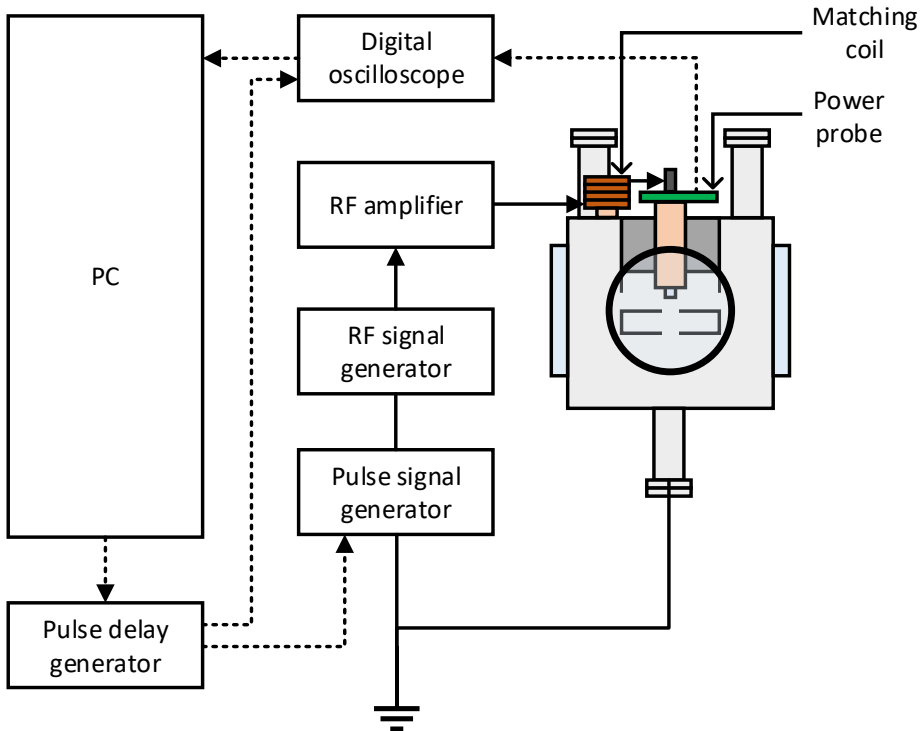


Figure 3.11: RF power supply for atmospheric pressure experiments. An RF signal generator provided a low-voltage sinusoidal signal amplified by an RF amplifier and transferred to the matching coil. The matching coil, together with the capacitance of the discharge gap, enabled tuning of the circuit's resonance frequency for optimal power transfer. After a discharge was created, the RF voltage, current and plasma absorbed power were monitored using the digital oscilloscope which allowed for optimizing the matching conditions. For pulsed discharge experiments, a pulse delay generator was used to trigger the pulse signal generator, the oscilloscope and the microwave system. As such, the RF power circuit was triggered simultaneously with diagnostic systems such as the microwave system and the power measurement. The computer configured the pulse delay generator, and acquired digitally the oscilloscope data.

The matching procedure was as follows. First, a discharge gas was chosen and installed through the discharge gap at a controlled flow rate. Second, continuous RF power was applied to the RF-powered (needle) electrode. Third, the RF voltage, current and absorbed power were monitored on the digital oscilloscope. Fourth, the inductance was changed to maximize the amount of absorbed power by monitoring the oscilloscope signals.

The same matching procedure was applied before pulsed discharge experiments were performed, because the capacitance of the discharge gap (without plasma) is the dominant factor determining the resonance frequency of the electrical circuit. However, for pulsed discharges, the pulse delay generator was set to a certain repetition frequency, and provided short pulses with a duration of $1\ \mu\text{s}$ to the pulse signal generator and oscilloscope. The pulse signal generator was necessary, because the pulse delay generator produced signals between $0 - 5\ \text{V}$, while the RF signal generator output required an input signal between $-5 - 5\ \text{V}$ to set its output between $0 - 5\ \text{V}$. The RF signal generator was set to burst mode so that, for each electronic pulse from the pulse signal generator, the RF signal was produced for a limited period of time (configured on the RF signal generator itself). Simultaneously, the oscilloscope was triggered at the same rate so that the RF current, voltage and power were monitored before, during and after the RF power pulse was applied.

The RF signals were measured using an in-house designed power probe integrated on a printed circuit board (PCB). The design was based on the original design by Beijer *et al* [5], and a detailed explanation of the electronic circuit and the measurement principles can be found in that reference. Here, it suffices to note that the RF voltage is acquired by capacitively coupling the high-voltage signal to a low-voltage measurement circuit. The RF current is measured using a resistor, connected in series with the grounded electrode, and the actual ground that formed the reference for the circuitry (such as the vessel). The RF voltage and current are multiplied in a multiplying probe on the PCB, using a fixed electrical circuit, which ensured that there were no changes possible in the phases between the voltage and current signal. In addition, the RF voltage induced a non-negligible signal in the RF current measurement path, and vice versa, which is termed cross-talk. This resulted in the measurement of a non-zero absorbed power, even when only a high-voltage RF signal was applied to the discharge gap, without creating a discharge. A cross-talk cancellation circuit was added and calibrated such that the absorbed power was equal to zero (within the noise band), when the RF current was absent. Moreover, a temperature correction circuit was integrated to avoid the effect of changing temperature causing drifts in the circuitry and leading to drift in the absorbed power measurement. The aforementioned elements were integrated onto a single PCB which was mounted directly on top of the vacuum flange. This ensured that the electrical components of the plasma jet (RF electrode, grounded electrode, stray capacitance) and the measurement circuit were fixed with respect to each other so that there were no changes in the phase angle between voltage and current after pre-experiment calibration.

3.2.4 Optics

The optical system was used for the application of the pulsed (ultraviolet) laser to induce photodetachment of negative ions, and for the 532 nm laser for the illumination of dust particles formed inside the discharge tube. The optical paths with respect to the optical components, plasma jet and microwave cavity are depicted in Fig. 3.12.

The pulsed ultraviolet (UV) laser was an EdgeWave InnoSlab IS6III-E configured at a wavelength 355 nm, with a pulse duration 7 – 10 ns, repetition frequency 1 – 15 kHz, and pulse energy ≤ 2 mJ. Mirrors (M1 to M3) were obtained from Thorlabs, type NB1-K08, designed for 355 nm pulsed laser light with a reflectance $\geq 99.5\%$, and a damage threshold exceeding the laser intensity used during experiments. The laser was steered using two mirrors (M1 and M2), and aligned in the horizontal plane using two apertures (A1 and A2). After alignment, the beam was clipped by the second aperture to allow only the most intense part of the beam to pass. The part indicated by M3 consisted of a periscope-type of setup, with a mirror pointing vertically upward onto another mirror steering the beam in the horizontal plane onto the first beam splitter (BS1). Therefore, the position of the laser beam (in the vertical direction) with respect to the gas discharge effluent could be manually controlled. After passing the vacuum windows, and vessel volume, the laser beam was reflected by the second beam splitter (BS2) and targeted onto the laser power sensor (LPS).

The source for laser light scattering experiments was a continuous wave laser (Nd:YAG, 532 nm, indicated by the green laser path), which was steered using multiple mirrors through the vacuum vessel. These mirrors were the same as used for the low pressure setup: Thorlabs NB1-K13, reflectance $\geq 98\%$. The laser beam first hit the mirror M4 and M5, and was aligned in the horizontal plane (perpendicular to the gravitational direction) using two apertures (A3 and A4). After reflection on M6, the laser beam was expanded in the vertical direction (parallel to the gravitational direction) by two cylindrical lenses, where L1 was a concave lens and L2 was a convex lens. After reflection on M7, the laser sheet propagated through the first beam splitter (BS1), merging the laser beams due to its orientation, and the vacuum window, and encountered the second vacuum window and second beam splitter (BS2), acting as an actual beam splitter in this orientation. The second beam splitter was positioned such that the green laser beam passed through it, after which it was filtered by a neutral density filter (F1) and its intensity was captured by the photodetector (PD). Part of the green laser beam was also scattered by dust grains, if present, and this scattered light was filtered by wavelength (F2) and, subsequently, captured using a high-speed camera (Photron Mini UX100).

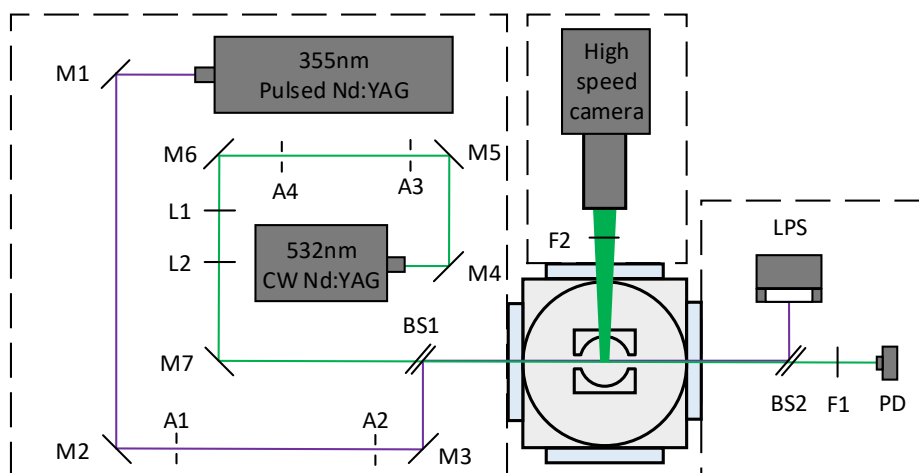


Figure 3.12: Optical systems and beam paths for laser light scattering and laser-induced photodetachment. A 532 nm laser sheet was produced by a continuous Nd:YAG laser, of which the circular beam shape was extended in the vertical direction (i.e. the direction of gravity) using two cylindrical lenses. The 355 nm laser beam was generated using a pulsed Nd:YAG laser, which was merged with the 532 nm laser beam by a beam splitter oriented in reversed direction. After passing the vessel and microwave cavity, the laser beams were monitored to determine the amount of laser intensity for extinction or stability measurements.

3.3 Bibliography

- [1] F M J H Van de Wetering. *Formation and dynamics of nanoparticles in plasmas*. Eindhoven University of Technology, 2016.
- [2] T. J. A. Staps, B. Platier, D. Mihailova, P. Meijaard, and J. Beckers. Numerical profile correction of microwave cavity resonance spectroscopy measurements of the electron density in low-pressure discharges. *Review of Scientific Instruments*, 92(9):093504, 2021.
- [3] T.J.A. Staps, T.J.M. Donders, B. Platier, and J. Beckers. In-situ measurement of dust charge density in nanodusty plasma. *Journal of Physics D: Applied Physics*, 2021.
- [4] Marc van der Schans, Bart Platier, Peter Koelman, Ferdi van de Wetering, Jan Van Dijk, Job Beckers, Sander Nijdam, and Wilbert IJzerman. Decay of the electron density and the electron collision frequency between successive discharges of a pulsed plasma jet in N₂. *Plasma Sources Science and Technology*, 28(3):035020, 2019.
- [5] P. A.C. Beijer, A. Sobota, E. M. Van Veldhuizen, and G. M.W. Kroesen. Multiplying probe for accurate power measurements on an RF driven atmospheric pressure plasma jet applied to the COST reference microplasma jet. *Journal of Physics D: Applied Physics*, 49:104001, 2016.

Effect of spatial electron density profiles on MCRS

Preface. Low-temperature plasmas are widely studied in laboratory environments and form the backbone of many industrial processes. Highly-energized electrons enable processes such as ionization, dissociation and plasma chemical reactions, while the heavy species such as neutral gas atoms and molecules remain near room temperature. Hence, understanding the electron dynamics is crucial to the control and optimization of plasmas and their applications. In this chapter, the impact of electron density profile correction on microwave cavity resonance spectroscopy (MCRS) as a diagnostic tool for low pressure discharges is investigated. Following standard practice, the volume-averaged electron density is first obtained by assuming a uniform plasma in the interpretation of the MCRS diagnostic technique. Second, the experiments are compared with a numerical model solved using PLASIMO software to evaluate the predictive capabilities. Third, profile-corrected electron densities are obtained by means of incorporating the numerically obtained distribution of the electron density and the numerical solution for the resonant microwave electric field in the interpretation of the experimental data obtained by microwave cavity resonance spectroscopy (MCRS). Although the volume-averaged data agrees closely with the electron density found from the numerical model, it is shown that implementing the spatial distribution of the electron density and the microwave electric field leads to a significant correction to the experimental data. The developed strategy could easily be implemented in other situations deploying microwave cavity resonance spectroscopy (MCRS) as a non-invasive technique for measuring the electron density.

This chapter has been published: T.J.A. Staps, B. Platier, D. Mihailova, P. Meijaard, and J. Beckers, *Numerical profile correction of microwave cavity resonance spectroscopy measurements of the electron density in low-pressure discharges*, Review of Scientific Instruments 92, 2 September 2021, 093504, DOI: 10.1063/5.0054851.

4.1 Introduction

A plasma is a (partially) ionized gas comprising free electrons, ions, radicals, and neutral particles. An important subset of the vastly different types of plasmas is constituted by low-temperature plasmas, in which the electrons have energies up to several electron-volts, while the thermal energy of heavy particles (i.e. ions, radicals, and neutrals) remains near room temperature. This allows for low-temperature chemistry that is widely applied in industrial processes such as those used for the production of solar cells [1] and functional coatings [2], the synthesis of (nano)materials [3, 4], and the plasma-based dissociation of CO_2 for fuel synthesis [5, 6]. Since free electrons dictate most of the elementary processes in plasmas, measuring their properties is of paramount importance to enhance the understanding and development of such applications.

A universe of diagnostic techniques for free electrons in plasmas has been developed with the goal of retrieving basic information regarding their density and temperature. The development of the Langmuir probe and associated collection theory was most likely the first endeavor in this regard [7]. However, the invasive nature of this technique and the necessity of complicated models to interpret the measurements are often undesired, e.g., in cases where negative ions are present and when the probe surface may become contaminated by means of plasma deposition [8]. In contrast, microwave-based techniques are able to probe a plasma non-intrusively by measuring the effect of the plasma's permittivity on the propagation (and attenuation) of microwaves. Specifically, microwave interferometry (MWIF) and microwave cavity resonance spectroscopy (MCRS) are well established techniques that are frequently used to monitor the dynamics of electrons in (pristine) radio-frequency discharges [9, 10, 11], microwave-induced plasmas [12, 13], dust-forming plasmas [14, 15], extreme ultraviolet photon-induced plasmas [16, 17, 18] and ultracold plasmas [19]. Despite the frequent use of these microwave-based techniques, one of the most stringent assumptions potentially undermining the accuracy of the methods is that of a uniform plasma medium, which is fundamental in the interpretation of the experimental data.

In this work, we probed an exemplary pristine low-temperature plasma using MCRS and numerically computed the electron density profile for the same conditions and geometry in order to facilitate a more detailed interpretation of the experimental data. The gas discharge was created, experimentally and numerically, in a low pressure argon environment inside a microwave cavity at different argon pressures ranging from 0.030 mbar to 0.300 mbar. First, the volume-averaged electron density was experimentally obtained using time-resolved MCRS for different argon pressures. Second, the numerical model was solved for the same geometry and background gas pressures using PLASIMO software. Finally, the numerically obtained electron density distribution was used for the conversion of the experimental data to obtain a so-called profile-corrected electron density for each pressure case. This facilitated a direct evaluation of the numerical model's performance and the effect of applying profile correction to the experimental data.

This chapter is structured as follows. Section 4.2 treats first the basics of MCRS by discussing the plasma permittivity and its effect on the resonant properties of

a microwave cavity. Section 4.3 discusses the experimental hardware to create the gas discharge under controlled conditions and the methodology by means of which time-resolved MCRES was performed to obtain the cavity response at high temporal resolution. Section 4.4 outlines the basics of the numerical model comprising the drift-diffusion framework, the plasma species and reactions taken into account, and the spatial solution of the electron density in quasi-steady state. Section 4.5 governs the main result of this work by presenting the (experimentally obtained) volume-averaged electron densities as a function of time, the profile correction method, and the comparison of the volume-averaged and profile-corrected experimental data as a function of the gas pressure. Section 4.6 completes this chapter with the conclusion.

4.2 Microwave cavity resonance spectroscopy

To understand the microwave cavity resonance spectroscopy (MCRES) technique, the dispersive property of plasma and the respective effect on electromagnetic (micro)wave propagation is discussed in Section 4.2.1. Subsequently, in Section 4.2.2, the operational principles of MCRES are explained by reviewing the effect of a gas discharge on eigenmodes excited in a resonant microwave cavity.

4.2.1 Refractive index of plasmas

Microwave-based diagnostic techniques exploit the dispersive property of plasmas. This is because a difference in optical path length (for the microwaves) is induced when traveling through plasma instead of, for instance, vacuum or surrounding air. The refractive index n indicates the relative velocity v of an electromagnetic wave in a medium compared to the velocity c , which the same wave would have in vacuum, as

$$n = \frac{c}{v} = \sqrt{\varepsilon_r \mu_r}, \quad (4.1)$$

with ε_r the relative permittivity and μ_r the relative magnetic permeability. Note that—by definition—in vacuum $v = c$ and therefore $n = 1$.

For an unmagnetized plasma, Eqn. (4.1) can be simplified because μ_r equals unity. The plasma's refractive index then becomes a function of its permittivity ε_p only,

$$\varepsilon_p = \varepsilon_0 \varepsilon_{r,p} = \varepsilon_0 \left(1 - \frac{f_{pe}^2}{f^2} \right), \quad (4.2)$$

where ε_0 the permittivity of vacuum, the relative (plasma) permittivity $\varepsilon_{r,p}$ is given by the Lorentz-Drude model [20], f the (microwave) excitation frequency (generally in the range of 1 – 10 GHz), and f_{pe} the electron plasma frequency. The electron plasma frequency can be seen as the time scale on which the plasma effectively shields external (electromagnetic) perturbations, and can be expressed as

$$f_{pe} = \frac{1}{2\pi} \sqrt{\frac{n_e e^2}{\varepsilon_0 m_e}}, \quad (4.3)$$

with n_e the electron density, e the elementary charge and m_e the electron mass. It should be noted that Eqn. (4.2) only holds for so-called collisionless plasmas, i.e. plasmas in which the typical frequency ν_m of elastic collisions between electrons and neutral species is much lower than the electron plasma frequency ($\nu_m \ll f_{pe}$). A detailed description of the effect of collisions on ε_p and the diagnostic method can be found in Platier *et al* [21].

The shielding property of plasmas characterized by f_{pe} in Eqn. (4.3) is important for MCRS. This is because only electromagnetic waves with frequencies $f \gg f_{pe}$ are able to propagate through the plasma, while electromagnetic waves with frequencies $f \ll f_{pe}$ are shielded, and subsequently reflected.

4.2.2 Principles of MCRS

MCRS is based on the effect of free electrons on standing (or resonant) microwaves. Low-power (\sim mW) microwaves are introduced in a (cylindrical) pillbox cavity which is electromagnetically closed in the range of 1 – 10 GHz. These microwaves are resonantly absorbed by the cavity at specific frequencies depending on the (fixed) size of—and the permittivity of the medium inside—the cavity.

Creating a discharge inside a microwave cavity leads to the presence of free electrons, which changes the permittivity compared to vacuum such that the resonance frequency goes to a higher pitch. Usually, f_p denotes the resonance frequency of a plasma-filled cavity and f_1 represents the resonance frequency—corresponding to the same resonant mode—in vacuum. This means that the difference $\Delta f = f_p - f_1$ in resonance frequency yields information about the change in permittivity due to plasma.

The nature of the MCRS technique is revealed by formalizing the relationship between the resonance frequency of a specific resonant mode, its (squared) electric field profile, and the change in permittivity of the medium $\Delta\varepsilon$ inside the volume of the cavity using the Slater perturbation equation [22],

$$\frac{\Delta f}{f_1} = - \frac{\iiint_{V_c} \Delta\varepsilon(\mathbf{r}) |\mathbf{E}(\mathbf{r})|^2 d^3\mathbf{r}}{2\varepsilon_0 \iiint_{V_c} |\mathbf{E}(\mathbf{r})|^2 d^3\mathbf{r}}, \quad (4.4)$$

where $\mathbf{E}(\mathbf{r})$ denotes the (microwave) electric field corresponding to the excited resonant mode without plasma, and the change in permittivity is defined as

$$\Delta\varepsilon(\mathbf{r}) = \varepsilon_p(\mathbf{r}) - \varepsilon_0. \quad (4.5)$$

Details on the resonant mode and corresponding electric field profile used in this work can be found in Section 4.3.2. Similar to the reasoning related to Eqn. (4.2), it should be noted that Eqn. (4.4) only holds for a collisionless plasma ($\nu_m \ll f_{pe}$).

The volume-averaged electron density can be found by a combined substitution of the expressions found from Eqn. (4.2), Eqn. (4.3), and Eqn. (4.5) into the formula for the frequency shift $\Delta f/f_1$ as denoted in Eqn. (4.4). Assuming a homogeneous electron density distribution so that $\Delta\varepsilon(\mathbf{r}) = \Delta\varepsilon$, the volume-averaged electron density \bar{n}_e follows by re-arranging terms so that the electron density is expressed in terms of the

frequency shift and other parameters as

$$\bar{n}_e = \frac{8\pi^2 \varepsilon_0 m_e f_p^2 \Delta f}{e^2 f_1 \mathcal{V}}. \quad (4.6)$$

Here, \mathcal{V} denotes the electric-field-squared-weighted ratio between the plasma volume V_p and the cavity volume V_c , and is defined as

$$\mathcal{V} = \frac{\iiint_{V_p} |\mathbf{E}(\mathbf{r})|^2 d^3\mathbf{r}}{\iiint_{V_c} |\mathbf{E}(\mathbf{r})|^2 d^3\mathbf{r}}. \quad (4.7)$$

In summary, MCRS allows to obtain the volume-averaged electron density \bar{n}_e by tracking the shift in resonance frequency Δf of a resonant mode excited inside a cavity. This approach can be applied in a temporally-resolved fashion (sample time $\tau_{tr} = 40$ ns) using the experimental setup and measurement scheme outlined in Section 4.3.

4.3 Experiment

First, we discuss the experimental configuration in Section 4.3.1 which is followed by the procedure applied to obtain the results, shown in Section 4.3.2.

4.3.1 Devices and interconnections

An overview of the experimental setup is shown in Fig. 4.1, where the main systems can be identified: the vacuum and gas handling, the MCRS (microwave cavity resonance spectroscopy) system, the plasma power supply and the discharge/MCRS cavity. It should be noted that the plasma under study was operated inside a cylindrical cavity which, on one hand, facilitated the MCRS measurements and, on the other hand, provided well-defined boundary conditions for the plasma volume enhancing the modeling and interpretation accuracy.

The heart of the experimental setup was a cylindrical cavity positioned in the center of the vacuum vessel, in which plasma discharges were generated in a controlled environment. The cavity had a diameter $D_{cav} = 168$ mm and height $H_{cav} = 78$ mm, which are indicated along with other geometric details in Fig. 4.2. An asymmetric capacitively-coupled discharge was created by powering the bottom (RF) electrode, which was insulated from the (grounded) cylindrical and (grounded) top walls of the cavity by a thin dielectric disk.

A large vacuum vessel with a base pressure of 2×10^{-6} mbar confined the discharge cavity in an argon atmosphere. The vacuum vessel had a diameter of 600 mm and a height of 450 mm. The argon pressure inside the vessel was maintained at pressures varying from 0.030 to 0.300 mbar by balancing the argon inflow rate of 150 sccm (gas inlet) set by a mass flow controller with the outflow rate which was regulated by the butterfly valve (while the shutter valve was closed) located between the vacuum vessel and the pumping system.

For the MCRS measurements, a microwave generator was used to generate microwaves with an (input) power P_{in} , which were coupled into the cavity—via

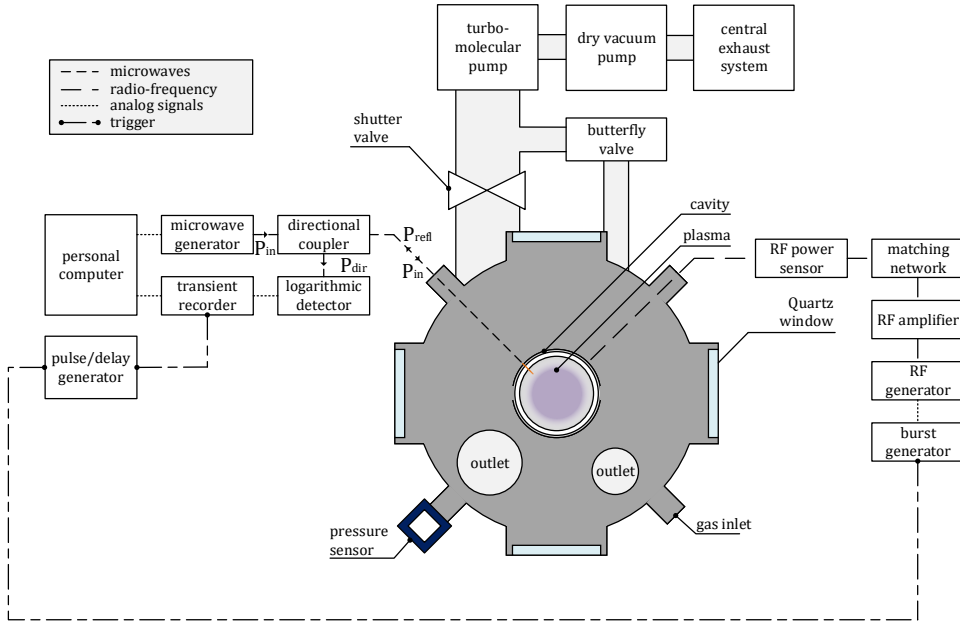


Figure 4.1: Overview of the experimental setup, including a cross sectional top view of the vacuum vessel and the individual devices used for gas handling, supply of RF power and installed microwave-based diagnostic system.

a directional coupler—by a monopole antenna. If the applied microwave frequency is close to the resonance frequency of a specific mode, the amount of reflected power approaches zero. Otherwise, the amount of reflected power is close to the input power. One tenth of the reflected power, i.e. the directed power $P_{\text{dir}} = 0.1P_{\text{refl}}$, was transferred to a logarithmic power detector for data registration by a fast transient recorder. A typical measurement of the directed power measured by the transient recorder is depicted as a function of microwave frequency in Fig. 4.3.

The plasma power supply system delivered power to the discharge at a radio-frequency (RF) of 13.56 MHz in a pulsed fashion. Hereto, a function generator in single-burst mode (burst generator) modulated the RF generator to create a pulsed RF signal. This signal was amplified by an RF amplifier in combination with an L-type matching network. An RF power sensor (Impedans OctivPoly) was used to obtain time-resolved measurements of the voltage, current and power at a temporal resolution of $10 \mu\text{s}$. The RF power was kept constant for each measurements at a (pulse-averaged) RF power of $5.0 \pm 0.2 \text{ W}$ using the power sensor and matching network.

A pulse/delay generator was used to synchronize the MCRS measurements with the plasma discharges. This was done by creating a trigger signal that triggered the burst generator of the RF power supply and the transient recorder to synchronize the MCRS response.

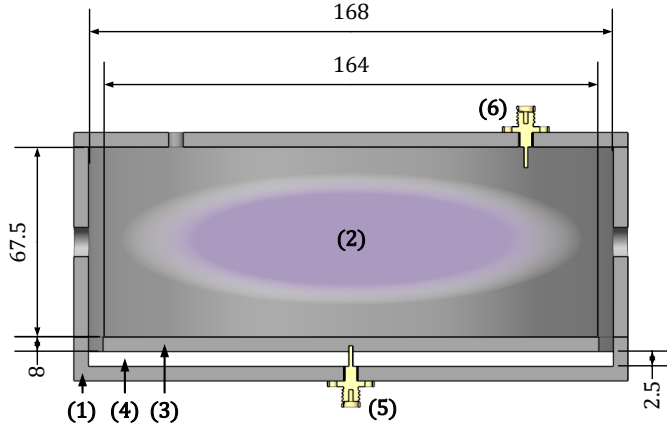


Figure 4.2: Cross sectional view of (1) the microwave cavity with (2) the plasma above (3) the RF electrode which was insulated from the grounded cavity by a (4) dielectric disk, (5) the RF connector and (6) microwave antenna for MCRS. Dimensions are denoted in millimeters. Dimensions in radial and axial direction have been measured within a symmetric tolerance of 1 mm and 0.1 mm, respectively.

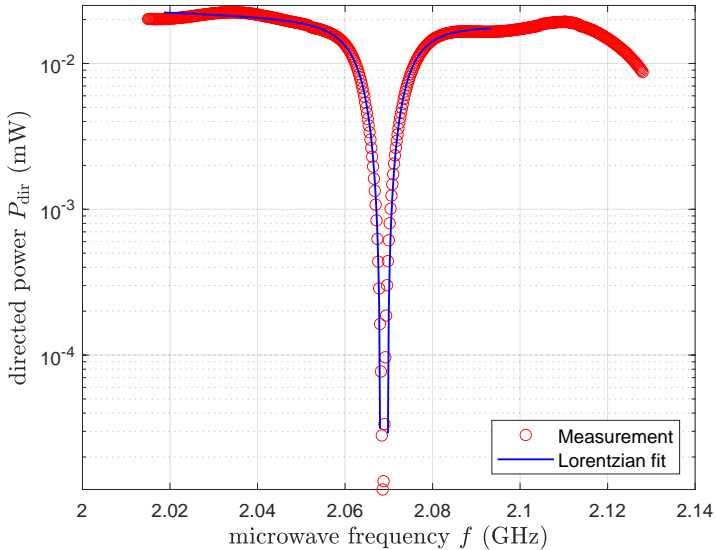


Figure 4.3: Spectral response of the cavity around the resonance frequency corresponding to the resonant mode TM_{110} at $t = -40 \mu\text{s}$ (relative to plasma ignition at $t = 0$ s) for the data set obtained for $p = 0.030$ mbar.

4.3.2 Methodology

Pulsed plasma discharges were generated inside the cavity with a repetition frequency of 40 Hz (pulse duration 25 ms) and a duty cycle of 16 % so that the plasma was sustained for 4 ms and consecutively allowed to decay for 21 ms. The time between pulses ensured that the plasma initiated during each pulse had completely decayed before the start of the next pulse, which was verified by the fact that the temporally-resolved shift in resonance frequency reached the noise band ($n_e \sim 1 \times 10^{10} \text{ m}^{-3}$) before the subsequent RF pulse. Hence, the resonance frequency f_1 could be obtained with an empty cavity before each and every plasma ignition.

The electron density \bar{n}_e was obtained through the shift in resonance frequency with respect to the situation without plasma. A typical spectral response of the cavity is depicted in Fig. 4.3, which allows characterization of the resonant mode TM_{110} . The electric field corresponding to this resonant mode is depicted in Fig. 4.4. This solution is obtained by solving for the eigenfrequency of the cavity in COMSOL Multiphysics®. The spectral response can be characterized by the resonance frequency f_{res} and quality factor Q , which were found experimentally as $f_1 = 2.069 \text{ GHz}$ and $Q = 130$ without plasma. The quality factor Q is a measure of the energy losses in the cavity and relates to the fundamental time response of the cavity $\tau_c = Q/\pi f_1 = 20 \text{ ns}$, which allowed to select the transient recorder sample frequency further on. The resonance frequency and quality factor were found by fitting a Lorentzian curve to the measurement data. The procedure has been described in detail by Van der Schans *et al* [23].

Obtaining the electron density temporally-resolved—as depicted for several values of the gas pressure in Fig. 4.10—required the spectral response at each sample time before, during and after the plasma pulse. However, the measurement time for obtaining a spectral response as shown in Fig. 4.3 would greatly exceed any reasonable temporal resolution when the measurement scheme would be based on a conventional (frequency sweep) approach such as a network analyzer. Therefore, a different measurement strategy was followed that allowed a reconstruction of the frequency response for each sample time. This was justified because the pulsed discharges were highly reproducible.

For a single microwave frequency, the temporal response of the cavity was sampled by a transient recorder at a rate of $f_{\text{tr}} = 25 \text{ MHz}$ for 32 consecutive discharges, which were averaged afterwards to reduce noise. This procedure was repeated for the frequency range of interest, i.e. $f = 2.015 - 2.148 \text{ GHz}$, with a spectral interval $f_{\text{step}} = 0.2 \text{ MHz}$. Finally, a combination of the temporal responses at each time instant along the frequency dimension allowed to reconstruct the spectral response for all time instances at which data was sampled (see Fig. 4.5). From these spectral responses, the resonance frequency was retrieved temporally-resolved with a time resolution of $2\tau_c (= 1/f_{\text{tr}})$.

Finally, the data was processed using a computer code in order to obtain absolute values for the electron densities from the MCRS signal. Hereto, the fitted resonance frequency was used to calculate the empty cavity value f_1 by averaging over $-2 \text{ ms} \leq t \leq 0 \text{ ms}$ (i.e. a period of 2 ms before the plasma pulse, see Fig. 4.10), after which the shift in resonance frequency was found as $\Delta f(t) = f(t) - f_1$ for each moment in time. The volume-averaged (MCRS) electron density \bar{n}_e was calculated using the shift in resonance frequency, which was provided by the fitted resonance frequency, and assuming a plasma volume ratio $\mathcal{V} = 1$.

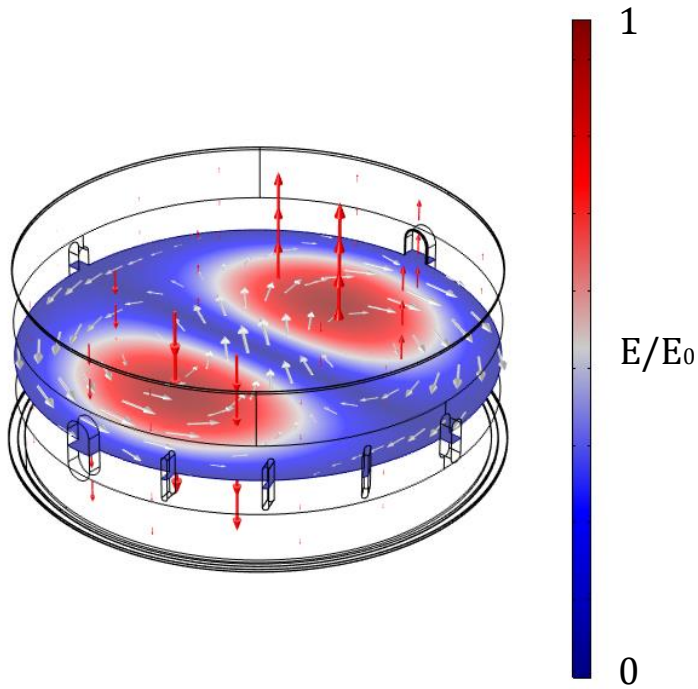


Figure 4.4: Normalized electric field (magnitude) corresponding to the resonant mode TM_{110} of the microwave cavity, computed using COMSOL Multiphysics[®]. Red and white vectors (direction and magnitude) correspond to the electric and magnetic field, respectively.

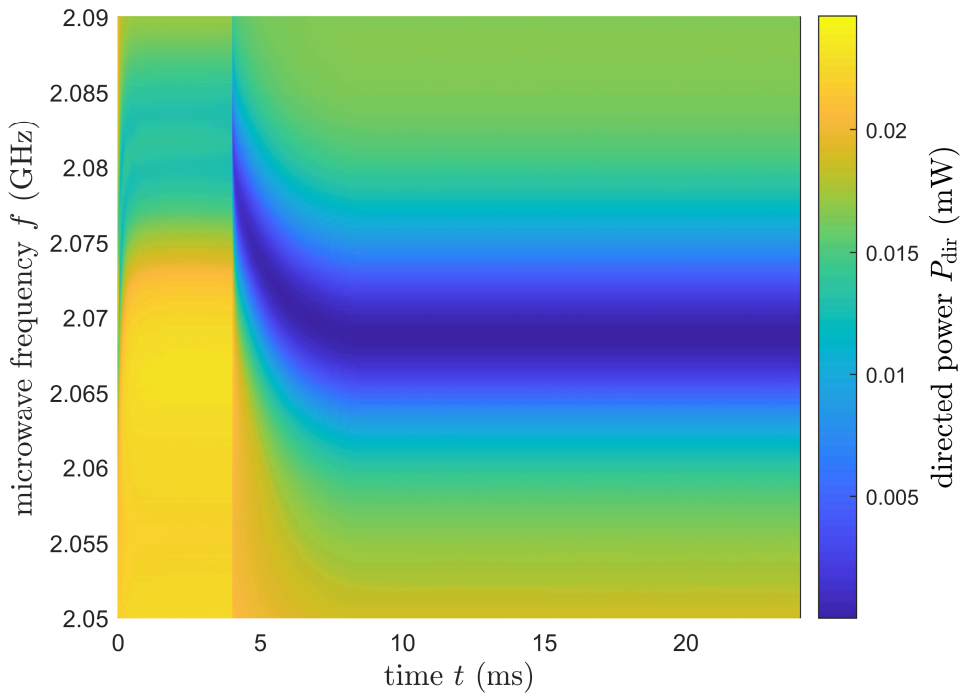


Figure 4.5: Reconstruction of the temporally-resolved frequency response during and after (for $t \geq 0$ ms) a single pulsed discharge.

4.4 Numerical model

The equations and boundary conditions underlying the drift-diffusion model are briefly outlined in Section 4.4.1, whereas the plasma chemistry and species for which the equations are solved are discussed in Section 4.4.2. Section 4.4.3 describes the results of solving the numerical model in PLASIMO software and discusses the implications of the electron density distributions.

4.4.1 Drift-diffusion equations and boundary conditions

The basic equations describing the balances of species and energy underlying the drift-diffusion model are treated briefly in this section, and the reader is referred to Van Dijk *et al* [24] for a detailed discussion. The temporal and spatial evolution of a specific species density n_s is described by the species density balance:

$$\frac{\partial n_s}{\partial t} + \nabla \cdot (n_s \mathbf{u}_s) = S_s, \quad (4.8)$$

where \mathbf{u}_s is the averaged species velocity, S_s is the net particle source (determined by the various reactions occurring in the plasma), and $\mathbf{\Gamma}_s = n_s \mathbf{u}_s$ denotes the flux density for species s . The flux density for the electrons $\mathbf{\Gamma}_e$ is solved in the drift-diffusion approximation by

$$\mathbf{\Gamma}_e = \mu_e \mathbf{E} n_e - D_e \nabla n_e, \quad (4.9)$$

where μ_e and D_e are the electron mobility and the governing diffusion coefficient, respectively, and \mathbf{E} the electric field. For the ions, the flux density results from solving the momentum balance equation given by

$$\frac{\partial \mathbf{u}_i}{\partial t} + (\mathbf{u}_i \cdot \nabla) \mathbf{u}_i + \frac{S_i}{n_i} \mathbf{u}_i = \frac{1}{m_i n_i} \frac{k_B T_i}{D_i} (\mu_i \mathbf{E} n_i - D_i \nabla n_i - n_i \mathbf{u}_i), \quad (4.10)$$

where μ_i and D_i are the ion mobility and the governing diffusion coefficient, respectively, k_B the Boltzmann constant, m_i the ion mass, and T_i the ion temperature. The mobility is taken to be positive for positively charged species, negative for negatively charged species, and zero for neutral species. It is assumed that the Einstein relation can be used to calculate the diffusion coefficient from the mobility using

$$D_s = \frac{k_B T_s \mu_s}{q_s}, \quad (4.11)$$

where q_s the species charge, T_s the species temperature corresponding to the energy of the random particle motion, and μ_s and D_s are the respective mobility and the governing diffusion coefficient of the species.

The electron energy is determined by solving the electron energy (density) balance equation,

$$\frac{\partial n_{\bar{e}}}{\partial t} + \nabla \cdot \mathbf{\Gamma}_{\bar{e}} = S_{\bar{e}}, \quad (4.12)$$

with energy flux density

$$\mathbf{\Gamma}_{\bar{\epsilon}} = \frac{5}{3}\mu_e \mathbf{E} n_{\bar{\epsilon}} - \frac{5}{3}D_e \nabla n_{\bar{\epsilon}}. \quad (4.13)$$

Here, $n_{\bar{\epsilon}} = n_e \bar{\epsilon}$ is the electron energy density, and $\bar{\epsilon}$ is the mean electron energy. The effective source term $S_{\bar{\epsilon}}$ includes Ohmic heating and energy losses due to elastic and inelastic collisions.

These equations are coupled to the Poisson equation for computation of the electric field defined as

$$\nabla \cdot (\varepsilon \mathbf{E}) = -\nabla \cdot (\varepsilon \nabla V) = \rho, \quad (4.14)$$

where ε is the dielectric permittivity, V the electrostatic potential, and ρ the space charge density of species s as

$$\rho = \sum_s q_s n_s. \quad (4.15)$$

At the open boundaries (i.e. symmetry axis), we apply homogeneous Neumann boundary conditions for all quantities, i.e. $\nabla n_s \cdot \mathbf{n} = 0$ with \mathbf{n} the normal vector to the boundary. For the physical boundaries, we apply constant Dirichlet conditions for the potential. The boundary conditions for the species densities are given by expressions for the flux densities $\mathbf{\Gamma}_s$,

$$\mathbf{\Gamma}_s \cdot \mathbf{n} = \alpha_s \mu_s (\mathbf{E} \cdot \mathbf{n}) n_s + \frac{1}{4} v_{\text{th},s} n_s, \quad (4.16)$$

where $v_{\text{th},s}$ is the thermal velocity of the species. The parameter α_s is set to 1 if the drift velocity is directed towards the wall, and to 0 otherwise:

$$\alpha_s = \begin{cases} 1 & \text{if } \mu_s \mathbf{E} \cdot \mathbf{n} > 0 \\ 0 & \text{if } \mu_s \mathbf{E} \cdot \mathbf{n} \leq 0 \end{cases} \quad (4.17)$$

We use the control volume method for solving Eqn. (4.8), (4.12) and (4.14) and the Scharfetter-Gummel's [25] exponential scheme for the spatial discretization of the flux densities. Time integration is done using Gummel's scheme, in which the variables are solved consequently. We first calculate the Poisson equation, i.e. Eqn. (4.14), followed by the species density equation, i.e. Eqn. (4.8), and the electron energy density equation—Eqn. (4.12). An implicit scheme is used for the calculation of the electrostatic potential [26, 27] and the electron energy [27], which allows using relatively large time steps.

4.4.2 Plasma species and reactions

In our model, the buffer gas atoms are uniformly distributed in time and space, i.e. the gas temperature, the gas pressure and the gas density are constant. The gas temperature is assumed equal to 300 K.

Table 4.1: List of species included in this model together with their transport coefficient and the corresponding references.

Nr	Species	Energy [eV]	$\mu_s N$ [$\text{m}^{-1}\text{V}^{-1}\text{s}^{-1}$]	$D_s N$ [$\text{m}^{-1}\text{s}^{-1}$]	Ref.
1	e	0	$f(\bar{\epsilon})$	Einstein relation	[28]
2	Ar ⁺	15.76	$f(E/N)$	Einstein relation	[29]
3	Ar*	11.55	-	2.06×10^{20}	[30]

Table 4.1 lists the set of species for which the balance equations denoted by Eqn. (4.8) and (4.12) are solved, together with the transport coefficients used in the model and the references from which the values have been obtained.

The reactions between the species are listed in Table 4.2, including the reaction rates and corresponding references. The local field approximation is used for the ions, while we calculate the energy distribution function for the electrons using the built-in BOLSIG+ library. The electron-related rate coefficients and the electron transport coefficients are internally used in the form of lookup tables as a function of the mean electron energy.

Since the metastable argon levels participate in similar reactions with very similar rate coefficients, they are combined into one effective level that lies at 11.55 eV above the ground state. Other excited states are not included in the model.

Table 4.2: Reactions and rate coefficients used in the model. The electron related reaction rate coefficients as a function of the mean electron energy are obtained from the built-in Boltzmann solver BOLSIG+ [28].

Nr	Reaction	Rate coefficient	Ref.
1	Ar + e \rightarrow Ar* + e	$f(\bar{\epsilon})$	[31]
2	Ar* + e \rightarrow Ar ⁺ + 2e	$f(\bar{\epsilon})$	[31]
3	Ar + e \rightarrow Ar ⁺ + 2e	$f(\bar{\epsilon})$	[31]
4	Ar* + e \rightarrow Ar + e	$f(\bar{\epsilon})$	[31]
5	Ar* \rightarrow Ar	$5 \times 10^5 \text{ s}^{-1}$	[32]
6	2Ar* \rightarrow Ar ⁺ + Ar + e	$1.17 \times 10^{-15} \text{ m}^3\text{s}^{-1}$	[33]

4.4.3 Solutions of the numerical model in PLASIMO software

The drift-diffusion module of PLASIMO software [24] is used to describe the behavior of the spatial plasma distribution. It is a time-dependent multi-fluid model solving three types of equations: the continuity equation for the evolution of the relevant species, the energy balance equation for the electrons and the Poisson equation to compute the electric field. This model employs the complete set of equations and assumptions outlined in Section 4.4.1. The drift-diffusion model has been applied to a wide variety of applications such as dielectric barrier discharges [34], and capacitively-coupled plasmas, e.g., in the Gaseous Electronics Conference (GEC) reference cell [35]. The drift-diffusion model of the GEC reference cell, as described by Boeuf and Pitchford

[36], has been compared with good agreement against experimental data obtained under the same conditions and geometry [36, 37, 38, 39]. Since the conditions (e.g., RF voltage, gas pressure) are comparable to those used in this work, the drift-diffusion model formed the basis for the model described in this work. The set of species and reactions as given in Section 4.4.2 was implemented in the model. This chemistry model was successfully applied by Mihailova *et al* [34] to describe the chemistry in a pristine argon gas, which was validated against experiments. The geometry used in the model is similar to the one shown in Fig. 4.2, except that (5) the RF connector, (6) the microwave antenna, and the openings in the side walls (for optical access) were left out of consideration to allow cylindrical symmetry (without affecting the plasma distribution inside the volume).

The (quasi-)steady state solutions of the model are shown in Fig. 4.6 to Fig. 4.9 for gas pressures 0.030, 0.060, 0.102 and 0.300 mbar, respectively. The electron density is displayed spatially in terms of the radial and axial coordinates r and z , respectively, where the data for $r < 0$ mm was obtained by mirroring the solution for $r > 0$ mm for the purpose of visualizing the structure across the whole cavity volume. The spatial solution was obtained in quasi-steady state by time-averaging the electron density profile over one full RF period, after the model had been running for at least 1 ms monitoring its temporal convergence.

As can be seen from Fig. 4.6 and Fig. 4.9, the highest electron density occurs in the axial and radial center of the discharge, whereas the electron density decays rapidly across the sheath regions that interface the material boundaries. However, for $p = 0.102$ mbar and 0.300 mbar, the region with maximum electron density shifts towards the radial edges which shows the importance of using a dedicated solution in the profile correction for each gas pressure. Clearly, the free electrons are non-uniformly distributed over the cavity volume, irrespective of the argon pressure, and this distribution differs qualitatively for each gas pressure. This—of course—affects the interpretation of the MCRS data, which is volume-averaged over the cavity volume and weighted by the (excited) microwave electric field. In Section 4.5.2, we explain how we disentangle this convoluted result of volume-averaging and microwave-electric-field-weighting of the actual electron density in the MCRS experiments using the numerical model solutions presented in this section.

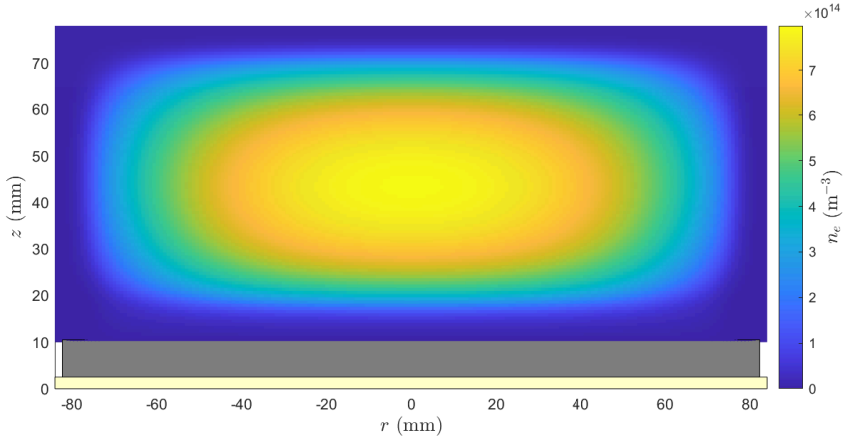


Figure 4.6: Quasi-steady state solution of the electron density profile for $p = 0.030$ mbar.

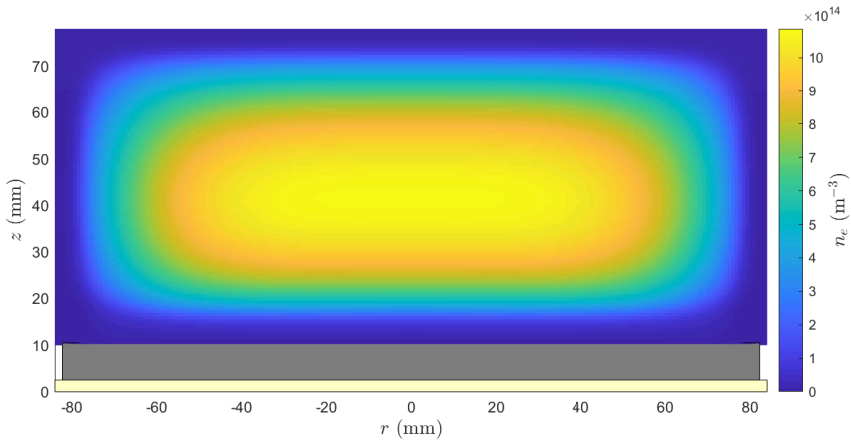


Figure 4.7: Quasi-steady state solution of the electron density profile for $p = 0.060$ mbar.

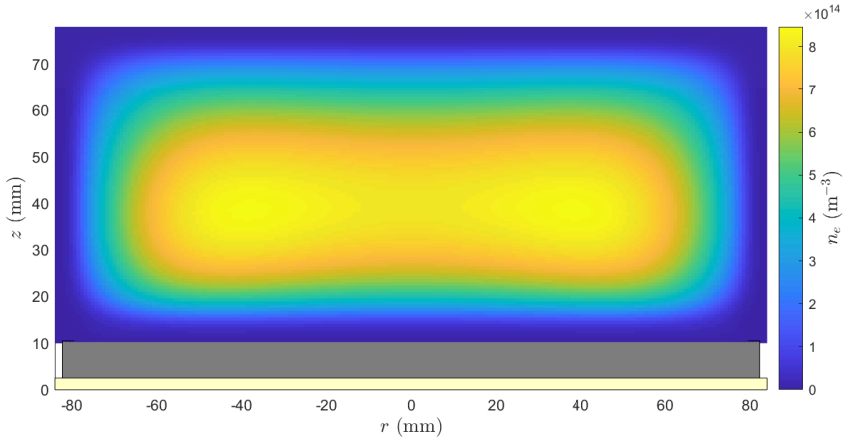


Figure 4.8: Quasi-steady state solution of the electron density profile for $p = 0.102$ mbar.

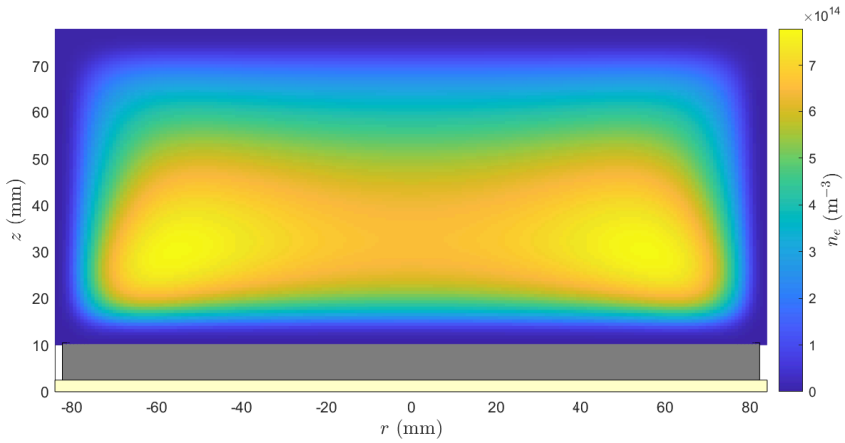


Figure 4.9: Quasi-steady state solution of the electron density profile for $p = 0.300$ mbar.

4.5 Results and discussion

This section presents first the time-resolved MCRS experiments in Section 4.5.1, from which we have extracted the quasi-steady state MCRS values used for further analysis using the uniform plasma assumption leading to volume-averaged MCRS data. In Section 4.5.2, we introduce the numerical electron density distribution/profile n_e^{NUM} into Eqn. (4.4) resulting in the profile-correction factor β , which forms the counter-part of the classical (microwave-field-weighted) volume ratio \mathcal{V} obtained by assuming a homogeneous plasma. In Section 4.5.3, the electron density values obtained using PLASIMO, volume-averaged MCRS values, and profile-corrected MCRS values are presented and compared as a function of argon pressure.

4.5.1 Typical electron density evolution during and after a pulsed discharge

The time-resolved MCRS signals are shown in Fig. 4.10 for the different argon pressures (i.e., 0.030, 0.060, 0.102 and 0.300 mbar). Three phases can be identified with respect to the moment of plasma ignition ($t = 0$ ms): the pre-plasma phase (-2 to 0 ms), the plasma on phase (0 to 4 ms), and the temporal plasma afterglow phase (4 to 24 ms). Specifically, an additional flat-top period is indicated during which free electron density in the plasma reaches a (quasi-)steady state value, which is used for further analysis. Lastly, it should be noted that the values for \bar{n}_e shown in Fig. 4.10 have been obtained using the measured $\Delta f(t)$, $f_p(t)$ and f_1 in Eqn. (4.6), and assuming that $\mathcal{V} = 1$ in Eqn. (4.7) (assuming a homogeneously distributed electron density).

First, the pre-plasma phase is defined as the period $-2 \text{ ms} \leq t \leq 0 \text{ ms}$ and clearly marks a situation in which there is no significant change in the electron density. This pre-discharge period is used to determine the resonance frequency without plasma, i.e. f_1 .

Second, at the moment of initiation of the RF power pulse at $t = 0$ ms, a sharp increase in electron density is observed indicating the transition into the plasma on period. After a brief transient of about $0.4 \text{ ms} - 1 \text{ ms}$ depending on the operating conditions, the electron density settles at a constant value marking the flat-top, or quasi-steady state, period of the discharge. Averaging of the data obtained during this flat-top phase results in a single value that represents the (volume-averaged and microwave-field-weighted) MCRS values in Fig. 4.11 in Section 4.5.3, which have been calculated using Eqn. (4.6) for $\mathcal{V} = 1$.

Third, the plasma-off period or temporal afterglow is initiated by terminating the RF power at $t = 4$ ms. Clearly, the electron density goes into decay until another steady state is reached in the subsequent pre-discharge period without plasma. It can be seen that the electron density decays more rapidly at lower values of the gas pressure. This is because the electrons can diffuse more quickly to the walls at lower pressure where they are subsequently lost through recombination. When the electron density has decayed sufficiently, the decay is no longer determined by ambipolar diffusion. From this point onwards, free diffusion governs the decay as can be seen from the steep decline of the signal before the noise band is reached [16].

The (quasi-)steady state electron density values depicted in Fig. 4.11 by the (volume-averaged) MCRS data points as a function of the argon pressure facilitate a comparison with the numerical model values for the electron density and the profile-corrected MCRS values obtained in Section 4.5.2.

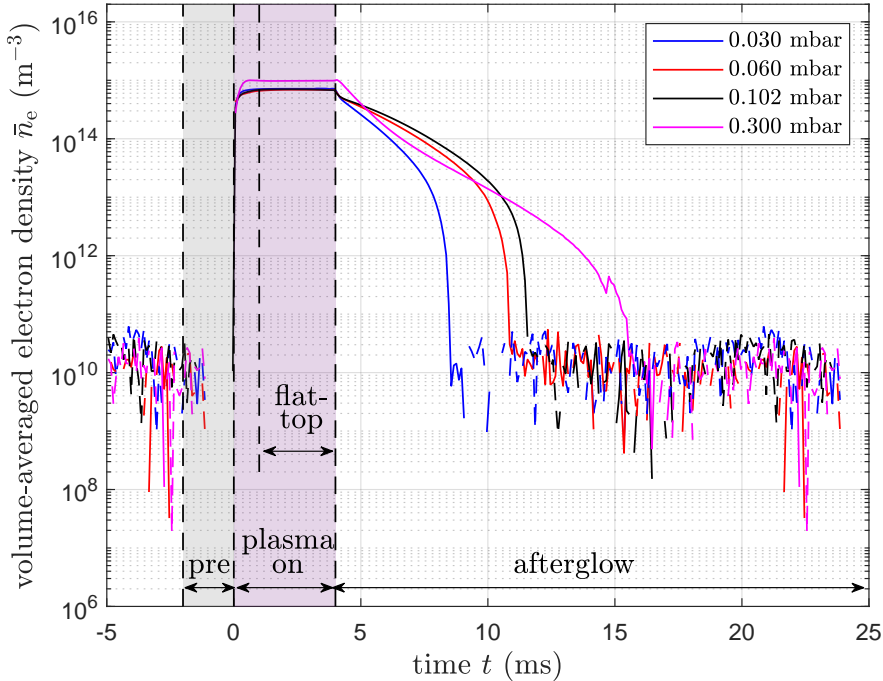


Figure 4.10: Time-resolved electron density obtained by MCRS at the specified argon pressures, where an RF power of 5 W was applied during the plasma on period ($0 \text{ ms} \leq t \leq 4 \text{ ms}$) indicated by the purple-shaded area. The pre-discharge period is depicted by the grey-shaded area, during which the resonance frequency without plasma was determined. The flat-top period defines the quasi-steady state of the discharge used for the comparison of the time-averaged values at different argon pressures.

4.5.2 Profile correction

There are two factors that need to be accounted for in the calculation from raw MCRS data to trustworthy electron density values: the non-uniform distribution of the microwave electric field and the spatial distribution of the electrons. First, the non-uniform microwave electric field implies that the resonant mode is mostly disturbed by the plasma present radially off-axis, whereas the resonant mode is uniformly sensitive in the axial direction, as can be seen from Fig. 4.4. Second, the presence of the sheath regions near plasma confining walls and, less steep, spatial

gradients in the bulk plasma need to be taken into account as well, as can be seen from Fig. 4.6 to Fig. 4.9.

To account for both non-uniformities, the electron density profile $n_e(\mathbf{r})$ and the square of the magnitude of the microwave electric field $|\mathbf{E}(\mathbf{r})|^2$ are included in the conversion of the measured shift in resonance frequency Δf to a (maximum) value for the electron density \hat{n}_e , which we term the profile-corrected MCRS value as opposed to the volume-averaged MCRS value denoted by \bar{n}_e . First, the electron density profile is redefined in terms of the numerical electron density distribution n_e^{NUM} (found from the PLASIMO solution for the numerical model normalized to unity), and the maximum electron density \hat{n}_e occurring throughout the plasma volume, as

$$n_e(\mathbf{r}) = n_e^{\text{NUM}}(\mathbf{r})\hat{n}_e. \quad (4.18)$$

Second, this expression is implemented in the formula for the shift in resonance frequency Δf , Eqn. (4.4), by using it for the spatially-dependent electron density $n_e(\mathbf{r})$, resulting in the profile-corrected MCRS electron density

$$\hat{n}_e = \frac{8\pi^2 \varepsilon_0 m_e f_p^2}{e^2 f_1} \frac{\Delta f}{\beta}. \quad (4.19)$$

Here, the electric-field-squared-weighted volume ratio between plasma and cavity volume \mathcal{V} has been replaced by

$$\beta = \frac{\int_0^{H_{\text{cav}}} \int_0^{R_{\text{cav}}} n_e^{\text{NUM}}(r, z) |\mathbf{E}(r, z)|^2 r \, dr \, dz}{\int_0^{H_{\text{cav}}} \int_0^{R_{\text{cav}}} |\mathbf{E}(r, z)|^2 r \, dr \, dz}, \quad (4.20)$$

based on the numerical electron density distribution $n_e^{\text{NUM}}(r, z)$ found from the PLASIMO model, and the numerical solution for the microwave electric field $\mathbf{E}(r, z)$ found from the microwave model built in COMSOL Multiphysics[®]. It should be noted that, using the axi-symmetric property of the discharge, the angular dependence of the integral drops out. The correction factor β can now be used to directly scale the volume-averaged MCRS values \bar{n}_e found from the experiments in Section 4.5.1 to profile-corrected MCRS values \hat{n}_e . This is possible because the volume-averaged MCRS data were obtained using $\mathcal{V} = 1$ in Eqn. (4.7), which is effectively the same as assuming $\beta = 1$.

4.5.3 Comparison of uniform and profile-corrected electron densities

Fig. 4.11 depicts the (non-weighted) volume-averaged and maximum value found from the PLASIMO model, the (microwave-field-weighted) volume-averaged MCRS value \bar{n}_e , and the profile-corrected MCRS value \hat{n}_e for the quasi-steady state electron density as a function of the gas pressure in the considered range. There are two important remarks considering the comparison of PLASIMO and MCRS data. First, the volume-averaged PLASIMO data was obtained by spatially averaging the numerical profile, whereas the volume-averaged MCRS data is weighted by the microwave electric field—due

to the measurement principle. This clearly shows that comparing volume-averaged values results in a larger discrepancy, and hence, motivates comparing the maximum PLASIMO values and profile-corrected MCRS values (which represent the maximum values obtained from the experiment, consult Eqn. (4.19)).

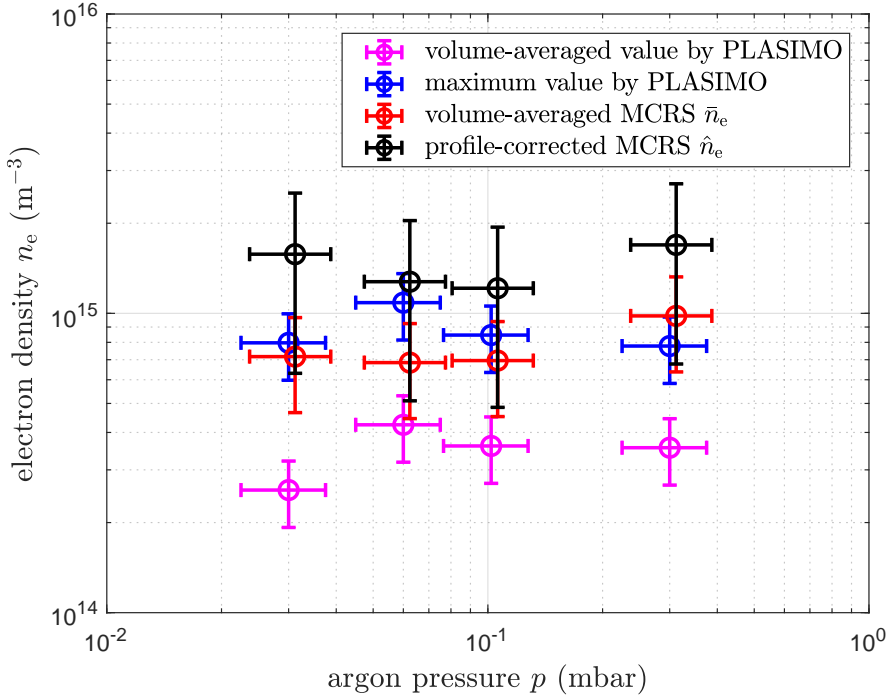


Figure 4.11: Comparison of quasi-steady state electron densities as a function of argon pressure: the volume-averaged values obtained by PLASIMO (magenta circles), the maximum values obtained by PLASIMO (blue circles), the volume-averaged MCRS results assuming a uniform plasma (red circles), and the profile-corrected MCRS results incorporating the numerical model and microwave eigenmode solution (black circles). The error margins for the pressure measurements are 25%, errors in the numerical model are taken at 25% (taken equal to the error in pressure, because the neutral gas pressure directly introduces the largest error in the model via the neutral gas density), and the error bars for the MCRS data are taken at 10% due to uncertainty in Δf (the error in determination of Δf is estimated as 1 MHz, compared to a plasma-induced shift of 10 MHz). The combined error in the numerical model and MCRS data add to the error of 35% for the profile-corrected MCRS data.

The profile-corrected MCRS results are depicted in Fig. 4.11 (indicated by the black circles) using the same experimental error bars as for the volume-averaged (uncorrected) MCRS data. These results have been obtained by evaluating Eqn. (4.18) and (4.19) for each argon pressure. For clarity, the experimental data is used to obtain Δf , f_1 and f_p , the PLASIMO model is used to obtain the (normalized) numerical profile

of the electron density n_e^{NUM} , and the microwave electric field $\mathbf{E}(\mathbf{r})$ is obtained from COMSOL Multiphysics[®]. The experimental and numerical data was loaded into a computer code for subsequent evaluation at each spatial location and solving the equations to arrive at a value for \hat{n}_e for each argon pressure under consideration. As a consequence, the PLASIMO values—representing the maximum electron density found from each model solution—are directly comparable to the profile-corrected MCRS data.

In conclusion, the maximum PLASIMO values are clearly located within the error margins of the MCRS experiments due to the measurement uncertainty in Δf and the gas pressure. The numerical model of the discharge shows that the correction factor β is significant for each pressure level, where β ranges from 0.45 to 0.58. However, we demonstrate that the PLASIMO results are well within the error margins of the profile-corrected MCRS results as well as the (uncorrected) volume-averaged MCRS results. This shows that, on the one hand, the PLASIMO model can be readily used to perform quantitative investigation of the absolute electron density by MCRS and that, on the other hand, the assumption of a uniform plasma leads to an acceptable error in the experimental results given the error margins of the experimental technique.

4.6 Conclusion

We investigated the effect of incorporating the (numerically determined) spatial distribution of the electrons in the analysis of MCRS measurements. Using the experimental and numerical data, the volume-averaged electron density (obtained using the standard approach to MCRS interpretation) was compared to the numerical model solution for the electron density. This comparison revealed that the used drift-diffusion model is readily capable of predicting the electron density found from the experiments. Consequently, the spatial distribution resulting from the numerical models was used to calculate the actual electron density values from the experimental MCRS data, without any simplifications with respect to the structure of the discharge or the structure of the microwave electric field used to probe the discharge. Although the correction factor $\beta \sim 0.45 - 0.58$ significantly improves the MCRS data interpretation, the numerical model solutions are readily found within the experimental error margins. This work thus proves that assuming a homogeneous discharge leads to acceptable results within the specified experimental error margins, that profile correction enhances the accuracy for detailed quantification of volume-averaged (MCRS) experiments, and that the numerical (drift-diffusion) model incorporates all necessary elements for successfully modeling and studying a pristine argon discharge under typical low-pressure conditions.

4.7 Bibliography

- [1] I. Adamovich, S. D. Baalrud, A. Bogaerts, P. J. Bruggeman, M. Cappelli, V. Colombo, U. Czarnetzki, U. Ebert, J. G. Eden, P. Favia, D. B. Graves, S. Hamaguchi, G. Hieftje, M. Hori, I. D. Kaganovich, U. Kortshagen, M. J. Kushner, N. J. Mason, S. Mazouffre, S. Mededovic Thagard, H. R. Metelmann, A. Mizuno, E. Moreau, A. B. Murphy, B. A. Niemira, G. S. Oehrlein, Z. Lj Petrovic, L. C. Pitchford, Y. K. Pu, S. Rauf, O. Sakai, S. Samukawa, S. Starikovskaia, J. Tennyson, K. Terashima, M. M. Turner, M. C.M. Van De Sanden, and A. Vardelle. The 2017 Plasma Roadmap: Low temperature plasma science and technology. *Journal of Physics D: Applied Physics*, 50(32), 2017.
- [2] Yuji Kasashima, Thorben Brenner, and Klaus Vissing. Development of a novel plasma probe for the investigation and control of plasma-enhanced chemical vapor deposition coating processes. *Plasma Processes and Polymers*, (June):1–9, 2020.
- [3] Gottlieb S. Oehrlein and Satoshi Hamaguchi. Foundations of low-temperature plasma enhanced materials synthesis and etching. *Plasma Sources Science and Technology*, 27(2), 2018.
- [4] Xiaoshuang Chen, Takafumi Seto, Uwe R. Kortshagen, and Christopher J. Hogan. Size and structural characterization of Si nanocrystal aggregates from a low pressure nonthermal plasma reactor. *Powder Technology*, 373:164–173, 2020.
- [5] Waldo Bongers, Henny Bouwmeester, Bram Wolf, Floran Peeters, Stefan Welzel, Dirk van den Bekerom, Niek den Harder, Adelbert Goede, Martijn Graswinckel, Pieter Willem Groen, Jochen Kopecki, Martina Leins, Gerard van Rooij, Andreas Schulz, Matthias Walker, and Richard van de Sanden. Plasma-driven dissociation of CO₂ for fuel synthesis. *Plasma Processes and Polymers*, 14(6):1–8, 2017.
- [6] P. W.C. Groen, A. J. Wolf, T. W.H. Righart, M. C.M. Van De Sanden, F. J.J. Peeters, and W. A. Bongers. Numerical model for the determination of the reduced electric field in a CO₂ microwave plasma derived by the principle of impedance matching. *Plasma Sources Science and Technology*, 28(7), 2019.
- [7] H. M. Mott-Smith and Irving Langmuir. The theory of collectors in gaseous discharges. *Physical Review*, 28(4):727–763, 1926.
- [8] Y. A. Ussenov, E. von Wahl, Zahra Marvi, T. S. Ramazanov, and H. Kersten. Langmuir probe measurements in nanodust containing argon-acetylene plasmas. *Vacuum*, 166(April):15–25, 2019.
- [9] G. Neumann, U. Bänziger, M. Kammeyer, and M. Lange. Plasma-density measurements by microwave interferometry and Langmuir probes in an rf discharge. *Review of Scientific Instruments*, 64(1):19–25, 1993.
- [10] K. Dittmann, C. Küllig, and J. Meichsner. 160GHz Gaussian beam microwave interferometry in low-density rf plasmas. *Plasma Sources Science and Technology*, 21(2), 2012.

-
- [11] B. Platier, T.J.A. Staps, M. van der Schans, W.L. IJzerman, and J. Beckers. Resonant microwaves probing the spatial afterglow of an RF plasma jet. *Applied Physics Letters*, 254103(December), 2019.
- [12] Manfred A. Biondi and Sanborn C. Brown. Measurements of Ambipolar Diffusion in Helium. *Physical Review*, 75(11), 1949.
- [13] C. H. Chang, C. H. Hsieh, H. T. Wang, J. Y. Jeng, K. C. Leou, and C. Lin. A transmission-line microwave interferometer for plasma electron density measurement. *Plasma Sources Science and Technology*, 16(1):67–71, 2007.
- [14] J. Berndt, E. Kovačević, V. Selenin, I. Stefanović, and J. Winter. Anomalous behaviour of the electron density in a pulsed complex plasma. *Plasma Sources Science and Technology*, 15(1):18–22, 2006.
- [15] F. M.J.H. Van De Wetering, J. Beckers, and G. M.W. Kroesen. Anion dynamics in the first 10 milliseconds of an argon-acetylene radio-frequency plasma. *Journal of Physics D: Applied Physics*, 45(48):1–8, 2012.
- [16] B. Platier, R. Limpens, A. C. Lassise, T.J.A. Staps, M.A.W. Van Nindhuijs, K. A. Daamen, O. J. Luiten, W. L. IJzerman, and J. Beckers. Transition from ambipolar to free diffusion in an EUV-induced argon plasma. *Applied Physics Letters*, 116(10), 2020.
- [17] J. Beckers, F. M.J.H. Van De Wetering, B. Platier, M. A.W. Van Nindhuijs, G. J.H. Brussaard, V. Y. Banine, and O. J. Luiten. Mapping electron dynamics in highly transient EUV photon-induced plasmas: A novel diagnostic approach using multi-mode microwave cavity resonance spectroscopy. *Journal of Physics D: Applied Physics*, 52(3), 2019.
- [18] Job Beckers, Tijn van de Ven, Ruud van der Horst, Dmitry Astakhov, and Vadim Banine. EUV-induced plasma: A peculiar phenomenon of a modern lithographic technology. *Applied Sciences (Switzerland)*, 9(14):1–23, 2019.
- [19] M. A.W. Van Nindhuijs, K. A. Daamen, J. G.H. Franssen, J. Conway, B. Platier, J. Beckers, and O. J. Luiten. Microwave cavity resonance spectroscopy of ultracold plasmas. *Physical Review A*, 100(6):61801, 2019.
- [20] G. G. Lister, Y.-M. Li, and V. A. Godyak. Electrical Conductivity in Metals. *Journal of Applied Physics*, 79(12):8993–8997, 1996.
- [21] Bart Platier, Tim Staps, Peter Koelman, Marc van der Schans, Job Beckers, and Wilbert IJzerman. Probing collisional plasmas with MCRS: Opportunities and challenges. *Applied Sciences (Switzerland)*, 10(12), 2020.
- [22] David M. Pozar. *Microwave Engineering*. Wiley, 2005.

- [23] Marc van der Schans, Bart Platier, Peter Koelman, Ferdi van de Wetering, Jan Van Dijk, Job Beckers, Sander Nijdam, and Wilbert IJzerman. Decay of the electron density and the electron collision frequency between successive discharges of a pulsed plasma jet in N₂. *Plasma Sources Science and Technology*, 28(3), 2019.
- [24] Jan van Dijk, Kim Peerenboom, Manuel Jimenez, Diana Mihailova, and Joost van der Mullen. The plasma modelling toolkit plasimo. *Journal of Physics D: Applied Physics*, 42(19):194012 (14pp), 2009.
- [25] D.L. Scharfetter and H.K. Gummel. Large-signal analysis of a silicon read diode oscillator. *Electron Devices, IEEE Transactions on*, 16(1):64–77, 1969.
- [26] P.L.G. Ventzek, R.J. Hoekstra, and M.J. Kushner. *J. Vac. Sci. Technol. B*, 12:461–477, 1994.
- [27] G.J.M. Hagelaar and G.M.W. Kroesen. Speeding up fluid models for gas discharges by implicit treatment of the electron energy source term. *J. Comput. Phys.*, 159:1–12, 2000.
- [28] G. J. M. Hagelaar and L. C. Pitchford. Solving the Boltzmann equation to obtain electron transport coefficients and rate coefficients for fluid models. *PSST*, 14(4):722–733, 2005.
- [29] H. W. Ellis, R. Y. Pai, E. W. McDaniel, E. A. Mason, and L. A. Viehland. Transport properties of gaseous ions over a wide energy range. *Atomic Data and Nuclear Data Tables*, 17(3):177, 1976.
- [30] A.V. Phelps and J.P. Molnar. Lifetimes of metastable states of noble gases. *Phys. Rev.*, 89:1202, 1953.
- [31] W. Lowell Morgan. Kinema research & software, 2020. Data type: differential scattering cross sections, www.lxcat.net/Morgan.
- [32] N. Balcon, G. J. M. Hagelaar, and J. P. Boeuf. Numerical model of an argon atmospheric pressure rf discharge. *IEEE Transactions on Plasma Science*, 36(5):2782–2787, 2008.
- [33] A. N. Klucharev and V. Vujnovic. Chemi-ionization in thermal-energy binary collisions of optically excited atoms. *Physics Reports*, 185(2):55–81, 1990.
- [34] D. Mihailova, J. van Dijk, G. Hagelaar, P. Belenguer, and P. Guillot. Modeling of low temperature plasma for surface and airborne decontamination. *Plasma Science, IEEE Transactions on*, 42(10):2760–2761, Oct 2014.
- [35] P. J. Hargis, K. E. Greenberg, P. A. Miller, J. B. Gerardo, J. R. Torczynski, M. E. Riley, G. A. Hebner, J. R. Roberts, J. K. Olthoff, J. R. Whetstone, R. J. Van Brunt, M. A. Sobolewski, H. M. Anderson, M. P. Splichal, J. L. Mock, P. Bletzinger, A. Garscadden, R. A. Gottscho, G. Selwyn, M. Dalvie, J. E. Heidenreich, Jeffery W. Butterbaugh, M. L. Brake, M. L. Passow, J. Pender, A. Lujan, M. E. Elta, D. B.

- Graves, H. H. Sawin, M. J. Kushner, J. T. Verdeyen, R. Horwath, and T. R. Turner. The Gaseous Electronics Conference radio-frequency reference cell: A defined parallel-plate radio-frequency system for experimental and theoretical studies of plasma-processing discharges. *Review of Scientific Instruments*, 65(1):140–154, 1994.
- [36] J. P. Boeuf and L. C. Pitchford. Two-dimensional model of a capacitively coupled rf discharge and comparisons with experiments in the Gaseous Electronics Conference reference reactor. *Physical Review E*, 51(2):1376–1390, 1995.
- [37] M B Hopkins. Langmuir Probe Measurements in the Gaseous Electronics Conference RF Reference Cell. *Journal of Research of the National Institute of Standards and Technology*, 100(4):415–425, 1995.
- [38] Lawrence J. Overzet and Michael B. Hopkins. Spatial variations in the charge density of argon discharges in the Gaseous Electronics Conference reference reactor. *Applied Physics Letters*, 63(18):2484–2486, 1993.
- [39] Mark A. Sobolewski. Electrical characterization of radio-frequency discharges in the Gaseous Electronics Conference Reference Cell. *Journal of Vacuum Science & Technology A: Vacuum, Surfaces, and Films*, 10(6):3550–3562, 1992.

Elastic electron collisions in dusty plasmas

Preface. Dusty plasmas comprise a complex mixture of neutrals, electrons, ions and dust grains, which are found throughout the universe and in many technologies. The complexity resides in the chemical and charging processes involving dust grains and plasma species, both of which impact the collective plasma behavior. For decades, the orbital-motion-limited theory is used to describe the plasma charging of dust grains, in which the electron current is considered collisionless. In this chapter, it is shown that the electron (momentum transfer) collision frequency exceeds the electron plasma frequency in a powder-forming plasma. This indicates that the electron current is no longer collisionless, and the orbital-motion-limited theory may need corrections to account for elastic electron collisions. This implication is especially relevant for higher gas pressure, lower plasma density, and larger dust grain size and density.

5.1 Introduction

Complex and dusty plasmas are ubiquitous throughout outer space (where they dictate astrophysical and astrochemical processes), in laboratories worldwide (as macroscopic model systems to study fundamental physical phenomena), and in industries (where they form the backbone of many manufacturing processes). For instance, extraterrestrial dust grains—often embedded in (partly) ionized media called plasmas—may play a critical role in interstellar space [1, 2], in planet and star formation [3, 4, 5], and even in the emergence of life [6, 7]. At the same time, the origin of cosmic dust [8] and its interplay with other cosmic constituents [9, 10]

This chapter has been published: T.J.A. Staps, M.I. van de Ketterij, B. Platier, and J. Beckers, *The underexposed effect of elastic electron collisions in dusty plasmas*, Communications Physics 4, 231 (2021), DOI: 10.1038/s42005-021-00734-w.

remains largely elusive. Closer to home, cosmic dust analogs are created on a daily basis in laboratory dusty plasmas [11] to study phase transitions at macroscopic length scales, fundamental plasma charging dynamics [12, 13], strongly coupled systems [14], and the crystallization of lattice structures [15]. In the semiconductor and solar cell industry, low-temperature plasmas are indispensable for the formation of thin, uniform layers such as coatings. The chemically reactive plasmas used for such applications have appeared more than once as breeding grounds for particulate formation, which is experienced as either beneficial or disadvantageous depending on the specific application. Moreover, with the recent introduction of extreme ultraviolet lithography to the field, semiconductor manufacturers are heavily investing in developing strategies to control contamination [16, 17], for which the only feasible way forward appears to be based on plasma technology involving Coulomb interaction between generated discharges and plasma-charged contaminants.

A crucial part of our understanding of cosmic and terrestrial complex and dusty plasmas lies in the complex yet elementary interaction between dust grains and the plasma environment in which they are embedded. Elementary interactions in a low-temperature plasma are by default dictated by free electrons, while the temperature of heavy species (ions and neutrals) remains close to room temperature. The low-energy part of the electron cloud determines the mean electron energy, the plasma conductivity, the Debye length and the ion sound speed in plasmas [18]. On the other hand, the high-energy part governs inelastic collision rates and the sheath potential [18], of which the latter dictates the ion energy distribution and ion flux towards plasma-facing surfaces [19]. Hence, from a fundamental perspective, the electrons dictate fundamental processes such as ionization and dissociation of plasma species, the creation and shielding of local electric fields, and the electrical charging of dust grains.

In particular, the process of plasma-based charging of nano- to micrometer-sized dust grains—along with its correlation with elementary electron dynamics—is crucial to understand with respect to all aforementioned research fields and applications. The field in general assumes that the electron plasma frequency greatly exceeds the electron-neutral momentum transfer collision frequency at low-pressure (typically, 500 MHz and 50 MHz, respectively, for pristine argon plasmas at 0.1 mbar), and therefore the electron-neutral (momentum transfer) collision frequency has been neglected when developing theoretical frameworks for plasma-dust charging. This assumption applies to the orbital-motion-limited (OML) theory, introduced by Irving Langmuir [20], which is the widely accepted theoretical framework for predicting the surface charge of dust grains in dusty plasmas.

In this chapter, experimental evidence (see Fig. 5.5) is provided to show that the electron-neutral collision frequency should be included in the dust charging theory by showing its dominance over other timescales in a dusty plasma. For this purpose, the electron-neutral collision frequency for momentum transfer (effective collision frequency ν_{eff}) was measured in addition to the electron plasma frequency f_{pe} (via the free electron density n_e). The free electron density is widely used in literature to indicate and monitor dust grain formation processes in plasmas. To achieve this, an exemplary case of dust grain formation was studied in a low pressure hexamethyldisiloxane (HMDSO) containing plasma (see Section 5.2 and Fig. 5.1) by application of microwave

cavity resonance spectroscopy (see Section 5.2.2). This diagnostic method is based on detecting the amount of detuning of a resonant mode of a plasma-filled microwave cavity. The resonant mode is characterized by its spectral response, and a typical cavity response to the dusty plasma is shown in Fig. 5.2 in Section 5.2.2. The growth behavior of dust grains as typically occurs in terrestrial dusty plasmas is observed. However, the results also show that the effective collision frequency exceeds the electron plasma frequency when dust grains are formed. Moreover, at the approximate moment that particle agglomeration sets in, a peculiar non-monotonous trend is observed in the electron collision frequency which has not been observed in prior studies. Hence, it is shown that the electron population is heavily affected by the formation of dust grains in addition to the well-established effect of electron depletion by dust grain charging [21, 22, 23]. This insight into the binary interaction between electrons and dust grains is of major importance for the earlier mentioned research fields and applications, and arguments that the effect should be incorporated in the existing paradigm and overall theoretical framework.

5.2 Methods

Section 5.2.1 describes the experimental setup briefly as used for the production of the dusty plasma, and the microwave measurements of the plasma characteristic frequencies. Section 5.2.2 discusses the MCRS technique in detail, with the underlying theoretical framework, and an uncertainty analysis. Section 5.2.3 presents the method used to calculate the effective collision frequency for electron-dust and electron-neutral momentum transfer collisions.

5.2.1 Experiment

The dust grains were grown in a gas discharge at room temperature produced in a vacuum vessel with controlled in- and outlet of neutral gas at a reduced pressure. A schematic overview of the experimental setup is shown in Fig. 5.1. The vessel had a diameter of 600 mm and a height of 450 mm, and it contained a cylindrical cavity with an inner diameter of $D_c = 66$ mm and an inner height of $H_c = 40$ mm. In this cavity, discharge electrodes were integrated to produce and confine the plasma. Vertical slits in the cylindrical wall allowed the laser beam to enter and exit the cavity, whereas a stainless steel mesh allowed scattered light to be observed by a camera. Meanwhile, the slits and mesh also allowed the gas to freely diffuse in and out of the cavity. Widely used in plasma processing, hexamethyldisiloxane (HMDSO, CAS Registry Number: 107-46-0, purity $\geq 99.5\%$) was introduced through evaporation from a liquid-containing volume connected to the vessel, while argon (purity $\geq 99.999\%$) was introduced using a mass flow controller. An operating pressure of 7.1×10^{-2} mbar was installed by balancing the inflow of the vapor-gas mixture by an outflow of gas species using a turbo-molecular and dry scroll pump in series (base pressure $\sim 1 \times 10^{-6}$ mbar (without inflow)), which were continuously running during the experiment to maintain a high purity level. Electrical power was capacitively coupled into the neutral gas mixture inside the plasma-confining cavity by applying an

alternating voltage to the (electrically isolated) top electrode, at a (radio-)frequency of 13.56 MHz, which is common for low-pressure discharges. The alternating voltage was generated using an RF signal generator combined with an amplifier. To optimize the transfer of electrical power, a matching network was used to adjust the total electrical impedance (impedance of the discharge cavity plus that of the matching network) observed by the RF amplifier to that of the amplifier output circuit, i.e., $50\ \Omega$. As a consequence, a strong electric field alternating at radio-frequency (RF) induced a gas discharge sustained at room temperature and subsequently induced the chemical reactions necessary for the polymerization, clustering, and agglomeration of molecular clusters, eventually resulting in (nanometer-sized) dust grains.

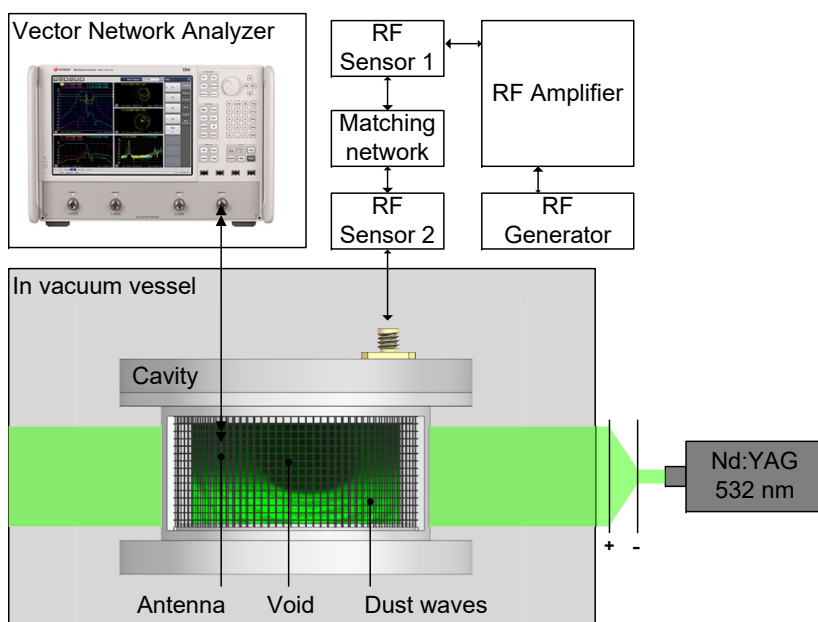


Figure 5.1: A schematic overview of the experimental setup. The microwave cavity confined the argon-hexamethyldisiloxane discharge used for growing dust grains in vacuum, where the grey box defines the elements that were located inside the vacuum. The RF system supplied electrical power to the discharge, where the RF generator and amplifier provided continuous power to the matching network which ensured optimal power transfer to the plasma. The RF power was measured using power sensors. Meanwhile, the plasma response was monitored by the Vector Network Analyzer, and the dust grains were observed by capturing scattered laser light on a high-speed camera. The green laser beam (continuous power, Nd:YAG, wavelength 532 nm) was expanded in the axial direction of the cavity by two cylindrical lenses, which allowed the creation of a laser sheet (indicated by bright green area) that entered and left the cavity through two slits in the cavity's side walls.

5.2.2 Microwave Cavity Resonance Spectroscopy

The gas discharge was produced inside a microwave cavity to enable microwave cavity resonance spectroscopy (MCRS) experiments, as depicted in Figure 5.1. A commercial vector network analyzer (E5072A, Keysight Technologies) was used to probe the spectral response of the fundamental mode TM_{010} by measuring the amount of reflected microwave power over a fixed microwave frequency range. The presence of free electrons created by the gas discharge de-tuned the resonant mode such that the corresponding resonance frequency and quality factor were shifted with respect to the case without plasma. At a sample rate of ~ 6 Hz, the network analyzer obtained spectral responses during the process of the formation of dust grains.

Microwave cavity resonance spectroscopy (MCRS) relies on the difference in (complex) permittivity between a gas discharge compared to vacuum:

$$\Delta\tilde{\epsilon} = \tilde{\epsilon}_1 - \epsilon_0, \quad (5.1)$$

where $\tilde{\epsilon}_1$ denotes the (complex) plasma permittivity, and ϵ_0 the vacuum permittivity. The (complex) plasma permittivity depends on the electron plasma frequency and on the effective collision frequency (due to elastic electron collisions with neutrals and dust) as [24]:

$$\tilde{\epsilon}_1 = \epsilon_0 \left(1 - \frac{(2\pi f_{\text{pe}})^2}{\nu_{\text{eff}}^2 + (2\pi f)^2} - i \frac{\nu_{\text{eff}}}{2\pi f} \frac{(2\pi f_{\text{pe}})^2}{\nu_{\text{eff}}^2 + (2\pi f)^2} \right), \quad (5.2)$$

with the electron plasma frequency f_{pe} , the effective collision frequency ν_{eff} , the microwave frequency f , and i the imaginary number. The relation between the electron plasma frequency and the free electron density reads:

$$f_{\text{pe}} = \frac{1}{2\pi} \sqrt{\frac{n_e e^2}{\epsilon_0 m_e}}, \quad (5.3)$$

with n_e the free electron density, e the elementary charge, and m_e the electron mass.

The change in permittivity is directly related to changes in the free electron density and in the effective collision frequency, which de-tune the characteristics of the cavity's resonant modes. A resonant mode is characterized by the spectral position of the resonance frequency f_{res} and the quality factor Q_{res} (related to the full-width-at-half-maximum of a resonance peak), which relate to changes in the (complex) permittivity $\Delta\tilde{\epsilon}$ of the medium contained inside the microwave cavity according to the Slater perturbation theorem as [25, 26, 27]:

$$\frac{\Delta f}{f_0} + i \frac{1}{2} \Delta \left(\frac{1}{Q} \right) = - \frac{\iiint_{V_c} \Delta\tilde{\epsilon} |\mathbf{E}|^2 d\mathbf{r}}{2\epsilon_0 \iiint_{V_c} |\mathbf{E}|^2 d\mathbf{r}}. \quad (5.4)$$

Here, $\Delta f = f_1 - f_0$ denotes the plasma-induced shift in resonance frequency, f_1 the resonance frequency with plasma, f_0 the resonance frequency without plasma, \mathbf{E} the (local) microwave electric field inside the cavity, V_p the plasma volume, V_c the cavity volume, and \mathbf{r} the spatial coordinate vector.

The electric-field-weighted volume ratio is often defined to express the ratio between the plasma volume V_p (i.e. the perturbed volume of the cavity) and the cavity volume:

$$\mathcal{V} = \frac{\iiint_{V_p} |\mathbf{E}|^2 d\mathbf{r}}{\iiint_{V_c} |\mathbf{E}|^2 d\mathbf{r}}. \quad (5.5)$$

This definition is allowed upon assuming that the perturbation homogeneously disturbs the resonant mode, and hence, the complex permittivity can be taken out of the integral in Eqn. (5.4). Consequently, the effective collision frequency and electron plasma frequency can be derived by combining Eqn. (5.4) with Eqn. (5.1) and (5.2) such that:

$$\nu_{\text{eff}} = \pi f_1^2 \frac{\Delta(1/Q)}{\Delta f}, \quad (5.6)$$

and

$$f_{pe} = \sqrt{\frac{2f_1 \Delta f}{\mathcal{V}}}. \quad (5.7)$$

As can be seen, the volume ratio does not affect the effective collision frequency, but enters the electron plasma frequency evaluation. The electric-field-weighted volume ratio was estimated equal to 0.54 using $V_p = \pi/4 D_p^2 H_p$ and $V_c = \pi/4 D_c^2 H_c$, with the plasma diameter $D_p = 56$ mm, and plasma height $H_p = 30$ mm (where a sheath size of 5 mm was assumed). This estimate for \mathcal{V} was included in the upper bound for f_{pe} .

A vector network analyzer was used to obtain the spectral response over the microwave frequency range $f = 3.228 - 3.478$ GHz, which includes the resonant peak of the empty cavity and that of the plasma-filled cavity. The plasma-induced shifts of the resonance frequency were in the order of ~ 100 MHz. A Lorentzian curve fit through the data around the resonant peak was then applied to obtain the resonance frequency and the quality factor. This fit curve was defined as:

$$P_r = A \frac{\left(\frac{f_{\text{res}}}{2Q_{\text{res}}}\right)^2}{(f - f_{\text{res}})^2 + \left(\frac{f_{\text{res}}}{2Q_{\text{res}}}\right)^2} + a_0 + a_1 (f - f_{\text{res}}), \quad (5.8)$$

where A , a_0 , and a_1 are scaling factors for the Lorentzian curve and linear offsets in the microwave system, and f_{res} and Q_{res} are the resonance frequency and quality factor. Figure 5.2 provides a typical spectral response of the plasma-filled cavity at a certain time. This microwave spectrum contains a (TM₀₁₀) resonant peak and some local resonances due to cabling and feedthroughs. The spectral position and shape of these background resonances were verified to be static and independent of the varying spectral position and shape of the resonant peak. The above mentioned Lorentzian fit was applied to the data set, where data points corresponding to the local minima were excluded from the fitting procedure to produce the nominal values for f_{pe} and ν_{eff} . To determine the upper limit of the measurement errors Δ_{f_0} , Δ_{f_1} , Δ_{Q_0} and Δ_{Q_1} , the complete data set (including the spectrally localized background resonances) was used.

The error propagation from f_{res} and Q_{res} to f_{pe} and ν_{eff} was established by applying linear perturbation analysis to Eqn. (5.6) and (5.7). Performing the algebra results in

the desired expression for the error in ν_{eff} as a function of the perturbed measurement variables:

$$\begin{aligned} \Delta_{\nu_{\text{eff}}} = & \left(\pi f_1^2 \frac{\Delta(1/Q)}{\Delta f^2} \right) \Delta_{f_0} + \left(\frac{\pi f_1^2}{\Delta f} \frac{1}{Q_0^2} \right) \Delta_{Q_0} \\ & + \left(2\pi f_1 \frac{\Delta(1/Q)}{\Delta f} - \pi f_1^2 \frac{\Delta(1/Q)}{\Delta f^2} \right) \Delta_{f_1} - \left(\frac{\pi f_1^2}{\Delta f} \frac{1}{Q_1^2} \right) \Delta_{Q_1}. \end{aligned} \quad (5.9)$$

A similar exercise applied to Eqn. (5.7) results in the error propagation for f_{pe} :

$$\begin{aligned} \Delta_{f_{\text{pe}}} = & \frac{1}{2} \left(\frac{(2\pi f_1)^2 + \nu_{\text{eff}}^2}{2\nu} \frac{\Delta f}{f_1} \right)^{-3/2} \times \\ & \left\{ \left(\frac{(2\pi f_1)^2 + \nu_{\text{eff}}^2}{2\nu} \frac{1}{f_1} \right) \Delta_{f_0} - \left(\frac{\pi f_1}{\nu} \frac{1}{Q_0^2} \right) \Delta_{Q_0} \right. \\ & \left. - \left(\frac{4\pi^2}{2\nu} (2f_1 - f_0) + \frac{\nu_{\text{eff}}^2}{2\nu} \frac{f_0}{f_1^2} \right) \Delta_{f_1} + \left(\frac{\pi f_1}{\nu} \frac{1}{Q_1^2} \right) \Delta_{Q_1} \right\}. \end{aligned} \quad (5.10)$$

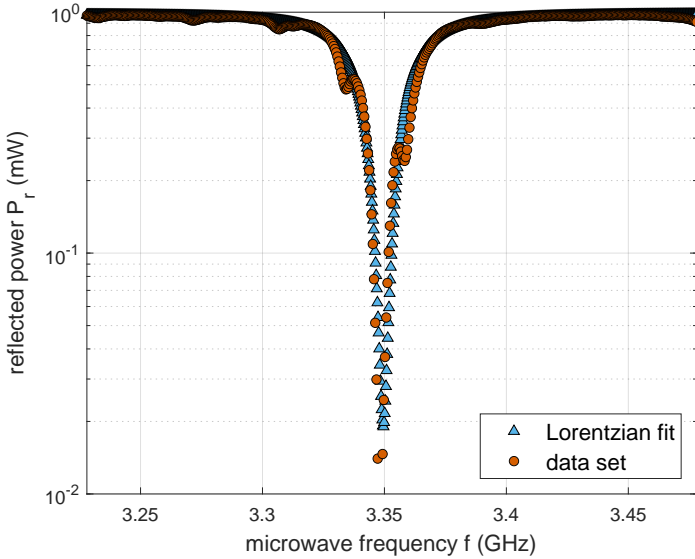


Figure 5.2: Typical microwave cavity response to dusty plasma. The spectral response of the microwave cavity is depicted in terms of reflected power P_r as a function of microwave frequency f , and corresponding Lorentzian fit, at $t = 32.8$ s. The Lorentzian fit is defined by the resonance frequency, at which the reflected power is minimal, and the quality factor which is related to the full-width-at-half-maximum of the Lorentzian curve.

5.2.3 Theoretical analysis

The total effective collision frequency of electrons with other species in dust grain-forming plasmas comprises the sum of effective collision frequencies due to electron-neutral and electron-dust collisions:

$$\nu_{\text{eff}} = \nu_{\text{eff}}^{\text{en}} + \nu_{\text{eff}}^{\text{ed}}. \quad (5.11)$$

Here, the electron-neutral collision frequency consists of the effective collision frequency due to multiple neutral gas species such as argon, hexamethyldisiloxane, and possibly by-products. The effective collision frequency originates from the fact that the momentum transfer collision frequency ν_m depends on the electron energy ϵ [28]:

$$\nu_{\text{eff}} = \frac{\int_0^\infty \epsilon^{3/2} \frac{\nu_m(\epsilon)}{\nu_m^2(\epsilon) + \omega^2} \frac{dF}{d\epsilon} d\epsilon}{\int_0^\infty \epsilon^{3/2} \frac{1}{\nu_m^2(\epsilon) + \omega^2} \frac{dF}{d\epsilon} d\epsilon}, \quad (5.12)$$

with $\omega = 2\pi f$ the (angular) microwave frequency and F the electron energy distribution function (EEDF). A Maxwellian EEDF is assumed with mean electron energy $\bar{\epsilon}$. The momentum transfer collision frequency follows by assuming a Lorentz gas such that

$$\nu_m = n\sigma_m\bar{v}_e, \quad (5.13)$$

which includes a fixed background of neutral gas or dust grains of density n , a momentum transfer cross section for electron-neutral or electron-dust collisions σ_m , and the electron thermal velocity \bar{v}_e .

The cross section and collision frequency for electron-dust momentum transfer, and the effective collision frequency for that process, are depicted in Figure 5.3 (for a Maxwell-Boltzmann electron energy distribution). The cross section for electron-dust momentum transfer follows from the theory [29, 30] and agrees well with the simulations by Choi and Kushner [31]. Fundamentally, the electron-dust interaction involves the electron scattering from charged dust grains and the attachment of electrons onto the surface. The elastic scattering of electrons due to the dust potential resembles the momentum transfer process, from which the electron-dust momentum transfer cross section can be derived [30]:

$$\sigma_m^{\text{ed}}(\epsilon) = \pi a_d^2 \left(-\frac{V_d}{\epsilon} \right)^2 \exp\left(\frac{2a_d}{\lambda_{\text{DL}}} \right) \ln \Lambda, \quad (5.14)$$

with the dust surface potential V_d , the Coulomb parameter

$$\Lambda = -\frac{\lambda_{\text{DL}} T_e}{a_d V_d}, \quad (5.15)$$

and λ_{DL} as the linearized Debye length [30].

Similarly, the electron-neutral momentum transfer frequency can be evaluated theoretically using Eqn. (5.12) and (5.13). Fig. 5.4 depicts the electron-neutral momentum transfer cross section, momentum transfer collision frequency, and effective collision frequency using cross section data for argon [32], tetraethylorthosilicate

(TEOS) [33, 34], and tetramethylsilane (TMS) [35, 33, 36]. Although several HMDSO-related plasma processes have been studied [37, 38], cross section data for electron-HMDSO momentum transfer is unavailable in literature, and hence, the calculations with the aforementioned precursors are considered as most representative.

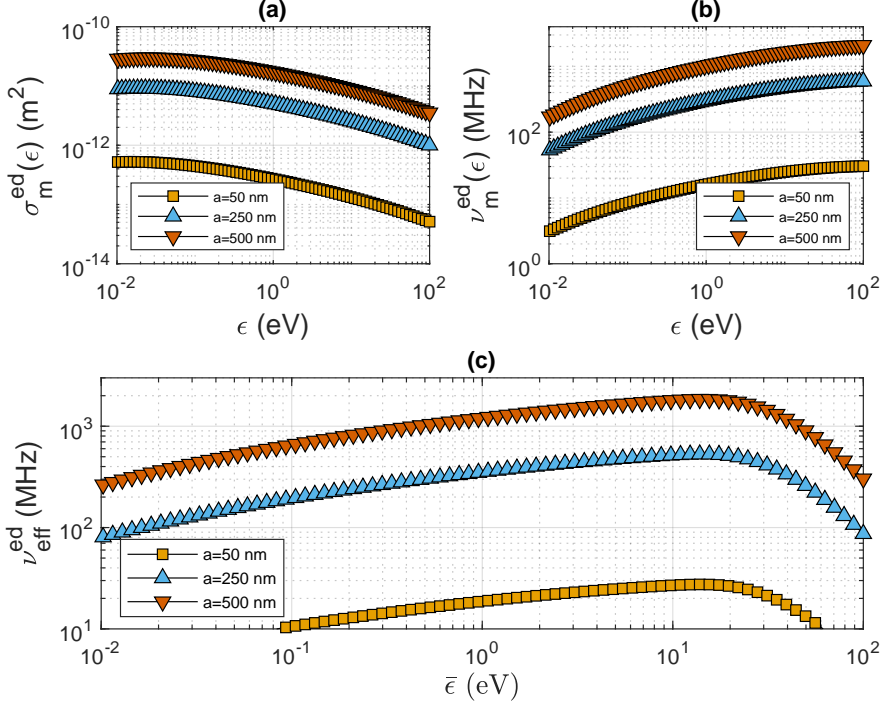


Figure 5.3: Theoretical evaluation of electron-dust momentum transfer collisions for different dust radii. (a) The momentum transfer cross section σ_m^{ed} is calculated using Eqn. (5.14) as a function of electron energy ϵ . (b) The momentum transfer collision frequency ν_m^{ed} follows from the electron-dust momentum transfer cross section in combination with Eqn. (5.13) as a function of the electron energy ϵ . (c) The effective collision frequency $\nu_{\text{eff}}^{\text{ed}}$ for electron-dust collisions is evaluated using Eqn. (5.12), which is evaluated as a function of the mean electron energy $\bar{\epsilon}$. In each panel, the calculation of σ_m^{ed} , ν_m^{ed} , and $\nu_{\text{eff}}^{\text{ed}}$ is performed for dust radii $a = 50$ nm (orange squares), $a = 250$ nm (blue upward-facing triangles) and $a = 500$ nm (red downward-facing triangles), for a fixed dust density $n_d = 10^{14} \text{ m}^{-3}$.

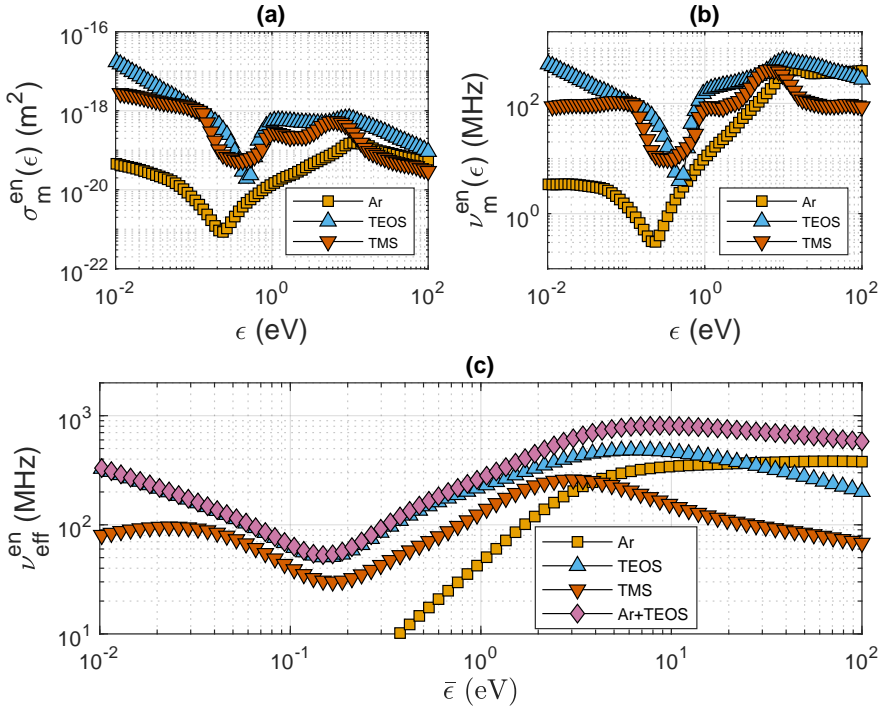


Figure 5.4: Theoretical evaluation of electron-neutral momentum transfer collisions for different neutral gas species. The neutral gas species are denoted in the legend as argon (Ar, orange squares), tetraethylorthosilicate (TEOS, blue upward-facing triangles), and tetramethylsilane (TMS, red downward-facing triangles). (a) The momentum transfer cross section σ_m^{en} is obtained from literature for argon [32], TEOS [33, 34], and TMS [35, 33, 36] as a function of electron energy ϵ . (b) The momentum transfer collision frequency ν_m^{en} is calculated using Eqn. (5.13) as a function of electron energy ϵ , using the neutral gas density $n_n = 1.75 \times 10^{21} \text{ m}^{-3}$ (for pressure $p = 7.1 \times 10^{-2} \text{ mbar}$ and the momentum transfer cross section). (c) The effective collision frequency $\nu_{\text{eff}}^{\text{en}}$ is calculated using Eqn. (5.12) as a function of the electron mean energy $\bar{\epsilon}$. The total effective collision frequency (Ar+TEOS, purple diamonds) was calculated using the argon and TEOS values weighted by the partial argon pressure $p_{\text{Ar}} = 5.4 \times 10^{-2} \text{ mbar}$ and partial TEOS pressure $p_{\text{TEOS}} = 1.7 \times 10^{-2} \text{ mbar}$, where the latter was defined equal to the partial hexamethyldisiloxane (HMDSO) pressure during the experiment.

5.3 Results

This section presents the main result of this chapter. Section 5.3.1 briefly introduces the experimental result, whereas Section 5.3.2 discusses the electron plasma frequency in more detail, and likewise Section 5.3.3 discusses the effective collision frequency.

5.3.1 Dust formation process

The process of dust formation in low pressure reactive plasmas—typically taking between 1 and 100 seconds depending on the plasma conditions—is widely recognized due to numerous exemplary studies conducted on discharges in acetylene [39, 40], silane [41], hexamethyldisiloxane [42, 43], methane [44] and fluorocarbon [45]. In agreement with these studies, our temporally-resolved experiments obtaining the electron plasma frequency for an exemplary low pressure argon-hexamethyldisiloxane plasma—as shown in Figure 5.5—indicate that the dust formation process chronologically follows three well-known phases: (I) nucleation, (II) agglomeration, and (III) accretion.

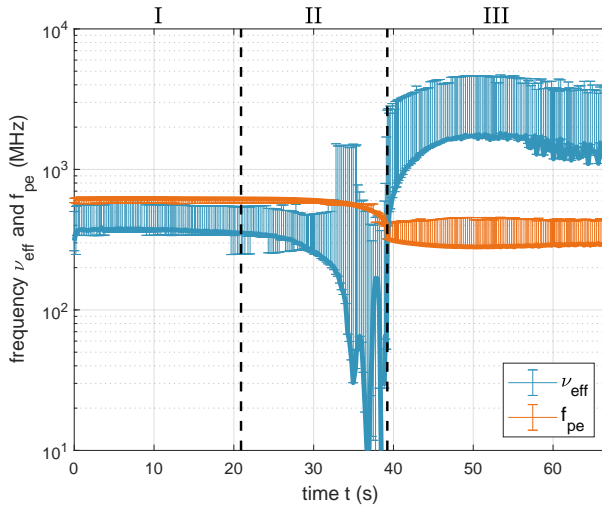


Figure 5.5: Characteristic frequencies of the plasma during dust grain formation. The effective collision frequency ν_{eff} (blue line and error bars) and electron plasma frequency f_{pe} (orange line and error bars) are obtained from microwave cavity resonance spectroscopy measurements as a function of time, with respect to the moment of plasma initiation at $t = 0$ s, during dust formation in a low-pressure radio-frequency driven capacitively-coupled argon-hexamethyldisiloxane (i.e. HMDSO) discharge. The error bars represent the effect of the (estimated) error in the determination of the resonance frequency and quality factor on the effective collision frequency and electron plasma frequency. The derivation of the error propagation is described in Section 5.2.2. The gas discharge was created under the following experimental conditions: partial argon pressure at 5.7×10^{-2} mbar, partial HMDSO pressure at 1.4×10^{-2} mbar, plasma volume of 42 cm^3 , and absorbed power density of 0.7 Wcm^{-3} .

5.3.2 Electron plasma frequency

In phase I, the electron density—and therefore, the electron plasma frequency f_{pe} —remains nearly constant during the formation of nanometer-sized solid protoparticles (also termed primary clusters or nuclei). It can be seen from Fig. 5.5 that the (phase I-averaged) electron plasma frequency is 619 ($-44/+12$) MHz (i.e., $n_e = 4 \times 10^{15}$ ($-3.45 \times 10^{15} / + 4.16 \times 10^{15}$) m^{-3}), which is typical for low-temperature discharges during the nucleation of dust grains [46, 47].

In phase II, the electron plasma frequency first decreases gradually, after which it starts to decrease more rapidly towards the end of this phase ($t \gtrsim 35$ s). This finding is also in agreement with the existing paradigm that the formation of clusters induces an additional electron loss channel due to electron attachment to the clusters, which lowers the overall electron density in the plasma [48].

In phase III, the electron plasma frequency during the accretion phase is characterized by a low (phase III-averaged) value of 290 ($-0/+150$) MHz. Comparing this value to the first phase, a threefold decrease of the electron plasma frequency means that the global electron density is nine times lower as these two quantities scale as $f_{pe} \propto \sqrt{n_e}$. Clearly, the effect of the permanent charging of the dust grains is visible, but the further growth of the dust grains does not significantly affect the absolute value of the electron plasma frequency throughout this third phase. While the dust grains grow in size and hence draw an increasing electron current from the discharge ($I_e \propto a^2$), this additional electron loss is balanced by an increased ionization rate through a surge of the mean electron energy. Meanwhile, the electron density remains constant as can be seen from Fig. 5.5.

The measurement of the electron plasma frequency (i.e., the global electron density) agrees well with experiments described in the literature and the existing theoretical framework. However, measurement of the effective collision frequency in a plasma-nanoparticle system has not been reported in literature before, although its measurement facilitates a direct comparison to the electron plasma frequency and provides insight into peculiarities.

5.3.3 Effective collision frequency

The time-resolved trace of the effective collision frequency throughout the three earlier mentioned phases reveals insight regarding the importance of elastic electron collisions in dusty plasmas.

In phase I, the effective collision frequency remains nearly constant at a (phase I-averaged) value of 368 ($-30/+207$) MHz. As can be seen from Fig. 5.5, this value is below that of f_{pe} , and as generally accepted by the field, the electron dynamics of low-energy electrons remain collisionless during this phase.

In phase II, the effective collision frequency remains relatively constant at first (within error bounds), whereas the results mainly show significant changes in the effective collision frequency during the final part of this phase. In particular, towards the end of the coagulation phase, the effective collision frequency decreases to values below that of the first phase, while the decline of the global electron density is much smaller and occurs only during the final part of this phase. It should be noted that

fluctuations of the effective collision frequency are a consequence of the measurement technique, because the quality factor approaches the pre-plasma value resulting in small values of $\Delta(1/Q)$ (see Section 5.2.2). The decrease of the effective collision frequency may be explained by the clustering of (prototypical) nanoparticles for which the physical interpretation and the relation with the observed phenomenon is treated in Section 5.4.

In phase III, the accretion phase is characterized by a surprisingly high (phase III-averaged) effective collision frequency of 1429 ($-0/+2601$) MHz, which exceeds the electron plasma frequency of 323 ($-0/+176$) MHz by almost a factor of five. Despite the predictive capability of the existing paradigm (see Section 5.2.3), such values for the effective collision frequency were not stated or measured as of yet and appear crucial to account for in the orbital-motion-limited (OML) theoretical framework describing dust grain formation and growth in plasmas, even at low pressure.

5.4 Discussion

The time evolution of the electron plasma frequency serves as a benchmark for the identification of the different phases (i.e., nucleation, agglomeration, and accretion) in the overall dust grain growth process inside the plasma. During the first stage of nucleation, the electron plasma frequency is 575 – 631 MHz (resulting from $n_e \sim 1 \times 10^{15} - 1 \times 10^{16} \text{ m}^{-3}$), which is typical for discharges driven by a radio-frequency voltage signal [46, 47] or by a direct current [49]. Hereafter, the electron plasma frequency falls off by a factor of three decrease throughout the coagulation phase, which is in close agreement with experiments performed by other workers in the field [50, 51]. As described in the literature, this trend is attributed to the permanent binding of electrons to dust grains.

During the second phase, i.e. the agglomeration phase, the effective collision frequency initially remains approximately constant. This finding agrees with measurements performed by other workers [39, 52], and it relates to the plasma and dust properties. Despite the possible formation of small clusters in this phase, the electron-dust momentum transfer cross section is still irrelevant with respect to the (elastic) electron-neutral collisions in both the first and second part of this phase (for dust grain radii $a \leq 50 \text{ nm}$ and dust density $n_d \leq 10^{14} \text{ m}^{-3}$, see Fig. 5.3). The irrelevance of the electron-dust cross section for momentum transfer implies that the electron loss channel due to attachment of electrons to dust grains is also insignificant up to this point, and this implication is reflected by the stability of the electron plasma frequency and effective collision frequency.

At the end of the agglomeration phase, the effective collision frequency reaches minimum values $\sim 10 - 100 \text{ MHz}$. A possible explanation for the low effective collision frequency is the attachment of high-energy electrons to the agglomerating dust grains. As a result of the growth of dust grains due to agglomeration of clusters that were formed during the first phase, the surface charge averaged over all protoparticles becomes increasingly negative when time progresses towards the end of the coagulation phase. The high-energy electrons collide most frequently with the dust grains, because they travel larger distances than their slower counterparts within the same time frame.

Consequently, the high-energy tail of the electron energy distribution is depleted which results in an effective decrease of the mean electron energy on timescales related to the absorption of electrons by the small protoparticles.

The observed temporal decay of the effective collision frequency compares well with the absorption timescale governed by the electron and ion currents[53]:

$$\tau_A \approx \left(\pi a_d^2 n_d \bar{v}_i \left(1 + \frac{V_d}{T_i} \right) \right)^{-1} \approx 0.65 \text{ s}, \quad (5.16)$$

where a_d and n_d denote the dust grain radius and number density, \bar{v}_i the ion thermal velocity, V_d the dust floating potential, and T_i the ion temperature, respectively. For this calculation, dust radius and density are $a_d = 1 \text{ nm}$ and $n_d = 10^{14} \text{ m}^{-3}$, dust floating potential [53] $V_d = -eq_d / (4\pi\epsilon_0 a_d) \approx -1.44 \text{ V}$ (with dust charge $q_d = 1$ [54], elementary charge e , and vacuum permittivity ϵ_0), and ion temperature $T_i = 0.026 \text{ eV}$ (i.e. 300 K). The effective collision frequency must follow this behavior, because the electron-dust momentum transfer cross section is much smaller than the electron-neutral momentum transfer cross section.

The steep increase of the effective collision frequency at the end of this phase shows that the depletion of electrons is terminated as they are repelled by the permanent negative surface potential of the formed and growing dust grains. In addition, further supporting the latter explanation, the electron plasma frequency suddenly decreases at the end of the coagulation phase due to this permanent charging of the dust grains, and this means that the energy input per electron increases as the (RF) electric field remains unchanged. The jump in the effective collision frequency can potentially be attributed to the effect of increasing electron mean energy on the electron-neutral momentum transfer cross section. From a theoretical investigation (see Fig. 5.3), it can be concluded that the electron-dust contribution is at most 24 MHz for $a_d = 50 \text{ nm}$ (assumed upper limit of the average dust radius just after coagulation[55, 56]). By contrast, the electron-neutral contribution ranges from 100 MHz to 400 MHz, for the mean electron energy $\bar{\epsilon} = 0.3 - 1.7 \text{ eV}$, respectively (as can be seen from Fig. 5.4). This implies that the electron mean energy is low before coagulation, and afterwards rapidly increases to higher values during the third phase.

During the third phase, i.e. the accretion phase, the presence of dust grains has a large impact on the electron dynamics via the effect of the electron mean energy on the electron-neutral (momentum transfer) collisions. In this phase, dust grain radii and number densities are typically in the range of 50 – 250 nm and $\sim 1 \times 10^{14} \text{ m}^{-3}$ in the discharge center [56, 57, 58]. This means that the contribution of electron-dust momentum transfer collisions to ν_{eff} is about 20 – 440 MHz for $\bar{\epsilon} \sim 1 - 3 \text{ eV}$ and $a_d = 50 - 250 \text{ nm}$ (see Fig. 5.3). Although the electron-dust contribution is non-negligible according to the theory, the electron-neutral contribution to the effective collision frequency remains dominant. It is well-known that the dust grain potential, mean electron energy, electron energy distribution, relevant collision partners, and corresponding cross sections change simultaneously during the third stage. Clearly, the effective collision frequency is governed by this complex interplay between plasma and dust grains.

5.5 Implications

The main experimental finding of the presented work is the fact that, in a dust-forming low pressure plasma, the effective electron collision frequency may become considerably higher than the electron plasma frequency. The implications of this finding are related to the most commonly used theory throughout the field to predict dust grain charging in low-temperature, low pressure plasmas: the orbital-motion-limited (OML) theory. There are three essential principles underlying the OML theory, of which we consider the first one: electrons and ions experience collisionless orbits in the electrostatic (Debye) vicinity of a dust grain immersed in a quasi-neutral plasma environment [59]. In plasma physical terms, this means that the following ordering of dust and plasma parameters must apply: $a_d \ll \lambda_D \ll l$, where λ_D is the Debye length and l the mean free path of the species under consideration. In other words, the Debye sphere virtually enclosing the dust grain is much larger than the grain itself, and collisions do not occur within the Debye sphere. Considering the electrons, the assumption that the electron mean free path is much larger than the electron Debye length means that the electron current towards the dust grain is collisionless.

Serious effort has been put into the extension, modeling and verification of the OML theory [60, 61, 62, 59, 63, 64]. For example, under certain conditions of pressure and dust grain size, there is a large probability that ions experience on average one collision with a neutral gas particle during their travel across the Debye sphere enclosing the dust grain [65, 66, 67]. In the hydrodynamic limit, ion-neutral collisions are so frequent that the ion dynamics can be described as a continuum [68]. Yet, in all such cases, the electron current has been considered collisionless until now. However, our results show that the electron current during the third phase—when permanently charged dust grains are in fact present in large quantities—resides in a similar situation as the ion current in the weakly collisional regime. This is because the electron mean free path is only $l_e = \bar{v}_e / \nu_{\text{eff}} = 364 \mu\text{m}$, while the electron Debye length is $\lambda_{De} = \bar{v}_e / f_{pe} = 2127 \mu\text{m}$, given that \bar{v}_e is the electron thermal velocity assuming $T_e = 1 \text{ eV}$. This implies that the electron current is collisional as $l_e \ll \lambda_{De}$ and that the expression for the electron current in the overall plasma-dust charging framework (e.g. the OML theory) should incorporate electron-neutral (momentum transfer) collisions occurring within the Debye sphere enclosing the dust grain. As a matter of fact, the elastic electron collisions suppress the ability of the electrons to shield perturbations, and therefore the Debye length will be larger for the same electron density in case of a significant effective collision frequency.

The relevance of the effective collision frequency also affects other fundamental processes in the plasma such as electron heating. The dusty plasma (probed during the accretion phase) operates in the so-called Ω -mode or drift-ambipolar mode [69, 70, 71, 72, 73], where a drift electric field accelerates electrons in the plasma bulk and an ambipolar field—created by electron density gradients—heats electrons near the sheath edge. The drift electric field is induced by the low bulk electrical conductivity due to electron depletion, which is similar to the effect of a high electron-neutral collision frequency in atmospheric pressure discharges [74, 75]. In addition to previous findings on electron depletion for Ω -mode operation, the significance of the effective

collision frequency in the presented low pressure plasma experiment suggests that the electrical conductivity is further reduced. Consequently, this implies that the drift electric field results in stronger electron heating compared to plasma conditions with insignificant effective collision frequency.

5.6 Conclusion

The experimental results show that the electron current towards a dust grain can be collisional during the accretion phase of a low pressure dusty plasma—which holds for $t \geq 39$ s in the presented measurements—in contrast to the existing paradigm. This conclusion is based on the measurements showing that the effective collision frequency exceeds the electron plasma frequency multiple times during the third phase of dust growth in a typical low pressure discharge. This translates into an electron mean free path smaller than the electron Debye length, meaning that the electrons in the dust grain sheath collide elastically multiple times before they complete their orbit. It is exactly this assumption of a collisionless electron current that forms an integral part of the widely accepted orbital-motion-limited theory in which electron-neutral collisions have always been neglected, up to now. It is expected that this result is also relevant for other plasmas in which dust grains are embedded, and that electron-neutral momentum transfer collisions become even more dominant in cases of higher gas pressure, lower electron density, and larger dust grain size.

5.7 Bibliography

- [1] N. C. Wickramasinghe. Small dust grains and the heating of HI clouds. *Nature*, 227(5258):587–588, 1970.
- [2] P. Merino, M. Švec, J. I. Martínez, P. Jelinek, P. Lacovig, M. Dalmiglio, S. Lizzit, P. Soukiasian, J. Cernicharo, and J. A. Martín-Gago. Graphene etching on SiC grains as a path to interstellar polycyclic aromatic hydrocarbons formation. *Nature Communications*, 5(1):3054, 2014.
- [3] F. J. Molster, I. Yamamura, L. B.F.M. Waters, A. G.G.M. Tielens, Th De Graauw, T. De Jong, A. De Koter, K. Malfait, M. E. Van Den Ancker, H. Van Winckel, R. H.M. Voors, and C. Waelkens. Low-temperature crystallization of silicate dust in circumstellar disks. *Nature*, 401(6753):563–565, 1999.
- [4] Tao Yang, Aaron M. Thomas, Beni B. Dangi, Ralf I. Kaiser, Alexander M. Mebel, and Tom J. Millar. Directed gas phase formation of silicon dioxide and implications for the formation of interstellar silicates. *Nature Communications*, 9(1):774, 2018.
- [5] Dejan Vinković. Radiation-pressure mixing of large dust grains in protoplanetary disks. *Nature*, 459(7244):227–229, 2009.
- [6] François Dulieu, Emanuele Congiu, Jennifer Noble, Saoud Baouche, Henda Chaabouni, Audrey Moudens, Marco Minissale, and Stéphanie Cazaux. How micron-sized dust particles determine the chemistry of our Universe. *Scientific Reports*, 3(1):1338, 2013.
- [7] Hideyuki Nakano, Naoki Hirakawa, Yasuhiro Matsubara, Shigeru Yamashita, Takuo Okuchi, Kenta Asahina, Ryo Tanaka, Noriyuki Suzuki, Hiroshi Naraoka, Yoshinori Takano, Shogo Tachibana, Tetsuya Hama, Yasuhiro Oba, Yuki Kimura, Naoki Watanabe, and Akira Kouchi. Precometary organic matter: A hidden reservoir of water inside the snow line. *Scientific Reports*, 10(1):7755, 2020.
- [8] Christa Gall, Jens Hjorth, Darach Watson, Eli Dwek, Justyn R. Maund, Ori Fox, Giorgos Leloudas, Daniele Malesani, and Avril C. Day-Jones. Rapid formation of large dust grains in the luminous supernova 2010jl. *Nature*, 511(7509):326–329, 2014.
- [9] Loretta Dunne, Stephen Eales, Rob Ivison, Haley Morgan, and Mike Edmunds. Type II supernovae as a significant source of interstellar dust. *Nature*, 424(6946):285–287, 2003.
- [10] S.P. Tarafdar and N.C. Wickramasinghe. Charged dust grains and excitation of rotational levels of interstellar molecular hydrogen. *Nature*, 254:203–205, 1975.
- [11] P. K. Shukla. A survey of dusty plasma physics. *Physics of Plasmas*, 8(5 II):1791, 2001.

- [12] M.R. Jana, A. Sen, and P.K. Kaw. Collective effects due to charge-fluctuation dynamics in a dusty plasma. *Physical Review E*, 48(4):3930–3933, 1993.
- [13] B. Van Minderhout, J. C.A. Van Huijstee, B. Platier, T. Peijnenburg, P. Blom, G. M.W. Kroesen, and J. Beckers. Charge control of micro-particles in a shielded plasma afterglow. *Plasma Sources Science and Technology*, 29(6):065005, 2020.
- [14] M. Lyon, S. D. Bergeson, G. Hart, and M. S. Murillo. Strongly-coupled plasmas formed from laser-heated solids. *Scientific Reports*, 5:1–7, 2015.
- [15] John Maddox. Plasma dust as model crystals. *Nature*, 370(6489):411, 1994.
- [16] Mark A. van de Kerkhof, Ernst Galutschek, Andrei Yakunin, Selwyn Cats, and Christian Cloin. Particulate and molecular contamination control in EUV-induced H₂-plasma in EUV lithographic scanner. *Proceedings SPIE*, 11489(August):114890K, 2020.
- [17] Job Beckers, Boy van Minderhout, Paul Blom, Gerrit Kroesen, and Ton Peijnenburg. Particle contamination control by application of plasma. *Proceedings SPIE*, 11323(March):113232L, 2020.
- [18] Vladimir Kolobov and Valery Godyak. Electron kinetics in low-temperature plasmas. *Physics of Plasmas*, 26(6):060601, 2019.
- [19] Micheal A. Lieberman and Allan J. Lichtenberg. *Principles of Plasma Discharges and Materials Processing*. John Wiley & Sons Inc, 2005.
- [20] I. Langmuir. Oscillations in ionized gases. *Proc. Natl. Acad. Sci. U.S.A.*, 14:627–637, 1928.
- [21] G. I. Sukhinin and A. V. Fedoseev. Influence of dust-particle concentration on gas-discharge plasma. *Physical Review E*, 81(1):016402, 2010.
- [22] Angela Douglass, Victor Land, Lorin Matthews, and Truell Hyde. Dust particle charge in plasma with ion flow and electron depletion near plasma boundaries. *Physics of Plasmas*, 18(8):083706, 2011.
- [23] Imke Goertz, Franko Greiner, and Alexander Piel. Effects of charge depletion in dusty plasmas. *Physics of Plasmas*, 18(1):013703, 2011.
- [24] Marc van der Schans, Bart Platier, Peter Koelman, Ferdi van de Wetering, Jan Van Dijk, Job Beckers, Sander Nijdam, and Wilbert IJzerman. Decay of the electron density and the electron collision frequency between successive discharges of a pulsed plasma jet in N₂. *Plasma Sources Science and Technology*, 28(3):035020, 2019.
- [25] John C. Slater. Microwave Electronics. *Reviews of Modern Physics*, 18(4):441–512, 1946.
- [26] Manfred A. Biondi. Measurement of the electron density in ionized gases by microwave techniques. *Review of Scientific Instruments*, 22(7):500–502, 1951.

-
- [27] R. F. Harrington. *Time-Harmonic Electromagnetic Fields*. Wiley-IEEE Press, New York, 2001.
- [28] W. McColl, C. Brooks, and M. L. Brake. Electron density and collision frequency of microwave-resonant-cavity-produced discharges. *Journal of Applied Physics*, 74(6):3724–3735, 1993.
- [29] I. B. Denysenko, H. Kersten, and N. A. Azarenkov. Electron energy distribution in a dusty plasma: Analytical approach. *Physical Review E*, 92(3):033102, 2015.
- [30] De Zhen Wang and J. Q. Dong. Kinetics of low pressure rf discharges with dust particles. *Journal of Applied Physics*, 81(1):38–42, 1997.
- [31] S. J. Choi and Mark J. Kushner. A Particle-in-Cell Simulation of Dust Charging and Shielding in Low Pressure Glow Discharges. *IEEE Transactions on Plasma Science*, 22(2):138–150, 1994.
- [32] L. C. Pitchford, L. L. Alves, K. Bartschat, S. F. Biagi, M. C. Bordage, A. V. Phelps, C. M. Ferreira, G. J.M. Hagelaar, W. L. Morgan, S. Pancheshnyi, V. Puech, A. Stauffer, and O. Zatsarinny. Comparisons of sets of electron-neutral scattering cross sections and swarm parameters in noble gases: I. Argon. *Journal of Physics D: Applied Physics*, 46(33):334001, 2013.
- [33] S. Kawaguchi, K. Takahashi, K. Satoh, and H. Itoh. Electron collision cross section sets of TMS and TEOS vapours. *Plasma Sources Science and Technology*, 26(5):054001, 2017.
- [34] W. Lowell Morgan, Carl Winstead, and Vincent McKoy. Electron collision cross sections for tetraethoxysilane. *Journal of Applied Physics*, 92(3):1663–1667, 2002.
- [35] P Kurunczi, A Koharian, K Becker, and K Martus. Dissociative excitation of tetramethylsilane (TMS) and hexamethyldisiloxane (HMDSO) by controlled electron impact. *Contributions to Plasma Physics*, 36(6):723–735, 1996.
- [36] R. T. Sugohara, M. T. Lee, G. L.C. De Souza, M. G.P. Homem, and I. Iga. Cross sections for elastic electron scattering by tetramethylsilane in the intermediate-energy range. *Physical Review A*, 84(6):062709, 2011.
- [37] Efe Kemaneci, Felix Mitschker, Jan Benedikt, Denis Eremin, Peter Awakowicz, and Ralf Peter Brinkmann. A numerical analysis of a microwave induced coaxial surface wave discharge fed with a mixture of oxygen and hexamethyldisiloxane for the purpose of deposition. *Plasma Sources Science and Technology*, 28:115003, 2019.
- [38] J. L. Jauberteau and I. Jauberteau. Comparison of hexamethyldisiloxane dissociation processes in plasma. *Journal of Physical Chemistry A*, 116(35):8840–8850, 2012.
- [39] Y. A. Ussenov, E. von Wahl, Zahra Marvi, T. S. Ramazanov, and H. Kersten. Langmuir probe measurements in nanodust containing argon-acetylene plasmas. *Vacuum*, 166(April):15–25, 2019.

- [40] I. B. Denysenko, E. Von Wahl, M. Mikikian, J. Berndt, S. Ivko, H. Kersten, E. Kovacevic, and N. A. Azarenkov. Plasma properties as function of time in Ar/C₂H₂ dust-forming plasma. *Journal of Physics D: Applied Physics*, 53(13):135203, 2020.
- [41] W. W. Stoffels, E. Stoffels, G. M.W. Kroesen, and F. J. De Hoog. Electron density fluctuations in a dusty Ar/SiH₄ rf discharge. *Journal of Applied Physics*, 78(8):4867–4872, 1995.
- [42] V. Garofano, L. Stafford, B. Despax, R. Clergereaux, and K. Makasheva. Cyclic evolution of the electron temperature and density in dusty low-pressure radio frequency plasmas with pulsed injection of hexamethyldisiloxane. *Applied Physics Letters*, 107(18):183104, 2015.
- [43] B. Despax, K. Makasheva, and H. Caquineau. Cyclic powder formation during pulsed injection of hexamethyldisiloxane in an axially asymmetric radiofrequency argon discharge. *Journal of Applied Physics*, 112(9):093302, 2012.
- [44] J. Beckers and G. M W Kroesen. Gas temperature dependence of coagulation onset times for nanoparticles in low pressure hydrocarbon plasmas. *Applied Physics Letters*, 103(12):123106, 2013.
- [45] M. Haverlag, G. M.W. Kroesen, T. H.J. Bisschops, and F. J. de Hoog. Measurement of electron densities by a microwave cavity method in 13.56-MHz RF plasmas of Ar, CF₄, C₂F₆, and CHF₃. *Plasma Chemistry and Plasma Processing*, 11(3):357–370, 1991.
- [46] T. Schlebrowski, H. Bahre, M. Böke, and J. Winter. Monitoring particle growth in deposition plasmas. *Plasma Sources Science and Technology*, 22(6):065014, 2013.
- [47] I. B. Denysenko, E. Von Wahl, S. Labidi, M. Mikikian, H. Kersten, T. Gibert, E. Kovačević, and N. A. Azarenkov. Modeling of argon-acetylene dusty plasma. *Plasma Physics and Controlled Fusion*, 61(1):014014, 2019.
- [48] André Bouchoule. *Dusty Plasmas*. John Wiley & Sons Inc, 1999.
- [49] A. Michau, G. Lombardi, C. Arnas, X. Bonnin, and K. Hassouni. Modeling of dust formation in a DC discharge. *Journal of Nuclear Materials*, 415(1 SUPPL):S1077–S1080, 2011.
- [50] J. Berndt, E. Kovačević, I. Stefanović, O. Stepanović, S. H. Hong, L. Boufendi, and J. Winter. Some aspects of reactive complex plasmas. *Contributions to Plasma Physics*, 49(3):107–133, 2009.
- [51] I. Stefanović, E. Kovačević, J. Berndt, and J. Winter. Non-equilibrium processes and dust formation in low pressure reactive plasmas. *Journal of Physics: Conference Series*, 71(1):012015, 2007.

-
- [52] Job Beckers. *Dust Particle(s) (as) Diagnostics in Plasmas*. Eindhoven University of Technology, 2011.
- [53] L. Couédel, M. Mikikian, L. Boufendi, and A. A. Samarian. Residual dust charges in discharge afterglow. *Physical Review E*, 74(2):026403, 2006.
- [54] A. Michau, C. Arnas, G. Lombardi, X. Bonnin, and K. Hassouni. Nanoparticle formation and dusty plasma effects in DC sputtering discharge with graphite cathode. *Plasma Sources Science and Technology*, 25(1):015019, 2016.
- [55] F. M.J.H. Van De Wetering, S. Nijdam, and J. Beckers. Conclusive evidence of abrupt coagulation inside the void during cyclic nanoparticle formation in reactive plasma. *Applied Physics Letters*, 109(4):043105, 2016.
- [56] A. Bouchoule and L. Boufendi. Particulate formation and dusty plasma behaviour in argon-silane RF discharge. *Plasma Sources Science and Technology*, 2(3):204–213, 1993.
- [57] L. Boufendi, A. Bouchoule, R. K. Porteous, J. Ph Blondeau, A. Plain, and C. Laure. Particle-particle interactions in dusty plasmas. *Journal of Applied Physics*, 73(5):2160–2162, 1993.
- [58] Benjamin Tadsen, Franko Greiner, Sebastian Groth, and Alexander Piel. Self-excited dust-acoustic waves in an electron-depleted nanodusty plasma. *Physics of Plasmas*, 22(11):113701, 2015.
- [59] Xian Zhu Tang and Gian Luca Delzanno. Orbital-motion-limited theory of dust charging and plasma response. *Physics of Plasmas*, 21(12):123708, 2014.
- [60] Harjindar Singh Chahl and Ranganathan Gopalakrishnan. High potential, near free molecular regime Coulombic collisions in aerosols and dusty plasmas. *Aerosol Science and Technology*, 53(8):933–957, 2019.
- [61] Vikram Suresh, Li Li, Joshua Redmond Go Felipe, and Ranganathan Gopalakrishnan. Modeling nanoparticle charge distribution in the afterglow of non-thermal plasmas and comparison with measurements. *Journal of Physics D: Applied Physics*, 54(27):275205, 2021.
- [62] J. E. Allen, B. M. Annaratone, and U. de Angelis. On the orbital motion limited theory for a small body at floating potential in a Maxwellian plasma. *Journal of Plasma Physics*, 63(4):299–309, 2000.
- [63] Gian Luca Delzanno and Xian Zhu Tang. Comparison of dust charging between orbital-motion-limited theory and particle-in-cell simulations. *Physics of Plasmas*, 22(11):113703, 2015.
- [64] Lori Scott, Naoki Ellis, Mudi Chen, Lorin S. Matthews, and Truell W. Hyde. Mapping the Plasma Potential in a Glass Box. *IEEE Transactions on Plasma Science*, 47(7):3079–3086, 2019.

- [65] S. A. Khrapak, S. V. Ratynskaia, M. H. Thoma, A. V. Zobnin, A. D. Usachev, V. V. Yaroshenko, M. Kretschmer, H. Höfner, G. E. Morfill, O. F. Petrov, and V. E. Fortov. Grain charge in the bulk of gas discharges. *AIP Conference Proceedings*, 799:177–180, 2005.
- [66] Martin Lampe, Valeriy Gavrilchaka, Gurudas Ganguli, and Glenn Joyce. Effect of trapped ions on shielding of a charged spherical object in a plasma. *Physical Review Letters*, 86(23):5278–5281, 2001.
- [67] William A. Hoppel and Glendon M. Frick. Ion—erosol attachment coefficients and the steady-state charge distribution on aerosols in a bipolar ion environment. *Aerosol Science and Technology*, 5(1):1–21, 1986.
- [68] Marco Gatti and Uwe Kortshagen. Analytical model of particle charging in plasmas over a wide range of collisionality. *Physical Review E*, 78(4):046402, 2008.
- [69] Carsten Killer, Gunnar Bandelow, Konstantin Matyash, Ralf Schneider, and André Melzer. Observation of Ω mode electron heating in dusty argon radio frequency discharges. *Physics of Plasmas*, 20(8):083704, 2013.
- [70] J. Schulze, A. Derzsi, K. Dittmann, T. Hemke, J. Meichsner, and Z. Donkó. Ionization by drift and ambipolar electric fields in electronegative capacitive radio frequency plasmas. *Physical Review Letters*, 107(27):275001, 2011.
- [71] J. Schulze, Z. Donkó, A. Derzsi, I. Korolov, and E. Schüengel. The effect of ambipolar electric fields on the electron heating in capacitive RF plasmas. *Plasma Sources Science and Technology*, 24(1):015019, 2015.
- [72] E. Schüengel, S. Mohr, S. Iwashita, J. Schulze, and U. Czarnetzki. The effect of dust on electron heating and dc self-bias in hydrogen diluted silane discharges. *Journal of Physics D: Applied Physics*, 46(17):175205, 2013.
- [73] J. P. Boeuf and Ph Belenguer. Transition from a capacitive to a resistive regime in a silane radio frequency discharge and its possible relation to powder formation. *Journal of Applied Physics*, 71(10):4751–4754, 1992.
- [74] T. Hemke, D. Eremin, T. Mussenbrock, A. Derzsi, Z. Donkó, K. Dittmann, J. Meichsner, and J. Schulze. Ionization by bulk heating of electrons in capacitive radio frequency atmospheric pressure microplasmas. *Plasma Sources Science and Technology*, 22(1):015012, 2013.
- [75] D. W. Liu, F. Iza, and M. G. Kong. Electron heating in radio-frequency capacitively coupled atmospheric-pressure plasmas. *Applied Physics Letters*, 93(26):261503, 2008.

Dust charge density of nanoparticles in dusty plasma

Preface. A dust grain immersed in a low pressure gas discharge obtains a permanent negative surface charge due to the high mobility of electrons compared to that of ions. This charge essentially governs all fundamental processes in dusty and complex plasmas involving dust grains, neutrals, (an)ions and electrons and—consequently—virtually all industrial applications of these types of plasmas are affected and steered by it. In this chapter, the surface charge is determined by application of laser-induced electron detachment from nanosized dust grains in concert with microwave cavity resonance spectroscopy and laser light extinction. The main result is that the electron release is governed by photodetachment rather than by thermionic emission, and that recharging of the dust grains occurs on timescales that are well in agreement with the orbital-motion-limited (OML) theory. The total surface charge density residing on the dust grains inside the laser volume follows from the saturation of the photodetachment signal, which was used in combination with dust density values derived from extinction measurements to estimate the mean dust charge. The negative dust charge on the 140 nm (average) diameter dust grains in this work is obtained to be in the range of 273 – 2519 elementary charges, of which the lower bound matches well with analytical predictions using the orbital-motion-limited (OML) theory.

6.1 Introduction

Complex and dusty plasmas comprise a mixture of (partially) ionized gas with nano- to micrometer sized dust grains [1, 2], and occur frequently in a wide variety of mature industrial processes and research niches such as semiconductor manufacturing [3, 4], nuclear fusion [5], and (functional) materials embedding nanoparticles [6, 7, 8]. The non-equilibrium between electron and heavy species temperatures provides a key advantage for low-temperature plasmas over conventional alternatives, resulting in (permanently and) negatively charged surfaces of, e.g., the reactor walls, electrodes and dust grains. For complex and dusty plasmas, the electric charge retained on the dust grains reflects a key parameter dictating fundamental processes such as Coulomb interactions—e.g. crystallization, instabilities, and Coulomb-induced collisions—in plasma-levitated dust crystals and dusty plasmas [9, 10, 11, 12, 13, 14], dust grain formation by nucleation, coagulation, and accretion [15, 16, 17, 18, 19, 20], void formation and laser-induced coalescence [21, 22, 23, 24, 25]. For applications, the effects of dust can be detrimental to, e.g., fusion energy reactors [3, 26] and plasmas created in semiconductor manufacturing [27, 4], which led to recent work focused on contamination control using plasmas [28, 29, 30]. The charge state of the dust particles in contact with the plasma is often a decisive factor in the dust retention mechanism. Therefore, it is of utmost importance, for current and future technologies and for plasma science, to understand the elementary charging processes driving dust-plasma interaction.

The floating potential—or the surface charge—acquired by plasma-embedded dust grains arises from the balance between the electron and ion currents, which results in permanently negatively charged dust grains for dust radii $a_d \gtrsim 10$ nm under typical dusty plasma conditions [31, 32]. The orbital-motion-limited (OML) theory is the governing theoretical framework predicting the floating potential of dust grains [33, 34], which has been extended with numerous advancements to include, e.g., the effect of ion-neutral collisions [35, 36, 37]. The theory has been successfully applied to microparticle charging in different plasma regions such as the plasma bulk [38, 39], the plasma sheath [40], and the spatial afterglow [41]. On the contrary, only a limited number of works provide experimental data on the charge of nanosized dust grains embedded in plasmas [42, 24, 43, 44]. This lack of experimental data is mainly caused by the fact that most diagnostics for obtaining information about the dust grain charge are based on optical principles which dramatically suffer from a decreasing signal when the grain size becomes smaller than the wavelength of the light used for the diagnostic [45, 46, 47].

In this chapter, laser-induced electron detachment from nanometer-sized dust grains is demonstrated experimentally in a low pressure dusty plasma using ultraviolet (UV) laser pulses in order to close the gap in experimental data. The dust grains were formed in-situ by a typical gas discharge in an argon-hexamethyldisiloxane gas mixture, and thereafter stably confined to the same volume in an argon-only discharge. The change in free electron density caused by the laser-dust interaction was consecutively measured with ns-time resolution using time-resolved microwave cavity resonance spectroscopy (MCRS) [48, 24, 49]. The experimental dust charge was estimated by the

ratio of the maximum free electron density released by the laser to the dust density obtained from laser light extinction measurements (see Section 6.6.1).

This chapter is organized as follows. In Section 6.2, the experimental procedure for dust growth and laser-induced electron detachment are explained in detail. In Section 6.3, the time-resolved electron density providing three important observations is discussed and analyzed in detail with respect to the current physical understanding of photodetachment. In Section 6.4, the measured dust charge density is used to estimate the dust charge, and the result is discussed in view of the current understanding in the literature. Additional information regarding elements of the results, discussion and interpretation can be found in Section 6.6.

6.2 Methods

In Fig. 6.1, a schematic top-view of the experimental setup is shown. Inside a vacuum vessel, a low pressure plasma was created in a stainless steel hollow pillbox cavity, driven by a radio-frequency signal ($f_{\text{RF}} = 13.56$ MHz) with a plasma power of $P_{\text{RF}} = 20$ W. During the experiments, argon (with a partial pressure of $p_{\text{Ar}} = 5.4 \times 10^{-2}$ mbar) was admixed with HMDSO ($p_{\text{HMDSO}} = 1.6 \times 10^{-2}$ mbar), of which the latter was the precursor to dust grain formation. These dust grains gained a permanent negative charge after reaching a size larger than ~ 10 nm [31, 32], enabling them to remain trapped in the discharge volume. A detailed description of the microwave cavity with integrated discharge electrodes and the dust collection system can be found in Section 6.6.2.

The complete experiment consisted of three separate stages. During the *growth phase*, an Ar/HMDSO plasma was generated for 60 seconds. Afterwards, the HMDSO flow was terminated, and the nanodusty plasma entered the *settling stage*, in which the plasma adjusted to the change in pressure, until the dust cloud found a steady state in terms of size and density. It should be noted that the electron density was strongly depleted during the coagulation phase, as a consequence of the permanent negative charging of the dust cloud, and remained depleted during subsequent experiments. Finally, the *measurement stage* consisted of six separate experiments with varying laser pulse energy. In each experiment, UV laser pulses were fired with a frequency of $f_{\text{laser}} = 20$ Hz, and the microwave response was temporally recorded per pulse. This microwave response, i.e. the change in resonance frequency of the used resonant mode, was caused by the additional photodetached electrons upon laser irradiation. The global electron density of the (dusty) plasma and laser light transmission through the dust cloud were monitored over the course of all three stages of the experiment, of which the signals can be found in Section 6.6.3.

For the actual laser-induced electron detachment experiments, a frequency-quadrupled ultraviolet (UV) laser (Quantel BigSky Ultra, wavelength $\lambda_{\text{ph}} = 266$ nm) was used to generate short (~ 8 ns) pulses which traveled through the cavity via a thin slit on each side. Upon interaction with the laser photons, electrons were released from the dust grains, and therefore, the free electron density of the plasma was temporally increased. It was verified, in vacuum at a pressure of $\sim 1 \times 10^{-6}$ mbar and with a pristine argon discharge, that no detectable amount of electrons was released from the

metal surfaces of the cavity and that photo-ionization did not result in a cavity response exceeding the noise band. The volume-averaged density of these free electrons was measured by means of microwave cavity resonance spectroscopy (MCRS), as previously applied to a multitude of plasma types [49, 24, 50, 48, 51, 6]. To this end, a microwave generator (Stanford Research Systems Model SG386) sent electromagnetic waves with a fixed frequency into the cavity. This microwave radiation had a fixed power of only $P_{\mu w} = 40 \text{ mW} \ll P_{\text{RF}}$ meaning that the microwaves were non-intrusive. A part of the microwave power was absorbed inside the cavity while the rest was reflected. Ten percent of the reflected power was sent to a logarithmic detector (Analog Devices HMC602LP4) using a directional coupler (Mini-Circuits ZHDC-16-63+). The detector voltage was eventually sampled using a transient recorder (Spectrum M3i.4121-exp) with a sample frequency of 250 MHz for a range of microwave frequencies close to the resonance frequency. In this way, the spectrum around a resonant eigenmode of the microwave cavity could be retrieved in a temporally-resolved fashion.

The frequency at which microwaves in the cavity are at resonance depends on the permittivity of the medium inside the cavity. This introduces a relation between the shift in resonance frequency Δf and the (change in) electron density n_e , as derived from the Slater perturbation theorem [52, 53, 54],

$$n_e(t) = \frac{8\pi^2 \varepsilon_0 m_e f_p^2(t) \Delta f(t)}{e^2 \mathcal{V} f_1}, \quad (6.1)$$

with n_e , m_e and e the electron density, mass and (elementary) charge, ε_0 the vacuum permittivity, f_p the resonance frequency with momentary perturbation, f_1 the resonance frequency without the perturbation, and $\Delta f = f_p - f_1$ the shift in resonance frequency. The parameter \mathcal{V} is defined as the (microwave-)electric-field-weighted ratio of laser beam V_b to cavity volume V_c as

$$\mathcal{V} = \frac{\iiint_{V_b} |\mathbf{E}(\mathbf{r})|^2 d^3\mathbf{r}}{\iiint_{V_c} |\mathbf{E}(\mathbf{r})|^2 d^3\mathbf{r}}. \quad (6.2)$$

Here, the microwave electric field $\mathbf{E}(\mathbf{r})$ for the TM_{010} resonant mode was computed using a numerical model of the microwave cavity in COMSOL Multiphysics[®] (see Section 6.6.4). Subsequently, the electric-field-weighted volume ratio \mathcal{V} was calculated by evaluating Eqn. (6.2) numerically using the measured laser beam diameter D_b the cavity diameter $D_c = 66 \text{ mm}$ and height $H_c = 40 \text{ mm}$, and the numerical solution for the microwave electric field \mathbf{E} . Details on the microwave electric field, the volume ratio and the position of the laser beam in the cavity can be found in Section 6.6.4.

In order to obtain a sufficient signal-to-noise ratio, a typical measurement consisted of a number of time series $N_{\text{meas}} = N_{\text{freq}} N_{\text{av}}$, with N_{freq} the number of probed frequencies and N_{av} the number of averages per frequency. It was therefore important that the plasma and dust conditions remained as stable as possible during the complete measurement set. Several diagnostics were implemented in order to globally monitor both the dust growth process and the stability of the sample thereafter (see measurement results in Section 6.6.3). First, global electrical parameters of the RF discharge, such as the plasma power and the phase angle between RF voltage and

current, were tracked by an Impedans OctivPoly 1.0 power sensor. Additionally, the dust cloud was visualized by laser light scattering (LLS) using a green (532 nm) laser sheet. The scattered light was detected by a Photron Mini UX100 FastCam with a laser line filter, while the transmitted light was monitored by a photodiode to perform extinction measurements. Furthermore, a vector network analyzer (VNA) was used to perform spectral scans of the microwave response at low temporal resolution (~ 100 ms), so that the electron density could still be monitored, even when the transient recorder-based MCRS system was not activated. The timing of the experiment was controlled by a BNC 577 Series pulse/delay generator, which sent trigger pulses to the VNA and the pulsed UV laser. The output of the pulsed UV laser was used as a trigger for the transient recorder such that jitter in the laser output was inherently corrected for.

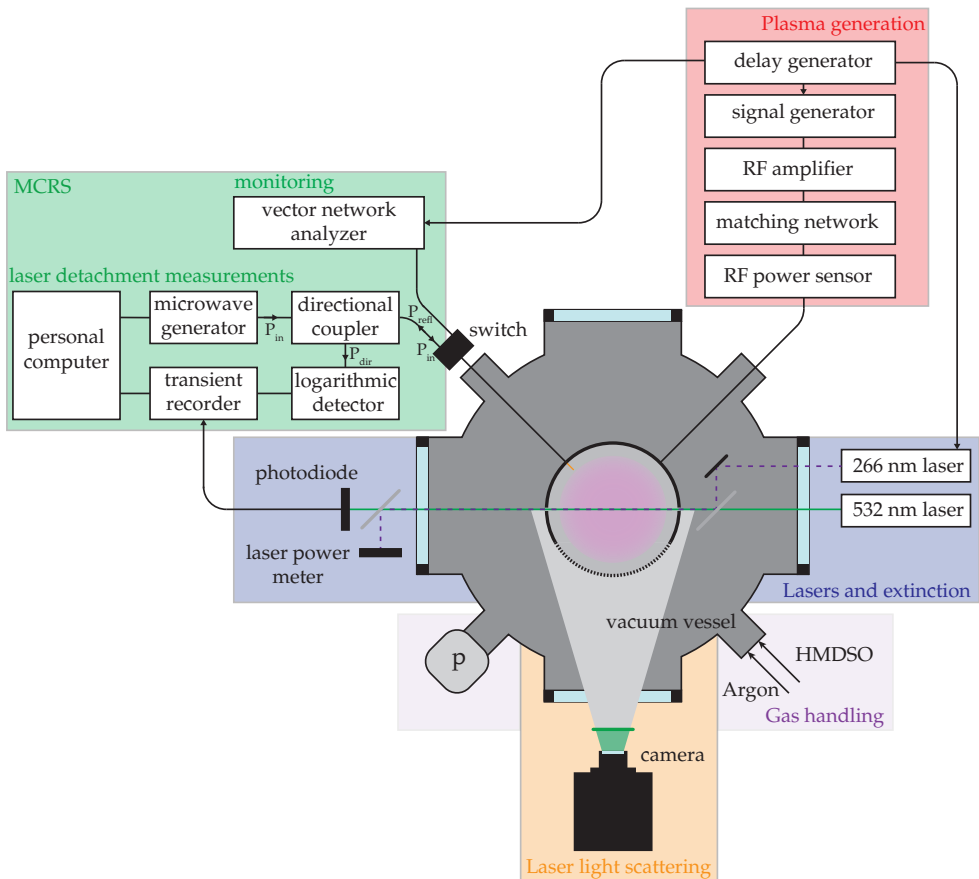


Figure 6.1: Schematic overview of the experimental setup used for creating, monitoring and probing the nanodusty plasma. The symbol P indicates pressure sensor.

6.3 Results

Fig. 6.2 depicts the measured laser-induced change of the electron density as a function of time, which has been measured for different laser pulse energies as indicated in the figure's legend. For each laser pulse energy, the time-resolved signals clearly show three distinct phases in the evolution of the free electron density. The reference value for the resonance frequency f_1 was obtained from phase (I), during which the dusty plasma is undisturbed. At the beginning of phase (II), i.e. $t = 0 \mu\text{s}$, the laser was shot and, subsequently, the free electron density increased rapidly within about 70 ns. After reaching a peak value at the end of phase (II), the laser-induced electron density decreased gradually following an exponential decay back to the steady state value observed in phase (I).

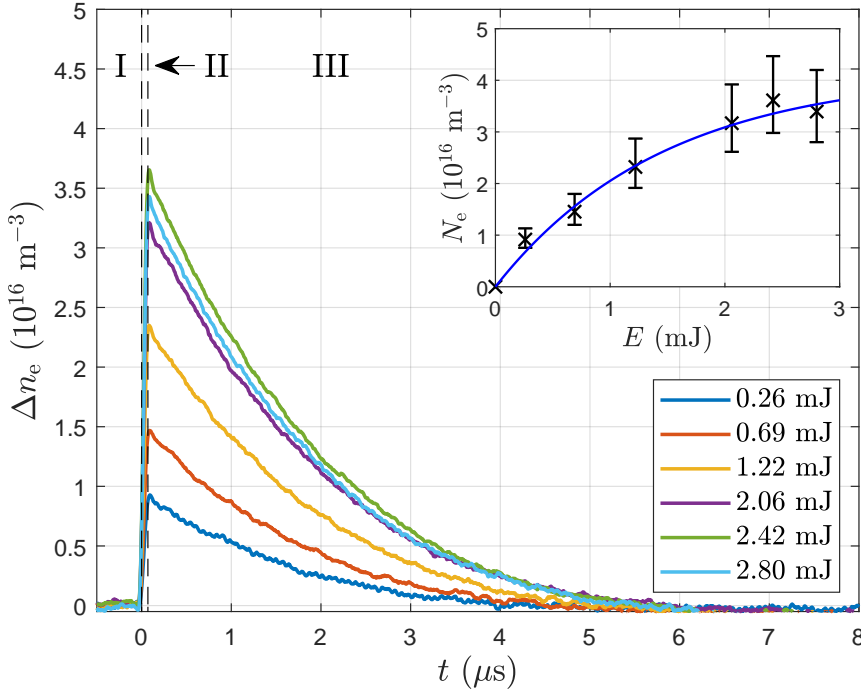


Figure 6.2: Time-resolved laser-induced electron density for different values of laser pulse energy, as defined by the colors/legend. The inset depicts the peak value of the laser-released electron density for each laser experiment.

From the results presented in Fig. 6.2, three distinct observations can be made:

- The fast rise time τ_{rise} during phase (II) is comparable to the fundamental cavity response time expected for an instantaneous change in the free electron density[55]. $\tau_{\text{rise}} \approx 3\tau_{\text{cavity}}$ and $\tau_{\text{cavity}} = Q_1/(2\pi f_1) \approx 18 \text{ ns}$. This limited

response time of a microwave resonant cavity is due to a minimum time the cavity-system needs in order to load or discharge the microwave energy associated with the excited resonant mode.

- As can be seen from the inset in Fig. 6.2, the peak value of the laser-induced electron density increases for increasing laser pulse energy, and saturates for sufficiently high laser pulse energies.
- The density of additionally released electrons decays exponentially in phase (III), of which the time constant is estimated to be $\tau_{\text{decay}} \approx 1.6 - 2.1 \mu\text{s}$ based on an exponential fit through the experimental data.

Besides the above mentioned observations, it is absolutely clear that a significant amount of free electrons is released upon irradiation of the dust cloud with the UV laser. In general, there are four widely accepted physical mechanisms that could explain the discharging of plasma-embedded dust grains.

Field emission[2], which is the release of electrons due to a strong electric field, is only important for dust grain radii larger than a micrometer whereas in our experiments the grain size is roughly a few hundred nanometers (see Section 6.6.5).

Secondary electron emission [34, 56], which is the release of electrons from the material after impact by high-energy electrons, is only relevant for high-energy electrons of which the density is very low under the conditions considered.

The two other mechanisms—i.e. thermionic emission [57, 58] and photon-induced electron detachment (also called photodetachment) [59, 60, 61, 62]—may be considered more likely to become dominant under the current conditions.

Here, thermionic emission is caused by a high surface temperature (possibly caused by laser-irradiation) transferring thermal energy to electrons such that they can overcome the work function, while in the case of photodetachment this energy is provided in the form of photon energy directly. It is due to this difference that the effect of photodetachment events—in contrast to the situation for thermionic emission—may be considered instantaneous compared to the sampling time [63]. To investigate which of the two latter mechanisms is dominantly responsible for the observed release of electrons, a model for thermionic emission, i.e. a coupled model for predicting the changes in dust grain temperature and the dust grain floating potential upon laser irradiation, has been constructed from which typical (de-)charging timescales can be retrieved (see Section 6.6.6 and 6.6.7). Under the current experimental conditions, it can be concluded from this model that the floating potential hardly changes due to the vast increase in the dust grain's temperature. This indicates that—under the current conditions—laser-induced photodetachment dominates over laser-induced thermionic emission. Moreover, this dominant contribution of photodetachment to the overall electron release process is supported by all of the three observations mentioned earlier as discussed further on.

The first observation was that the signal grows during phase (II) up to the peak value within approximately $3\tau_{\text{cavity}}$. As photodetachment occurs almost instantaneously for the duration of the laser shot ($\sim 8 \text{ ns}$) [63], the signal reflects the cavity response to a

sudden perturbation as described by Van Nindhuijs *et al* [55]:

$$\Delta f_m = \Delta f \left(1 - \exp \left(-\frac{t}{\tau_{\text{cavity}}} \right) \right), \quad (6.3)$$

with Δf_m the measured frequency shift, and Δf the actual frequency shift. By contrast, thermionic emission exhibits a rise time of about $0.6 \mu\text{s}$ in an extreme case with low work function of the dust grain. As a consequence, the rise time strongly indicates that photodetachment is responsible for the release of electrons.

The second observation strongly suggested that the total released electron density saturated for increasing laser pulse energy (see the inset in Fig. 6.2). From literature, it is known that the number of electrons N_e released by photodetachment saturates for sufficiently high laser pulse energies following an exponential curve [64, 60, 65]:

$$N_e = \hat{N}_e \left(1 - \exp \left(-\frac{\sigma_{\text{pd}} E_{\text{laser}}}{E_{\text{ph}} S} \right) \right). \quad (6.4)$$

Here, the laser pulse energy is represented by E_{laser} , the photon energy is denoted by $E_{\text{ph}} = 4.66 \text{ eV}$ (i.e., $\lambda_{\text{ph}} = 266 \text{ nm}$), and the laser cross section $S = 0.031 \text{ cm}^2$. Fitting Eqn. (6.4) to the saturation data yields an asymptotic value of $\hat{N}_e = 4.15 \times 10^{16} \text{ m}^{-3}$ and photodetachment cross section $\sigma_{\text{pd}} = 1.6 \times 10^{-17} \text{ m}^2$. Consequently, there are two interesting notes with respect to the saturation study. First, the photodetachment cross section is much smaller than the hard sphere cross section, based on the dust size, $\sigma \sim \pi a_d^2 \approx 6 \times 10^{-14} \text{ m}^2$ by three orders of magnitude. Second, note that if laser-induced thermionic emission would have been dominant, an opposite curvature of this curve would have been expected. This is because, with thermionic emission being the dominant electron release mechanism, the dependence of the density of released electrons on the laser pulse energy would have been stronger than linear (see Section 6.6.7).

The third observation concerned the temporal decay of the released electron densities back to their quasi-steady state values. Based on the orbital-motion-limited (OML) theory, the time scale on which the electron and ion currents restore the equilibrium floating potential of the dust grains can be calculated from the following equation, which has been derived in Section 6.6.8 from the electron and ion current:

$$\tau_{\text{charging}} = \left(\frac{e^2 a_d n_i v_{T_i}}{4\epsilon_0 k_B T_e} \left(\frac{T_e}{T_i} + \frac{n_e v_{T_e}}{n_i v_{T_i}} \exp \left(\frac{e \bar{V}_d}{k_B T_e} \right) \right) \right)^{-1}. \quad (6.5)$$

Here, T_e denotes the electron temperature, a_d the dust grain radius, n_i the ion density, and T_i the ion temperature. It should be noted that this equation has been derived considering that $n_e \neq n_i$, whereas in other works the charging timescale is often given for fixed ratio of T_e/T_i or for $n_e = n_i$ [66, 34, 67, 2, 68]. The plasma and dust parameters used for the evaluation of the charging timescale are as follows: $T_e = 1 - 3 \text{ eV}$, $n_e = 2 \times 10^{15} \text{ m}^{-3}$ (equal to n_e for $t \geq 70 \text{ s}$ in Fig. 6.6 in Section 6.6.3), $T_i = 0.026 \text{ eV}$, $n_i = 9.2 \times 10^{15} \text{ m}^{-3} - 4.15 \times 10^{16} \text{ m}^{-3}$, and $a_d = 140 \text{ nm}$ (obtained by SEM images in Section 6.6.5). The range for the ion density is motivated by using a lower limit equal to the electron density during the nucleation phase without

electron depletion ($\tilde{n}_i = 9.2 \times 10^{15} \text{ m}^{-3}$, equal to n_e for $t \leq 30 \text{ s}$, see Section 6.6.3), and assuming that the ion density does not change during the subsequent phases. However, it is likely that the ion density increases due to an increase in the electron mean energy, which balances the decrease in ionization caused by electron depletion due to the permanent charging of dust particles. Therefore, an upper limit is assumed equal to the total dust charge density measured plus the free electron density of the discharge ($\hat{n}_i = 4.15 \times 10^{16} \text{ m}^{-3}$, i.e. equal to $\hat{N}_e + n_e$). This upper limit is motivated by the fact that quasi-neutrality should be obeyed, and hence, that the ion density is balanced by the total dust charge density. Due to electron depletion, the free electron density is much lower than the contribution of the negatively charged dust particles to the quasi-neutrality condition. Under these conditions, the charging timescale ranges between $1.3 \mu\text{s}$ ($T_e = 1 \text{ eV}$ and $n_i = 4 \times 10^{16} \text{ m}^{-3}$) and $4.4 \mu\text{s}$ ($T_e = 3 \text{ eV}$ and $n_i = 9.2 \times 10^{15} \text{ m}^{-3}$). It should be noted that a change in the ion density dominates over the effect of a change in electron temperature, and thus it is important to account for the fact that $n_e \neq n_i$ in the evaluation of the charging timescale. Considering the measured τ_{decay} , the experimental values agree well with the estimates for τ_{charging} . The charging timescale for heated dust grains is almost two orders of magnitude larger ($\tau \sim 100 \mu\text{s}$) due to the thermionic emission current. As a consequence, the agreement with the timescale based on only the OML currents implies that the thermionic emission current is irrelevant. In conclusion, this observation suggests also that photodetachment is the dominant detachment process.

The total density of detached electrons can be used to estimate the dust charge, which equals $q_d = \hat{N}_e/n_d$ in case of saturation—meaning that all electrons have been released from the dust grain. The assumption here is that the dust grains irradiated by the laser beam are mono-disperse, which seems a reasonable assumption based on the SEM images (see Section 6.6.5). The saturated electron density \hat{N}_e results from the measurement of the peak value of the electron density as a function of laser pulse energy, which involves three measurements errors estimated as $\Delta_{\Delta f} = \Delta_{f_p} = 3 \times 10^5 \text{ Hz}$ based on the noise band of f_p , and $\Delta_{\nu} = 1.4 \times 10^{-4}$ based on the uncertainty in the laser beam cross section (see Section 6.6.4). This implies that $\hat{N}_e = 3.0 \times 10^{16} \text{ m}^{-3} - 5.3 \times 10^{16} \text{ m}^{-3}$ by linearization of Eqn. (6.1) to calculate the error in N_e for $E_{\text{laser}} = 2.80 \text{ mJ}$. The dust density n_d is estimated from extinction measurements (see Section 6.6.1), which provides a dust density between $n_d = 2.1 \times 10^{13} \text{ m}^{-3}$ and $n_d = 1.1 \times 10^{14} \text{ m}^{-3}$, for dust radius $a_d = 140 \text{ nm}$, depending on the assumed material and its complex refractive index. As a consequence, the dust charge is estimated in the range $q_d \cong 273 - 2519$ elementary charges.

6.4 Discussion

The dust charge density $q_d n_d = \hat{N}_e = 4.15 \times 10^{16} \text{ m}^{-3}$ indicates that the number of dust-confined electrons largely exceeds the free electron density ($n_e < 2 \times 10^{15} \text{ m}^{-3}$ (see Section 6.6.3). This effect is captured by the Havnes parameter [46]:

$$P = 4\pi\epsilon_0 a_d \frac{T_e}{e} \frac{n_d}{n_i} \cong 0.2 - 3.2, \quad (6.6)$$

given the same set of parameters as before, using $n_d = 2.1 \times 10^{13} \text{ m}^{-3} - 1.1 \times 10^{14} \text{ m}^{-3}$ and $n_i = 1 \times 10^{16} \text{ m}^{-3} - 4 \times 10^{16} \text{ m}^{-3}$. The dust charge measurements by Tadsen *et al* [42] were performed under conditions where the free electron density was severely depleted ($P \approx 10-50$) and found much lower values for the dust charge, i.e. $q_d \approx 10-60$ elementary charges. Although the dusty plasma considered in this work suffered from electron depletion, the effect was not as severe as in the work of, e.g., Tadsen *et al* [42] and Deka *et al* [44].

To account for electron depletion, the dust charge is evaluated theoretically using the OML theory with the density and temperature of the electrons and ions as before. Using the OML theory, the electron and ion current towards the dust grain with floating potential V_d are described as:

$$I_e = -e\pi a_d^2 n_e v_{T_e} \exp\left(\frac{eV_d}{k_B T_e}\right), \quad (6.7)$$

$$I_i = e\pi a_d^2 n_i v_{T_i} \left(1 - \frac{eV_d}{k_B T_i}\right), \quad (6.8)$$

where $v_{T_s} = \sqrt{\frac{k_B T_s}{2\pi m_s}}$ with species $s = e, i$ for electrons and ions, respectively. Balancing Eqn. (6.7) and (6.8), the floating potential of the dust grain provides a theoretical dust grain charge in the range:

$$q_d = 4\pi\epsilon_0 a_d V_d \cong (-189 e) - (-386 e), \quad (6.9)$$

using the same (pure argon) plasma parameters as before ($T_e = 3 \text{ eV}$, $T_i = 0.026 \text{ eV}$, $n_e = 2 \times 10^{15} \text{ m}^{-3}$, $n_i = 1 \times 10^{16} \text{ m}^{-3} - 4 \times 10^{16} \text{ m}^{-3}$, $a_d = 140 \text{ nm}$). For the purpose of comparison, the dust charge is also evaluated by setting $n_e = 4 \times 10^{16} \text{ m}^{-3}$, which results in a theoretical charge of $-688 e$ in case the electrons are not depleted. Consequently, the non-depleted OML charge ($q_d = -688 e$) provides an upper bound for our measurement, and measurements performed under severe electron depletion provide a lower bound ($q_d = (-10 e) - (-80 e)$ [42, 44]). Moreover, this demonstrates that an accurate measurement of the dust density is necessary to eliminate the uncertainty in the dust charge in order to perform a quantitative comparison to the theory and literature.

There are two important adaptations to the basic OML theory that are applicable to the experimental conditions considered in this work. First, Tang and Delzanno [69] found that accounting for the ion density response to the presence of dust grains often leads to a significant increase of the dust charge, but this does not apply in our case because the dust grain radius is much smaller than the electron Debye length. Second, the effect of ion-neutral collisions is apparent for sufficiently small Knudsen numbers, where $\text{Kn}_{R_0} = 24$ under our conditions according to the definition by Gatti and Kortshagen [35]. This implies that the transition regime between the collisionless (OML) and the collision-enhanced regime is applicable, and that a charge reduction due to ion-neutral collisions can be expected. Nevertheless, the OML prediction seems to provide a reasonable expectation for the dust grain charge under the conditions considered in this work.

6.5 Conclusion

In conclusion, the negative surface charge of dust grains immersed in a low-pressure dusty plasma was probed by exposing them to pulsed laser irradiation. As a consequence, laser-induced electron detachment caused a sudden change in the free electron density, which was measured time-resolved using microwave cavity resonance spectroscopy (MCRS). The results demonstrate that electrons were quickly removed from the dust grains due to photodetachment and, subsequently, that the dust grains recharged to their steady state charge on timescales predicted by orbital-motion-limited (OML) theory. The total dust charge density was used in combination with the estimated number density of dust grains to calculate a mean dust charge. Comparing the experimental dust charge in the range 273 – 2519 to the OML theory, it was found that the OML prediction, i.e. 189 – 386, is close to the experimental lower bound. However, experimental findings by others [42, 44] are much lower due to severe electron depletion under their (different) conditions. More detailed knowledge of the complex refractive index (e.g., by ex-situ measurement of the refractive index of a collected dust sample) and radius such as measured by Groth *et al* [45] would lead to an improved accuracy of the measured dust charge, and consequently, facilitate a quantitative comparison and evaluation of the OML theory. For future experiments, we are currently investigating different options to measure the dust particle properties in-situ, such as the dust density and size, and to determine the refractive index ex-situ, which could be combined with dust charge density measurements for the accurate determination of the dust charge.

6.6 Appendix

This documents provides supplementary information concerning the analysis and discussion of the main results in the order in which the information is referred to in this chapter. Section 6.6.1 provides the interpretation of the extinction measurement for different materials, from which a feasible range for the dust density n_d is calculated. Section 6.6.2 is concerned with a detailed description of the microwave cavity with integrated discharge electrodes, and the dust collection system. Section 6.6.3 visualizes the timetraces of the monitoring diagnostics in order to show the stability of the dust cloud over the entire measurement period. Section 6.6.4 calculates the electric-field-weighted volume ratio for the laser beam volume used in the experiment, which provides a correction factor in the calculation of the released electron density. Section 6.6.5 shows scanning electron microscope (SEM) images of nanoparticles (collected on sample stubs in-situ), which were deposited after the laser experiments had finished by terminating the plasma and gas flows. Section 6.6.6 describes the developed model used for determining the significance of thermionic emission, which allows to calculate the temporal evolution of the dust temperature and the dust floating potential. Section 6.6.7 denotes the model solution for the case of silicon- and carbon-like nanoparticles since both can be created in HMDSO-containing discharges. Here it can be seen that the contribution by thermionic emission for silicon-like particles becomes of the order of the other heat fluxes and currents. In Section 6.6.8 the timescale for the charging of

an initially neutral dust grain is derived by equating the electron and ion currents according to the orbital-motion-limited theory, without any assumption on the density or temperature of the electron and ions.

6.6.1 Extinction

Table 6.1 denotes the evaluation of the extinction measurements obtained during laser experiments for different materials. The dust density n_d was estimated from extinction measurements, which were conducted using a photodiode monitoring the change of (532 nm) laser light intensity transmitted through the dust cloud [42, 70], according to:

$$n_d = \frac{-\log\left(\frac{I}{I_0}\right)}{\pi a_d^2 Q_{\text{ext}} L}. \quad (6.10)$$

Here, the optical depth $\tau = -\log(I/I_0) = 0.29$, and the optical path length $L = 56$ mm. The dust radius varied between $a_d = 120$ nm – 160 nm according to the scanning electron microscope (SEM) images depicted in Section 6.6.5, which agree well with expected dust grain diameter measured in-situ during this stage of dust formation by Groth *et al* [45]. The extinction efficiency Q_{ext} was calculated for the different materials, each with a complex refractive index $N = n + ik$, at a fixed wavelength $\lambda = 532$ nm using the Mie theory [71, 72, 73]. Finally, the dust density was evaluated using the same extinction measurement, at fixed wavelength, and for an average dust grain radius 140 nm using the different material properties.

Table 6.1: Real n and imaginary k components of the complex refractive index ($N = n + ik$) for different materials, the extinction efficiency Q_{ext} calculated using Mie theory, and corresponding dust density n_d calculated using the extinction measurement.

Material	n	k	Q_{ext}	n_d	Ref.
Si (bulk)	1.51	0.008	1.10	$7.6 \times 10^{13} \text{ m}^{-3}$	[74]
SiO (bulk)	1.98	0.000	3.96	$2.1 \times 10^{13} \text{ m}^{-3}$	[75]
SiO ₂ (bulk)	1.55	0.000	1.27	$6.6 \times 10^{13} \text{ m}^{-3}$	[76]
SiO ₂ (film)	1.47	0.000	0.88	$9.5 \times 10^{13} \text{ m}^{-3}$	[77]
C (bulk)	4.22	0.060	1.19	$7.0 \times 10^{13} \text{ m}^{-3}$	[78]
Ar-C ₂ H ₂ (dust)	1.52	0.020	1.30	$6.4 \times 10^{13} \text{ m}^{-3}$	[45]
Ar-C ₂ H ₂ (dust)	1.44	0.000	0.76	$1.1 \times 10^{14} \text{ m}^{-3}$	[45]
Ar-C ₂ H ₂ (dust)	1.95	0.043	3.72	$2.2 \times 10^{13} \text{ m}^{-3}$	[79]

6.6.2 Microwave cavity with integrated discharge electrodes and dust collection system

Fig. 6.3 shows the microwave cavity comprising a top disk (1) with gas inlet (2), onto which a temperature sensor (3) was mounted to measure the cavity temperature and an RF antenna (4) was positioned for connecting the RF-powered electrode with the RF power supply via a vacuum feedthrough. The base of the cavity was a hollow cylinder (5) containing two vertical slits (6) allowing the laser beams to pass through the discharge volume, and a welded steel mesh (7) to allow scattered laser light to leave the cavity and be captured by a high-speed camera. At the bottom of the cavity, a shutter plate (8) was mounted containing a specific hole pattern, which could be translated in the y-direction using a linear push-pull solenoid (9) with two positions. Below the shutter plate, there was a substrate holder (10) containing at most seven aluminum stubs (11) for collecting dust grains from the discharge, which were organized in a pattern that matched that of the shutter plate.

The hole pattern in the shutter plate can be seen from the top (in the y-z plane) in two positions in Fig. 6.4. In panel (a), the shutter plate is shown in the normal position when the solenoid was not powered. In this case, the hole pattern matched that of the holes located between the stubs, so dust grains falling out of the discharge were not able to reach the stub surfaces. In panel (b), the position of the shutter plate is shown when the solenoid was powered, and the stubs were exposed to the dust grains and discharge. When terminating the RF power, the plasma-induced electric field confining the dust grains was removed and dust grains fell onto the stub surfaces.

Fig. 6.5 depicts a cross sectional view of the microwave cavity and other components in the x-z plane looking into the y-direction. The discharge geometry was an asymmetric capacitively coupled discharge, where the top flat electrode was powered by an RF voltage, while the cylindrical base of the cavity and the bottom mesh electrode were grounded. The RF-powered electrode (1) was located at the top of the cavity's interior, which was insulated by a dielectric material (2, PEEK) from the grounded cavity. It should be noted that the RF-powered electrode contained a hole pattern (diameter 0.5 mm) that could be used for a shower head-type of gas injection into the cavity in combination with the perforated dielectric barrier. However, for the presented experiments, the gas was injected into the vessel and allowed to enter the cavity via diffusion through the slits and the steel mesh functioning as viewing window (as indicated by (7) in Fig. 6.3). The bottom of the cavity was made from a steel mesh (3) that allowed dust grains to fall down onto the SEM substrates for collection. The steel meshes were welded to the base of the microwave cavity in order to ensure proper electrical conductivity for the currents involved in the excited resonant modes. Microwaves were injected via an antenna (4) located in the cylindrical wall of the cavity at half of the height of cavity in the axial direction, and under an angle of 90° in the y-z plane with respect to the slits.

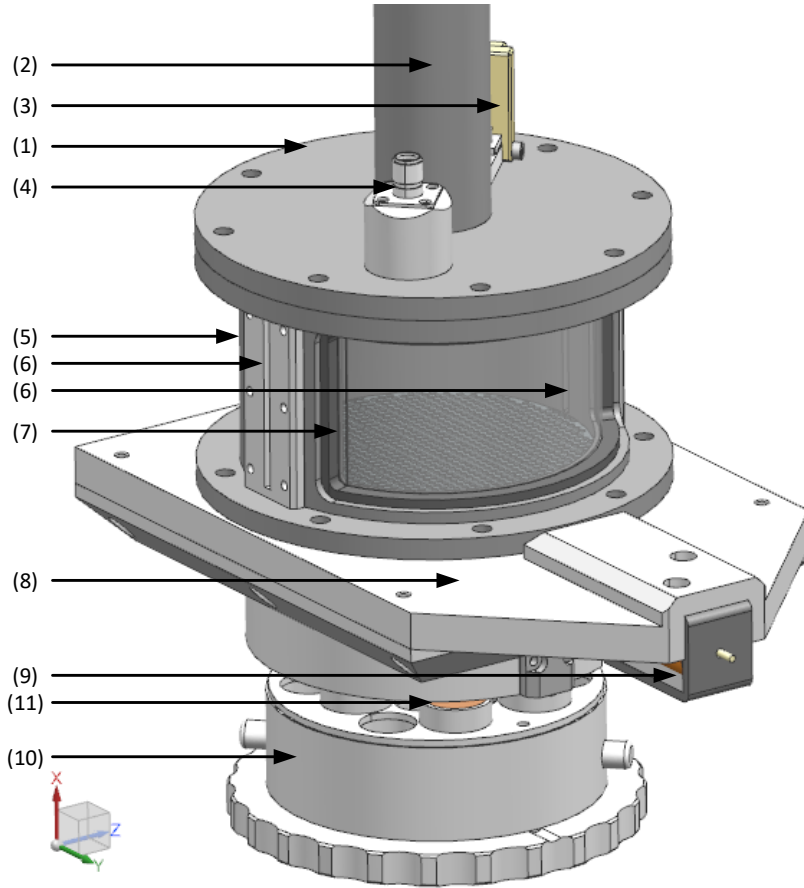


Figure 6.3: A three-dimensional view of the microwave cavity with integrated discharge electrodes and dust collection system. The top of the cavity (1) contained a gas inlet (2, not used during presented experiments), a temperature sensor (3), and the RF antenna (4). The base of the cavity (5) was formed by a hollow metal cylinder, which included two slits (6) for the lasers beam, and a steel viewing mesh (7) for camera imaging while ensuring proper electrical conductivity for microwave measurements. A shutter plate (8) was actuated by a linear solenoid (9) to collect dust grain sample at the operator's request on SEM stubs (11) mounted in a holder (10).

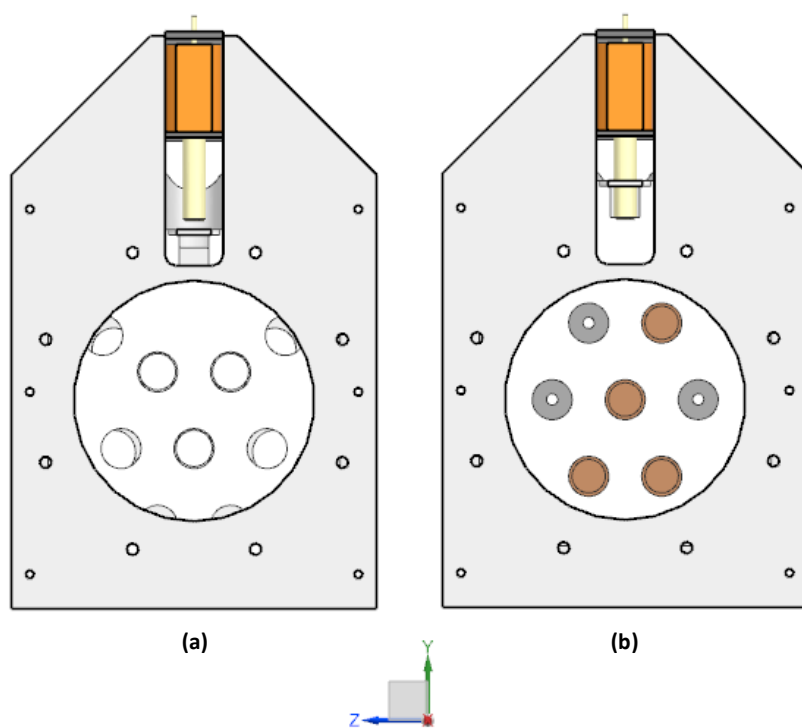


Figure 6.4: The shutter plate had two possible positions: (a) the shutter holes aligned with open holes in the stub holder so that dust grains could not reach the stub surfaces, or (b) the shutter holes matched the locations of the SEM stubs for the collection of dust grains after terminating the RF power.

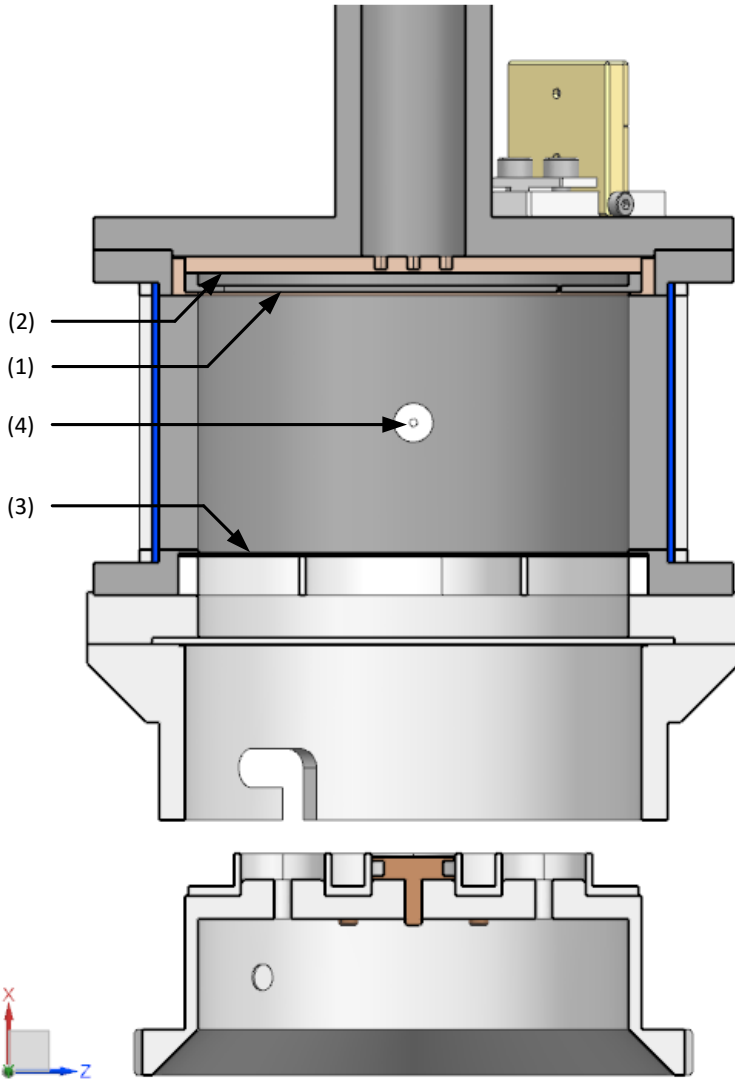


Figure 6.5: A cross sectional view of the discharge cavity and dust collection system. The RF-powered electrode (1) was located at the top of the microwave cavity, which was insulated from the grounded cavity components by a dielectric disk (2). The grounded mesh electrode (3) was located at the bottom of the cavity and was welded to its cylindrical base. Microwave power was injected into the cavity via the microwave antenna (4).

6.6.3 Stability of dust and plasma parameters

Fig. 6.6 depicts the plasma diagnostics for the duration of the complete measurements, i.e. during dust formation, settling of the dust cloud in an argon-only plasma, and during the pulsed laser experiments. As can be seen, the transmittance (equal to I/I_0 based on the green laser light extinction) and free electron density behaves similarly according to several phases. This section defines the time by t_{exp} , which equals zero at the beginning of the experiment, and marks the end of the experiments after about 750 s. Please note that the time variable t is used to denote the time with respect to each laser shot used to probe the particle charge during the laser experiments.

First, the plasma is ignited at $t_{\text{exp}} = 0$ s, which initiates the dust growth process, leading to an initial steep increase in free electron density. Second, at around $t_{\text{exp}} = 50$ s, coagulation induces the formation of larger dust grains from clusters formed earlier, which become permanent negatively charged. This depletes the free electron density. At $t_{\text{exp}} = 60$ s, the HMDSO valve is closed which coincides with the jump in n_e . Afterwards, the electron density settles to a steady state value and remains at that value until the end of the experiment. This observation holds also for the TM₁₁₀ and TE₀₁₁ modes with a different spatial sensitivity. As these two higher-order resonant modes were less sensitive to the perturbed volume, these were not used to measure the photodetachment signal.

The optical transmittance follows similar behavior, which decays when the dust grains have grown sufficiently in size and density. The signal reaches a minimum after the HMDSO valve was closed, indicating that dust growth proceeds some time after the HMDSO supply is terminated. Thereafter, a part of the dust grains are lost from the cavity as observed from camera images capturing laser light scattered by dust grains. After the settling phase, the transmittance signal resembles a quasi-steady state with a small drift from 0.75 to 0.78, which results in a drift of 14 % in the calculated dust density.

The camera images shown in the figure visualize laser light (532 nm, CW) scattered by the dust grains, where the camera was positioned under a 90 degree angle with respect to the laser sheet. From left to right, and from top to bottom, the camera images were captured at moments that correspond chronologically to the red vertical lines in the transmittance and electron density measurements as indicated by the corresponding indices 1 to 8. The first three images, which have been captured for $t_{\text{exp}} \leq 50$ s, indicate that there is no significant scattering from the dust grains. Directly after the coagulation step, i.e. the steep decline in transmittance and free electron density, a dust cloud becomes visible. Thereafter, the dust scattering pattern hardly changes, except for a bright emission region just below the sheath at the RF-powered (top) electrode that becomes visible from image 6 onwards. The UV laser beam propagated from right to left at half of the cavity axial dimension, and radially through the center of the cavity.

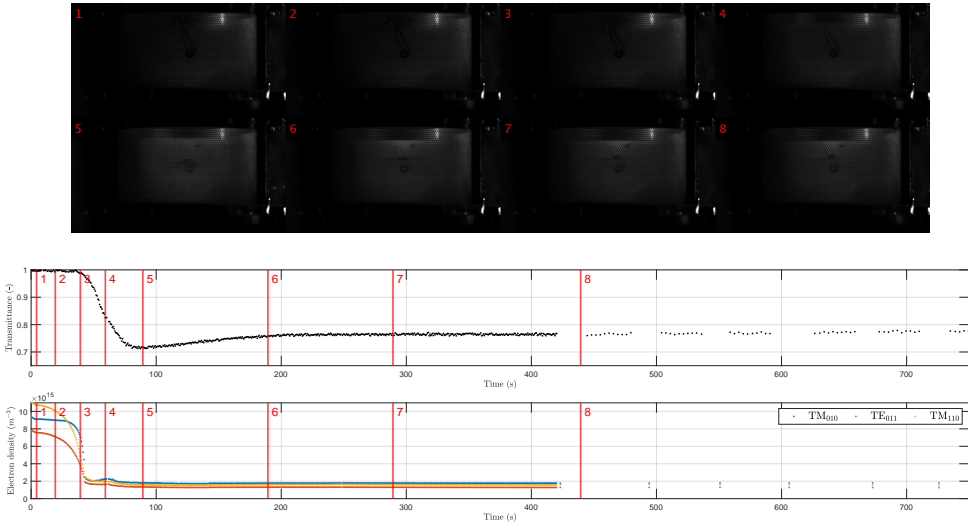


Figure 6.6: Diagnostic signals measured during the total duration of the experiment as a function of the time with respect to the beginning of the experiment t_{exp} , i.e. dust formation, settling, and pulsed laser experiment stages. The bottom graph presents the free electron density measured by three resonant modes: TM_{010} , TE_{011} and TM_{110} , where the electron density is maximum during nucleation, drops rapidly during coagulation due to the formation and charging of larger dust grains, and attains a minimum during the accretion phase by permanent charging of the dust cloud. A similar behavior is observed from the transmitted intensity from the continuous wave (CW) 532 nm laser beam used for the visualization of the dust cloud. The laser beam intensity drops during coagulation due to an increased amount of scattering and absorption by the dust grains, and obtains a minimum during the accretion phase, when the density and size of dust particles is maximum. Afterwards, it can be seen that the dust size and density drop a little and that the transmitted intensity increases slightly to a stationary state. When the signals, both electron density and transmittance, are stable, the laser photodetachment experiments were started and both signals were monitored between experiments at different laser energy levels to ensure stability of the dusty plasma. At the top of the figure, several laser light scattering images are depicted that have been captured during various moments in the dust formation process, of which the corresponding times are indicated in the graphs showing the electron density and transmittance.

6.6.4 Calculation of electric-field-weighted volume ratio

The electric-field-weighted volume ratio is inherent to the conversion of the measured shift in resonance frequency Δf to the electric-field-weighted volume-averaged electron density n_e , which is defined in Section 6.2 and restated for clarity:

$$\mathcal{V} = \frac{\iiint_{V_b} |\mathbf{E}(\mathbf{r})|^2 d^3\mathbf{r}}{\iiint_{V_c} |\mathbf{E}(\mathbf{r})|^2 d^3\mathbf{r}}. \quad (6.11)$$

The (laser beam) perturbed volume is denoted by V_b , the cavity volume by V_c , and the microwave electric field $\mathbf{E}(\mathbf{r})$ as a function of the spatial coordinate \mathbf{r} .

The microwave electric field is calculated using COMSOL Multiphysics[®], which solves the Maxwell equations to obtain the eigenmode solution for the TM_{010} resonant mode as depicted in Fig. 6.7. The geometry is based on the microwave cavity used in the experiments. As can be seen from the figure, the magnitude of the electric field is independent of the axial coordinate z , and decreases from the maximum at the radial center towards zero in the positive radial direction \mathbf{r} .

The microwave electric field can be directly used in the evaluation of the integrals considering the (laser) perturbed volume and the cavity volume. The perturbed volume is defined by the laser beam, which was aligned through the radial center of the cavity and at half height in the axial direction. The integration was performed numerically using an in-house developed program for MATLAB. The electric-field-weighted volume ratio was evaluated for the nominal laser beam radius, i.e. $R_{\text{laser}} = 1.0$ mm, from which it follows that $\mathcal{V} = 6.7 \times 10^{-4}$. Evaluating Eqn. (6.11) for $\hat{R}_{\text{laser}} = 0.9$ mm and $\hat{R}_{\text{laser}} = 1.1$ mm, respectively, as lower and upper bound, results in $\hat{\mathcal{V}} = 5.4 \times 10^{-4}$ and $\hat{\mathcal{V}} = 8.1 \times 10^{-4}$. This provided an estimate for the uncertainty $\Delta_{\mathcal{V}}$, which was used in the error margin for Δn_e and N_e .

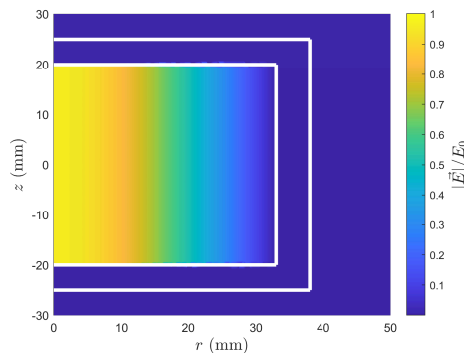


Figure 6.7: Structure of the (microwave) electric field, normalized to E_0 , corresponding to the TM_{010} resonant mode of the microwave cavity. The field solution is computed by solving for the eigenmode in COMSOL Multiphysics[®]. The resulting eigenfrequency or resonance frequency equals $f_0 = 3.477$ GHz.

6.6.5 SEM micrographs of collected nanoparticles

The micrographs obtained using scanning electron microscopy (SEM) provided information on the collected dust grain size. Fig. 6.8 depicts a local overview, where mostly single dust grains can be seen. In addition, a doublet and triplet were collected which comprise, respectively, two and three dust grains with a size similar to the individual dust grains. Fig. 6.9 depicts a single dust grains using a fourfold magnification compared to Fig. 6.8, from which it can be confirmed that the dust grains are (nearly) spherical with minor surface roughness compared to the dust grain's diameter. Fig. 6.10 contains the same image as depicted in Fig. 6.8, including the (digitally) measured dust grain diameters. The average diameter is rounded to $2a_d = 280$ nm, based on individual diameters ranging from 241 nm to 315 nm, and consequently, the nominal dust radius is defined as $a_d = 140$ nm for the analysis and discussion in Section 6.3 and 6.4, and the solution of the thermionic emission model in Section 6.6.7.

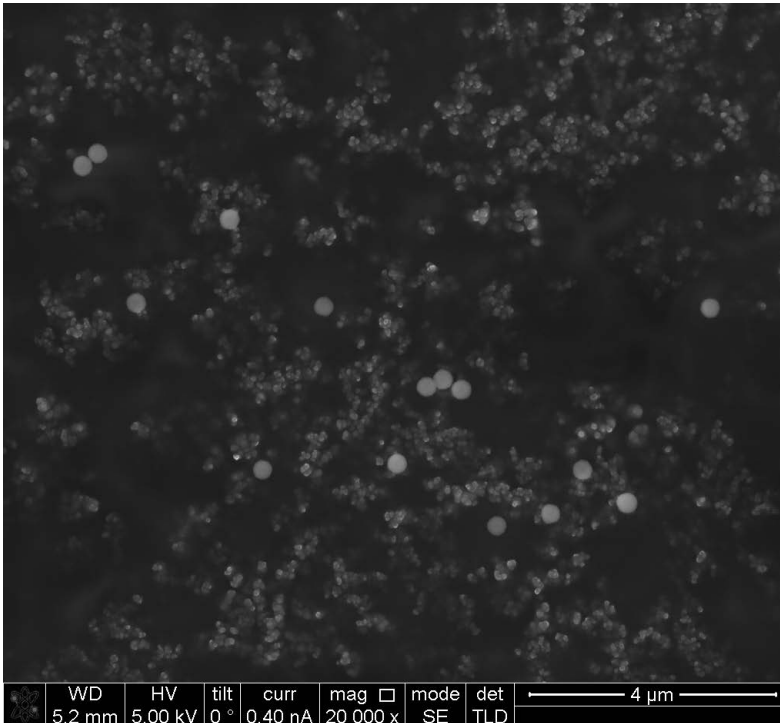


Figure 6.8: SEM image of a collection of (nearly spherical) nanoparticles showing mostly singlet nanoparticles. Additionally, doublet and triplet particles can be seen where the constituent particles possess approximately the same diameter as the singlets.

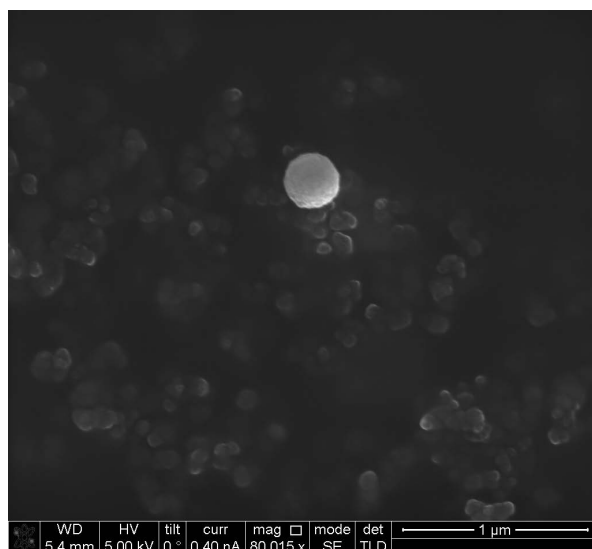


Figure 6.9: SEM image of a single (nearly) spherical nanoparticle.

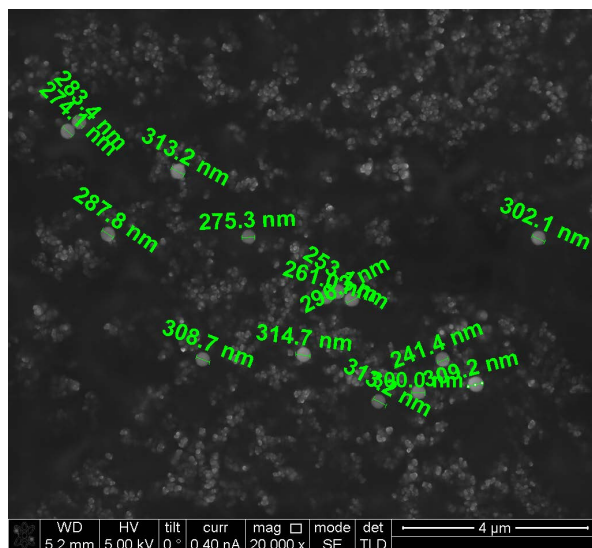


Figure 6.10: SEM image of a collection of nanoparticles with size measurements (diameter) indicated by the green rulers overlaying the dust grains.

6.6.6 Model description

The model solves simultaneously for the two state variables, the dust temperature T_d and the dust floating potential V_d , by numerically integrating the coupled system of differential equations. The source and sink terms define the in- and outflux of heat Q_s , particles Γ_s , and charge I_s into and from a single dust grain. Most of the variables and parameters used in this section are defined in Table 6.2, including the declaration and values used to solve the model, and otherwise, the variables are stated directly following their first appearance via the equations. The nanoparticle radius was obtained by SEM images, from which an average radius of 140 nm was found (see Section 6.6.5). The absorption efficiencies C_{abs} were calculated by evaluating the Mie theory [71] using the MATLAB program designed by Mätzler [73], and by assuming refractive indices for silicon dioxide (Si) [78] and graphite (C) [74] at an optical wavelength $\lambda = 266$ nm.

Table 6.2: Variables and symbols used in the definition of the model equations, including the values used to solve the model. Where Si or C is indicated between brackets following a value, these values have been used respectively in case silica or carbon was considered in the evaluation of the model.

Symbol	Definition	Value	Unit
ρ_d	mass density of dust grain	1870 (SiO ₂) [80] / 2300 (C) [81]	kg m ⁻³
c_p	specific heat capacity of dust grain	821 (Si) [82] / 2270 (C) [83]	J kg ⁻¹ K ⁻¹
C_{abs}	absorption coefficient	0.50 (Si) / 1.09 (C)	-
ϕ	work function	4 – 5 (Si) [84] / 5.0 (C) [84]	eV
a_d	dust radius	140	nm
ζ_d	emissivity of dust grain	0.6 (Si) [85] / 0.4 (C) [58]	-
E_{laser}	laser pulse energy	2.80	mJ
A_{laser}	laser beam cross section	$3.14 \cdot 10^{-6}$	m ²
T_e	electron temperature	$3.4814 \cdot 10^4$	K
T_i	ion temperature	300	K
n_e	electron density	$2 \cdot 10^{15}$	m ⁻³
n_i	ion density	$4 \cdot 10^{16}$	m ⁻³
k_B	Boltzmann constant	$1.381 \cdot 10^{-23}$	J K ⁻¹
ϵ_0	vacuum permittivity	$8.854 \cdot 10^{-12}$	F m ⁻¹
e	elementary charge	$1.602 \cdot 10^{-19}$	J eV ⁻¹
m_e	electron mass	$8.8 \cdot 10^{-31}$	kg
A_0	Richardson constant	$1.2 \cdot 10^6$	A m ⁻²
σ_{SB}	Stefan-Boltzmann constant	$5.670 \cdot 10^{-8}$	W m ⁻² K ⁻⁴
h	Planck's constant	$6.626 \cdot 10^{-34}$	m ² kg s ⁻¹
c	speed of light	$2.998 \cdot 10^8$	m s ⁻¹
E_{ion}	ionization energy	15.8	eV
p_g	neutral gas pressure	7	Pa
α	thermal accommodation coefficient	0.1 [58]	-
T_g	neutral gas temperature	300	K
γ	adiabatic constant of gas	5/3	-
m_g	mass of neutral gas particle	$6.634 \cdot 10^{-26}$	kg

The temperature and floating potential of a dust grain immersed in a low pressure plasma are well described using the continuity equations. The dust temperature is modeled by balancing the change in enthalpy with the in- and outflux of heat [86, 25]:

$$m_d c_p \frac{dT_d}{dt} = A_d \left(Q_{\text{laser}} + \Gamma_e(V_d) 2k_B T_e + \Gamma_i(V_d) eV_d + \Gamma_e(V_d) E_{\text{ion}} - \Gamma_t(V_d, T_d) (\phi + \Delta\phi) - Q_c(T_d) - Q_r(T_d) \right), \quad (6.12)$$

with the dust mass, surface area, and floating potential m_d , A_d , and V_d , respectively. Q_{laser} denotes the laser-induced energy density influx equal to $E_{\text{laser}} C_{\text{abs}} / (4A_{\text{laser}})$ (J/m^2), which lasts only during the time frame $0 \leq t \leq 8$ ns.

The floating potential is governed by electric currents imposed on the dust grain, where the dust grain acts as a capacitor storing charge q_d at floating potential V_d with respect to the plasma [34]:

$$4\pi\epsilon_0 a_d \frac{dV_d}{dt} = eA_d (-\Gamma_e(V_d) + \Gamma_i(V_d) + \Gamma_t(V_d, T_d)). \quad (6.13)$$

As can be seen from Eqn. (6.12) and (6.13), the mutual dependency of the rate of change in dust temperature and dust floating potential requires simultaneous consideration of both states.

The electron flux towards the dust surface Γ_e follows from the orbital-motion-limited theory [35]:

$$\Gamma_e = \frac{1}{4} n_e \left(\frac{k_B T_e}{2\pi m_e} \right)^{1/2} \exp \left(\frac{eV_d}{k_B T_e} \right). \quad (6.14)$$

The ion flux towards the dust surface Γ_i follows from the same theory, in which ion-neutral collisions are neglected [35]:

$$\Gamma_i = \frac{1}{4} n_i \left(\frac{k_B T_i}{2\pi m_i} \right)^{1/2} \left(1 - \frac{eV_d}{k_B T_i} \right), \quad (6.15)$$

Ions are accelerated to a mean kinetic energy of eV_d across the sheath surrounding the dust grain, whereas the electrons carry $2k_B T_e$ of energy as they have overcome the Coulomb barrier.

The thermionic electron emission is both a relevant heat transfer process as well as an electron current leaving the grain surface. It can be described by a modified version of the Richardson-Dushman equation [57]:

$$\Gamma_t = \frac{A_0 T_d^2}{e} \exp \left(-\frac{\phi + \Delta\phi}{k_B T_d} \right). \quad (6.16)$$

Here, the Γ_t denotes the thermionic electron flux, and $\Delta\phi$ the electrostatic potential barrier for further electron release:

$$\Delta\phi = eV_d = \frac{eq_d}{4\pi\epsilon_0 a_d}. \quad (6.17)$$

Here, q_d denotes the surface charge of the dust grain.

The heat flux carried away by thermionic electron emission comprises the product of the thermionic electron flux and the energy barrier overcome by the emitted electron. It should be noted that the energy barrier $\Delta\phi$ is time-varying via the dust floating potential V_d , which in turn depends on the dust temperature via the thermionic electron current.

The neutral gas colliding with the dust grain surface carries away heat by conduction [86, 87], for which we turn to Knudsen's expression in the free molecular regime [88]:

$$Q_c = \frac{\alpha p_g}{16} \frac{\gamma + 1}{\gamma - 1} \left(\frac{8k_B T_g}{\pi m_g} \right)^{1/2} \left(\frac{T_d}{T_g} - 1 \right). \quad (6.18)$$

It should be noted that only the argon flow is maintained during the experiment, and therefore, argon is considered as the neutral gas species responsible for conduction.

Radiative heat loss Q_r from nanoparticles, for which the Rayleigh criterion is satisfied, occurs as a volumetric process described as:

$$Q_r = \frac{2\pi a_d \zeta_d \sigma_{SB} k_B}{hc} 4T_d^5. \quad (6.19)$$

In the subsequent section, the solution to this model is obtained using a MATLAB code to solve the differential equations.

6.6.7 Model solution for Si- and C-like nanoparticles

The solutions of the model described in Section 6.6.6 are depicted in this section by showing the heat fluxes, the currents, and the resulting floating potential and temperature of the dust grain as a function of time. The heat fluxes are shown in terms of power (W) in the subplot at the top of each figure in the following order: laser power (P_l), electron flux (P_e), ion flux (P_i), recombination flux (P_{rec}), thermionic emission (P_t), conduction (P_c), and radiation (P_{rad}). The currents are depicted in the subplot in the middle of each figure: electron current (I_e), ion current (I_i), and thermionic emission current (I_t). The bottom subplot depicts the floating potential and the dust temperature, using the left- and right-hand side axis, respectively. In the discussion in this section, the floating potential is used as a measure in comparing the model with the released electron density observed from the experiments. This is based on the fact that the released electron density results directly from an equal decrease of the (total) dust charge, or the increase of the floating potential.

The solution of the model for C-like grains is depicted in Fig. 6.11, which shows that thermionic emission is irrelevant due to an insignificant rise of the dust temperature in combination with a relatively high work function. This is different for Si-like grains as shown in Fig. 6.12, which exhibit a higher dust temperature, although the thermionic emission heat flux and current remain well below the other fluxes and currents. Consequently, the floating potential is not disturbed by thermionic emission for both C- and Si-like dust grains.

Since the dust temperature is significantly higher for Si-like properties, the work function is varied using the Si-like properties to study scenarios for which the thermionic

emission heat flux and current become relevant. Assuming $\phi = 4.5 \text{ eV}$ and all other parameters equal to those denoted for Si-like grains, a solution of the model for Si-like grains is obtained as shown in Fig. 6.13. This results in a significant increase of the heat flux and current due to thermionic emission. The heat flux exceeds the heat flux due to the ions, but remains insignificant with respect to the dominant radiation heat flux. The thermionic emission current, however, temporarily becomes significant with respect to the electron and ion current, which causes a disturbance to the floating potential. Nevertheless, the floating potential takes about $10 \mu\text{s}$ to reach its peak value, and thereafter the equilibrium floating potential is restored only after several tens of μs .

As an extreme case, the work function is even further reduced to 4 eV to study the effect of a larger contribution of the thermionic emission. In Fig. 6.14, the model solution is depicted for this case, again the properties for Si-like grains are used. Interestingly, the thermionic emission heat flux is now of the same order of magnitude as the heat flux by conduction, exceeding the plasma-induced fluxes (due to electrons, ion, and recombination). The thermionic emission current is in this case more than one order of magnitude larger than the electron and ion current. The latter observation in the currents results in an interesting phenomenon, because temporarily, between $3 - 30 \mu\text{s}$, the electron current is balanced by the thermionic emission current, while the ion current has completely vanished. Nevertheless, it can be seen from the bottom figure in Fig. 6.14 that the rise time of the floating potential is about $1 \mu\text{s}$ and the decay time to restore equilibrium is about $100 \mu\text{s}$. The latter delay in the decay time is due to the slow thermal timescale, which results in a significant contribution of the thermionic emission current as long as the dust grains remain sufficiently hot.

In conclusion, the observations based on the model solutions are summarized in view of the experimental observations. First, the rise time in case of significant thermionic emission current is about $1 \mu\text{s}$, whereas the rise time in free electron density observed in the experiments is about an order of magnitude smaller at 70 ns . Second, if the work function is sufficiently small, it is observed that the thermionic current can be significantly higher than the electron and ion current. However, the fact that the thermionic current is significant also implies that the dust temperature is high, which holds for a long time period due to the thermal timescale. This in turn implies that the timescale to restore the floating potential is much larger than the few μs timescale observed from the experiments. Hence, compared to the timescales observed in the experiment, both the rising and falling timescale of the floating potential (and thereby the change in the free electron density) are much slower than the observed timescales, which means that thermionic emission cannot be responsible for the observations.

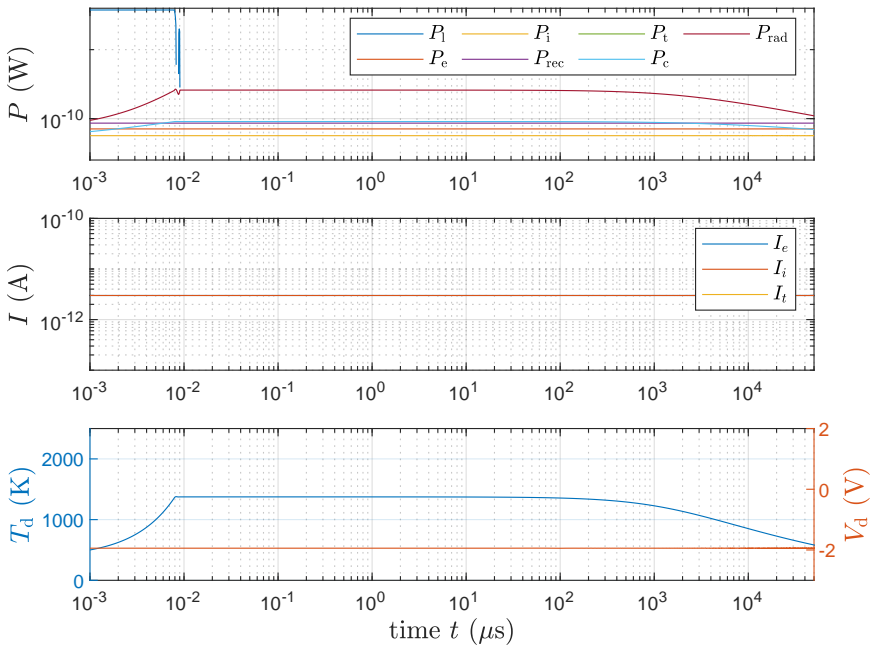


Figure 6.11: Model solution for C-like dust grains as a function of time t . The top subplot depicts the heat fluxes, the middle subplot shows the currents, and the bottom subplot visualizes the dust floating potential and temperature.

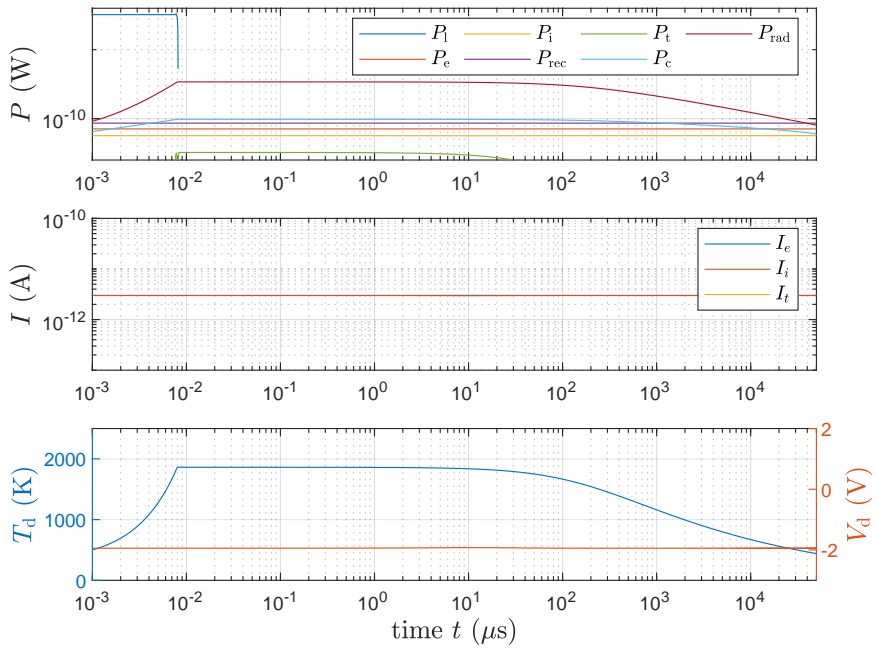


Figure 6.12: Model solution for Si-like dust grains as a function of time t using $\phi = 5$ eV. The top subplot depicts the heat fluxes, the middle subplot shows the currents, and the bottom subplot visualizes the dust floating potential and temperature.

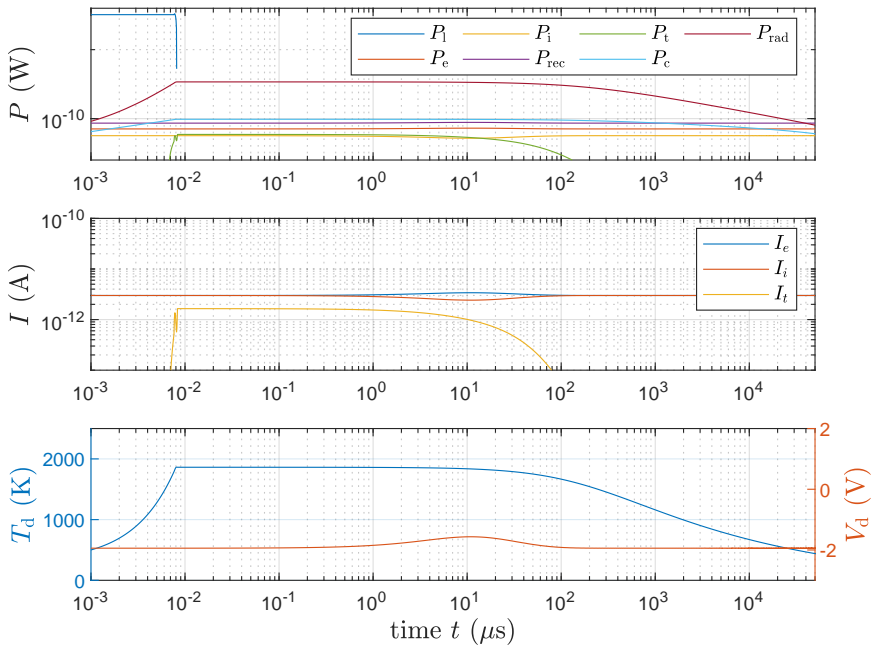


Figure 6.13: Model solution for Si-like dust grains as a function of time t using $\phi = 4.5\text{eV}$. The top subplot depicts the heat fluxes, the middle subplot shows the currents, and the bottom subplot visualizes the dust floating potential and temperature.

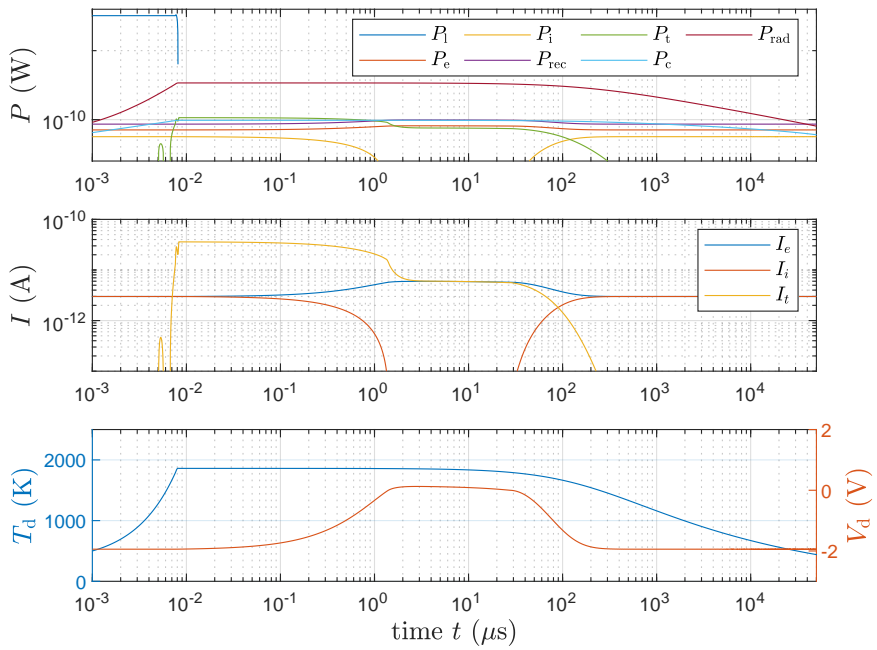


Figure 6.14: Model solution for Si-like dust grains as a function of time t using $\phi = 4$ eV. The top subplot depicts the heat fluxes, the middle subplot shows the currents, and the bottom subplot visualizes the dust floating potential and temperature.

6.6.8 Derivation of charging timescale

The charging timescale of an initially uncharged dust grain has been derived for different situations, e.g. in case of OML currents or secondary electron emission imposed on the dust grain. However, the assumption that $n_e = n_i$ is made in the found literature [66, 34, 67, 2, 68], which is not appropriate for the presented experiment due to electron depletion. Moreover, the charging timescale relation is often defined using pre-factors that have been calculated for fixed temperature ratios. Therefore, the charging timescale is derived from the basis of the OML theory to provide freedom in the use of values for the temperature and density of the electrons and ions. This section provides the mathematical derivation for the dust charging timescale due to the OML currents in a pure argon discharge, which is based on a similar approach used by Shukla and Mamun [2] (Section 2.5.1 in this book).

The OML currents were already stated in Section 6.4 and Chapter 2, but are restated here for clarity:

$$I_e = -e\pi a_d^2 n_e v_{T_e} \exp\left(\frac{eV_d}{k_B T_e}\right), \quad (6.20)$$

$$I_i = e\pi a_d^2 n_i v_{T_i} \left(1 - \frac{eV_d}{k_B T_i}\right), \quad (6.21)$$

where $v_{T_s} = \sqrt{\frac{k_B T_s}{2\pi m_s}}$ with species $s = e, i$ for electrons and ions, respectively. The rate of change of the dust charge follows from the difference between charges carried away and towards the dust grain's surface, which is easily described using the following ordinary differential equation:

$$\frac{dq_d}{dt} = I_e + I_i. \quad (6.22)$$

The differential equation can be easily converted into an expression governing the floating potential by considering the dust grain as a spherical capacitor:

$$q_d = 4\pi\epsilon_0 a V_d. \quad (6.23)$$

The differential equation Eqn. (6.22), redefined in terms of the floating potential, can be used to obtain the equilibrium potential (and therewith equilibrium charge), and the timescale at which an initially uncharged grain attains the equilibrium potential. Introducing the floating potential Eqn. (6.23) and OML currents, Eqn. (6.20) and (6.21), into Eqn. (6.22) and rearranging terms results in an expression for the rate of change of the floating potential of the dust grain:

$$\frac{dV_d}{dt} = C_1 \left(1 - \frac{eV_d}{k_B T_i} - \frac{n_e v_{T_e}}{n_i v_{T_i}} \exp\left(\frac{eV_d}{k_B T_e}\right)\right), \quad (6.24)$$

with

$$C_1 = \frac{e a n_i v_{T_i}}{4\epsilon_0}. \quad (6.25)$$

Redefining the floating potential $V_d = \bar{V}_d + \tilde{V}_d$, with the equilibrium floating potential \bar{V}_d and perturbation \tilde{V}_d , the differential equation can be linearized using

$$\frac{dV_d}{dt} \approx F(\bar{V}_d) + \left. \frac{dF}{dV_d} \right|_{\bar{V}_d} \tilde{V}_d \quad (6.26)$$

to arrive at the following linearized form of Eqn. (6.24), where $\frac{d\bar{V}_d}{dt} = 0$:

$$\frac{d\tilde{V}_d}{dt} \approx C_1 \left(1 - \frac{e\bar{V}_d}{k_B T_i} - \frac{n_e v_{T_e}}{n_i v_{T_i}} \exp\left(\frac{e\bar{V}_d}{k_B T_e}\right) \right) \quad (6.27)$$

$$- C_1 \left(\frac{e}{k_B T_i} + \frac{n_e v_{T_e}}{n_i v_{T_i}} \exp\left(\frac{e\bar{V}_d}{k_B T_e}\right) \frac{e}{k_B T_e} \right) \tilde{V}_d. \quad (6.28)$$

For clarity, we define the pre-factors as C_2 and C_3 :

$$C_2 = 1 - \frac{e\bar{V}_d}{k_B T_i} - \frac{n_e v_{T_e}}{n_i v_{T_i}} \exp\left(\frac{e\bar{V}_d}{k_B T_e}\right) = 0, \quad (6.29)$$

which equals zero because of the equilibrium condition $I_e = I_i$, and

$$C_3 = -C_1 \left(\frac{e}{k_B T_i} + \frac{n_e v_{T_e}}{n_i v_{T_i}} \exp\left(\frac{e\bar{V}_d}{k_B T_e}\right) \frac{e}{k_B T_e} \right). \quad (6.30)$$

The solution to the ordinary differential equation can be seen easily with the redefinition of the pre-factors:

$$\frac{d\tilde{V}_d}{dt} = C_3 \tilde{V}_d, \quad (6.31)$$

from which it can be seen that the following expression for the perturbed part of the floating potential provides a solution:

$$\tilde{V}_d(t) = \exp(C_3 t). \quad (6.32)$$

The charging timescale follows by using the standard definition of the e-folding timescale of an exponential function, from which it follows that $\tau_{\text{charging}} = -\frac{1}{C_3}$:

$$\tau_{\text{charging}} = \left(\frac{e^2 a n_i v_{T_i}}{4 \varepsilon_0 k_B T_e} \left(\frac{T_e}{T_i} + \frac{n_e v_{T_e}}{n_i v_{T_i}} \exp\left(\frac{e\bar{V}_d}{k_B T_e}\right) \right) \right)^{-1}. \quad (6.33)$$

6.7 Bibliography

- [1] M.Y. Pustyl'nik, A.A. Pikalev, A.V. Zobnin, I.L. Semenov, H.M. Thomas, and O.F. Petrov. Physical aspects of dust–plasma interactions. *Contributions to Plasma Physics*, (September):202100126, 2021.
- [2] P.K. Shukla and A.A. Mamun. *Introduction to dusty plasma physics*. Institute of Physics Publishing Ltd, Bristol, 2002.
- [3] Robert L. Merlino and John A. Goree. Dusty plasmas in the laboratory, industry, and space. *Physics Today*, 57(7):32–38, 2004.
- [4] Job Beckers, Tijn van de Ven, Ruud van der Horst, Dmitry Astakhov, and Vadim Banine. EUV-induced plasma: A peculiar phenomenon of a modern lithographic technology. *Applied Sciences (Switzerland)*, 9(14):1–23, 2019.
- [5] J. Winter. Dust: A new challenge in nuclear fusion research? *Physics of Plasmas*, 7(10):3862–3866, 2000.
- [6] L. Boufendi, M. Ch Jouanny, E. Kovacevic, J. Berndt, and M. Mikikian. Dusty plasma for nanotechnology. *Journal of Physics D: Applied Physics*, 44(17):174035, 2011.
- [7] Jungmi Hong, Samuel Yick, Edith Chow, Adrian Murdock, Jinghua Fang, Dong Han Seo, Annalena Wolff, Zhaojun Han, Timothy Van Der Laan, Avi Bendavid, Kostya Ostrikov, and Anthony B. Murphy. Direct plasma printing of nano-gold from an inorganic precursor. *Journal of Materials Chemistry C*, 7(21):6369–6374, 2019.
- [8] Wooik Jung, Yoon Ho Jung, Peter V. Pikhitsa, Jicheng Feng, Younghwan Yang, Minkyung Kim, Hao Yuan Tsai, Takuo Tanaka, Jooyeon Shin, Kwang Yeong Kim, Hoseop Choi, Junsuk Rho, and Mansoo Choi. Three-dimensional nanoprinting via charged aerosol jets. *Nature*, 592(7852):54–59, 2021.
- [9] V. E. Fortov and F. Petrov. Crystal and liquid structures in strongly nonideal dusty plasmas under laboratory and microgravity conditions. *High Temperature*, 48(6):943–956, 2010.
- [10] John Maddox. Plasma dust as model crystals. *Nature*, 370(6489):411, 1994.
- [11] S. Khrapak and G. Morfill. Basic processes in complex (dusty) plasmas: Charging, interactions, and ion drag force. *Contributions to Plasma Physics*, 49(3):148–168, 2009.
- [12] Ranganathan Gopalakrishnan and Christopher J. Hogan. Coulomb-influenced collisions in aerosols and dusty plasmas. *Physical Review E - Statistical, Nonlinear, and Soft Matter Physics*, 85(2):1–14, 2012.

-
- [13] V. S. Filinov, O. F. Petrov, V. E. Fortov, V. I. Molotkov, A. D. Khakhaev, and S. F. Podrjadchikov. Coulomb instability of dusty particle system in gas-discharge plasma. *Contributions to Plasma Physics*, 45(3-4):176–184, 2005.
- [14] H. Thomas, G. E. Morfill, V. Demmel, J. Goree, B. Feuerbacher, and D. Möhlmann. Plasma crystal: Coulomb crystallization in a dusty plasma. *Physical Review Letters*, 73(5):652–655, 1994.
- [15] Steven L. Girshick. Particle nucleation and growth in dusty plasmas: On the importance of charged-neutral interactions. *Journal of Vacuum Science & Technology A*, 38(1):011001, 2020.
- [16] I. A. Belov, A. S. Ivanov, D. A. Ivanov, A. F. Pal, A. N. Starostin, A. V. Filippov, A. V. Dem'yanov, and Yu V. Petrushevich. Coagulation of charged particles in a dusty plasma. *Journal of Experimental and Theoretical Physics*, 90(1):93–101, 2000.
- [17] M. Horanyi and C. K. Goertz. Coagulation of dust particles in a plasma. *The Astrophysical Journal*, 361(1):155, 1990.
- [18] L. S. Matthews, V. Land, and T. W. Hyde. Charging and coagulation of dust in protoplanetary plasma environments. *Astrophysical Journal*, 744(1):8, 2012.
- [19] J. Berndt, E. Kovačević, I. Stefanović, O. Stepanović, S. H. Hong, L. Boufendi, and J. Winter. Some aspects of reactive complex plasmas. *Contributions to Plasma Physics*, 49(3):107–133, 2009.
- [20] Ryan S. Marshall, Kil-Byoung Chai, and Paul M. Bellan. Identification of Accretion as Grain Growth Mechanism in Astrophysically Relevant Water–Ice Dusty Plasma Experiment. *The Astrophysical Journal*, 837(1):56, 2017.
- [21] Maxime Mikikian, Marjorie Cavarroc, Lénaïc Couëdel, Yves Tessier, and Laïfa Boufendi. Dust particles in low-pressure plasmas: Formation and induced phenomena. *Pure and Applied Chemistry*, 82(6):1273–1282, 2010.
- [22] I. Stefanović, E. Kovačević, J. Berndt, and J. Winter. Non-equilibrium processes and dust formation in low pressure reactive plasmas. *Journal of Physics: Conference Series*, 71(1):012015, 2007.
- [23] W. W. Stoffels, E. Stoffels, G. Ceccone, and F. Rossi. Laser-induced particle formation and coalescence in a methane discharge. *Journal of Vacuum Science & Technology A: Vacuum, Surfaces, and Films*, 17(6):3385–3392, 1999.
- [24] E. Stoffels, W. W. Stoffels, G. M. W. Kroesen, and F. J. de Hoog. Dust formation and charging in an Ar/SiH₄ radio-frequency discharge. *Journal of Vacuum Science & Technology A: Vacuum, Surfaces, and Films*, 14(2):556–561, 1996.
- [25] W. W. Stoffels, E. Stoffels, G. M. W. Kroesen, and F. J. de Hoog. Detection of dust particles in the plasma by laser-induced heating. *Journal of Vacuum Science & Technology A: Vacuum, Surfaces, and Films*, 14(2):588–594, 1996.

- [26] J. Winter, V. E. Fortov, and A. P. Nefedov. Radioactive dust levitation and its consequences for fusion devices. *Journal of Nuclear Materials*, 290-293:509–512, 2001.
- [27] Laïfa Boufendi and André Bouchoule. Industrial developments of scientific insights in dusty plasmas. *Plasma Sources Science and Technology*, 11(3 A):A211, 2002.
- [28] Mark A. van de Kerkhof, Ernst Galutschek, Andrei Yakunin, Selwyn Cats, and Christian Cloin. Particulate and molecular contamination control in EUV-induced H₂-plasma in EUV lithographic scanner. *Proceedings SPIE*, 11489(August):114890K, 2020.
- [29] Job Beckers, Boy van Minderhout, Paul Blom, Gerrit Kroesen, and Ton Peijnenburg. Particle contamination control by application of plasma. *Proceedings SPIE*, 11323(March):113232L, 2020.
- [30] Judith van Huijstee, Boy van Minderhout, Robert M. H. Rompelberg, Paul Blom, Ton Peijnenburg, and Job Beckers. Plasma assisted particle contamination control: plasma charging dependence on particle morphology. *Proceedings SPIE*, 11611(February):116113A, 2021.
- [31] A. Bouchoule and L. Boufendi. Particulate formation and dusty plasma behaviour in argon-silane RF discharge. *Plasma Sources Science and Technology*, 2(3):204–213, 1993.
- [32] L. Boufendi, A. Bouchoule, R. K. Porteous, J. Ph Blondeau, A. Plain, and C. Laure. Particle-particle interactions in dusty plasmas. *Journal of Applied Physics*, 73(5):2160–2162, 1993.
- [33] I. Langmuir. Oscillations in ionized gases. *Proc. Natl. Acad. Sci. U.S.A.*, 14:627–637, 1928.
- [34] J Goree. Charging of particles in a plasma. *Plasma Sources Science and Technology*, 3(3):400–406, 1994.
- [35] Marco Gatti and Uwe Kortshagen. Analytical model of particle charging in plasmas over a wide range of collisionality. *Physical Review E*, 78(4):046402, 2008.
- [36] L. G. D’yachkov, A. G. Khrapak, S. A. Khrapak, and G. E. Morfill. Model of grain charging in collisional plasmas accounting for collisionless layer. *Physics of Plasmas*, 14(4):042102, 2007.
- [37] M. V. Salnikov, A. V. Fedoseev, and G. I. Sukhinin. Plasma potential around a single-dimensional dust particle chain placed in an external electric field. *Journal of Physics: Conference Series*, 1393(1):012022, 2019.
- [38] Manis Chaudhuri, Sergey A. Khrapak, and Gregor E. Morfill. Experimental determination of particle charge in highly collisional plasma. *AIP Conference Proceedings*, 1397(November):263–264, 2011.

-
- [39] S. Ratynskaia, S. Khrapak, A. Zobnin, M. H. Thoma, M. Kretschmer, A. Usachev, V. Yaroshenko, R. A. Quinn, G. E. Morfill, O. Petrov, and V. Fortov. Experimental determination of dust-particle charge in a discharge plasma at elevated pressures. *Physical Review Letters*, 93(8):8–11, 2004.
- [40] J. Beckers, T. Ockenga, M. Wolter, W. W. Stoffels, J. Van Dijk, H. Kersten, and G. M. W. Kroesen. Microparticles in a collisional rf plasma sheath under hypergravity conditions as probes for the electric field strength and the particle charge. *Physical Review Letters*, 106(11):115002, 2011.
- [41] B. Van Minderhout, J. C.A. Van Huijstee, B. Platier, T. Peijnenburg, P. Blom, G. M.W. Kroesen, and J. Beckers. Charge control of micro-particles in a shielded plasma afterglow. *Plasma Sources Science and Technology*, 29(6):065005, 2020.
- [42] Benjamin Tadsen, Franko Greiner, Sebastian Groth, and Alexander Piel. Self-excited dust-acoustic waves in an electron-depleted nanodusty plasma. *Physics of Plasmas*, 22(11):113701, 2015.
- [43] M. A. Smith, J. Goodrich, H. U. Rahman, and U. Mohideen. Measurement of grain charge in dusty plasma Coulomb crystals. *IEEE Transactions on Plasma Science*, 29(2 I):216–220, 2001.
- [44] Tonuj Deka, A. Boruah, S. K. Sharma, and H. Bailung. Observation of self-excited dust acoustic wave in dusty plasma with nanometer size dust grains. *Physics of Plasmas*, 24(9):093706, 2017.
- [45] Sebastian Groth, Franko Greiner, Benjamin Tadsen, and Alexander Piel. Kinetic Mie ellipsometry to determine the time-resolved particle growth in nanodusty plasmas. *Journal of Physics D: Applied Physics*, 48(46):465203, 2015.
- [46] Franko Greiner, André Melzer, Benjamin Tadsen, Sebastian Groth, Carsten Killer, Florian Kirchschrager, Frank Wieben, Iris Pilch, Harald Krüger, Dietmar Block, Alexander Piel, and Sebastian Wolf. Diagnostics and characterization of nanodust and nanodusty plasmas. *European Physical Journal D*, 72(5):81, 2018.
- [47] Benjamin Tadsen, Franko Greiner, and Alexander Piel. On the amplitude of dust-density waves in inhomogeneous dusty plasmas. *Physics of Plasmas*, 24(3):1–6, 2017.
- [48] B. Platier, T.J.A. Staps, M. van der Schans, W.L. IJzerman, and J. Beckers. Resonant microwaves probing the spatial afterglow of an RF plasma jet. *Applied Physics Letters*, 115:254103, 2019.
- [49] M. Haverlag, G. M.W. Kroesen, T. H.J. Bisschops, and F. J. de Hoog. Measurement of electron densities by a microwave cavity method in 13.56-MHz RF plasmas of Ar, CF₄, C₂F₆, and CHF₃. *Plasma Chemistry and Plasma Processing*, 11(3):357–370, 1991.

- [50] J. Beckers, F. M.J.H. Van De Wetering, B. Platier, M. A.W. Van Nindhuijs, G. J.H. Brussaard, V. Y. Banine, and O. J. Luiten. Mapping electron dynamics in highly transient EUV photon-induced plasmas: A novel diagnostic approach using multi-mode microwave cavity resonance spectroscopy. *Journal of Physics D: Applied Physics*, 52(3):034004, 2019.
- [51] Marc van der Schans, Bart Platier, Peter Koelman, Ferdi van de Wetering, Jan Van Dijk, Job Beckers, Sander Nijdam, and Wilbert IJzerman. Decay of the electron density and the electron collision frequency between successive discharges of a pulsed plasma jet in N₂. *Plasma Sources Science and Technology*, 28(3):035020, 2019.
- [52] John C. Slater. Microwave Electronics. *Reviews of Modern Physics*, 18(4):441–512, 1946.
- [53] Manfred A. Biondi. Measurement of the electron density in ionized gases by microwave techniques. *Review of Scientific Instruments*, 22(7):500–502, 1951.
- [54] David M. Pozar. *Microwave Engineering*. Wiley, 2005.
- [55] M A W Van Nindhuijs, K A Daamen, J Beckers, and O J Luiten. Design and characterization of a resonant microwave cavity as a diagnostic for ultracold plasmas. *Review of Scientific Instruments*, 92:013506, 2021.
- [56] W Chow and M Rosenberg. Grains at High Electron Energies. *IEEE Transactions on p*, 22(2):179–186, 1994.
- [57] J. M. Mitrani, M. N. Shneider, B. C. Stratton, and Y. Raiteses. Modeling thermionic emission from laser-heated nanoparticles. *Applied Physics Letters*, 108(5):054101, 2016.
- [58] M. N. Shneider. Carbon nanoparticles in the radiation field of the stationary arc discharge. *Physics of Plasmas*, 22(7):1–5, 2015.
- [59] W. W. Stoffels, E. Stoffels, G. M.W. Kroesen, and F. J. De Hoog. Electron density fluctuations in a dusty Ar/SiH₄ rf discharge. *Journal of Applied Physics*, 78(8):4867–4872, 1995.
- [60] M. Bacal. Photodetachment diagnostic techniques for measuring negative ion densities and temperatures in plasmas. *Review of Scientific Instruments*, 71(11):3981–4006, 2000.
- [61] C. Küllig, K. Dittmann, and J. Meichsner. A novel approach for negative ion analysis using 160 GHz microwave interferometry and laser photodetachment in oxygen cc-rf plasmas. *Plasma Sources Science and Technology*, 19(6):065011, 2010.
- [62] Min Park, Byungkeun Na, Jong Gu Kwak, Tae Seong Kim, Bongki Jung, Sung Ryul Huh, and Seung Ho Jeong. Hydrogen negative ion density measurement by laser photodetachment and the effect of H recombination on the walls. *Physics of Plasmas*, 28(2):023505, 2021.

- [63] M. Ossiander, J. Riemensberger, S. Nepl, M. Mittermair, M. Schäffer, A. Duensing, M. S. Wagner, R. Heider, M. Wurzer, M. Gerl, M. Schnitzenbaumer, J. V. Barth, F. Libisch, C. Lemell, J. Burgdörfer, P. Feulner, and R. Kienberger. Absolute timing of the photoelectric effect. *Nature*, 561(7723):374–377, 2018.
- [64] D. H. Lee, D. J. Pegg, and D. Hanstrop. Photodetachment cross sections: Use of a saturation technique in laser-ion beam interactions. *AIP Conference Proceedings*, 475:189–192, 1999.
- [65] Philippe Babilotte and Mickael Vandevraye. Photodetachment cross-section evaluation using asymptotic considerations. *Journal of Theoretical and Applied Physics*, 11(2):87–95, 2017.
- [66] T. S. Basha and A. Abbas. Charging times for dust particles in plasma. *European Journal of Physics*, 10(2):151–156, 1989.
- [67] Chunshi Cui and J. Goree. Fluctuations of the Charge on a Dust Grain in a Plasma. *IEEE Transactions on Plasma Science*, 22(2):151–158, 1994.
- [68] Micheal A. Lieberman and Allan J. Lichtenberg. *Principles of Plasma Discharges and Materials Processing*. John Wiley & Sons Inc, 2005.
- [69] Xian Zhu Tang and Gian Luca Delzanno. Orbital-motion-limited theory of dust charging and plasma response. *Physics of Plasmas*, 21(12):1–7, 2015.
- [70] Craig F. Bohren and Donald R. Huffman. Optical Properties of Particles. In *Absorption and Scattering of Light by Small Particles*, chapter 11, pages 287–324. WILEY-VCH Verlag GmbH & Co. KGaA, Weinheim, 2004.
- [71] Gustav Mie. Beiträge zur Optik trüber Medien speziell kolloidaler Goldlösungen (contributions to the optics of diffuse media, especially colloid metal solutions). *Annalen der Physik*, 25:377–445, 1908.
- [72] Helmuth Horvath. Gustav Mie and the scattering and absorption of light by particles: Historic developments and basics. *Journal of Quantitative Spectroscopy and Radiative Transfer*, 110(11):787–799, 2009.
- [73] Christian Mätzler. MATLAB Functions for Mie Scattering and Absorption. *IAP Res Rep*, 2002-08(July 2002):1139–1151, 2002.
- [74] AB; Djuriši and EH Li. Optical properties of graphite. *Journal Of Applied Physics*, 85(10):7404–7410, 1999.
- [75] Georg Hass and Calvin D. Salzberg. Optical Properties of Silicon Monoxide in the Wavelength Region from 0.24 to 14.0 Microns. *Journal of the Optical Society of America*, 44(3):181–187, 1954.
- [76] Gorachand Ghosh. Dispersion-equation coefficients for the refractive index and birefringence of calcite and quartz crystals. *Optics Communications*, 163(1):95–102, 1999.

- [77] Luis V. Rodríguez-de Marcos, Juan I. Larruquert, José A. Méndez, and José A. Aznárez. Self-consistent optical constants of SiO₂ and Ta₂O₅ films. *Optical Materials Express*, 6(11):3622, 2016.
- [78] D.E. Aspnes and A.A. Studna. Dielectric functions and optical parameters of Si, Ge, GaP, GaAs, GaSb, InP, InAs, and InSb from 1.5 to 6.0 eV. *Physical Review B*, 27(2):985–1009, 1983.
- [79] Maren Dworschak, Oguz Han Asnaz, and Franko Greiner. A minimally invasive electrostatic particle extractor for nanodusty plasmas and its application for the verification of in situ Mie polarimetry. *Plasma Sources Science and Technology*, 30(3), 2021.
- [80] Shigeru Kimoto, William D. Dick, Ben Hunt, Wladyslaw W. Szymanski, Peter H. McMurry, Daryl L. Roberts, and David Y.H. Pui. Characterization of nanosized silica size standards. *Aerosol Science and Technology*, 51(8):936–945, 2017.
- [81] F. M.J.H. Van De Wetering, W. Oosterbeek, J. Beckers, S. Nijdam, E. Kovačević, and J. Berndt. Laser-induced incandescence applied to dusty plasmas. *Journal of Physics D: Applied Physics*, 49(29), 2016.
- [82] Jr. M.W. Chase. *NIST-JANAF Thermochemical Tables*. J. Phys. Chem. Ref. Data, Monograph 9, 4 edition, 1998.
- [83] A. T.D. Butland and R. J. Maddison. The specific heat of graphite: An evaluation of measurements. *Journal of Nuclear Materials*, 49(1):45–56, 1973.
- [84] Herbert B. Michaelson. The work function of the elements and its periodicity. *Journal of Applied Physics*, 48(11):4729–4733, 1977.
- [85] N. M. Ravindra, B. Sopori, O. H. Gokce, S. X. Cheng, A. Shenoy, L. Jin, S. Abedrabbo, W. Chen, and Y. Zhang. Emissivity measurements and modeling of silicon-related materials: An overview. *International Journal of Thermophysics*, 22(5):1593–1611, 2001.
- [86] G. H.P.M. Swinkels, H. Kersten, H. Deutsch, and G. M.W. Kroesen. Microcalorimetry of dust particles in a radio-frequency plasma. *Journal of Applied Physics*, 88(4):1747–1755, 2000.
- [87] H. R. Maurer and H. Kersten. On the heating of nano- and microparticles in process plasmas. *Journal of Physics D: Applied Physics*, 44(17), 2011.
- [88] M. Knudsen. Die molekulare Wärmeleitung der Gase und der Akkommodationskoeffizient. *Annalen der Physik*, 34(593), 1911.

Characterization of afterglow electron dynamics

Preface. Low-temperature gas discharges are driven by energetic electrons, the ensemble of which is often characterized by the density of free electrons and their mean energy. In this chapter, microwave cavity resonance spectroscopy (MCRS) is demonstrated as a measurement method for the electron density and the effective collision frequency—i.e. a measure for the mean electron energy—at atmospheric pressure. In the spatial afterglow using helium as a discharge gas, an electron density of $1.7 \pm 0.3 \times 10^{18} \text{ m}^{-3}$ and effective collision frequency of $0.12 \pm 0.01 \text{ THz}$ were found during times that the gas discharge was actively powered. The results demonstrate the ability of using MCRS to characterize the free electron cloud in the plasma jet’s afterglow. This provides a starting point for studying the effect of dust formation on the spatial afterglow, and the development of laser-induced photodetachment at atmospheric pressure as a means to detect negative ions in the spatial afterglow.

This chapter has been published: B. Platier, T.J.A. Staps, M. van der Schans, W.L. IJzerman, and J. Beckers, *Resonant microwaves probing the spatial afterglow of an RF plasma jet*, Applied Physics Letters 115 (25), 254103 (2019), DOI: <https://doi.org/10.1063/1.5127744>, and included as Chapter 7 in the PhD thesis of the first author of this publication.

7.1 Introduction

Radio-frequency (RF) driven atmospheric pressure plasma jets are extremely important tools for numerous industrial processes such as plasma-assisted cleaning and coating [1], deposition [2] and sterilization [3]. Furthermore, these sources show high potential in plasma medicine [4] with respect to wound healing [5] and cancer treatment [6]. The combination of low gas temperatures, high concentrations of reactive species and no need for expensive vacuum systems is a major advantage of RF jets over conventional plasma sources [7].

The electron density n_e is one of the most important plasma parameters and accurately diagnosing the electron dynamics is key to further develop and optimize the aforementioned applications. Up to now, several electron diagnostics have been used in experiments. For instance, the broadening of spectral emission lines can be used to determine n_e [8]. Application of this principle, however, is restricted to only those regions where plasma emission is of sufficient intensity. Another strong diagnostic, Thomson scattering—based on the scattering of laser light by free electrons—has been applied to measure the electron density in atmospheric pressure radio-frequency and microwave driven plasmas [9, 10, 11]. Although the temporal and spatial resolutions are high, the lower detection limit of it is around $1 \times 10^{18} \text{ m}^{-3}$ [9]. In most applications of RF plasma jets, the interaction of the plasma with the treated target takes place downstream from the position where the plasma is generated. Especially from this so-called spatial plasma afterglow region, light emission is too faint to retrieve information about the free electrons from optical emission spectroscopy measurements. At the same time, electron densities in this spatial afterglow region are expected at or below the detection limit of Thomson scattering.

This chapter introduces the application of microwave cavity resonance spectroscopy (MCRS) to monitor in-situ the electron dynamics temporally resolved with $\sim 1 \mu\text{s}$ time resolution in this highly interesting afterglow region. Since the development of MCRS in the 1940s [12], it has been used to study various types of low pressure plasmas; pristine RF driven plasmas [13, 14], etching plasmas [15], powder-forming plasmas [16, 17, 18], and extreme ultraviolet photon-induced plasmas [19, 20]. In all these works, the plasma-induced change in resonant behaviour of a standing wave in a cavity—a void enclosed by conductive walls—due to a change in permittivity of the medium inside the cavity is used to determine plasma parameters. Only recently, Van der Schans *et al* [21] extended the operational range of MCRS by demonstrating that MCRS can be used on atmospheric pressure plasmas as well to determine the electron density and effective electron collision frequency between successive discharges in a high-voltage pulsed plasma jet in N_2 feed gas. Moreover, the resolution of the diagnostic has been improved in recent publications [20, 21].

In this chapter, MCRS is applied to an RF-driven plasma jet, and more specifically to the spatial afterglow of such a jet. The spatial afterglow region where electrons have thermalized to values close to room temperature due to multiple collisions with the background gas is investigated to demonstrate the renewed capabilities—in resolution and operating range—of the diagnostic method. In contrast to earlier work, where

only the decay of the plasma could be investigated [21], the formation, the steady state and the decay phases are studied in the presented experiments. Furthermore, the method is enhanced by compensation for thermal expansion of the cavity while the resolution in the real part of the permittivity is increased by one order of magnitude.

7.2 Experiment

The main components of the experimental setup were the plasma source and the microwave cavity including the control and read-out electronics. A schematic overview of the experimental setup is shown in Fig. 7.1, while a more detailed view of the discharge geometry can be found in Fig. 7.2. A detailed description of the complete experimental setup can be found in Chapter 3.

The atmospheric pressure discharges were generated with an excitation frequency of 13.56 MHz in He working gas (purity of 99.999 %) flowing at a volumetric rate of 1000 sccm into surrounding air. A function generator, an RF amplifier and a tunable coil for impedance matching were used to generate the plasma. The function generator was amplitude modulated by a second function generator which was gated by a pulse/delay generator in order to generate pulsed plasma discharges with a temporal width of 50 μs at a repetition rate f_{rep} set between 125 to 8000 Hz. With these settings, the duty cycle was varied from 40 % to 0.625 %. The RF voltage was applied to an electrode that had a radius of 0.5 mm and a tip angle of approximately 40°. This needle electrode was placed concentrically inside a quartz tube of inner radius 1 mm and outer radius 2 mm, with the end of the pin located 3.5 mm before the end of the quartz tube. The cylindrical shell shaped grounded electrode was placed around and in contact with the dielectric. The parasitic capacitance of the plasma source was predefined by shielding the electrodes. For the electrical characterization of the plasma, i.e. measurement of the driving voltage, current and power, a multiplying probe—which was insensitive to changes in the load impedance—as described in [22] was further developed and incorporated in the plasma source. The temporal resolution of the power was limited by an electronic filter to 30 μs . An oscilloscope was used to monitor the outputs of the probe. This probe was used to investigate the influence of the cavity on the plasma. No change in the load impedance was observed which strongly suggested that the discharge was unaffected by the presence of the cavity.

As the MCRS diagnostic and method are already described in several other works [21, 20], describing only the key features suffices here. The resonant behaviour of a standing wave in a cavity is described by the spectral position of the resonance peak f_{res} and the full-width-at-half-maximum (FWHM) of the peak Γ_{res} which is indicated by the quality factor Q_{res} given by $Q_{\text{res}} = f_{\text{res}}/\Gamma_{\text{res}}$.

Assuming a uniform plasma volume and following the approach of Van der Schans *et al* [21], the change in relative resonance frequency $\Delta f/f_1$ and reciprocal quality factor $\Delta(1/Q)$ are the parameters to be measured and used to determine the effective collision frequency ν_{eff} ,

$$\nu_{\text{eff}} = \pi f_1 \frac{\Delta(1/Q)}{\Delta f/f_1}, \quad (7.1)$$

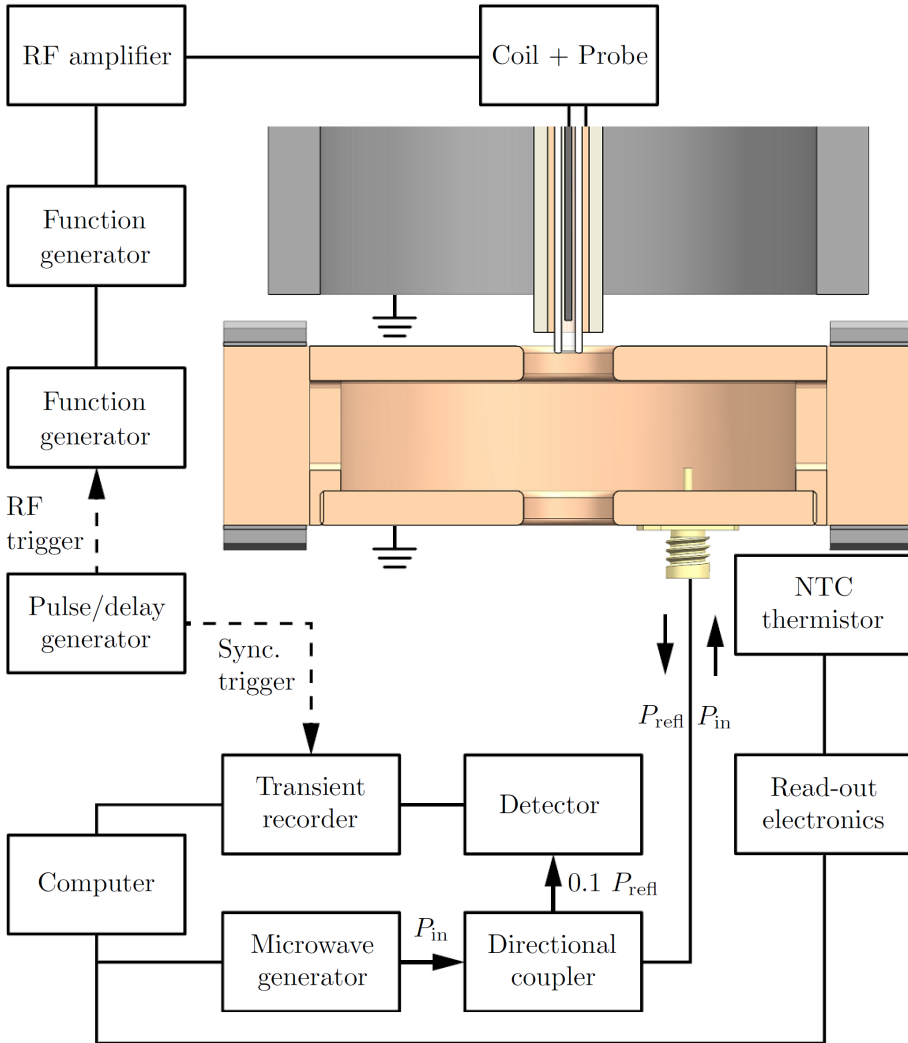


Figure 7.1: A schematic overview of the experimental setup consisting of the plasma source and cavity including the control and read-out electronics.

and the electron density n_e ,

$$n_e = 2 \frac{\varepsilon_0 m_e \nu_{\text{eff}}^2 + 4\pi^2 f_p^2}{e^2 \mathcal{V}} \frac{\Delta f}{f_1}, \quad (7.2)$$

where ε_0 is the vacuum permittivity, m_e the mass of an electron, e the elementary charge and f_1 the resonance frequency of the empty cavity. \mathcal{V} is the ratio of the effective (microwave-field-squared-weighted) plasma volume and the effective (microwave-field-squared-weighted) cavity volume given by:

$$\mathcal{V} = \frac{\iiint_{V_p} |\mathbf{E}_1|^2 d^3\mathbf{r}}{\iiint_{V_c} |\mathbf{E}_1|^2 d^3\mathbf{r}}, \quad (7.3)$$

where V_c and V_p are the occupied volume of the cavity and plasma, respectively.

A cylindrical copper microwave cavity with an inner radius of 33 mm, a height of 16 mm and a resonance frequency f_{res} of 3.5 GHz for the TM_{010} mode was used. This mode had a quality factor of $Q_{\text{res}} = 4 \times 10^3$ and therefore provided a temporal resolution of $\sim 1 \mu\text{s}$. The parts of the cavity were vacuum soldered together, resulting in a very high mechanical stability which translated in excellent reproducibility compared to the aforementioned works. Concentric holes of 13 mm in diameter in the top and bottom flat walls allowed the gas flow and discharge to enter and exit the cavity. Note that at the position, i.e. the cavity axis, where the plasma afterglow entered the cavity volume, the electric field of the mode was highest, resulting in the highest MCRS signal per free electron. The quartz tube of the plasma source protruded the top hole by 1 mm which had no significant influence on the resonant behaviour of the cavity as a whole.

A microwave signal with frequency $f = \omega/2\pi$ and power P_{in} (1 mW) was generated by a microwave generator. These microwaves travelled through a directional coupler and were applied to a straight antenna that protruded a few mm into the cavity. Reflected microwaves returned to the directional coupler where 10% of the power was directed to a logarithmic power detector. The reflected power P_{ref} depended on the applied frequency as the cavity was only able to absorb power when the applied frequency matched a resonance frequency. The temporal response of the power detector was sampled at 10 MHz using a transient recorder which was triggered by the same pulse/delay generator to synchronize the measurements with the discharges. Allowed by the extremely high reproducibility of the discharge dynamics, multiple discharges were used to create a spectral response for each time step and to reduce noise by averaging. Computer code was used to set the applied frequency and save the data of the transient recorder. In this experiment, 256 discharges were used to determine the temporal response of the cavity at each frequency. Frequencies ranging from 3.509 GHz to 3.516 GHz with intervals of 5 kHz were probed.

For each set of discharges with the same f , the temperature of the cavity T_c was logged with sub-mK resolution by an NTC thermistor in combination with in-house developed read-out electronics. This high resolution was needed to compensate for the apparent frequency shift due to thermal expansion of the cavity caused by fluctuations in the lab temperature of ~ 1 K.

In contrast to most MCRS measurements on low pressure plasmas, in the experiment presented here the plasma only filled a fraction of the cavity and therefore $\mathcal{V} \ll \text{unity}$. In order to determine the effective plasma volume ratio, the resonant field profile and the plasma volume were required. The electric field profile of the TM_{010} mode for the empty cavity $|\mathbf{E}_1|$ was calculated with the frequency domain electromagnetic wave toolbox in COMSOL [23] and is presented in Fig. 7.2. V_p was determined by imaging the light-emitting volume with a camera with a macro zoom lens. From the simulated electric field profile and the camera images, it was estimated that $\mathcal{V} \approx 1.7 \times 10^{-6}$. The level of accuracy of this estimation is the order of its magnitude, which in its turn limits the accuracy of the electron densities presented below.

The camera images show that the light-emitting volume of the plasma extends to 2mm outside the quartz tube. At atmospheric pressure, the energy relaxation length [24] is $< 50 \mu\text{m}$ for electrons with $\leq 10 \text{ eV}$ kinetic energy to cool down to room temperature. As the probed region here is relatively far away from the RF electrode and partially outside the glass tube, the electrons are expected to be near room temperature and gas mixing, i.e. mixing with surrounding air, is likely to occur.

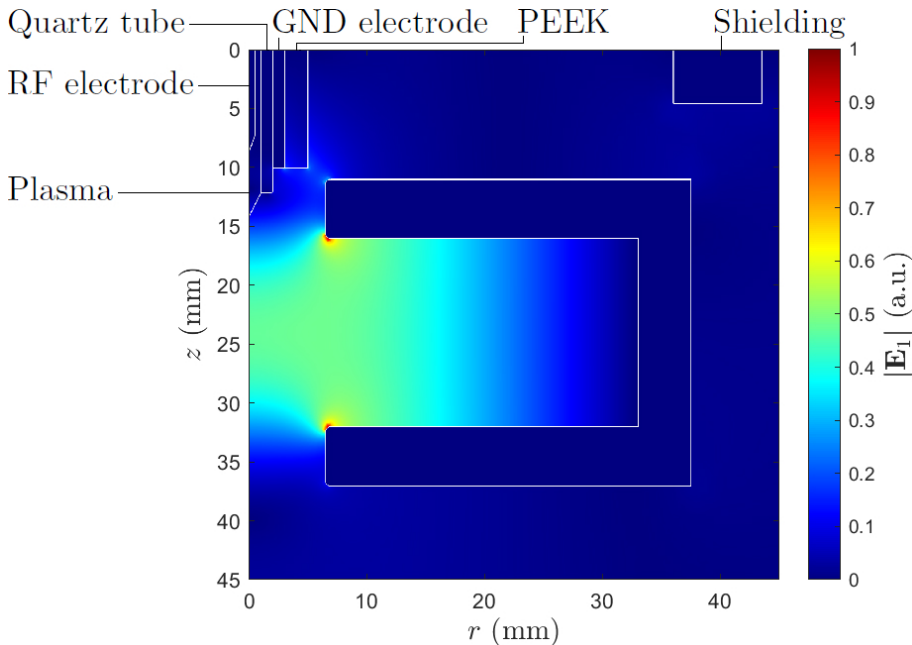


Figure 7.2: A schematic of the plasma source geometry and the resonance cavity with the electric field magnitude of the TM_{010} mode.

7.3 Results and discussion

For the repetition rates 125, 500, 2000 and 8000 Hz, $\Delta f/f_1$ and $\Delta(1/Q)$, and derived values for n_e and ν_{eff} , are shown as a function of time in Fig. 7.3a-d. In this time frame, the plasma was ignited at $t = 50 \mu\text{s}$ and the RF power was provided for a duration of $50 \mu\text{s}$. Four consecutive plasma dynamical phases can be identified which are indicated in the figures by Roman numerals and will be described individually hereafter.

Phase I is used to determine f_1 and Q_1 for the 'empty' cavity. Fig. 7.3a-b show clearly that the response for $f_{\text{rep}} = 8000 \text{ Hz}$ was still converging during these $10 \mu\text{s}$ before ignition of the next plasma event. This leads to an error in the results for this repetition rate. From the response of the other repetition rates, it can be seen that the noise level in the resonance frequency is decreased by one order of magnitude with respect to Van der Schans *et al* [21] to a standard deviation $1-\sigma < 25 \text{ Hz}$. In *phase II*, the plasma is formed and an increase in electron density and the effective collision frequency is observed over roughly $20 \mu\text{s}$.

In *phase III*, the plasma power measured by the multiplying probe converges at $20.0 \pm 0.2 \text{ W}$. Nevertheless, it can be assumed that this is the power during the whole phase as steady state is reached. The standard deviations of the plasma parameters within one f_{rep} are smaller than 3%. For all f_{rep} combined, the found n_e and ν_{eff} are $1.7 \pm 0.3 \times 10^{18} \text{ m}^{-3}$ and $0.12 \pm 0.01 \text{ THz}$, respectively. Following the approach of [25], near the electrode n_e is estimated as $5 \times 10^{18} \text{ m}^{-3}$ and the typical length over which electrons can diffuse $\sim 1 \text{ mm}$. As this length is comparable with the size of the plasma, the estimation of n_e is also valid for the probed region for which very similar densities were found experimentally. ν_{eff} , unlike n_e , is unaffected by the systematic error arising from the effective volume. The value of ν_{eff} is close to the 0.15 THz which was calculated from the effective electron-neutral collision cross sections [26] for atmospheric pressure He and electrons at room temperature. The small difference in the experimental and theoretical value can be attributed to in-mixing, as similar calculations provided ν_{eff} for N_2 and O_2 of 0.08 and 0.03 THz , respectively. This approach might be an elegant way to measure the composition of the background gas in future experiments.

In *phase IV*, after turning off the RF power, n_e and ν_{eff} decrease as can be seen in Fig. 7.3e. Approximately 200 ns later, a brief increase in the electron density is observed. As described earlier in literature [27], this effect can most likely be attributed to Penning ionization. Δn_e , i.e. the difference between the n_e at the end of the previous phase ($t = 100 \mu\text{s}$) and the maximum in phase IV, is indicated in Fig. 7.3f for several values of f_{rep} . The error in Δn_e is dominated by a term which relates to the fact that the cavity was not fast enough to follow the changes in the plasma at this moment in the evolution. A trend in the number of additionally created electrons is observed: Δn_e increases while decreasing the time between the RF pulses. This can be attributed to, e.g., the less decay of remnant species of previous discharges or a change in reaction rates due to gas heating.

After this brief increase in n_e , the decay of the electron density and of the effective collision frequency continues. At $t = 175 \mu\text{s}$, the start of the successive discharge for a repetition rate of 8000 Hz can be seen in Fig. 7.3a-d.

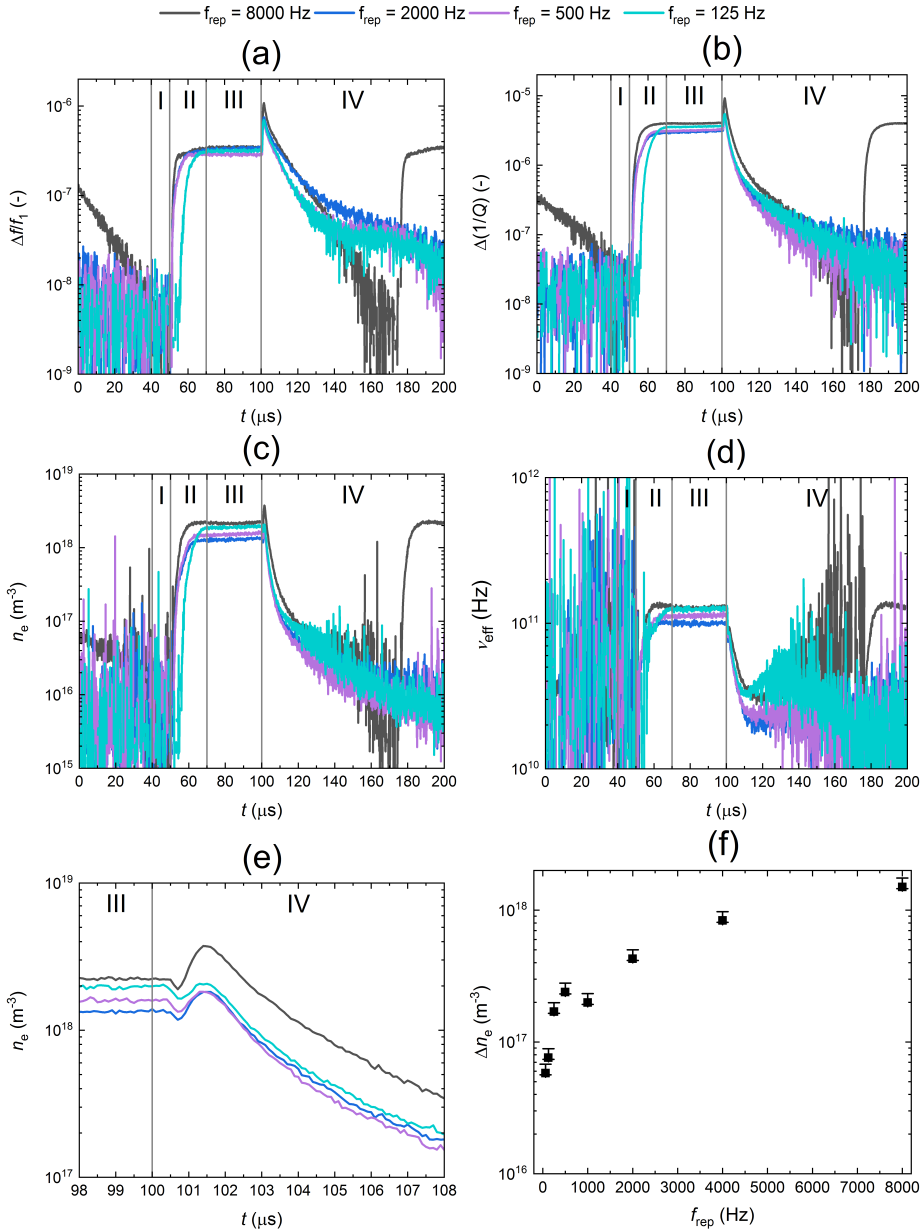


Figure 7.3: Temporal evolution of (a) the relative frequency shift, (b) the change of the reciprocal quality factor, (c) the electron density, (d) the effective electron collision frequency—for different plasma repetition frequencies—and (e) the electron density around the moment of turning off the RF power. The difference in electron density between $t = 100 \mu\text{s}$ and in the peak ($t \approx 101.4 \mu\text{s}$) as a function of the repetition frequency is shown in (f). The Roman numerals indicate the four phases in the experiment.

The obtained temporal evolution from $t \approx 120 \mu\text{s}$ onwards would have been below the noise level without the advancements in the integrated design of the plasma jet and microwave cavity (see Chapter 3 for a detailed description of the design). The improved mechanical stability and higher Q_{res} of the cavity, and the increased number of responses used in the analysis resulted in an $1\text{-}\sigma$ in the real part of the relative permittivity of 1×10^{-8} . The lowest value of the electron density which can be detected depends on ν_{eff} and \mathcal{V} . If the collisions can be neglected and the plasma fills the whole cavity, the lower detection limit is $\sim 2 \times 10^9 \text{ m}^{-3}$. For $\nu_{\text{eff}} = 1 \text{ THz}$ and $f_{\text{res}} = 3.5 \text{ GHz}$, this limit is $\sim 4 \times 10^{12} \text{ m}^{-3}$ when the whole cavity is filled and $\sim 2 \times 10^{18} \text{ m}^{-3}$ for $\mathcal{V} = 1.7 \times 10^{-6}$. During phase III the resolution in n_e is $\sim 3 \times 10^{16} \text{ m}^{-3}$, which is 2% of the measured value. When the changes in resonant behaviour are very small with respect to the empty cavity, the properties of the electrons can no longer be assumed to be the only contributors to changes in permittivity. This opens up a playground for exploring other (plasma-induced) phenomena affecting the permittivity.

7.4 Conclusion

Microwave cavity resonance spectroscopy is capable of resolving the electron dynamics during all phases of the evolution of the spatial afterglow of a pulsed radio-frequency driven atmospheric pressure plasma jet. Furthermore, no changes in the electrical characteristics of the plasma due to the presence of the cavity were observed which strongly suggested that the cavity did not affect the discharge. This result provides a starting point for the experiments presented in Chapter 8 and 9. In these experiments, the effect of dust formation and negative ions is studied in the spatial afterglow in a controlled atmosphere using the same experimental setup.

7.5 Bibliography

- [1] R. Foest, E. Kindel, H. Lange, A. Ohl, M. Stieber, and K. D. Weltmann. RF capillary jet - A tool for localized surface treatment. *Contributions to Plasma Physics*, 47(1-2):119–128, 2007.
- [2] Oleksiy V. Penkov, Mahdi Khadem, Won Suk Lim, and Dae Eun Kim. A review of recent applications of atmospheric pressure plasma jets for materials processing. *Journal of Coatings Technology and Research*, 12(2):225–235, 2015.
- [3] R. Brandenburg, J. Ehlbeck, M. Stieber, T. V. Woedtke, J. Zeymer, O. Schlüter, and K. D. Weltmann. Antimicrobial treatment of heat sensitive materials by means of atmospheric pressure Rf-driven plasma jet. *Contributions to Plasma Physics*, 47(1-2):72–79, 2007.
- [4] M. G. Kong, G. Kroesen, G. Morfill, T. Nosenko, T. Shimizu, J. Van Dijk, and J. L. Zimmermann. Plasma medicine: An introductory review. *New Journal of Physics*, 11, 2009.
- [5] J Winter, R Brandenburg, and K-D Weltmann. Atmospheric pressure plasma jets: an overview of devices and new directions. *Plasma Sources Science and Technology*, 24(6):064001, 2015.
- [6] Michael Keidar, Dayun Yan, Isak I. Beilis, Barry Trink, and Jonathan H. Sherman. Plasmas for Treating Cancer: Opportunities for Adaptive and Self-Adaptive Approaches. *Trends in Biotechnology*, 36(6):586–593, 2018.
- [7] Andreas Schütze, James Y. Jeong, Steven E. Babayan, Jaeyoung Park, Gary S. Selwyn, and Robert F. Hicks. The atmospheric-pressure plasma jet: A review and comparison to other plasma sources. *IEEE Transactions on Plasma Science*, 26(6):1685–1694, 1998.
- [8] A. Yu Nikiforov, Ch Leys, M. A. Gonzalez, and J. L. Walsh. Electron density measurement in atmospheric pressure plasma jets: Stark broadening of hydrogenated and non-hydrogenated lines. *Plasma Sources Science and Technology*, 24(3), 2015.
- [9] A. F H Van Gessel, E. A D Carbone, P. J. Bruggeman, and J. J A M Van Der Mullen. Laser scattering on an atmospheric pressure plasma jet: Disentangling Rayleigh, Raman and Thomson scattering. *Plasma Sources Science and Technology*, 21(1), 2012.
- [10] Bram Van Gessel, Ronny Brandenburg, and Peter Bruggeman. Electron properties and air mixing in radio frequency driven argon plasma jets at atmospheric pressure. *Applied Physics Letters*, 103(6):1–5, 2013.
- [11] Simon Hübner, Joao Santos Sousa, Joost Van Der Mullen, and William G. Graham. Thomson scattering on non-thermal atmospheric pressure plasma jets. *Plasma Sources Science and Technology*, 24(5), 2015.

-
- [12] Manfred A. Biondi and Sanborn C. Brown. Measurements of ambipolar diffusion in helium. *Physical Review*, 75(11), 1949.
- [13] James Franek, Samuel Nogami, Mark Koepke, Vladimir Demidov, and Edward Barnat. A Computationally Assisted Ar I Emission Line Ratio Technique to Infer Electron Energy Distribution and Determine Other Plasma Parameters in Pulsed Low-Temperature Plasma. *Plasma*, 2(1):65–76, 2019.
- [14] Jan Faltýnek, Vít Kudrle, Jakub Tesař, Martina Volfová, and Antonín Tálský. Numerical enhancements of the microwave resonant cavity method for plasma diagnostics. *Plasma Sources Science and Technology*, 2019.
- [15] E. Stoffels, W. W. Stoffels, D. Vender, M. Kando, G. M.W. Kroesen, and F. J. De Hoog. Negative ions in a radio-frequency oxygen plasma. *Physical Review E*, 51(3):2425–2435, 1995.
- [16] J. Beckers, W. W. Stoffels, and G. M W Kroesen. Temperature dependence of nucleation and growth of nanoparticles in low pressure Ar/CH₄ RF discharges. *Journal of Physics D: Applied Physics*, 42(15), 2009.
- [17] G. Wattieaux, N. Carrasco, M. Henault, L. Boufendi, and G. Cernogora. Transient phenomena during dust formation in a N₂-CH₄capacitively coupled plasma. *Plasma Sources Science and Technology*, 24(1), 2015.
- [18] G. Alcouffe, M. Cavarroc, G. Cernogora, F. Ouni, A. Jolly, L. Boufendi, and C. Szopa. Capacitively coupled plasma used to simulate Titan’s atmospheric chemistry. *Plasma Sources Science and Technology*, 19(1), 2010.
- [19] R. M. Van Der Horst, J. Beckers, S. Nijdam, and G. M W Kroesen. Exploring the temporally resolved electron density evolution in extreme ultra-violet induced plasmas. *Journal of Physics D: Applied Physics*, 47(30):7–11, 2014.
- [20] J. Beckers, F. M.J.H. Van De Wetering, B. Platier, M. A.W. Van Ninhuijs, G. J.H. Brussaard, V. Y. Banine, and O. J. Luiten. Mapping electron dynamics in highly transient EUV photon-induced plasmas: A novel diagnostic approach using multi-mode microwave cavity resonance spectroscopy. *Journal of Physics D: Applied Physics*, 52(3), 2019.
- [21] Marc van der Schans, Bart Platier, Peter Koelman, Ferdi van de Wetering, Jan Van Dijk, Job Beckers, Sander Nijdam, and Wilbert IJzerman. Decay of the electron density and the electron collision frequency between successive discharges of a pulsed plasma jet in N₂. *Plasma Sources Science and Technology*, 28(3):1–13, 2019.
- [22] P. A.C. Beijer, A. Sobota, E. M. Van Veldhuizen, and G. M.W. Kroesen. Multiplying probe for accurate power measurements on an RF driven atmospheric pressure plasma jet applied to the COST reference microplasma jet. *Journal of Physics D: Applied Physics*, 49(10), 2016.

- [23] COMSOL. Modeling Software for RF, Microwave, and Millimeter-Wave Designs, <https://www.comsol.com/rf-module>, accessed on August 26 2019.
- [24] M. S. Benilov. Can the temperature of electrons in a high-pressure plasma be determined by means of an electrostatic probe? *Journal of Physics D: Applied Physics*, 33(14):1683–1696, 2000.
- [25] S. Hofmann, A. F.H. Van Gessel, T. Verreycken, and P. Bruggeman. Power dissipation, gas temperatures and electron densities of cold atmospheric pressure helium and argon RF plasma jets. *Plasma Sources Science and Technology*, 20(6), 2011.
- [26] Phelps database, www.lxcat.net, accessed on August 5 2019.
- [27] R. Deloche, P. Monchicourt, M. Cheret, and F. Lambert. High-pressure helium afterglow at room temperature. *Physical Review A*, 13(3):1140, 1976.

Effect of dust formation on the spatial afterglow of an atmospheric pressure plasma jet

Preface. The formation of dust grains by an atmospheric pressure gas discharge is studied in this chapter using microwave cavity resonance spectroscopy (MCRS). Pulsed discharges are produced in a dust-forming helium-hexamethyldisiloxane (HMDSO) gas mixture, and compared to pristine helium discharges. The temporal dynamics of the electron density and effective collision frequency lead to the observation of several differences caused by the addition of HMDSO. The main results are that the formation of dust grains does not seem to affect the electron density drastically, in contrast to what has been observed in low pressure dust-forming discharges, and that the decay time of the electron density is of the order of the neutralization time of the dust grain charge.

8.1 Introduction

Atmospheric pressure plasmas have emerged in the field of plasma-based material processing due to their advantages over conventional methods [1, 2, 3]. The widespread use of nanoparticles and -crystals has driven the development of plasma-based synthesis of such nanoparticles [4, 5, 6, 7, 8, 9, 10], which provides more degrees-of-freedom and precise control over, for example, the material, the crystallinity, and the size (distribution) [9]. On the other hand, the deposition of thin films using atmospheric pressure plasma sources for various purposes [11, 12, 13, 14] provides an interesting alternative to the well-established industrial processes using low-temperature plasmas under vacuum conditions, where nanoparticles are intended as inclusions in the film but can be also undesired due to electrode contamination [15]. In plasma-based material processing, the growth process of dust grains—which concerns the conversion

of molecular species into grains in the nano- to micrometer size range—represents a fundamental mechanism for the performance of plasma sources during the synthesis of nanoparticles and the deposition of thin films.

The impact of the formation and charging of dust grains on low pressure plasma parameters has promoted the application of a wide variety of diagnostics instruments [16]. As such, the techniques used for determining the electron density [17, 18], negative ion concentration [19, 20, 21], dust charge [22, 23, 24], and dust size [25, 26] facilitated the detailed study of the dust formation process under low pressure conditions for several decades [27, 28, 29]. These efforts have resulted in the well-established theoretical three-step growth model for dust grains describing the nucleation, the coagulation, and the accretion phase [30, 31].

Due to the flow-through character of atmospheric pressure plasma reactors, the spatial afterglow of atmospheric pressure dust-forming plasmas forms a crucial extension of the bulk growth region with important consequences for the dust grain formation and deposition [32, 33]. While dust grains are negatively charged in the bulk, the rapid loss of electrons may lead to the discharging, neutralization, and charge reversal (to positive charge) of nanoparticles passing an ion-rich spatial afterglow [34, 35, 36, 37, 38]. The neutralization and positive charging of dust grains in the afterglow has been observed also under low pressure conditions [39]. An important consequence is that aggregation of the formed nanoparticles can be promoted due to discharging and charge reversal [37, 40, 41]. Therefore, the dust charge governed by the electron and ion fluxes towards the dust grains is crucial to the overall formation and deposition processes, especially in the afterglow region.

The decay of the electron and ion densities constitutes the major processes dictating the charge distribution in the bulk plasma, and the spatial afterglow. These decay processes can be affected, for example, by the application of a bias voltage which enhances the ion losses to the walls and limits neutralization of the dust charge [42, 43]. Regardless of biasing, the plasma chemical and physical processes in the afterglow are important for the prediction of the charge distribution and growth process using numerical models [34, 36]. The electron density in such numerical models is often derived from the quasi-neutrality requirement or experimental methods such as Stark broadening or electrical characterization [44, 36, 45, 34]. However, the quasi-neutrality condition and such experimental methods are not applicable in the spatial afterglow where the electron density decays rapidly, and quasi-neutrality is lost.

In this chapter, we demonstrate the feasibility of time-resolved measurements of the electron density and effective collision frequency in the spatial afterglow region of a dust-forming atmospheric pressure plasma reactor. The atmospheric pressure plasma reactor used was a radio-frequency (RF) driven gas discharge which was fed with a mixture of helium and hexamethyldisiloxane (HMDSO) to promote the formation of dust grains. The spatial afterglow of the RF discharge was probed using microwave cavity resonance spectroscopy (MCRS), where the dust-forming discharge was created in a mixture of helium and hexamethyldisiloxane (HMDSO) and a pristine discharge was generated in helium only for comparison. Using repetitive pulsed discharges for an RF pulse duration T between 0.050 ms and 2.000 ms, the electron density and effective collision frequency was measured with 4 ns time resolution during the formation, the

steady state, and the decay of the spatial plasma afterglow. The formation of dust grains was verified using laser light scattering. This provided evidence for the formation of dust grains, and an approximate set of conditions for which dust formation occurred, of which the results can be found in Section 8.6.

This chapter is organized as follows. Section 8.2 explains the experimental setup in detail as it was used for imaging the dust cloud in the spatial afterglow, as well as for the microwave system used for MCRS measurements of the electron dynamics. Section 8.3 treats the MCRS experiments performed on the dust-forming discharge afterglow produced by short RF pulses in detail. After the results, a timescale analysis is presented in Section 8.4 by studying the loss of electrons compared to that of the ions, and neutralization of dust grains. Afterwards, the findings are discussed in view of the numerical models and predictions concerning the electron density in the literature. Section 8.5 concludes this chapter with a brief summary of the key findings and an outlook for further research. Section 8.6 presents an appendix with specific experimental details and calculations.

8.2 Experiment

An atmospheric pressure plasma reactor was used for the growth of dust grains in the nanometer-size range (typically $\sim 1 - 100$ nm), of which the main components are shown in Fig. 8.1. The plasma reactor was based on a cylindrically symmetric capacitively-coupled discharge geometry with a dielectric barrier between the powered and grounded electrodes, which was used in Chapter 7 and by Platier *et al* [46, 47]. The experimental setup is described in detail in Chapter 3. The plasma species created by the discharge entered periodically into the microwave cavity, which allowed to determine the temporal evolution of the spatial plasma afterglow using microwave cavity resonance spectroscopy (MCRS). The whole plasma jet geometry and microwave cavity were integrated in a vacuum vessel in order to control the type and impurity level of the background gas reacting with the discharge in the spatial afterglow.

The presence of dust grains was observed by capturing laser light (continuous Nd:YAG laser, wavelength $\lambda = 532$ nm) scattered by the dust grains under an angle of 90° using a high-speed camera (Photron Mini UX100, 125 fps). In this case, the microwave cavity was removed and a substrate was present for the collection of dust grains, and subsequent ex-situ analysis. The results of this verification study can be found in Section 8.6.

Two types of experiments were performed to study the effect of dust formation on the plasma characteristics. First, the discharge was fed with a mixture of helium at a flow rate of 1000 sccm and hexamethyldisiloxane (HMDSO) at a flow rate of 100 sccm to promote the formation of nanosized dust grains. Second, the discharge was fed with pristine helium at a flow rate of 1000 sccm. In both cases, the discharge gas was fed to the electrode gap via the gas mixing inlet at the top, as can be seen from Fig. 8.1. The impurity level was controlled by the pre-experiment vacuum pressure ($p_{\text{vessel}} \sim 0.1$ mbar) after which the vessel was filled with pristine helium up to atmospheric pressure ($p_{\text{vessel}} \approx 1020$ mbar). The combined (continuous) flow of helium in the background, the plasma species and discharge gas left the vessel through

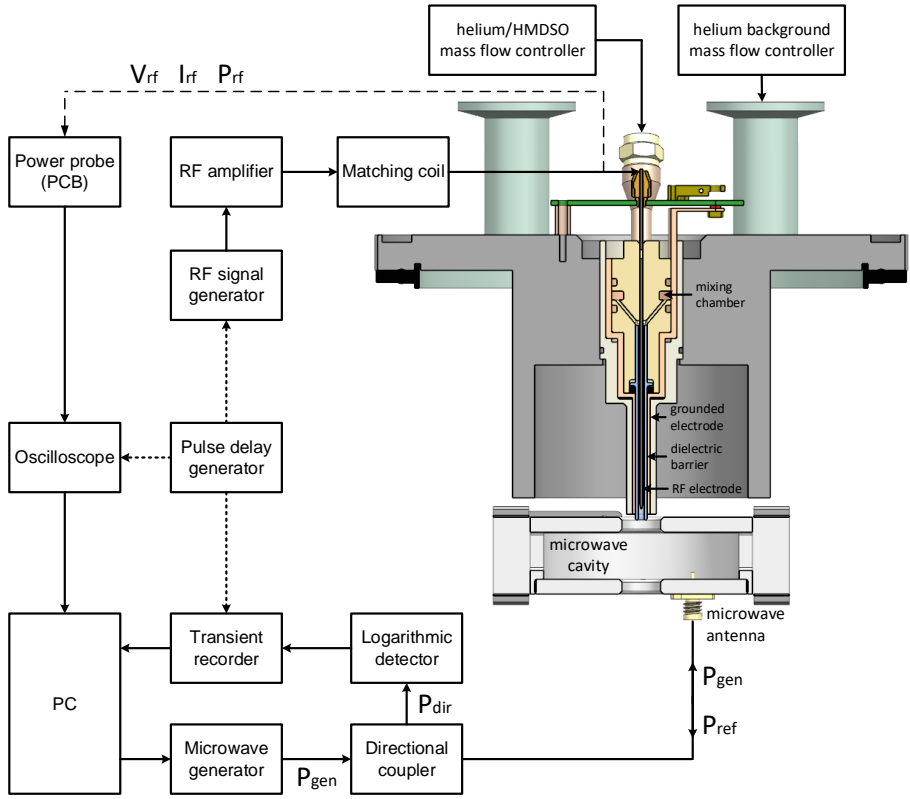


Figure 8.1: Experimental setup for the measurement of the electron density and effective collision frequency in the spatial afterglow of a dust-forming atmospheric pressure discharge by microwave cavity resonance spectroscopy (MCRS). The integrated design of the plasma reactor and microwave cavity are depicted in the form of a cross sectional view. The plasma reactor, from top to bottom, comprises a gas inlet on top for the injection of the helium-hexamethyldisiloxane mixture into the discharge gap. The discharge gap constitutes a tungsten electrode, surrounded by a dielectric barrier, and a grounded electrode, which formed the capacitively-coupled discharge geometry. The microwave cavity was mounted below the plasma reactor exit. The microwave system was used to perform MCRS, including a microwave generator, directional coupler, logarithmic detector, and transient recorder. The cavity response was acquired and stored digitally using a computer (PC). Pulsed discharges were created using the RF power supply system, of which the RF signal generator was triggered simultaneously with the transient recorder and oscilloscope in order to synchronize the measurements with the plasma pulses.

the main exhaust of the laboratory.

Pulsed discharges were created in the annular gap between the RF and grounded electrode. The RF powered electrode had the form of a solid tungsten cylinder with an outer diameter of 1 mm and with a sharp tip at the bottom end that lowered the ignition voltage. The grounded electrode was formed by a hollow copper cylinder with an inner diameter of 4 mm that was covered, on the inside, by a quartz tube with an inner diameter of 2 mm serving as dielectric barrier. A radio-frequency (RF) voltage was generated using an RF signal generator, with fixed frequency 13.56 MHz, and amplified by an RF amplifier, as indicated in Fig. 8.1. The capacitance of the discharge gap in combination with the inductance of the matching coil resulted in an amplification to $V_{\text{rms}} \approx 700$ V and an absorbed RF power of $P_{\text{RF}} \approx 26$ W for the helium-HMDSO experiments and $P_{\text{RF}} \approx 22$ W for the pristine helium experiments. The RF voltage, RF current and absorbed RF power were monitored using the power probe described by Beijer *et al* [48]. A pulse delay generator (PDG) was used to modulate the RF signal generator at a frequency of 30 Hz for varying pulse duration between 50–2000 μs . This allowed the formation of a pulsed dielectric barrier discharge along the gap with a length of about 70 mm, of which part of the plasma species entrained into the spatial afterglow region when leaving the discharge gap.

Microwave cavity resonance spectroscopy (MCRS) was used as the diagnostic for determining the electron density and effective collision frequency in a time-resolved fashion. The time-resolved measurement scheme of the microwave technique has been applied previously, in numerous studies conducted by researchers in the Eindhoven group, to pristine discharges at atmospheric pressure [46, 49, 50], (dust-forming) discharges at low pressure [19, 18, 51, 20, 52, 53], extreme ultraviolet induced discharges [54, 49, 55], and ultra-cold plasmas [56, 57].

A microwave cavity was mounted downstream of the discharge gap in a concentric fashion so that the radial center of the cavity coincided with the radial center of the cylindrically symmetric discharge gap. The microwave cavity had an interior diameter 66 mm and an interior height 16 mm, and two holes with diameter 13 mm also coinciding radially with the center of cavity and discharge gap. Microwaves were injected by the microwave generator (see Fig. 8.1) continuously, at a frequency f and with a power $P_{\text{gen}} = 4$ mW, through the directional coupler and via the antenna into the cavity. The resonance frequency of the cavity corresponded to one of the resonant eigenmodes (i.e. TM_{010} in this chapter), of which the electric field was calculated using COMSOL Multiphysics[®] as shown in Section 8.6. The quality factor Q_{res} was the second parameter characterizing the resonant mode, which related to the full-width-at-half-maximum (FWHM or Γ_{res}) of the resonance peak. When f was close to f_{res} , the microwaves were efficiently absorbed by the cavity, and the amount of reflection back into the transmission line was minimal. Overall, the resonant behavior of the microwave cavity was determined by measuring the reflected power P_{ref} as a function of f in a close range below and above the resonance frequency. As can be seen from Fig. 8.2, this resulted in a typical Lorentzian-type of absorption curve with a minimum at f_{res} and a FWHM providing Q_{res} .

By application of RF power pulses to the discharge gap, a plasma was produced inside the discharge gap of which part of the plasma species entered the cavity volume.

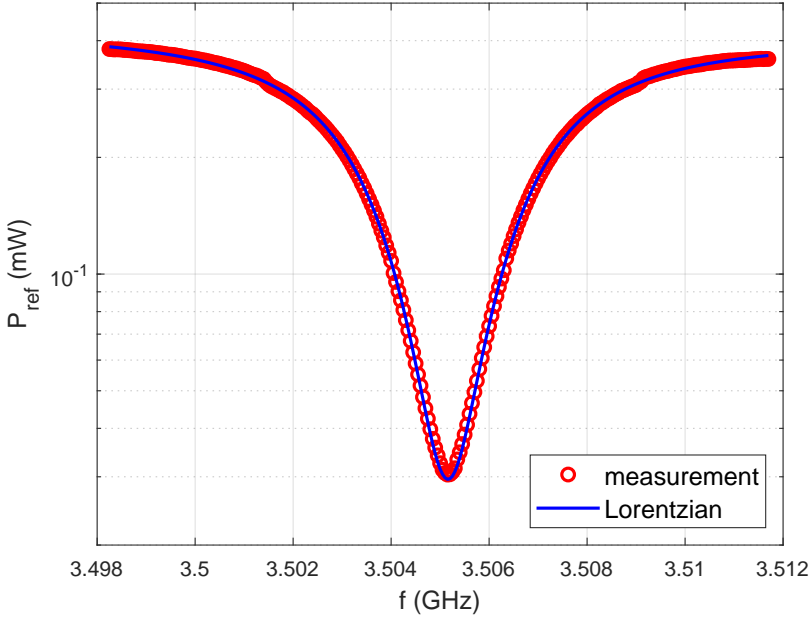


Figure 8.2: Lorentzian curve fit applied to the spectral response of the microwave cavity. The measured data (red circles) is represented by the reflected power P_{ref} as a function of the microwave frequency f . The Lorentzian curve fit is depicted by the solid blue line, from which the resonance frequency f_1 and quality factor Q_1 are derived. The presented data set was obtained at $t = -10 \mu\text{s}$ without gas discharge.

The ions did not respond to the microwaves, and vice versa, due to their inertia, but the electrons readily interacted with the electromagnetic fields oscillating at microwave frequency. Hence, the presence of free electrons resulted in (relative) changes in the complex permittivity $\tilde{\epsilon}/\epsilon_0$ of the medium (relative to vacuum), which is expressed for a gas discharge with electron plasma frequency ω_{pe} and effective (electron-neutral) collision frequency ν_{eff} , as follows:

$$\frac{\Delta\tilde{\epsilon}}{\epsilon_0} = -\frac{\omega_{\text{pe}}^2}{\nu_{\text{eff}}^2 + \omega^2} + i\frac{\nu_{\text{eff}}}{\omega} \frac{\omega_{\text{pe}}^2}{\nu_{\text{eff}}^2 + \omega^2}. \quad (8.1)$$

In this equation, $\omega = 2\pi f$ denotes the angular microwave frequency, ϵ_0 represents the vacuum permittivity, and i describes the imaginary unit. As a consequence of the interaction of free electrons and microwaves, the resonance frequency and quality factor were also subjected to changes, which are formally denoted by the Slater equation [58, 59]:

$$\frac{\Delta f}{f_1} + i\Delta\left(\frac{1}{Q}\right) = -\frac{\iiint_{V_c} \Delta\tilde{\epsilon}(\mathbf{r})|\mathbf{E}(\mathbf{r})|^2 d\mathbf{r}}{2\epsilon_0 \iiint_{V_c} |\mathbf{E}(\mathbf{r})|^2 d\mathbf{r}}. \quad (8.2)$$

In this equation, $\Delta f = f_p - f_1$ and $\Delta(1/Q)$ denote the shift in resonance frequency and

reciprocal quality factor due to $\Delta\tilde{\varepsilon}$, \mathbf{E} represents the (spatially-dependent) microwave electric field, \mathbf{r} describes the spatial coordinate vector, and V_c presents the cavity volume. Without a gas discharge or other form of perturbation, the resonance frequency and quality factor are described by the variables f_1 and Q_1 . These have been measured with the gas flows present, but without free electrons. During the application of the RF power, the resonance frequency and quality factor depend on the number density of electrons and their effective collision frequency. This resulted in a time-dependent f_p and Q_p , while the electrons were created during application of the RF power and vanished when the power was no longer applied. As a consequence, the electron density n_e and effective collision frequency ν_{eff} could be determined time-resolved through Δf and $\Delta(1/Q)$:

$$n_{e,\text{max}} = \frac{2\varepsilon_0 m_e \nu_{\text{eff}}^2 + 4\pi^2 f_p^2 \Delta f}{e^2 \mathcal{V} f_1}, \quad (8.3)$$

and

$$\nu_{\text{eff}} = \pi f_1^2 \frac{\Delta(1/Q)}{\Delta f}. \quad (8.4)$$

In Eqn. (8.3), m_e denotes the electron mass at rest, e the elementary charge, and \mathcal{V} the so-called microwave-electric-field-weighted volume ratio of the perturbed volume V_p with respect to the cavity volume V_c . Please note that Eqn. (8.3) defines the free electron density in terms of the maximum value due to the definition of the electric-field-weighted volume ratio. This is because the electron density profile is accounted for in this chapter using camera images.

As can be seen from Eqn. (8.3) and (8.4), the effective collision frequency is independent of the perturbed volume, while the electron density is inversely proportional to the volume ratio (and the uncertainty in that parameter). To account for this volume correction, the plasma volume was estimated from camera images of the light emitting volume in the afterglow for each experiment. The volume was then converted into a two-dimensional electron density profile by Abel inversion, and plugged into the following equation defining the volume ratio \mathcal{V} :

$$\mathcal{V} = \frac{\iiint_{V_p} n_e(\mathbf{r})/n_{e,\text{max}} |\mathbf{E}(\mathbf{r})|^2 d\mathbf{r}}{\iiint_{V_c} |\mathbf{E}(\mathbf{r})|^2 d\mathbf{r}}. \quad (8.5)$$

Details of the procedure used to convert the camera images into a spatial electron density profile, and subsequent evaluation of \mathcal{V} , are explained in Section 8.6.2 as well as the calculated values of \mathcal{V} for each MCRS experiments for both discharge gases.

The cavity response was determined in a time-resolved fashion in order to determine the changes in n_e and ν_{eff} before, during and after application of the RF power pulse. For this purpose, the reflected power P_{ref} was directed via the directional coupler that allowed 10% of the reflected power $P_{\text{dir}} = 0.1P_{\text{ref}}$ to be transmitted to the logarithmic detector (see Fig. 8.1). A transient recorder acquired the directed power P_{dir} as a function of time by sampling the voltage output of the detector at a sample rate of 100 MHz for a duration of 4 ms. The cavity response, at a fixed frequency f , was sampled for a number of pulses $N_{\text{av}} = 32$, which were averaged afterwards to increase the accuracy of the measurement. The average cavity response was determined

subsequently for a set of microwave frequencies $f = 3.498 - 3.512$ GHz with a step size of 50 kHz, which was centered around the resonance frequency $f_1 = 3.505$ GHz. After the average response was determined for each microwave frequency, the spectral response in terms of P_{ref} as a function of f could be reconstructed for each time instant, and f_p and Q_p were determined using a Lorentzian fit to the data.

The cavity response was acquired simultaneously with the RF power pulse and the oscilloscope monitoring the RF signals (i.e. voltage, current, and absorbed power). This ensured that the measurement time of the microwave system at $t = 0 \mu\text{s}$ coincided with the moment of applying the RF power. During the experiment, the pulse delay generator (PDG) provided a trigger signal (indicated by dashed lines in Fig. 8.1) to the transient recorder, the RF signal generator, and the digital oscilloscope.

8.3 Results

The electron density and effective collision frequency are depicted in Fig. 8.3 and Fig. 8.4, respectively. In each respective figure, the panel (a) contains the measurements for the helium-hexamethyldisiloxane (HMDSO) mixture, and panel (b) depicts the measurements conducted with pristine helium. The data sets obtained for the RF pulse widths $T = 100, 500, 1000,$ and $2000 \mu\text{s}$ are shown only for clarity of the figures. However, experiments were also performed for $T = 50, 250,$ and $1250 \mu\text{s}$. The characteristics of the unperturbed resonant mode were determined just before the RF pulse. At this moment in time, the discharge had fully decayed thanks to the sufficiently long inter-pulse time of 30 ms. This allowed to determine the resonance frequency and quality factor f_1 and Q_1 of the cavity containing the gas mixture only.

At $t = 0 \mu\text{s}$, the RF pulse is applied which ignites the discharge in the inter-electrode gap. At first, the shift in resonance frequency goes to values below zero, where a minimum value is obtained around $t \approx 10 \mu\text{s}$ for each RF pulse duration. By contrast, $\Delta(1/Q)$ increases directly to positive values. Around $t \approx 26 - 43 \mu\text{s}$, the resulting effect is that the effective collision frequency tends to infinity when Δf becomes small upon the transition from negative to positive values. Because the electron density equation contains the effective collision frequency squared (see Eqn. (8.3)), this value shows the same behavior and peaks during the first $\sim 50 \mu\text{s}$. This behavior is attributed to instability of the ignition of the discharges, which differs between subsequent pulses causing jitter in the MCRS measurements for the first $50 \mu\text{s}$. An investigation of the ignition mechanism is required to gain further understanding of this effect.

Near the end of the pulse period, it can be seen that the steady state values are relatively similar for the longer pulse durations, for each respective discharge gas. The effective collision frequency in the afterglow is approximately the same between the pure helium and helium/HMDSO discharges, as can be seen from Fig. 8.4. This indicates that the mean electron energy does not change significantly in the spatial afterglow.

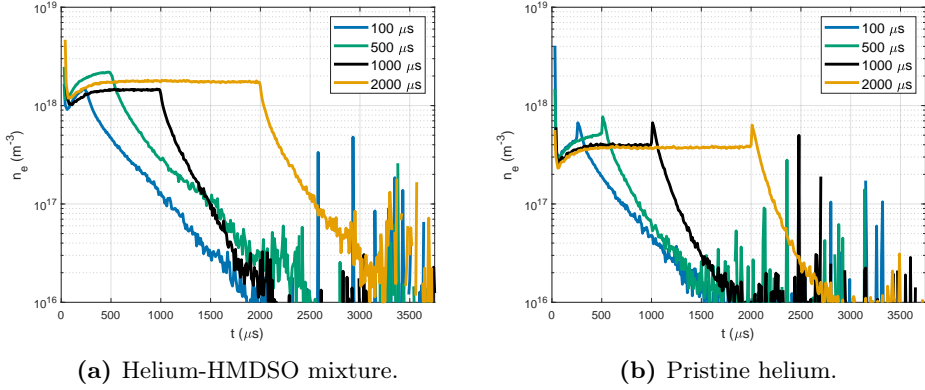


Figure 8.3: Measurements of the free electron density in the afterglow region for (a) the helium/HMDSO mixture and (b) pristine helium discharges, for different RF pulse duration. At $t = 0 \mu\text{s}$, the discharge is ignited which lasts for the pulse duration indicated by the corresponding legend item. After terminating the RF power, the decay of the free electron density follows on a timescale τ_{decay} due to various electron loss processes such as recombination, negative ion formation, or dust charging.

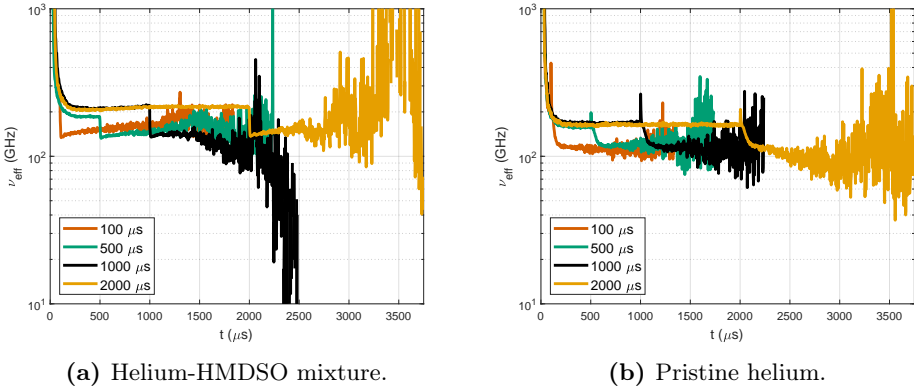


Figure 8.4: Measurements of the effective collision frequency in the afterglow region for (a) the helium/HMDSO mixture and (b) pristine helium discharges, for different RF pulse duration. At $t = 0 \mu\text{s}$, the discharge is ignited which lasts for the pulse duration indicated by the corresponding legend item. After termination of the RF power, the effective collision frequency drops rapidly to a lower value due to electron energy losses by, e.g., electron-neutral collisions.

For helium/HMDSO discharges, the steady state values are in the range of $n_e = 1.45 \pm 0.02 \times 10^{18} \text{ m}^{-3}$ for $T = 1000 \mu\text{s}$ to $n_e = 1.73 \pm 0.02 \times 10^{18} \text{ m}^{-3}$ for $T = 2000 \mu\text{s}$. For pristine helium discharges, the steady state values for the electron density are $n_e = 3.96 \pm 0.07 \times 10^{17} \text{ m}^{-3}$ for $T = 1000 \mu\text{s}$ to $n_e = 3.81 \pm 0.04 \times 10^{17} \text{ m}^{-3}$ for $T = 2000 \mu\text{s}$. It should be noted that these electron density values constitute the microwave-electric-field-weighted and volume averaged values obtained by the use of Eqn. (8.3) and (8.4), where the volume ratios \mathcal{V} have been obtained by evaluation of Eqn. (8.5) as described in Section 8.6.2. Clearly, the electron density is about 3 – 4 times higher by addition of HMDSO to the discharge gas, while the effective collision frequency remains practically unchanged.

The moment of terminating the RF power can be identified in Fig. 8.3 and 8.4 at times corresponding to the discharge pulse widths in the range $T = 100 - 2000 \mu\text{s}$. The effective collision frequency shows a sudden drop to a lower value within about $10 \mu\text{s}$ for the He/HMDSO mixture, which is the same as the decay time for the absorbed power. Concerning the pristine helium measurements, the decay of ν_{eff} is completed within about $100 \mu\text{s}$, which is significantly longer than with HMDSO added to the discharge gas. It is interesting to note that ν_{eff} determined during and after the RF power pulse are of the same order of magnitude, in the range of 100 – 200 GHz, with a minor drop of about 30 – 40%. By contrast, the effective collision frequency for pristine helium is about 1 THz for a mean electron energy equal to $\bar{\epsilon} = 1 \text{ eV}$, which is representative for conditions in the plasma bulk. This implies that the mean energy of the free electrons during the active discharge is already close to room temperature in the spatial afterglow.

The decay of the free electron density is significantly different from the decay of the effective collision frequency which occurs much more rapidly. First, the free electron density—in case of a pristine He discharge—reaches a temporary maximum within about $2 \mu\text{s}$ after terminating the RF power. This rapid increase of the free electron density was previously observed in MCRS measurements in the spatial afterglow of pristine helium discharge interacting with ambient air (see Platier *et al* [46] and Chapter 7). A hypothetical explanation provided previously was based on Penning ionization, e.g., due to helium metastable species colliding with nitrogen molecules. Second, after the peak is reached, the free electron density decays on a timescale of the order of $\sim 100 \mu\text{s}$. This decay timescale of the free electron density is useful for comparison with the timescale of, e.g., ion losses, dust charge neutralization, and numerical findings on the decay time of the electron density.

8.4 Discussion

This section discusses first the non-observability of electron depletion during the MCRS experiments and provides a theoretical prediction of the depleted electron density due to dust charging, in Section 8.4.1. Second, the decay time of the electron density is compared in Section 8.4.2 to the timescales of ion loss, dust charge neutralization, and the decay time of the electron density found from literature.

8.4.1 Electron depletion

Electron depletion, unlike under low pressure conditions, does not seem to occur under the experimental conditions used here. The impact of dust formation on the spatial plasma afterglow conditions is estimated using the dust charging theory. Considering an estimated dust density and average dust charge, the expected depletion of electrons can be estimated to see whether it is reasonable that electron depletion is not observable under the experimental conditions used.

Due to the varying ratio of the ion mean free path and the dust radius, the collisionless ion current provided by the orbital-motion-limited (OML) theory is not applicable under all conditions. Therefore, the analytical model described by Gatti and Kortshagen [60] for varying (ion) collisionality is deployed for the calculation of the dust floating potential for dust radii $a = 1 - 1000$ nm under the conditions used in the experiment. Please consult Chapter 2 for a detailed discussion of the ion current contributions in the various regimes, of which the framework is restated here for completeness of this chapter. The estimated dust charge is used to predict the potential effect of dust charging on the free electron density.

The theory for dust charging by Gatti and Kortshagen [60] is based on the combination of three contributions to the total ion current: the orbital-motion-limited (OML) current I_i^{OML} , the collision-enhanced (CE) current I_i^{CE} , and the hydrodynamic (HYD) current I_i^{HYD} . The capture radius Knudsen number $\text{Kn}_{R_0} = l_i/(2\alpha R_0)$, where $\alpha = 1.22$, dictates the dominant regime for the ion current, where the capture radius R_0 is defined as:

$$R_0 = \frac{e|V_d|a_d \left(1 + \frac{a_d}{\lambda_{\text{DL}}}\right)}{E_i + e|V_d|\frac{a_d}{\lambda_{\text{DL}}}}. \quad (8.6)$$

Here, V_d represents the floating potential of the dust grain, E_i denotes the ion kinetic energy, and λ_{DL} the linearized Debye length (see Eqn. (2.2) in Chapter 2).

The probability for each ion current regime is established by the Knudsen number, which results in a weighted contribution of each current to the total ion current depending, in principle, on the dust radius a_d and the mean free path of the ions $l_i = (n_g \sigma_{\text{in}})^{-1} \approx 58$ nm (with $\sigma_{\text{in}} = 15 \times 10^{-20}$ m² for helium ions in helium both at room temperature [61]). This results in the following definition of the total ion current, as described in detail in Section 2.5:

$$I_i = P_0 I_i^{\text{OML}} + P_1 I_i^{\text{CE}} + P_2 I_i^{\text{HYD}}. \quad (8.7)$$

Under low pressure conditions, the dust radius is usually much smaller than the Debye length λ_{DL} , which in turn is much smaller than the mean free path of the electrons and ions $\lambda_{i,e}$. Under such conditions, the OML theory describes the electron and ion current, respectively, as follows:

$$I_e = e\pi a_d^2 n_e \bar{v}_e \exp\left(\frac{eV_d}{k_B T_e}\right), \quad (8.8)$$

$$I_i^{\text{OML}} = e\pi a_d^2 n_i \bar{v}_i \left(1 - \frac{eV_d}{k_B T_i}\right). \quad (8.9)$$

Here, k_B represents the Boltzmann constant, $\bar{v}_s = \sqrt{8k_B T_s / \pi m_s}$ denotes the thermal velocity, m_s represents the species mass, and T_s describes the species temperature, for species $s = i, e$ for the ions and electrons, respectively.

When the dust grains grow larger in size, the increasing ratio of the dust radius and the ion mean free path results in the transition to the collisional regimes for the ion current. The collision-enhanced current is applicable when ions collide approximately once in the sheath around the dust grain. This leads to an increased ion current with respect to the OML current:

$$I_i^{\text{CE}} = e\pi(\alpha R_0)^2 n_i \bar{v}_i, \quad (8.10)$$

and a further increase in the collisionality leads to the hydrodynamic regime:

$$I_i^{\text{HYD}} = e4\pi a_d n_i \mu_i V_d, \quad (8.11)$$

with μ_i the ion mobility, which is taken equal to $\mu_{\text{He}^+} = 1 \times 10^{-1} \text{ ms}^{-1}$ for $E = 1 \times 10^2 \text{ Vm}^{-1}$ [59] for helium ions in a helium atmosphere.

Fig. 8.5 depicts the calculated dust floating potential and dust charge as a function of dust radius for $a_d = 1 - 1000 \text{ nm}$. The dust grain charge follows from the (spherical) capacitor model, where $q_d = 4\pi\epsilon_0 a_d V_d$. It can be seen that the dust charge is only about 1 elementary charge for a dust radius of 100 nm. Assuming a dust density of $1 \times 10^{14} \text{ m}^{-3}$, this implies that a free electron density of about $1 \times 10^{14} \text{ m}^{-3}$ is permanently retained on the surface of the dust grains. As a consequence of $n_d q_d \ll n_e$, the effect of electron depletion due to dust charging is not noticed from the measurements. It is interesting, however, to note that the effect of dust charging on the free electron density could become apparent, if the dust density $n_d \geq 1 \times 10^{16} \text{ m}^{-3}$ and the dust size $a_d \geq 100 \text{ nm}$.

8.4.2 Analysis of decay timescales

The decay timescale of the electron density is derived from the data sets presented in Fig. 8.3 and 8.4 by fitting an exponential function to the data obtained after the RF power was switched off. The obtained decay times τ_{decay} are shown in Fig. 8.6 as a function of the pulse duration T for both experimental data sets, obtained for the helium/HMDSO mixture and for the pristine helium discharges. It can be seen that the decay times are longer for the helium/HMDSO discharges compared to the pristine helium discharges, for each pulse duration, except for $T = 2000 \mu\text{s}$. Furthermore, it is observed that the decay time decreases strongly with prolonged pulse duration for both data sets, which appear to approach an asymptotic value of $\tau_{\text{decay}} \approx 100 \mu\text{s}$.

The decay time of the electron density found from numerical models $\tau_{\text{decay}}^{\text{num}}$ is mostly much shorter than that found from the MCRS experiments, denoted by τ_{decay} . Husmann *et al* calculated (using a constant number Monte Carlo model) that the electron density had decayed about three orders of magnitude, from $n_e \approx 1 \times 10^{18} \text{ m}^{-3}$ to $n_e \approx 1 \times 10^{15} \text{ m}^{-3}$, for 1 ms after the discharge pulse [34], which resembles a situation that is similar to the decay timescale obtained from the experimental results. However, Chen *et al* found from their numerical model (constant number Monte Carlo simulation) that the electron density fully decayed in a period less than $100 \mu\text{s}$ [36],

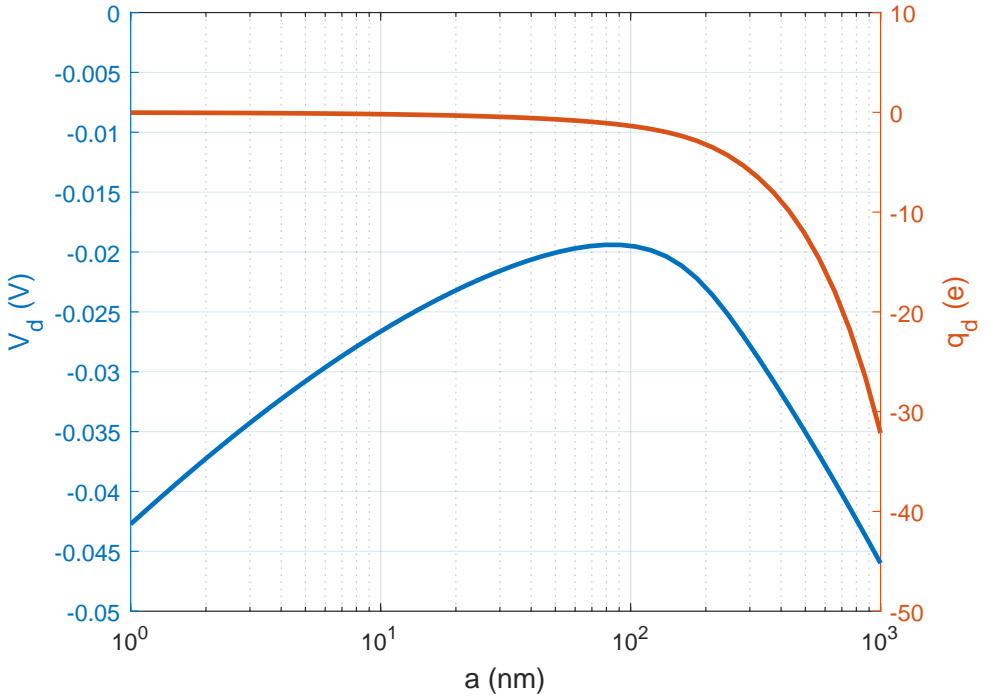


Figure 8.5: The dust floating potential V_d and dust charge q_d as a function of dust grain radius a_d .

indicating a decay time much less than that. Abyuzid *et al* [44] show results from their molecular dynamics simulation (constant number Monte Carlo), which indicates that the electron density decays within 10 ns for high dust density $n_d > 1 \times 10^{16} \text{ m}^{-3}$, and does not significantly decay for smaller dust density. Consequently, this shows that the electron density decay time depends strongly on the conditions considered in the numerical models, and that the timescale of electron decay found by Husmann *et al* [34] agrees best with our experimental finding.

Comparing the electron density decay with the transient timescales of other species, it can be concluded that the electron density decays rapidly. The timescales of ion loss and dust charge neutralization (in an ion-rich environment) are found from literature:

- The decay timescale of the ions lost to the reactor walls and by neutralization of negatively charged dust grains: $\tau_{\text{ion}} \sim 1000 \mu\text{s}$ [42].
- The neutralization timescale of dust grains with size $a_d = 40 \text{ nm}$ [42] using Fuchs' charging theory [62]:
 - $\tau_{\text{neutralization}} \approx 100 \mu\text{s}$ for $n_i = 1 \times 10^{16} \text{ m}^{-3}$
 - $\tau_{\text{neutralization}} \approx 10 \mu\text{s}$ for $n_i = 1 \times 10^{17} \text{ m}^{-3}$

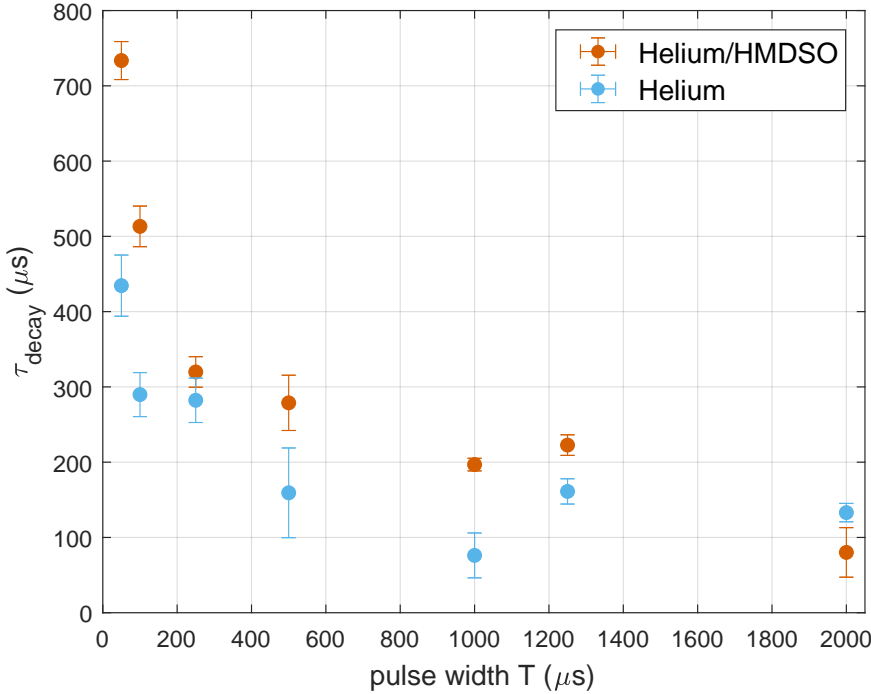


Figure 8.6: Decay timescale of the free electron density as a function of discharge pulse width T for the experiments using the helium/HMDSO mixture (red) and pristine helium (blue) as discharge gas. The error bars (symmetric) are based on the root-mean-square error of the curve fit with respect to the measurement data.

This shows that the ion density decays on a significantly longer timescale, τ_{ion} , with respect to the electrons. As a consequence, it is reasonable that an ion-rich environment is formed downstream of the discharge in the spatial afterglow. However, for such ion densities, neutralization of the dust charge proceeds on a timescale $\tau_{\text{neutralization}}$ close to the measured timescale for the electron density decay. This implies that electrons remain present in large numbers, and that the electron current likely prevails as one of the two bipolar charging currents. Hence, this reveals a discrepancy in the analysis of the dust neutralization in an ion-rich environment, because the resulting timescale predicts that the electron current should be accounted for during this period of time.

8.5 Conclusion

In conclusion, this work demonstrates that the free electron density and effective collision frequency in the spatial afterglow of a dust-forming atmospheric pressure plasma reactor can be effectively determined using microwave cavity resonance

spectroscopy (MCRS). Due to the time-resolved nature of the measurements, dust-forming discharges generated in a helium-hexamethyldisiloxane (He-HMDSO) mixture and a pristine helium gas could be directly compared during the formation, steady state, and decay of the spatial plasma afterglow. The experimental results show two major findings.

The first finding is that the charging of dust grains has (most probably) a negligible influence on the electron density and effective collision frequency in the spatial afterglow of the dust-forming discharge produced in a He-HMDSO gas mixture. However, several important differences have been observed by comparing the temporal behavior of the free electron density. During the steady state period, the electron density is about 3-4 times higher in case of adding HMDSO to the discharge gas. Directly after terminating the RF power, a spike in the electron density is observed for the pristine helium discharge—possibly due to Penning ionization—and this spike vanishes by the addition of HMDSO. Following the decay of the free electron density, it appears that the electron density is lost more slowly by addition of HMDSO. In most low pressure dust-forming discharges, the addition of a reactive gas most often results in the formation of negative ions and dust grains, both of which decrease the free electron density compared to pristine discharges due to the negative charge they acquire. This experiment shows that the effect of dust formation is actually opposite, because the electron density is larger (possibly due to lower ionization energy of HMDSO with respect to He) and the decay time is longer with HMDSO addition (which could be due to detachment processes of electrons from negative ions formed in the bulk upstream).

The second finding shows that the decay timescale of the electron density is close to the predicted timescale of dust charge neutralization due to the ion-rich afterglow. For sufficiently high ion density, which remains close to the electron density within the decay timescale of the electrons, the neutralization timescale is of the same order of magnitude as the electron density decay time. In retrospect, the main assumption in the use of Fuchs' charging theory—used to predict the neutralization timescale in an ion-rich afterglow—is that ions are the dominant charged species in the environment surrounding the dust grain. However, the presence of the electrons breaks this assumption and shows that the electron current imposes a significant flux towards the dust grains on timescales on the order of the electron decay. This reveals a discrepancy between the assumption that the electron current is absent, and the use of Fuchs' charging theory for dust charging in an ion atmosphere.

Future research could extend the implications of this chapter by studying the electron dynamics in case of a higher HMDSO content, and/or extended residence time of the gas mixture inside the plasma reactor. Both conditions will most likely result in the formation of dust at a higher number density and/or average dust size. Related to the manipulation of the dust charge, it would be interesting to perform similar measurements with an extended dielectric tube containing a DC bias electrode, by which electrons/ions can be attracted/repelled as a means to influence their spatial and temporal presence.

8.6 Appendix

8.6.1 Laser light scattering experiments on dust grains in the afterglow

Fig. 8.7 shows a high-speed camera image of laser light scattering by dust grains formed in the atmospheric pressure plasma upstream, whereas the microwave cavity was removed from the experimental setup. At the top of the figure, the exit of the glass tube can be seen, while at the bottom, a substrate was located for the deposition of dust grains. The discharge was created in a mixture of helium (at a flow rate of 1000 sccm) and hexamethyldisiloxane (carried by a helium flow rate of 50 sccm) with an absorbed power of 20 ± 1 W. The RF pulse duration was 2.5 s so that a large amount of dust was created for the purpose of visualization. Similar experiments were also performed for shorter pulse durations, including 2 ms, for which a fainter dust cloud was observed. Below this pulse duration, a dust cloud was no longer visible.

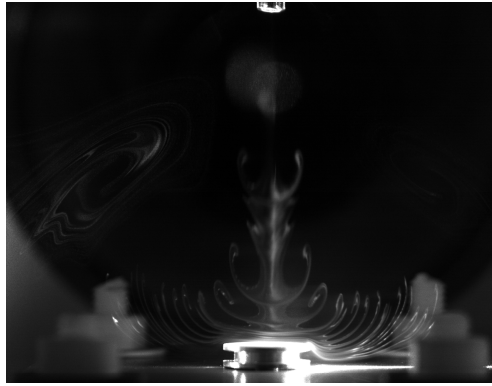


Figure 8.7: High-speed camera image of laser light scattered by dust grains in the spatial afterglow.

8.6.2 Microwave-electric-field-weighted volume ratio

The microwave-electric-field-weighted volume ratio \mathcal{V} was already stated in Eqn. (8.5), and restated for clarity:

$$\mathcal{V} = \frac{\iiint_{V_c} n_e(\mathbf{r})/n_{e,\max} |\mathbf{E}|^2 d^3\mathbf{r}}{\iiint_{V_c} |\mathbf{E}|^2 d^3\mathbf{r}}. \quad (8.12)$$

The microwave electric field \mathbf{E} is determined by means of solving a numerical model representing the microwave cavity in COMSOL Multiphysics[®], of which the result is depicted in Fig. 8.8. The effective collision frequency ν_{eff} is determined from the measurement and assumed to be constant throughout the plasma volume. In Chapter 7 and Platier *et al* [46], $n_e(\mathbf{r})$ was determined by using a binary mask on camera images of the plasma intensity [46, 50].

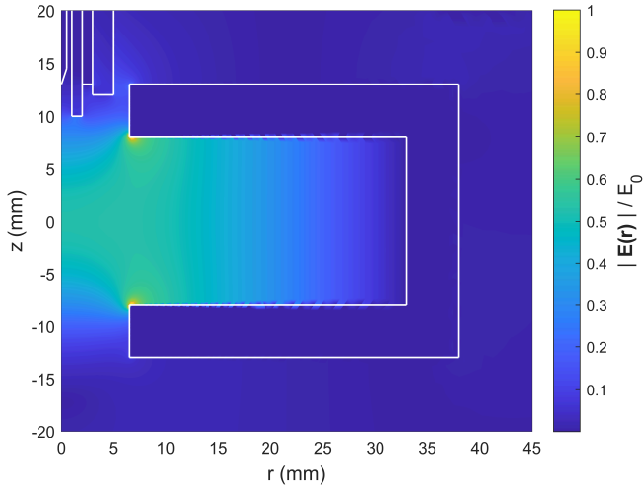


Figure 8.8: Microwave electric field $\mathbf{E}(\mathbf{r})$ obtained from a numerical model of the microwave cavity using COMSOL Multiphysics[®].

In this chapter, this method is extended by determining the full spatial profile based on the camera images with a spatial resolution of 0.046 mm/pixel, which were obtained using the following experimental procedure:

1. The camera is positioned perpendicular to the plasma jet's axis such that the spatial afterglow could be observed.
2. The microwave cavity was removed from the setup.
3. One thousand camera images were taken of the light emitted by the spatial afterglow, while the discharges were produced using the settings provided in Section 8.2.
4. The average of the images is symmetrized around the vertical axis of the plasma jet and smoothed by a Gaussian kernel with a sigma equal to 1 pixel to mitigate pixel noise.
5. The spatial resolution is then doubled using 2D linear interpolation.

The resulting profile represents light emission of the plasma afterglow integrated over the line of sight.

The numerical procedure used to extract the spatial electron density profile from the camera images was as follows, under the assumption that the light emission is proportional to the local electron density:

1. Using Abel inversion [63, 64], the normalized electron density profile $n_e(\mathbf{r})/n_{e,\max}$ is found.

2. Using forward Abel transformation, it is found that the determined spatial profile is a good approximation for the camera images.
3. Using trapezoidal integration, the normalized electron density profile $n_e(\mathbf{r})/n_{e,\max}$ is used in combination with the microwave electric field \mathbf{E} to numerically evaluate Eqn. (8.12) in order to calculate \mathcal{V} for each experiment.

Fig. 8.9 depicts the determined values of \mathcal{V} as a function of the pulse duration T for both experimental data sets: He/HMDSO and pristine He.

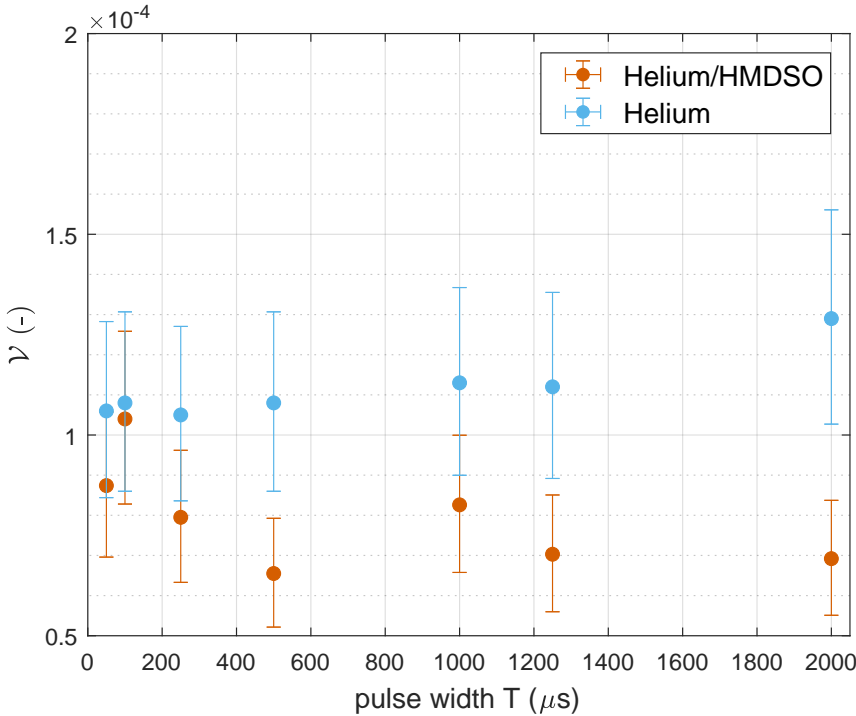


Figure 8.9: Calculated values of \mathcal{V} for different pulse duration T for the He/HMDSO experiments (red) and pristine He discharges (blue). The error bars for both discharge gases are based on the uncertainty in the electric field magnitude $\Delta_{|\mathbf{E}|}^2 \approx 21\%$, which is due to the uncertainty in the boundary of the plasma volume taken as 0.2 mm (equal to 5 pixels). The volume ratio \mathcal{V} is larger under the pristine discharge conditions, and an upward trend is observed for prolonged pulse duration. On the contrary, the volume ratio for the He/HMDSO discharges is overall smaller compared to pristine discharges, and follows a slight downward trend as a function of T .

8.7 Bibliography

- [1] Daphne Pappas. Status and potential of atmospheric plasma processing of materials. *Journal of Vacuum Science & Technology A: Vacuum, Surfaces, and Films*, 29(2):020801, 2011.
- [2] T. Belmonte, G. Henrion, and T. Gries. Nonequilibrium atmospheric plasma deposition. *Journal of Thermal Spray Technology*, 20(4):744–759, 2011.
- [3] Wei Hung Chiang, Davide Mariotti, R. Mohan Sankaran, J. Gary Eden, and Kostya Ostrikov. Microplasmas for Advanced Materials and Devices. *Advanced Materials*, 32(18), 2020.
- [4] Romain Le Picard, Aram H. Markosyan, David H. Porter, Steven L. Girshick, and Mark J. Kushner. Synthesis of Silicon Nanoparticles in Nonthermal Capacitively-Coupled Flowing Plasmas: Processes and Transport. *Plasma Chemistry and Plasma Processing*, 36(4):941–972, 2016.
- [5] Uwe Kortshagen. Nonthermal Plasma Synthesis of Nanocrystals: Fundamentals, Applications, and Future Research Needs. *Plasma Chemistry and Plasma Processing*, 36(1):73–84, 2016.
- [6] Lorenzo Mangolini, Elijah Thimsen, and Uwe Kortshagen. High-yield plasma synthesis of luminescent silicon quantum dots. *Nano Letters*, 5(4):655–659, 2005.
- [7] Ryan Gresback, Nicolaas J. Kramer, Yi Ding, Ting Chen, Uwe R. Kortshagen, and Tomohiro Nozaki. Controlled doping of silicon nanocrystals investigated by solution-processed field effect transistors. *ACS Nano*, 8(6):5650–5656, 2014.
- [8] David Jurbergs, Elena Rogojina, Lorenzo Mangolini, and Uwe Kortshagen. Silicon nanocrystals with ensemble quantum yields exceeding 60%. *Applied Physics Letters*, 88(23), 2006.
- [9] N. J. Kramer, E. S. Aydil, and U. R. Kortshagen. Requirements for plasma synthesis of nanocrystals at atmospheric pressures. *Journal of Physics D: Applied Physics*, 48(3), 2015.
- [10] S. Askari, I. Levchenko, K. Ostrikov, P. Maguire, and D. Mariotti. Crystalline Si nanoparticles below crystallization threshold: Effects of collisional heating in non-thermal atmospheric-pressure microplasmas. *Applied Physics Letters*, 104(16), 2014.
- [11] Z. C. Holman and U. R. Kortshagen. A flexible method for depositing dense nanocrystal thin films: Impaction of germanium nanocrystals. *Nanotechnology*, 21(33), 2010.
- [12] Iryna Kuchakova, Maria Daniela Ionita, Eusebiu Rosini Ionita, Andrada Lazea-Stoyanova, Simona Brajnicov, Bogdana Mitu, Gheorghe Dinescu, Mike De Vrieze, Uroš Cvelbar, Andrea Zille, Christophe Leys, and Anton Yu Nikiforov.

- Atmospheric pressure plasma deposition of organosilicon thin films by direct current and radio-frequency plasma jets. *Materials*, 13(6), 2020.
- [13] Yu Chun Lin and Meng Jiy Wang. Fabrication of hydrophobic/hydrophilic HMDSO films by atmospheric pressure plasma jet deposition. *Japanese Journal of Applied Physics*, 58(SA):3–8, 2019.
- [14] Uwe Lommatzsch and Jörg Ihde. Plasma polymerization of HMDSO with an atmospheric pressure plasma jet for corrosion protection of aluminum and low-adhesion surfaces. *Plasma Processes and Polymers*, 6(10):642–648, 2009.
- [15] J. Benedikt, V. Raballand, A. Yanguas-Gil, K. Focke, and A. Von Keudell. Thin film deposition by means of atmospheric pressure microplasma jet. *Plasma Physics and Controlled Fusion*, 49(12 B):419–427, 2007.
- [16] Franko Greiner, André Melzer, Benjamin Tadsen, Sebastian Groth, Carsten Killer, Florian Kirchschrager, Frank Wieben, Iris Pilch, Harald Krüger, Dietmar Block, Alexander Piel, and Sebastian Wolf. Diagnostics and characterization of nanodust and nanodusty plasmas. *European Physical Journal D*, 72(5):81, 2018.
- [17] M. Haverlag, G. M.W. Kroesen, T. H.J. Bisschops, and F. J. de Hoog. Measurement of electron densities by a microwave cavity method in 13.56-MHz RF plasmas of Ar, CF₄, C₂F₆, and CHF₃. *Plasma Chemistry and Plasma Processing*, 11(3):357–370, 1991.
- [18] E. Stoffels, W. W. Stoffels, G. M. W. Kroesen, and F. J. de Hoog. Dust formation and charging in an Ar/SiH₄ radio-frequency discharge. *Journal of Vacuum Science & Technology A: Vacuum, Surfaces, and Films*, 14(2):556–561, 1996.
- [19] M. Haverlag, G. M.W. Kroesen, T. H.J. Bisschops, and F. J. de Hoog. Measurement of electron densities by a microwave cavity method in 13.56-MHz RF plasmas of Ar, CF₄, C₂F₆, and CHF₃. *Plasma Chemistry and Plasma Processing*, 11(3):357–370, 1991.
- [20] F.M.J.H.van de Wetering, J. Beckers, and G. M. W. Kroesen. Probing the first stage of dust formation in argon / acetylene plasmas using laser-induced photodetachment. 2011.
- [21] Cedric Pattyn, Eva Kovacevic, Thomas Strunskus, Thomas Lecas, and Johannes Berndt. Formation and behavior of negative ions in low pressure aniline-containing RF plasmas. *Scientific Reports*, 9(1):1–9, 2019.
- [22] Benjamin Tadsen, Franko Greiner, Sebastian Groth, and Alexander Piel. Self-excited dust-acoustic waves in an electron-depleted nanodusty plasma. *Physics of Plasmas*, 22(11):113701, 2015.
- [23] M. A. Smith, J. Goodrich, H. U. Rahman, and U. Mohideen. Measurement of grain charge in dusty plasma Coulomb crystals. *IEEE Transactions on Plasma Science*, 29(2 I):216–220, 2001.

-
- [24] Tonuj Deka, A. Boruah, S. K. Sharma, and H. Bailung. Observation of self-excited dust acoustic wave in dusty plasma with nanometer size dust grains. *Physics of Plasmas*, 24(9):093706, 2017.
- [25] Sebastian Groth, Franko Greiner, Benjamin Tadsen, and Alexander Piel. Kinetic Mie ellipsometry to determine the time-resolved particle growth in nanodusty plasmas. *Journal of Physics D: Applied Physics*, 48(46):465203, 2015.
- [26] Maren Dworschak, Oguz Han Asnaz, and Franko Greiner. A minimally invasive electrostatic particle extractor for nanodusty plasmas and its application for the verification of in situ Mie polarimetry. *Plasma Sources Science and Technology*, 30(3), 2021.
- [27] L. Boufendi, M. Ch Jouanny, E. Kovacevic, J. Berndt, and M. Mikikian. Dusty plasma for nanotechnology. *Journal of Physics D: Applied Physics*, 44(17):174035, 2011.
- [28] J. Berndt, S. Hong, E. Kovačević, I. Stefanović, and J. Winter. Dust particle formation in low pressure Ar/CH₄ and Ar/C₂H₂ discharges used for thin film deposition. *Vacuum*, 71(3 SPEC.):377–390, 2003.
- [29] J. Berndt, E. Kovačević, I. Stefanović, O. Stepanović, S. H. Hong, L. Boufendi, and J. Winter. Some aspects of reactive complex plasmas. *Contributions to Plasma Physics*, 49(3):107–133, 2009.
- [30] A. Bouchoule and L. Boufendi. Particulate formation and dusty plasma behaviour in argon-silane RF discharge. *Plasma Sources Science and Technology*, 2(3):204–213, 1993.
- [31] L. Boufendi, A. Bouchoule, R. K. Porteous, J. Ph Blondeau, A. Plain, and C. Laure. Particle-particle interactions in dusty plasmas. *Journal of Applied Physics*, 73(5):2160–2162, 1993.
- [32] Jesse J. Cole, En Chiang Lin, Chad R. Barry, and Heiko O. Jacobs. Continuous nanoparticle generation and assembly by atmospheric pressure arc discharge. *Applied Physics Letters*, 95(11):93–96, 2009.
- [33] J P Borra, N Jidenko, and E Bourgeois. Atmospheric pressure plasmas for aerosols processes in materials and environment. *The European Physical Journal - Applied Physics*, 47(02):null–null, 2009.
- [34] Eric Husmann, Elijah Thimsen, and Xiaoshuang Chen. Particle charge distributions in the effluent of a flow-through atmospheric pressure low temperature plasma. *Plasma Sources Science and Technology*, 30(7), 2021.
- [35] Girish Sharma, Nabel Abuyazid, Sukrant Dhawan, Sayali Kshirsagar, R Mohan Sankaran, and Pratim Biswas. Characterization of particle charging in low-temperature, atmospheric-pressure, flow-through plasmas. *Journal of Physics D: Applied Physics*, 53(245204), 2020.

- [36] Xiaoshuang Chen and Christopher J. Hogan. Nanoparticle dynamics in the spatial afterglows of nonthermal plasma synthesis reactors. *Chemical Engineering Journal*, 411(October 2020):128383, 2021.
- [37] V. Vekselman, Y. Raitses, and M. N. Shneider. Growth of nanoparticles in dynamic plasma. *Physical Review E*, 99(6):1–5, 2019.
- [38] M. Horanyi and C. K. Goertz. Coagulation of dust particles in a plasma. *The Astrophysical Journal*, 361(1):155, 1990.
- [39] B. Van Minderhout, J. C.A. Van Huijstee, A. T. Peijnenburg, P. Blom, G. M.W. Kroesen, and J. Beckers. Charge neutralisation of microparticles by pulsing a low-pressure shielded spatial plasma afterglow. *Plasma Sources Science and Technology*, 30(4), 2021.
- [40] Lavanya Ravi and Steven L. Girshick. Coagulation of nanoparticles in a plasma. *Physical Review E - Statistical, Nonlinear, and Soft Matter Physics*, 79(2):1–9, 2009.
- [41] Steven L. Girshick. Particle nucleation and growth in dusty plasmas: On the importance of charged-neutral interactions. *Journal of Vacuum Science & Technology A*, 38(1):011001, 2020.
- [42] Sukrant Dhawan, Abhay Vidwans, Girish Sharma, Nabil Hilmy Abuyazid, R. Mohan Sankaran, and Pratim Biswas. Enhancing charging and capture efficiency of aerosol nanoparticles using an atmospheric-pressure, flow-through RF plasma with a downstream DC bias. *Aerosol Science and Technology*, 54(11):1249–1254, 2020.
- [43] Shuji Matsusaka. Control of particle charge by atmospheric pressure plasma jet (APPJ): A review. *Advanced Powder Technology*, 30(12):2851–2858, 2019.
- [44] Nabil H. Abuyazid, Xiaoshuang Chen, Davide Mariotti, Paul Maguire, Christopher J. Hogan, and R. Mohan Sankaran. Understanding the depletion of electrons in dusty plasmas at atmospheric pressure. *Plasma Sources Science and Technology*, 29(7), 2020.
- [45] Lorenzo Mangolini and Uwe Kortshagen. Selective nanoparticle heating: Another form of nonequilibrium in dusty plasmas. *Physical Review E - Statistical, Nonlinear, and Soft Matter Physics*, 79(2):1–8, 2009.
- [46] B. Platier, T.J.A. Staps, M. van der Schans, W.L. IJzerman, and J. Beckers. Resonant microwaves probing the spatial afterglow of an RF plasma jet. *Applied Physics Letters*, 115:254103, 2019.
- [47] B. Platier, T. J.A. Staps, C. C.J.M. Hak, J. Beckers, and W. L. Ijzerman. Resonant microwaves probing acoustic waves from an RF plasma jet. *Plasma Sources Science and Technology*, 29:045024, 2020.

-
- [48] P. A.C. Beijer, A. Sobota, E. M. Van Veldhuizen, and G. M.W. Kroesen. Multiplying probe for accurate power measurements on an RF driven atmospheric pressure plasma jet applied to the COST reference microplasma jet. *Journal of Physics D: Applied Physics*, 49:104001, 2016.
- [49] B. Platier, R. Limpens, A. C. Lassise, T. J.A. Staps, M. A.W. Van Ninhuijs, K. A. Daamen, O. J. Luiten, W. L. IJzerman, and J. Beckers. Transition from ambipolar to free diffusion in an EUV-induced argon plasma. *Applied Physics Letters*, 116(10), 2020.
- [50] Marc van der Schans, Bart Platier, Peter Koelman, Ferdi van de Wetering, Jan Van Dijk, Job Beckers, Sander Nijdam, and Wilbert IJzerman. Decay of the electron density and the electron collision frequency between successive discharges of a pulsed plasma jet in N₂. *Plasma Sources Science and Technology*, 28(3):035020, 2019.
- [51] E. Stoffels, W. W. Stoffels, D. Vender, M. Kando, G. M.W. Kroesen, and F. J. De Hoog. Negative ions in a radio-frequency oxygen plasma. *Physical Review E*, 51(3):2425–2435, 1995.
- [52] T. J. A. Staps, B. Platier, D. Mihailova, P. Meijaard, and J. Beckers. Numerical profile correction of microwave cavity resonance spectroscopy measurements of the electron density in low-pressure discharges. *Review of Scientific Instruments*, 92(9):093504, 2021.
- [53] F. M.J.H. Van De Wetering, J. Beckers, and G. M.W. Kroesen. Anion dynamics in the first 10 milliseconds of an argon-acetylene radio-frequency plasma. *Journal of Physics D: Applied Physics*, 45(48):1–8, 2012.
- [54] R. M. Van Der Horst, J. Beckers, S. Nijdam, and G. M.W. Kroesen. Exploring the temporally resolved electron density evolution in extreme ultra-violet induced plasmas. *Journal of Physics D: Applied Physics*, 47(30), 2014.
- [55] R. Limpens, B. Platier, A. C. Lassise, T. J.A. Staps, M. A.W. Van Ninhuijs, O. J. Luiten, and J. Beckers. Influence of a magnetic field on an extreme ultraviolet photon-induced plasma afterglow. *Journal of Physics D: Applied Physics*, 54:435205, 2021.
- [56] M. A.W. Van Ninhuijs, K. A. Daamen, J. G.H. Franssen, J. Conway, B. Platier, J. Beckers, and O. J. Luiten. Microwave cavity resonance spectroscopy of ultracold plasmas. *Physical Review A*, 100(6):61801, 2019.
- [57] M A W Van Ninhuijs, K A Daamen, J Beckers, and O J Luiten. Design and characterization of a resonant microwave cavity as a diagnostic for ultracold plasmas. *Review of Scientific Instruments*, 92:013506, 2021.
- [58] John C. Slater. Microwave Electronics. *Reviews of Modern Physics*, 18(4):441–512, 1946.

- [59] Manfred A. Biondi and Sanborn C. Brown. Measurements of Ambipolar Diffusion in Helium. *Physical Review*, 75(11):1700–1705, 1949.
- [60] Marco Gatti and Uwe Kortshagen. Analytical model of particle charging in plasmas over a wide range of collisionality. *Physical Review E*, 78(4):046402, 2008.
- [61] S. A. Maiorov, S. K. Kodanova, R. I. Golyatina, and T. S. Ramazanov. Kinetic characteristics of ions in the gas discharge and on the target surface. *Physics of Plasmas*, 24(6), 2017.
- [62] N. A. Fuchs. On the stationary charge distribution on aerosol particles in a bipolar ionic atmosphere. *Geofisica Pura e Applicata*, 56(1):185–193, 1963.
- [63] Daniel D. Hickstein, Stephen T. Gibson, Roman Yurchak, Dhrubajyoti D. Das, and Mikhail Ryazanov. A direct comparison of high-speed methods for the numerical Abel transform. *Review of Scientific Instruments*, 90(6), 2019.
- [64] Vladimir Dribinski, Alexei Ossadtchi, Vladimir A. Mandelshtam, and Hanna Reisler. Reconstruction of Abel-transformable images: The Gaussian basis-set expansion Abel transform method. *Review of Scientific Instruments*, 73(7):2634, 2002.

Laser-induced photodetachment of negative oxygen ions

Preface. The presence of molecular species with high electron affinity in combination with plasma electrons results inevitably in the formation of negative ions, which may contribute significantly to the balance of charges as the free electrons do. In low pressure plasmas, the formation of negative ions has been studied in electronegative (e.g., oxygen) and dust-forming (e.g., acetylene) plasmas and their role in the formation of nanoparticles is widely recognized. At atmospheric pressure, little is known about the formation and destruction of negative ions due to a lack of experiments. In this chapter, we dive into the physics of the formation and destruction of negative ions at atmospheric pressure. In addition to a theoretical analysis, experiments are presented by which microwave cavity resonance spectroscopy is shown as an effective method in detecting electrons detached from negative ions using high-intensity laser pulses. As a consequence of this development, the combination of a high-intensity pulsed laser and the microwave cavity method shows promise as a means to detect the surface charge residing on nanoparticles at atmospheric pressure and to study the effect of negative ions on dust (de)charging.

9.1 Introduction

Atmospheric pressure (low-temperature) plasmas [1, 2] are promising for biomedical applications [3, 4, 5], deposition and synthesis of (nano)materials [6, 7, 8, 9, 10], and the treatment of air pollution [11, 12, 13, 14]. The key advantage of such plasmas resides

This chapter has been submitted for publication: T.J.A. Staps, T.J.M. Donders, B. Platier, and J. Beckers, *Laser-induced photodetachment of negative oxygen ions in the spatial afterglow of an atmospheric pressure plasma jet*.

in their capability to generate charged species, radicals, and ultraviolet radiation in large quantities under low-temperature and atmospheric pressure conditions, which allows for easy integration in existing processes aiming to treat delicate materials. Such low-temperature plasmas operate far from thermal equilibrium [15], because the electrons are energized by the (driving) electric field, while the heavy species—such as (negative) ions, metastables and neutrals—remain near room temperature.

Oxygen-based reactive species are among the most important contributors to bacterial inactivation [16, 17], surface modification [18], and the formation of complex negative ions and molecules [19]. Although the properties and dynamics of various neutral and positively charged plasma species has been extensively investigated [20, 21, 22], there is a lack of understanding with respect to the role of negative ions. Negative ions—such as O^- , O_2^- , O_3^- , NO^- , NO_2^- , and OH^- —are created in the spatial afterglow downstream from the active plasma region, where the plasma species mix and react with nitrogen, oxygen and water vapor. The relative yields of various negative ion species were measured by Bruggeman *et al* [23] in a radio-frequency excited atmospheric pressure glow discharge in a mixture of helium and water vapor using mass spectrometry, where OH^- was found as the dominant anion. It was concluded that negative ions had an equally important effect in case of oxygen-containing discharges. Also, negative oxygen ions, and specifically O^- , play a vital role in corona discharges [19] in the production of negatively charged molecules and other reactive species. Despite the importance of negative ions for the chemistry and targeted performance of atmospheric pressure plasmas, the role of negative ions is less understood compared to the role of other species. The lack of understanding of the role of negative ions is mainly caused by the limited diagnostic capabilities for detecting negative ions and, correspondingly, the limited availability of experimental data.

In this chapter, measurements of the negative oxygen ion density are presented as obtained in the spatial afterglow of an atmospheric pressure plasma jet driven by a 13.56 MHz radio-frequency (RF) voltage signal. This discharge was created in a capacitively-coupled cylindrically symmetric geometry, where the plasma was confined between the RF- powered electrode and a dielectric (quartz) tube covering the inside of the grounded electrode. The spatial afterglow, formed downstream of the discharge, culminated in a chamber with a controlled atmosphere where the negative ions were formed by the interaction of afterglow electrons with the argon-oxygen gas mixture. A pulsed ultraviolet laser ($\lambda = 266$ nm) was used to liberate electrons from the negative oxygen ions by photodetachment. The contribution of the photodetached electrons to the free electron density was measured by microwave cavity resonance spectroscopy (MCRS) with a sampling time of 4 ns. By determination of the photodetached electron density as a function of laser pulse energy towards saturation, the photodetachment cross section and local number density of negative ions were found.

This chapter is structured as follows. Section 9.2 describes the experimental setup and measurement methodology, and explains the diagnostic microwave cavity resonance spectroscopy in more detail. Section 9.3 presents the experimental results obtained in this work, of which three main features are highlighted in detail: the argon discharge afterglow before the laser pulse, the saturation study, and decay of the photodetached electron density. Section 9.4 provides an interpretation of the results leading to the

identification of the major negative ion species, the reactions governing the decay of the photodetached electron density, and a discussion of the energy relaxation mechanisms. This chapter is concluded in Section 9.5 with a brief summary of the main findings.

9.2 Experiment

An atmospheric pressure plasma in pure argon was created using a cylindrically symmetric dielectric barrier discharge (DBD) as shown in Fig. 9.1, of which the plasma species reacted with an argon-oxygen mixture in the spatial afterglow downstream of the glow discharge region. The glow discharge was produced in the gap between the RF-powered electrode (a needle with a diameter of 1 mm and a sharp tip) and the grounded electrode (hollow copper cylinder with an inner diameter of 4 mm) which was covered on the inside by a dielectric (quartz tube with inner diameter of 2 mm and outer diameter of 4 mm). The powered electrode was connected to an RF power supply delivering a continuous power of 13.5 ± 0.2 W to the discharge, of which the electrical characteristics were monitored during the experiments using a power probe [24] to ensure steady state plasma conditions and measure the plasma power. Pure argon gas was introduced into the discharge gap via the top at a flow rate of 3000 sccm, while a mixture of argon-oxygen gas (supplied by gas bottles with 99.999 % purity) was introduced into the vessel as background gas. The plasma jet was integrated in a vacuum-tight vessel so that the ambient air could be removed to a pressure below 1 mbar prior to each experiment. During the experiments, a controlled atmosphere inside the vessel was maintained at 1 bar using the mass flow controllers at a flow rate of 2000 sccm argon and 150 sccm oxygen, by closing the valve to the vacuum pump, and by opening a valve connecting the vessel to the central exhaust of the laboratory. Thereby, the experimental setup allowed to generate a stable argon plasma, which created negative oxygen ions in the afterglow located downstream of the discharge gap.

A microwave cavity (with an interior diameter of 66 mm and an inner height of 16 mm) was mounted directly below the plasma jet such that the plasma-produced species could enter the probing volume and, subsequently, the number density of free electrons could be measured using MCRS. The MCRS technique relies on the dependence of the resonant behavior of a resonant microwave mode on the complex permittivity of the medium inside the cavity's probing volume. The complex permittivity was perturbed by changes in the number density and collision frequency of free electrons inside the cavity volume. Moreover, electrons were released from negative oxygen ions in the spatial afterglow of the plasma jet by photodetachment in addition to the electrons generated by the continuously driven discharge.

The change in resonance frequency f_{res} and quality factor of the resonant mode Q_{res} are formalized through the Slater perturbation theorem, which relates the resonant mode characteristics to the (spatially-dependent) change in complex permittivity [25, 26, 27]:

$$\frac{\Delta f}{f_1} + i\frac{1}{2}\Delta\left(\frac{1}{Q}\right) = -\frac{\iiint_{V_c} \Delta\tilde{\epsilon}(\mathbf{r})|\mathbf{E}(\mathbf{r})|^2 d^3\mathbf{r}}{2\epsilon_0 \iiint_{V_c} |\mathbf{E}(\mathbf{r})|^2 d^3\mathbf{r}}. \quad (9.1)$$

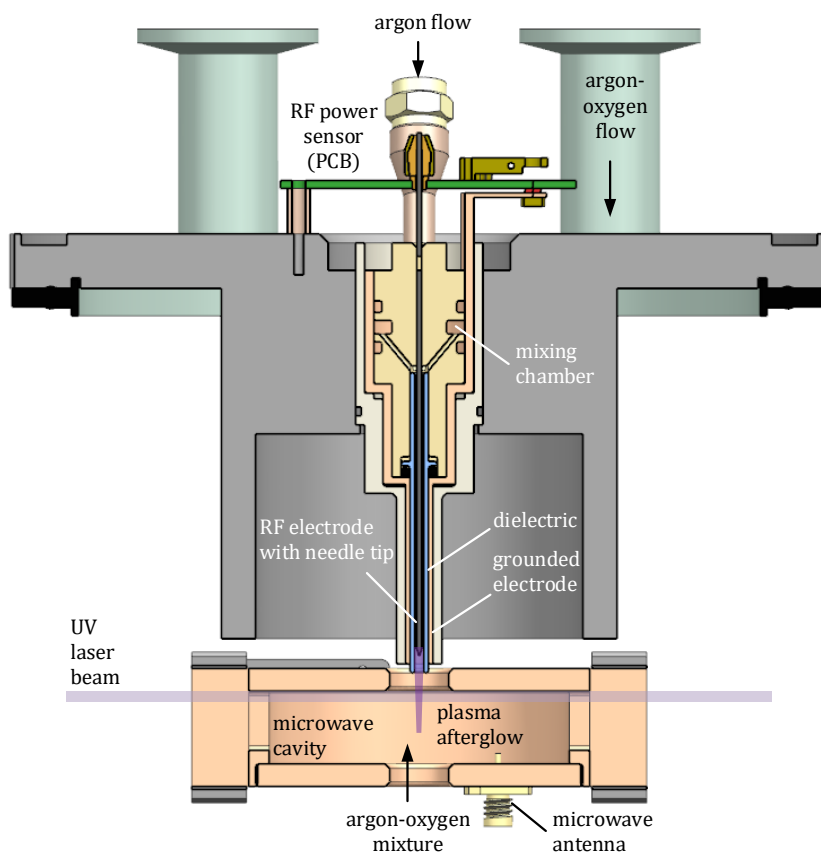


Figure 9.1: Schematic overview of the experimental setup. The overview depicts the plasma jet discharge geometry, the gas flows, the ultraviolet laser beam, and the microwave cavity. The plasma jet comprises several elements, where the argon flow entered the discharge gap from the top into the annular space between the RF-powered needle electrode, the dielectric (quartz) tube and the grounded electrode. The actual measurement volume was a combination of the spatial plasma afterglow and the ultraviolet laser beam, which perturbed the microwave cavity simultaneously. Next to the argon flow, a background gas flow comprising the argon-oxygen mixture was introduced into the vessel via an additional inlet, which could freely entrain the vessel and the microwave cavity volume. The RF power sensor (printed circuit board; PCB) is located at the top, outside the vessel, which monitored the RF current, voltage, and power.

Here, the shift in resonance frequency is $\Delta f = f_p - f_1$ and the change in inverse quality factor is $\Delta(1/Q) = 1/Q_p - 1/Q_1$, where the subscript p denotes the perturbed state (caused by the argon discharge and laser-detached electrons) and the subscript 1 denotes the cavity state with only neutral gas. Furthermore, the imaginary unit is denoted by i , the (microwave) electric field corresponding to the excited TM_{010} mode by $\mathbf{E}(\mathbf{r})$, the vacuum permittivity by ε_0 , and the shift in complex permittivity by $\Delta\tilde{\varepsilon}$, with

$$\frac{\Delta\tilde{\varepsilon}}{\varepsilon_0} = -\frac{\omega_{\text{pe}}^2}{\nu_{\text{eff}}^2 + \omega^2} + i\frac{\nu_{\text{eff}}}{\omega} \frac{\omega_{\text{pe}}^2}{\nu_{\text{eff}}^2 + \omega^2}. \quad (9.2)$$

Here, $\omega_{\text{pe}} = 2\pi f_{\text{pe}}$ and $\omega = 2\pi f$ with f_{pe} the electron plasma frequency and f the applied microwave frequency. As can be seen, the change in complex permittivity depends on the number density and the (effective) collision frequency of the electrons. When assuming a homogeneous plasma region, the free electron density and effective collision frequency are given, respectively, by:

$$n_e = \frac{2\varepsilon_0 m_e}{e^2} \frac{\nu_{\text{eff}}^2 + 4\pi^2 f_p^2}{\mathcal{V}} \frac{\Delta f}{f_1}, \quad (9.3)$$

and

$$\nu_{\text{eff}} = \pi f_1^2 \frac{\Delta(1/Q)}{\Delta f}. \quad (9.4)$$

Here, Δf and $\Delta(1/Q)$ are determined from the measured signals, \mathcal{V} denotes the (microwave-electric-field-weighted) volume ratio (see Section 9.6.1), n_e represents the (microwave-electric-field-weighted volume-averaged) free electron density, and ν_{eff} represents the effective collision frequency. Please consult Section 9.6.2 for the specific equations used for the calculation of the (additional) electron density and the (change in) effective collision frequency caused by the discharge and the laser photodetachment events.

The time-resolved measurement scheme to determine the resonance frequency and quality factor was deployed previously at atmospheric pressure to study pulsed high-voltage discharges in nitrogen [28] and radio-frequency discharges in helium interacting with ambient air presented in Chapter 7 and by Platier *et al* [29, 30]. From an experimental point of view, first, microwave power was introduced via an antenna into the cavity to excite the TM_{010} resonant mode. This was done by injecting sequentially microwaves with frequencies in the spectral neighborhood of the resonant mode which had a resonance frequency $f_1 = 3.5029$ GHz and a quality factor $Q_1 = 725$, in case the cavity was filled with the argon-oxygen gas mixture without discharge or laser perturbation, and at a cavity temperature $T_1 = 26.642$ °C. After the creation of the discharge, a continuous flow of plasma species entered the cavity, which increased the resonance frequency to f_p and decreased the quality factor to Q_p . Part of the microwave power was reflected, depending on the frequency of the injected microwaves—ranging $f = 3.498 - 3.510$ GHz with frequency step size 250 kHz—and the complex permittivity in the cavity volume. The reflected power was converted by a logarithmic power detector to an analog voltage signal, which was measured using a transient recorder sampling at a rate of 250 MHz. For each applied microwave frequency and laser pulse energy, the temporal response was sampled for

4096 (photodetachment) events and averaged afterwards. By measuring the reflected power as a function of time, for each microwave frequency, each average cavity response at a fixed time instant could be reconstructed due to the excellent repeatability of the experiment.

The photodetachment events were induced by short ultraviolet laser pulses, with a duration of 9 ns, from an EdgeWave InnoSlab IS6III-E (Nd:YAG) laser at a wavelength $\lambda_{\text{ph}} = 266$ nm, corresponding to a photon energy $E_{\text{ph}} = 3.49$ eV. The laser pulse energy was measured using a laser power sensor (Ophir PE50-DIF-C pyroelectric sensor with an Ophir Starbright meter). The laser beam propagated through two thin slits (each 2 mm wide and the height matching that of the cavity interior height) located in the side walls of the cavity, just below the glass tube exit, and through the radial center of the cavity. It was verified that no electrons were released from the walls inside the cavity. The volume initially perturbed by the laser beam resulted from the intersection of the laser beam and the spatial afterglow of the plasma column. The laser beam cross section was measured equal to 8.9×10^{-3} cm², and details of the beam cross section measurement can be found in Section 9.6.3.

9.3 Results

This section discusses the results obtained from the time-resolved MCRS measurements before, during and after the moment that the laser was shot. In Section 9.3.1, the change in resonance frequency and inverse quality factor are shown as a function of time for several values of the laser pulse energy. In Section 9.3.2, the values of the free electron density and the effective collision frequency before the laser shot are discussed, which allow to characterize the spatial afterglow of the continuous argon discharge. In Section 9.3.3, the change in free electron density and effective collision frequency due to laser-induced photodetachment are discussed, from which valuable information is derived about the photodetachment process. In Section 9.3.4, the decay time of the photodetached electron density and the relaxation of the effective collision frequency are treated providing insight in the decay process and the thermalization of the photodetached electrons with the afterglow electrons.

9.3.1 Time-resolved cavity response

The time-resolved scheme discussed in Section 9.2 directly results in the determination of the shift in relative resonance frequency $\Delta f(t)/f_1 = (f_p(t) - f_1)/f_1$ and the shift in reciprocal quality factor $\Delta(1/Q(t)) = 1/Q_p(t) - 1/Q_1$, which are depicted for several laser pulse energies in Fig. 9.2 and 9.3, respectively.

The shifts measured for $t < 0$ μ s, with respect to the neutral gas-filled cavity f_1 and Q_1 , are caused by the plasma electrons in the spatial afterglow. As the diagnostic method is very sensitive, the temperature of the structure forming the cavity was measured with sub-mK resolution in order to correct the monitored resonant behavior for thermal expansion of the metal structure. Section 9.6.4 presents a description of this correction method.

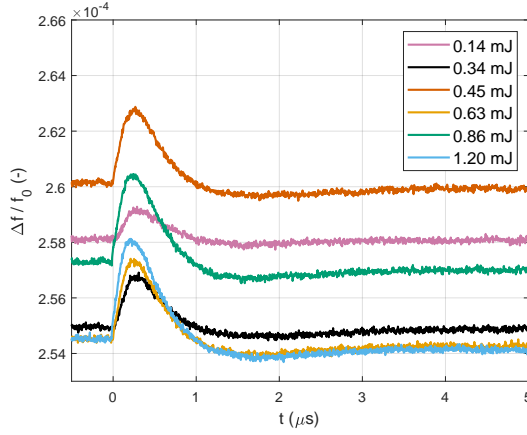


Figure 9.2: Time-resolved shift of the relative resonance frequency $\Delta f/f_1$ resulting from laser-induced photodetachment for different laser pulse energies. The change in resonance frequency, for $t < 0 \mu\text{s}$, originates from electrons in the spatial plasma afterglow of the continuous argon discharge. At $t = 0 \mu\text{s}$, the laser was shot and electrons were liberated from negative ions by photodetachment. The signal decays again after reaching the peak value due to loss processes.

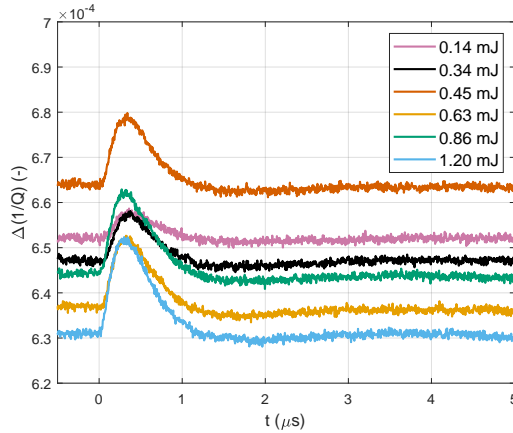


Figure 9.3: Time-resolved shift of the reciprocal quality factor $\Delta(1/Q)$ resulting from laser-induced photodetachment for different laser pulse energies. The change in reciprocal quality factor, for $t < 0 \mu\text{s}$, originates from momentum transfer collisions of electrons in the spatial plasma afterglow with argon atoms, oxygen atoms and oxygen molecules. After the laser is shot at $t = 0 \mu\text{s}$, the electron-neutral collisions induce additional attenuation of the microwaves, which causes changes in the quality factor. After reaching the peak value, the collisions become again less frequent.

Additionally, there are minor differences in $\Delta f/f_1 \sim 5.5 \times 10^{-6}$ and in $\Delta(1/Q) \sim 3.4 \times 10^{-5}$, measured before the laser shot, for the different laser experiments, which are attributed to fluctuations in the plasma absorbed power.

In addition to the plasma-induced shifts, additional shifts for $t > 0 \mu\text{s}$ were caused by the laser photodetached electrons. Photodetached electrons increased the shifts temporally, which vanished again after several $\sim \mu\text{s}$. Consequently, the change in resonance frequency and the inverse quality factor can be used to calculate the free electron density and effective collision frequency in the perturbed volume occupied by the intersection of the spatial afterglow and laser volume.

9.3.2 Argon discharge afterglow

The shifts of the resonance frequency and the inverse quality factor, as shown in Fig. 9.2 and 9.3, can be used directly in combination with Eqn. (9.3) and (9.4) to obtain the free electron density and the effective collision frequency of the medium perturbing the microwave cavity. It should be noted that the definition of both quantities involves the assumption of a homogeneous medium such that the change in (complex) permittivity can be taken out of the electric-field-weighted integral. Under this assumption, the electron density derived represents an electric-field-weighted value that is averaged over the volume comprising the spatial plasma afterglow. The free electron density and effective collision frequency have been calculated as a function of time, which are shown in Fig. 9.4 and 9.5, respectively.

Before the laser was shot through the cavity and afterglow, i.e. $t < 0 \mu\text{s}$, the free electron density in the spatial afterglow caused by the argon discharge is about $n_{e,p} \approx 2.8 \pm 0.1 \times 10^{17} \text{ m}^{-3}$ with an effective collision frequency $\nu_{\text{eff},p} \approx 27.7 \pm 0.5 \text{ GHz}$. This volume-averaged electron density in the afterglow is approximately an order of magnitude smaller than the electron density in the glow discharge region [31, 32, 33], $n_e \sim 1 \times 10^{18} \text{ m}^{-3}$, which is in agreement with the expected rapid decay of the electron density in the afterglow region downstream of the discharge gap [34].

Based on theoretical calculations (see Section 9.6.5), it is found that $\nu_{\text{eff}} \approx 28 \text{ GHz}$ for $\bar{\epsilon} = 0.032 \text{ eV}$ ($= 370 \text{ K}$) considering electron momentum transfer collisions with argon neutrals. Because the neutral argon density is much higher than the neutral oxygen density in the afterglow, only the electron collisions with argon are considered. This shows that the mean electron energy is significantly lower than the electron mean energy in the glow discharge region where $\bar{\epsilon} \sim 1 - 3 \text{ eV}$ [32, 33, 35, 36, 37].

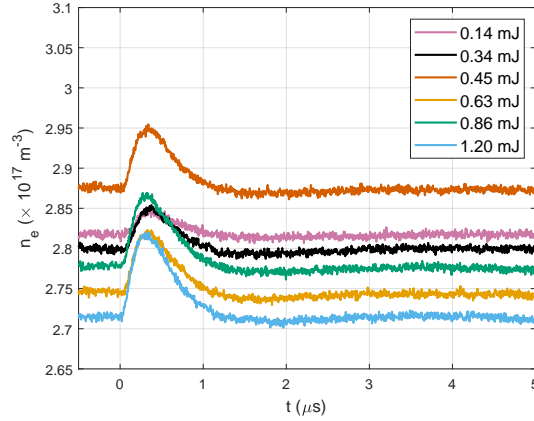


Figure 9.4: Time-resolved shift of the free electron density n_e (in units $1 \times 10^{17} \text{ m}^{-3}$) resulting from laser-induced photodetachment for different laser pulse energies. The electron density obtained for $t < 0 \mu\text{s}$ is due to the continuous argon discharge. For $t > 0 \mu\text{s}$, the change in the electron density is due to electrons liberated by photodetachment, which are lost again due to various processes after the maximum density is reached.

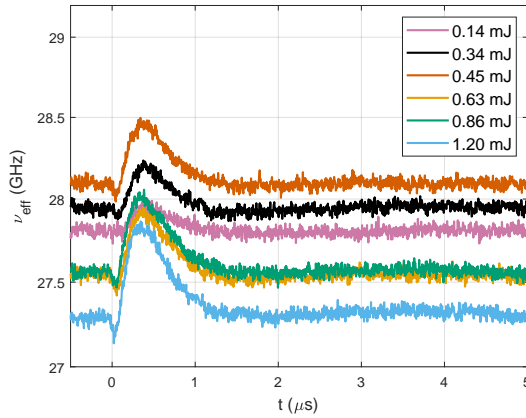


Figure 9.5: Time-resolved shift of the effective collision frequency ν_{eff} (in units GHz) resulting from laser-induced photodetachment for different laser pulse energies. The effective collision frequency before the laser shot at $t = 0 \mu\text{s}$ is due to the continuous argon discharge, which is typical for the spatial plasma afterglow in which the electrons are near room temperature. For $t > 0 \mu\text{s}$, the collision frequency suddenly changes due to photodetached electrons.

9.3.3 Laser-induced photodetachment

Due to laser-induced photodetachment events, a sudden rise in the electron density and effective collision frequency are observed in Fig. 9.4 and 9.5, respectively, for $t > 0 \mu\text{s}$. This sudden rise is caused by the laser shot with a pulse duration of $\sim 9 \text{ ns}$ leading to changes in resonant behavior on a timescale that follows from the cavity response time $\tau_{\text{cav}} = Q_1/(\pi f_1) = 66 \text{ ns}$ [30]. This cavity response time determines the typical time it takes to (de)charge energy into or from a resonant mode. In fact, the cavity was made from stainless steel in order to decrease the cavity response time compared to the copper cavity (with the same geometry) used in Chapter 7 and by Platier *et al* [29]. However, the effective collision frequency decreases during the first 40 – 70 ns—being limited by the response time of the cavity—before rising gradually to a peak value which exceeds the values determined for $t < 0 \mu\text{s}$. This peak value is also limited by the cavity response, while the loss process already sets in during the rise time. The initial rapid decline of ν_{eff} is caused by the relatively stronger increase of Δf with respect to the relative increase of $\Delta(1/Q)$, where it should be noted that $\nu_{\text{eff}} \propto \Delta(1/Q)/\Delta f$. A possible explanation of this behavior is that the resonance frequency shift due to the photodetached electrons temporally increases more strongly than the quality factor does due to elastic collision losses, and therefore, the effective collision frequency of the medium as a whole decreases.

From the peak values in time, as shown in Fig. 9.4, it can be observed that the maximum number of photodetached electrons increases with the laser pulse energy, given the fixed beam cross section. The photodetached electron density in the laser perturbed volume provides valuable information on the negative ion species, which is analyzed in two steps.

First, the electron density caused by laser photodetachment N_e is calculated by correcting the free electron density $n_e(t)$ for the base line electron density created by the argon discharge afterglow $n_{e,p}$, and scaling the photodetached electron density with the (microwave-electric-field-weighted) ratio of the plasma and laser volume (see Section 9.6.1). The maximum value of the photodetached electron density, N_e^{max} , for all applied laser pulse energies, E_{laser} , is depicted in Fig. 9.6 (by the colored data points). In this figure, it can be seen that the number of photodetached electrons increases as a function of laser pulse energy. As the number of negative ions is finite, a sufficient fluence of laser photons results in the saturation of the number of photodetached electrons as can be observed clearly from Fig. 9.6.

Second, the trend in N_e^{max} can be fitted with the photodetachment saturation model, as shown in Fig. 9.6 by the dotted line, to derive the photodetachment cross section σ_{pd} and saturated photodetached electron density N_e^{sat} :

$$N_e^{\text{max}} = N_e^{\text{sat}} \left(1 - \exp \left(- \frac{\sigma_{\text{pd}} E_{\text{laser}}}{E_{\text{ph}} S} \right) \right). \quad (9.5)$$

Here, the laser pulse energy is denoted by E_{laser} , the photon energy by $E_{\text{ph}} = 3.49 \text{ eV}$, and the laser beam cross section by $S = 8.9 \times 10^{-3} \text{ cm}^2$ which is based on the $1/e$ -diameter of the laser beam cross section (see Section 9.6.3). Based on the model fitted to the data, the cross section for photodetachment in this experiment is found to be $\sigma_{\text{pd}} = 8 \times 10^{-18} \text{ cm}^2$, and the saturated photodetached electron density $N_e^{\text{sat}} =$

$2 \times 10^{18} \text{ m}^{-3}$. At saturation, the (saturated) photodetached electron density N_e^{sat} equals the negative ion density in the laser volume assuming singly charged negative ions.

Finally, it should be noted that a homogeneous plasma volume was assumed during the derivation of Eqn. (9.3) and (9.4). However, the uniformity of the electron density is not guaranteed due to the complex interplay of the (undetermined) spatial mixing of oxygen and electrons in the afterglow forming negative ions, and the Gaussian distribution of the laser beam intensity. For verification of the uniformity of ν_{eff} , the thermalization time of the electrons was studied [38]. This time is about 9 ns for electrons with a mean electron energy $\bar{\epsilon} = 2.02 \text{ eV}$ in argon at atmospheric pressure. Here, the mean electron energy $\bar{\epsilon} = E_{\text{ph}} - E_{\text{A}}$ follows from the difference between the photon energy $E_{\text{ph}} = 3.49 \text{ eV}$ and the electron affinity of the negative ions $E_{\text{A}} = 1.47 \text{ eV}$ (for O^- [39], which is expected as the dominant negative ion species (see Section 9.4.1)). Consequently, the electrons quickly lose their energy in the afterglow, and the effective collision frequency can serve as a measure for both volumes.

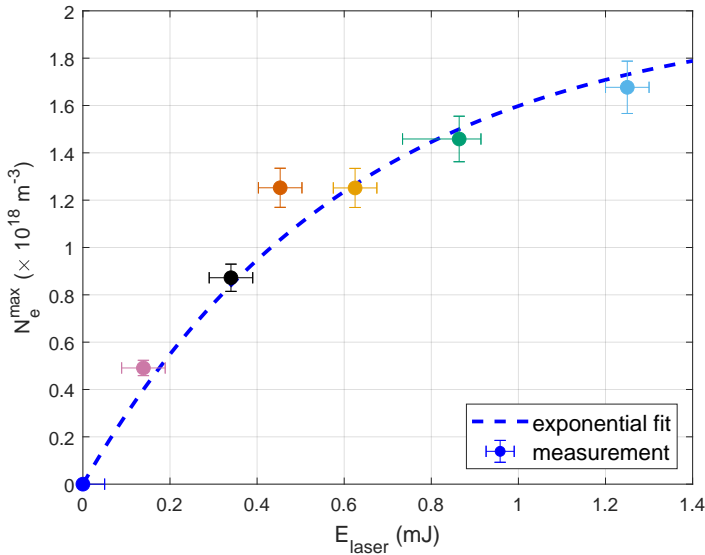


Figure 9.6: Saturation study of the photodetached electron density. The maximum photodetached electron density $N_e^{\text{max}} = \max(N_e(t))$ (in units $1 \times 10^{18} \text{ m}^{-3}$) is shown as a function of laser pulse energy E_{laser} . The horizontal error describes the statistical measurement error of $50 \mu\text{J}$ in the laser power sensor measurement, and if applicable, an additional drift of the laser power over the course of the experiment (e.g., $80 \mu\text{J}$ drift was observed for the measurement at $E_{\text{laser}} = 0.864 \text{ mJ}$). The vertical error bar represents the uncertainty in the plasma power ($\tilde{P}_{\text{rf}} = 0.89 \text{ W}$), where it was assumed that the negative ion density depends linearly on the electron density and, thereby, on the absorbed power in the discharge.

9.3.4 Decay of photodetached electrons

After reaching the temporal peak value, the photodetached electron density follows an exponential decay back to the steady state value, which equals the pre-laser shot value of the spatial afterglow of the plasma. An exponential curve fit was applied to the determined signals for the free electron density, which are shown for the considered time frame by the solid lines in Fig. 9.7. The exponential curve fits are depicted in Fig. 9.7 by the dashed lines. The data was fitted for measurements times between $t \sim 0.320 - 0.376 \mu\text{s}$ (i.e. the moment of the peak value) and $t = 2.0 \mu\text{s}$ (where the signal approximated the pre-laser shot value). Likewise, an exponential curve fit was also applied to data measured for the effective collision frequency. For all settings, the mean and standard deviation of the decay time of the free electron density is $0.366 \pm 0.029 \mu\text{s}$, and a mean and standard deviation of $0.368 \pm 0.007 \mu\text{s}$ was found for the decay time of the effective collision frequency. The fact that the decay of the signals agrees well with an exponential curve indicates that the loss of electrons and the relaxation of their energy is caused by a first-order process, which is discussed in detail in Section 9.4.2 and 9.4.3.

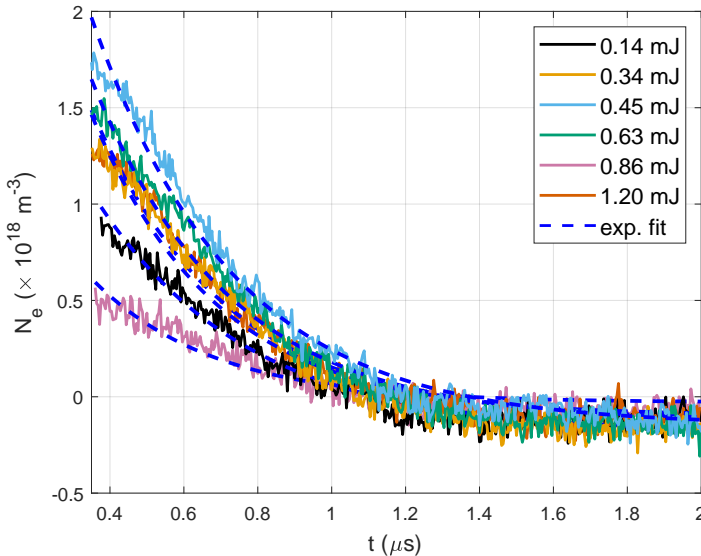


Figure 9.7: The decay period of the photodetached electron density N_e (in units $1 \times 10^{18} \text{ m}^{-3}$) for different values of the laser pulse energy. The experimental data for the different laser pulse energies is shown by the solid lines. An exponential curve fit is applied to each data set, which are depicted by the blue dashed lines. In addition, the curve fit provides a timescale for the exponential decay, denoted by τ_{decay} .

9.4 Discussion

This section contains the interpretation of the major findings from the experimental results presented in this chapter. Section 9.4.1 covers the interpretation of the found photodetachment cross section and negative ion density, and concludes with the identification of the major negative ion species present in the afterglow. Section 9.4.2 provides the validity of using the interaction of the spatial afterglow and the laser beam cross section as the perturbed volume, which is substantiated by investigation of the lifetime of the major negative ion species. Section 9.4.3 discusses the different mechanisms for the loss of electrons by negative ion formation and recombination, of which the timescales are compared to the experimentally determined decay time of the electron density and effective collision frequency. Section 9.4.4 treats the relaxation of the electron energy in detail with a specific focus on the thermalization of the electron energy after the photodetachment events, and the relaxation of the mean electron energy as observed from the determined effective collision frequency signals.

9.4.1 Identification of anion species

The found photodetachment cross section of $\sigma_{\text{pd}} = 8 \pm 2 \times 10^{-18} \text{ cm}^2$ agrees well with experimental and theoretical values, obtained from literature, for the negative atomic oxygen ion at $\lambda_{\text{laser}} = 354 \text{ nm}$: $8 \times 10^{-18} \text{ cm}^2$ by Branscomb *et al* [40], $10 \times 10^{-18} \text{ cm}^2$ by Génévriez *et al* [41], and—to a lesser extent—to the value $\sim 12 \times 10^{-18} \text{ cm}^2$ by Jackson *et al* [42]. By contrast, the cross section obtained from the measurement is significantly higher than those reported in literature for O_2^- and O_3^- , which equal $\sigma_{\text{O}_2^-} = 3.7 \times 10^{-18} \text{ cm}^2$ and $\sigma_{\text{O}_3^-} = 2 \times 10^{-18} \text{ cm}^2$, respectively, at 350 nm [43, 44]. Besides oxygen species, the formation of anions containing hydrogen is likely due to water vapor left prior to the experiment (the pre-experiment vacuum pressure was $\leq 9.8 \times 10^{-1} \text{ mbar}$). Common negative ions involving hydrogen are H^- and OH^- , for which the respective photodetachment cross sections equal $\sigma_{\text{H}^-} = 20 \times 10^{-18} \text{ cm}^2$ at 354 nm [45] and $\sigma_{\text{OH}^-} = 7.6 \times 10^{-18} \text{ cm}^2$ at 350 nm [46], respectively. As a consequence, based on the photodetachment cross sections, the fitted cross section suggests that the dominantly present negative ions can be O^- and/or OH^- .

The absolute value of the negative ion density is the main outcome of the saturation study, which hints towards the negative ion species that is predominantly formed by the interaction of the argon discharge with the argon-oxygen background gas mixture. Numerical modeling by van Gaens and Bogaerts [47] shows that the number density of the negative oxygen ion O^- is dominant over other negative ion species such as O_2^- , O_3^- , H^- , OH^- , and NO_2^- in the early afterglow, i.e. within a distance of 2 mm from the nozzle exit. In that model [47], in which an argon jet propagates in ambient air (containing nitrogen, oxygen and water molecules), the density of negative atomic oxygen ions equaled $n_{\text{O}^-} \approx 1 \times 10^{16} \text{ m}^{-3}$, and this value was found to be approximately three orders of magnitude smaller than the electron density. In a model by Park *et al* [37], however, values of $n_e \approx 3 \times 10^{17} \text{ m}^{-3}$ and $n_{\text{O}^-} \approx 1 \times 10^{17} \text{ m}^{-3}$ were found in an argon-oxygen mixture using a power density of $1 \times 10^8 \text{ W m}^{-3}$ at a radio-frequency of 13.56 MHz. The power density ($0.9 \times 10^8 \text{ W m}^{-3}$) during the

presented experiment was similar to that, but the oxygen density in the afterglow could have been higher due to mixing of the argon discharge with the argon-oxygen background mixture. In a (geometrically) similar plasma jet studied by Van Gessel *et al* [48], the partial air density quickly reached values close to 20 % of the discharge gas density (argon in our experiment) due to mixing of ambient air with the discharge gas flow. By comparison of the current experiment to the model by Park *et al* [37], it is found that the negative ion density measured in this experiment is an order of magnitude higher than calculated from models under similar discharge conditions. This is most probably due to a higher mixing ratio in this experiment compared to the mixing ratio used in their model. Comparing to the model by Van Gaens and Bogaerts [47], it can be concluded that the chemistry in the argon-oxygen mixture is potentially much simpler by the lack of nitrogen- and (dominant) hydrogen-containing species.

In conclusion, the photodetachment cross section suggests that the negative ion species detected are most likely O^- and/or OH^- . The saturated photodetached electron density provides a measure for the negative ion density. Comparing this value to those found from numerical models suggests that negative atomic oxygen ions are probably dominant in the early afterglow (directly following the exit of the discharge region, or glass tube in our experiments). Considering the low content of water vapor in our measurement, it is concluded that atomic oxygen most probably is the major negative ion species present at a density of $2 \times 10^{18} \text{ m}^{-3}$ in the early spatial afterglow.

9.4.2 Detachment processes from O^-

With the identification of the major negative ion, the validity of the assumed perturbed volume can be further investigated by studying the lifetime of O^- . The volume governed by the intersection of the spatial afterglow and the laser beam cross section was used as the perturbed volume by laser-induced photodetachment, which is included in the calculation of the electric-field-weighted volume ratio \mathcal{V} . However, it is not excluded that negative ions are present outside this volume, for instance, through radial diffusion if their lifetime is long enough.

The lifetime of the negative ions created in the spatial afterglow can be estimated by studying processes of detachment. Detachment processes occur through collisional detachment with neutrals, electron-induced three-body collisional detachment, and associative detachment. Electron-induced collisional detachment is expected to be negligible compared to the neutral variant [49], because the electron density is much smaller than the neutral gas density (of Ar and O_2). Collisional detachment with neutrals can proceed by collisions with, e.g., oxygen [50],



but the timescale for this process goes to infinity for ion temperatures near room temperature. On the other hand, associative detachment follows from collisions between negative atomic oxygen ions with atomic [51] and molecular oxygen [52],





The timescale τ_i for the i -th first-order reaction scheme, i.e. for Reaction (R1) to (R3), is derived in Section 9.6.6 using the reaction rate coefficient k_i and the density of reacting species n_r :

$$\tau_i = \frac{1}{k_i n_r}. \quad (9.6)$$

The values of the species densities n_r are listed in Table 9.1, which are based on the numerical model of Van Gaens and Bogaerts [47]. Eqn. (9.6) is used to calculate the timescale for each reaction resulting in $\tau_{\text{R2}} = 71 \mu\text{s}$ and $\tau_{\text{R3}} = 13 \text{ ns}$.

The detachment timescale implies that negative ions are quickly destroyed by collisions with neutral gas particles, leading to a short lifetime. This means that the negative ions cannot travel far from the spatial afterglow region. Consequently, the intersection of the spatial afterglow and the laser beam cross section provides an excellent estimate for the perturbed volume.

Table 9.1: Number density n_r for the different species used to calculate the reaction timescales [47].

Species	Number density (cm^{-3})
e	1×10^{12}
Ar	2.5×10^{19}
Ar ⁺	1×10^{10}
Ar ₂ ⁺	1×10^{13}
O	1×10^{14}
O ⁺	1×10^{11}
O ₂	2.5×10^{17}
O ₂ ⁺	2×10^{11}
O ₃	1×10^9

9.4.3 Decay of the photodetached electron density

The decay of the photodetached electron density back to its pre-laser pulse value can be caused by various processes, including diffusion, advection, wall losses, recombination with positive ions, and negative ion formation.

First, diffusion and advection can move electrons to regions where the resonant microwave mode is less sensitive to perturbations, for example, at locations away from the radial center, whereas wall losses can lead to the physical loss of free electrons. The movement of electrons through the cavity is considered based on the length scales associated with (ambipolar) diffusion and advection. Ambipolar diffusion governs the diffusive movement during the experiment for which $n_e \sim 10^{17} \text{ m}^{-3}$. This can be verified by studying the ratio of the characteristic diffusion length $\Lambda = 4.8 \text{ mm}$ [53], which is more than 100 times larger than the Debye length $\lambda_{\text{De}} \approx 20 \mu\text{m}$ in the current experiment. Therefore, this characteristic length ratio largely exceeds the threshold for the transition to the free diffusion regime [54, 53, 55]. The length scale for (ambipolar)

diffusion is $\Lambda_{\text{diff}} = \sqrt{D_{\text{amb}}\tau_{\text{decay}}} \approx 0.3 \text{ mm}$ using the ambipolar diffusion coefficient [56] equal to $D_{\text{amb}} = 0.3 \text{ m}^2\text{s}^{-1}$ (at $E/N = 0.1 \text{ Td}$) and $\tau_{\text{decay}} = 0.37 \mu\text{s}$ as obtained from the experiment in Section 9.3.4. The length scale for advection, i.e. electrons carried by the gas flow, is estimated (in worst-case) by using the gas velocity in the glass tube ($v_g \approx 15 \text{ ms}^{-1}$) such that $\Lambda_{\text{adv}} = v_g\tau_{\text{decay}} = 5.8 \mu\text{m}$. From the above, it can be directly concluded that the electrons are not able to reach the walls within the timescales of the observed decay. Furthermore, the expansion of the electron cloud due to diffusion and advection leads to at most a factor 1.3 increase in plasma volume, because the radial expansion is leading the volumetric expansion of the spatial afterglow such that $((R_{\text{plasma}} + \Lambda_{\text{diff}})/R_{\text{plasma}})^2$. This implies that diffusion, advection and wall losses are not dominant processes under the current conditions.

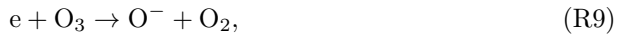
Second, a major electron loss channel could be due to recombination, which is stimulated in the spatial afterglow by an electron mean energy that is decreasing over time after the laser pulse. Recombination of electrons with positive ions can proceed by a two or three body process, where Ar^+ [57], Ar_2^+ [58], and O^+ [59] are considered as positive ion species:



Third, the formation of atomic negative oxygen ions (found as the main species in Section 9.4.1) proceeds by radiative attachment, electron-impact dissociative attachment, and three-body stabilized attachment [49]. Radiative attachment [49] produces a negative oxygen ion and a photon $h\nu$:



Dissociative attachment occurs by interaction of an energetic electron with O_2 [49] or O_3 [37]:



Electron attachment stabilized by a third body [59] occurs, with O_2 or Ar as the stabilizing agent, in case its density is sufficiently high:



Again, the definition of the timescale denoted in Eqn. (9.6) is used to calculate the values for the different reactions, which are listed in Table 9.2, based on the species densities listed in Table 9.1 and the reaction rate coefficients found from the literature stated for each reaction. Concerning recombination, the smallest timescale follows from the recombination with molecular argon ions denoted by Reaction (R5), which equals

$\tau_{R5} = 2.96 \mu\text{s}$ for an electron mean energy $\bar{\epsilon} = E_{\text{ph}} - E_{\text{A}} = 2.03 \text{ eV}$. It should be noted, however, that this timescale is close to the observed timescale for an electron mean energy close to room temperature (0.026 eV). The smallest timescale for negative ion formation is derived from Reaction (R10) providing $\tau_{R10} = 0.4 \mu\text{s}$ for an electron mean energy $\bar{\epsilon} = 2.03 \text{ eV}$, with $k_{R10} = 8.8 \times 10^{-11} \exp(-4.4/T_e) \text{ cm}^3\text{s}^{-1}$ from Phelps [49], $n_{\text{O}_2} = 0.01n_{\text{Ar}}$ (assumed), and $n_{\text{Ar}} = 2.5 \times 10^{19} \text{ cm}^{-3}$ from Van Gaens and Bogaerts [47].

Table 9.2: Calculated timescale for the i -th reaction.

Reaction	τ_{Ri}	Unit
R4	40.31	s
R5	2.96	μs
R6	2680	s
R7	268031	s
R8	7.69	s
R9	100	s
R10	0.40	μs
R11	400	ms
R12	4	ms

In summary, two reactions are found that provide a timescale close to the experimental decay time of the signal. First, the recombination of electrons with molecular argon ions (Reaction (R5)) provides a timescale value that is about an order of magnitude larger than the experimental value, but comes close to it for electron temperatures near room temperature. Second, negative ion formation through dissociative attachment by electron impact (Reaction (R10)) provides a timescale well in agreement with the measured decay time. Considering atomic oxygen as the dominant negative ion species, the energy gained by the electrons directly after photodetachment largely exceeds the energy at room temperature. Hence, the formation of negative atomic oxygen ions through electron-impact dissociative attachment of O_2 is the most likely reattachment process causing the loss of electrons after the peak electron density is reached.

9.4.4 Electron energy relaxation

The change in the effective collision frequency depends strongly on the mean electron energy. During the laser photodetachment phase, a gradual rise of the effective collision frequency is observed. This value for ν_{eff} is used for the determination of the electron density created by the argon discharge and that created by the photodetachment events. This section discusses the validity of ν_{eff} for the entire perturbed volume by investigating the thermalization of energetic electrons—resulting from photodetachment—and afterglow electrons with a mean energy close to room temperature.

Collisions of photodetached electrons with afterglow electrons govern the electron energy distribution, and thereby the relaxation of the photodetached electrons' energy

to the cold afterglow electron temperature. The timescale of the electron-electron collisions depends strongly on the ratio of the electron-neutral mean free path λ_{en} , the Debye length λ_{De} and the distance of closest approach between electrons $r_0 = \lambda_{\text{De}}/(2N_{\text{De}})$ (where N_{De} denotes the Debye number, i.e. the number of electrons in the Debye sphere) [38]. The electron-neutral mean free path for photodetached electrons with energy $\epsilon = 2.03 \text{ eV}$ equals $\lambda_{\text{en}} = v_e \nu_{\text{en}}^{-1}$ with the electron velocity $v_e = \sqrt{2e\epsilon/m_e}$. In this work, the electron-neutral collision frequency of the photodetached electrons directly after photodetachment equals, for argon, $\nu_{\text{en}} \approx 571 \text{ GHz}$, and for oxygen, $\nu_{\text{en}} \approx 1413 \text{ GHz}$ (see Section 9.6.5). This results in an electron-neutral mean free path of $\lambda_{\text{e-Ar}} \approx 1.5 \mu\text{m}$ for argon collisions and $\lambda_{\text{e-O}_2} \approx 0.6 \mu\text{m}$ for collisions with oxygen. The Debye length is defined as $\lambda_{\text{De}} = \sqrt{\epsilon_0 \epsilon / (n_e e^2)} \approx 20 \mu\text{m}$, and consequently, the distance of closest approach $r_0 = 0.035 \mu\text{m}$. Clearly, the following ordering applies to our experiments where $r_0 \ll \lambda_{\text{en}} \ll \lambda_{\text{De}}$, which implies that the electrons collide frequently with neutrals in the Debye sphere. As a result, the energy equilibration of electrons occurs on a timescale $\tau_{\text{e-e}} = N_{\text{De}}/(2\pi f_{\text{pe}}) = 9.5 \text{ ns}$, and the electron energy gained by photodetachment is rapidly distributed among the electrons in the afterglow.

After the photodetachment peak, the effective collision frequency decays analogous to the electron density and on a similar time scale $\tau_{\text{decay}} \sim 0.26 - 0.46 \mu\text{s}$. The energy relaxation of the electrons proceeds by electron-neutral collisions, during which an electron efficiently transfers energy to the heavier particle. The timescale of energy exchange $\tau_{\text{en}} = \nu_{\text{en}}^{-1} m_{\text{Ar}}/m_e$ equals $\tau_{\text{e-Ar}} = 0.129 \mu\text{s}$ for argon, and $\tau_{\text{e-O}_2} = 0.021 \mu\text{s}$ for oxygen. It should be noted that during each electron-neutral encounter, part of the electron's energy is lost, which decreases the momentum transfer collision frequency ν_{en} and increases the energy exchange timescale along the process. In conclusion, this means that the energy exchange timescale provides a lower limit, whereas the timescale for energy relaxation will be larger in practice.

In conclusion, the energy relaxation of the electrons in the afterglow proceeds on short timescales through electron-electron collisions. These collisions are responsible for the energy equilibration between energetic photodetached electrons and cold afterglow electrons, and serve as a motivation for the use of ν_{eff} determined by MCRS for the calculation of the electron density by the argon discharge afterglow and photodetached electron density. On longer timescales of the order $\sim 0.1 \mu\text{s}$, the energy relaxation proceeds by electron-neutral collisions during which energy is efficiently exchanged to the cold neutral gas. This timescale is also observed from the measurements.

9.5 Conclusion

This chapter demonstrates that negative ions can be detected in the spatial afterglow of an atmospheric pressure discharge using laser-induced photodetachment in combination with microwave cavity resonance spectroscopy as a diagnostic technique for detecting the density and effective collision frequency of the electrons photodetached from negative ions. The temporal behavior of the photodetached electrons was successfully determined using microwave cavity resonance spectroscopy, which provided the free electron density and effective collision frequency as a function of time before, during and after the laser shot. As a consequence, the number density and collision frequency

caused by the discharge afterglow and the photodetachment events could be determined providing insight in the dynamics of the major negative ion species.

Based on the photodetachment cross section and negative ion density derived from the presented experiments, it was found that the atomic oxygen ion formed the major negative ion species. After the photodetached electron density and the effective collision frequency reached their respective maxima, dissociative attachment was most probably responsible for the decay of the photodetached electron density after the laser shot.

The combination of laser-induced photodetachment and microwave cavity resonance spectroscopy opens a path for studying negative ions created by atmospheric pressure discharges, which are vital plasma agents in the formation of reactive oxygen species and the plasma afterglow chemistry as a whole. Future experiments in the same setup could be targeting the spatial dependence of the negative ion species, and selectively probing different negative ions due to the distinct electron affinity by using different laser wavelengths. In addition, the technique demonstrated in this work could be extended towards gas discharges excited by, e.g., pulsed high-voltage or microwaves, and in different gas mixtures.

9.6 Appendix

9.6.1 Electric-field-weighted volume ratio

The electric-field-weighted volume ratio is an important factor in the determination of the free electron density based on the cavity response. The solution of the microwave electric field is shown in Fig. 9.8, which was obtained using COMSOL Multiphysics[®] by solving the Maxwell equations for the cavity and plasma jet geometry for the (fundamental) resonant mode TM₀₁₀. This solution was used in a custom MATLAB program to evaluate the electric-field-weighting integrals over the plasma and laser volumes with respect to the total cavity volume. As a result, the fact that the cavity was only partially perturbed in a region should be corrected for using \mathcal{V} in the evaluation of the electron density based on the determined Δf and $\Delta(1/Q)$ from microwave cavity resonance spectroscopy (MCRS) measurements.

The expression for \mathcal{V} follows by definition, when converting the Slater perturbation equation to equations defining the free electron density and effective collision frequency, as:

$$\mathcal{V}_p = \frac{\iiint_{V_p} |\mathbf{E}(\mathbf{r})|^2 d\mathbf{r}}{\iiint_{V_c} |\mathbf{E}(\mathbf{r})|^2 d\mathbf{r}} = 7.3 \times 10^{-4}, \quad (9.7)$$

$$\mathcal{V}_l = \frac{\iiint_{V_l} |\mathbf{E}(\mathbf{r})|^2 d\mathbf{r}}{\iiint_{V_c} |\mathbf{E}(\mathbf{r})|^2 d\mathbf{r}} = 4.2 \times 10^{-6}. \quad (9.8)$$

Here, \mathcal{V}_p denotes the electric-field-weighted plasma volume ratio, and \mathcal{V}_l the electric-field-

weighted laser volume ratio. The integral in the numerator of each of the equations is calculated over the estimated plasma or laser volume. The laser volume is formed by

the region where the plasma and laser volume intersect, where the laser cross section is obtained by CCD camera images (see Section 9.6.3). The integral over the whole cavity volume V_c was obtained by integrating over the complete extent of the radial and axial axes.

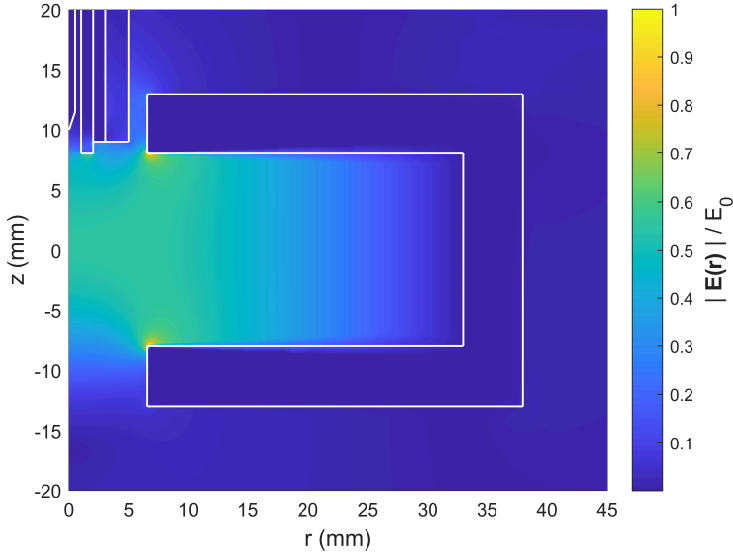


Figure 9.8: Solution of the microwave electric field for the TM_{010} resonant mode in a cylindrically symmetric geometry. The electric field magnitude $|\mathbf{E}|(\mathbf{r})$ is normalized to E_0 (the maximum field strength) and depicted in a cylindrical coordinate system using the radius r (mm) and axial position z (mm). The edges of the cavity and plasma jet components are marked by the white lines. The plasma jet components are depicted in the top left, showing from left to right: the powered electrode with needle tip, Quartz tube, copper grounded electrode, and dielectric (PEEK) insulator confining the interior components. The cross section of the cavity shows the internal dimensions and the holes allowing the discharge and gas flow to enter and leave the cavity.

9.6.2 Calculation of the photodetached electron density

The relation between the change in complex permittivity $\Delta\tilde{\epsilon}$, the shift in the resonance frequency Δf , and the change in inverse quality factor $\Delta(1/Q)$ are formalized by the Slater equation [25, 60, 27]:

$$\frac{\Delta f}{f_1} + i\frac{1}{2} \left(\Delta \frac{1}{Q} \right) = - \frac{\iiint_{V_c} \Delta\tilde{\epsilon} |\mathbf{E}|^2 d\mathbf{r}}{2\epsilon_0 \iiint_{V_c} |\mathbf{E}|^2 d\mathbf{r}}. \quad (9.9)$$

For a homogeneous medium, $\Delta\tilde{\epsilon}$ in the numerator integral in Eqn. (9.9) is non-zero only inside the perturbed volume (due to electrons from the plasma or created by

photodetachment). Hence, the change in complex permittivity can be taken outside the integral due to homogeneity and the numerator integral can be taken over the perturbed volume, V_p , only:

$$\frac{\Delta f}{f_1} + i\frac{1}{2}\Delta\left(\frac{1}{Q}\right) = -\frac{\Delta\tilde{\epsilon}}{2\varepsilon_0}\mathcal{V}, \quad (9.10)$$

with the electric-field-weighted volume ratio \mathcal{V} defined as:

$$\mathcal{V} = \frac{\iiint_{V_p} |\mathbf{E}|^2 d\mathbf{r}}{\iiint_{V_c} |\mathbf{E}|^2 d\mathbf{r}}. \quad (9.11)$$

The electron density and effective collision frequency are found by relating the real and imaginary part of the left- and right-hand sides in Eqn. (9.10). In this experiment, two homogeneous regions—with the same collision frequency—will be assumed as explained below.

For the continuous gas discharge, the shift in resonance frequency and inverse quality factor for $t < 0 \mu\text{s}$, the electron density and effective collision frequency can be derived as follows:

$$\frac{\Delta f}{f_1} = \frac{e^2}{2\varepsilon_0 m_e} \frac{n_{e,p}}{\nu_{\text{eff},p}^2 + \omega_p^2} \mathcal{V}_p, \quad (9.12)$$

where the subscript p indicates plasma-related quantities. Similarly, the inverse quality factor can be defined in terms of measured quantities:

$$\Delta(1/Q) = \frac{e^2}{2\pi\varepsilon_0 m_e f_1} \frac{n_{e,p} \nu_{\text{eff},p}}{\nu_{\text{eff},p}^2 + \omega_p^2} \mathcal{V}_p, \quad (9.13)$$

By rewriting the equation for $n_{e,p}$ and $\nu_{\text{eff},p}$, the expressions can be evaluated based on the measured shifts Δf and $\Delta(1/Q)$.

$$n_{e,p} = \frac{2\varepsilon_0 m_e}{e^2} \frac{\nu_{\text{eff},p}^2 + \omega_p^2}{\mathcal{V}_p} \frac{\Delta f}{f_1}, \quad (9.14)$$

$$\nu_{\text{eff},p} = \pi f_1^2 \frac{\Delta(1/Q)}{\Delta f}. \quad (9.15)$$

For $t > 0 \mu\text{s}$, when the signals start to change due to photodetachment, the situation is a bit more complicated due to the presence of two volumes with a different permittivity. The first volume is the plasma volume described above without the laser perturbed volume. This volume is occupied by the electron density determined from the signals for $t < 0 \mu\text{s}$. The second volume is the laser perturbed volume, which contains a different electron density. Hence, the following equation can be derived for the electron density in the laser volume based on the measured frequency shift for $t > 0 \mu\text{s}$:

$$\frac{\Delta f}{f_1} = \frac{e^2}{2\varepsilon_0 m_e} \left(\frac{n_{e,p}}{\nu_{\text{eff},p}^2 + \omega_1^2} (\mathcal{V}_p - \mathcal{V}_1) + \frac{n_{e,p} + n_{e,1}}{\nu_{\text{eff},1}^2 + \omega_1^2} \mathcal{V}_1 \right). \quad (9.16)$$

The effective collision frequency is assumed to be equal in both volumes as discussed in Section 9.4.3. Using $\nu_{\text{eff,p}} = \nu_{\text{eff,l}}$, the following expression for the laser-induced electron density can be derived:

$$n_{e,l} = \frac{2\varepsilon_0 m_e}{e^2} \frac{\nu_{\text{eff,l}}^2 + \omega_l^2}{\mathcal{V}_l} \frac{\Delta f}{f_l} - \frac{\mathcal{V}_p}{\mathcal{V}_l} n_{e,p}. \quad (9.17)$$

This equation is used for the calculation of the photodetached electron density, which provides the peak values for Fig. 9.6 and the data for curve fitting for Fig. 9.7.

9.6.3 Beam cross section

The cross section of the laser beam S is required for the evaluation of the saturation curve and to determine the laser perturbed volume. To obtain the value of this parameter, the experimental setup was slightly adapted with the following changes. First, the second vacuum window (quartz) was removed to avoid distortions due to the window, which ensured that the laser beam shape was monitored in the way it interacted with the plasma afterglow. Second, a charge-coupled device (CCD) camera was placed after the cavity to capture the laser light. Third, a neutral density filter with reduction order 2.0 was placed in front the CCD camera so that the laser intensity was reduced by a factor 1×10^2 .

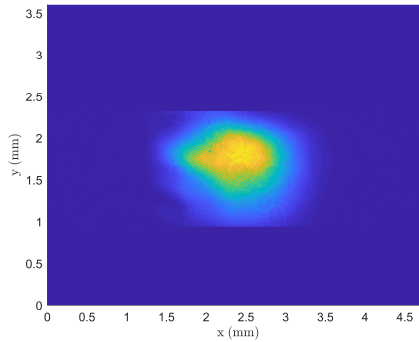


Figure 9.9: Beam cross section of the pulsed ultraviolet laser. The image was obtained by directing the laser light, at low laser pulse energy, onto a charge-coupled device (CCD) camera via a 2.0 neutral density filter reducing the intensity by a factor of 1×10^2 .

As can be seen at the top of Fig. 9.9, the beam is approximately circular with a peak intensity in the center that falls off radially. The top figure depicts an average of 50 images obtained under the same conditions to average out fluctuations in the laser intensity. A Gaussian beam fit was applied to the measured data, which resulted in Fig. 9.10.

The beam cross section is obtained by numerically integrating the region with significant light intensity, i.e. $I > 1/e \times I_{\text{max}}$. First, each pixel, sized $3.75 \mu\text{m}$ in width and height direction, gains a value equal to 0 if the intensity is below this threshold,

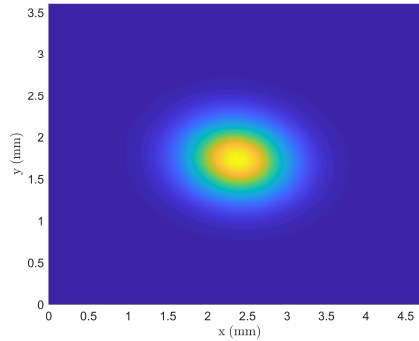


Figure 9.10: Gaussian beam fit based on measured laser intensity distribution. The Gaussian beam fit provides an experimental value for the beam cross section $S = 8.9 \times 10^{-3} \text{ cm}^2$.

or 1 if the intensity exceeds the threshold. This resulted in a beam cross section equal to $S = 9 \times 10^{-3} \text{ cm}^2$, which corresponds to a beam radius of 0.53 mm.

9.6.4 Temperature-correction of resonance frequency

The resonance frequency of the cavity depends strongly its temperature. An NTC thermistor was mounted on the cavity to monitor the temperature with 1 mK resolution for each microwave frequency probed during the MCRS measurements. Fig. 9.11 depicts the average cavity temperature per experiment (for each laser pulse energy) with the corresponding resonance frequency before the laser shot, but with the continuous argon discharge entering the cavity. The cavity temperature was rising during each experiment, so the average was noted here for the purpose of analysis. The relationship between the resonance frequency and the temperature of the cavity appears—as expected—linear from the graph. Therefore, the following linear relationship is proposed based on the idea that the linear thermal expansion in length $\alpha\Delta T$ (resonance wavelength) is inversely proportional to the resonance frequency:

$$f_1(T_{\text{cav}}) = f_1(T_1) (1 - \alpha\Delta T). \quad (9.18)$$

Using linear regression, the resonance frequency at the starting temperature equals $f_1(26.642^\circ\text{C}) = 3.5038 \text{ GHz}$, and the coefficient $\alpha = 18 \times 10^{-6} \text{ K}^{-1}$. The linear coefficient agrees well with the (linear) thermal expansion coefficient of stainless steel which is $17 \times 10^{-6} \text{ K}^{-1}$ for type 304, and $16 \times 10^{-6} \text{ K}^{-1}$ for type 316. A difference can be expected from the fact that the cavity is cylindrical and the strain is not homogeneously in the axial and radial direction. To compensate for the expansion of the cavity volume due to changes in the temperature of the metal structure forming the cavity, the probing frequencies are spectrally shifted following the method described by Platier *et al* [61]. In conclusion, the resonance frequency in an argon-oxygen background measured before the experiments, $f_1(T_1)$, was corrected for the temperature changes, which provided $f_1(T)$ and served as a reference for each experiment.

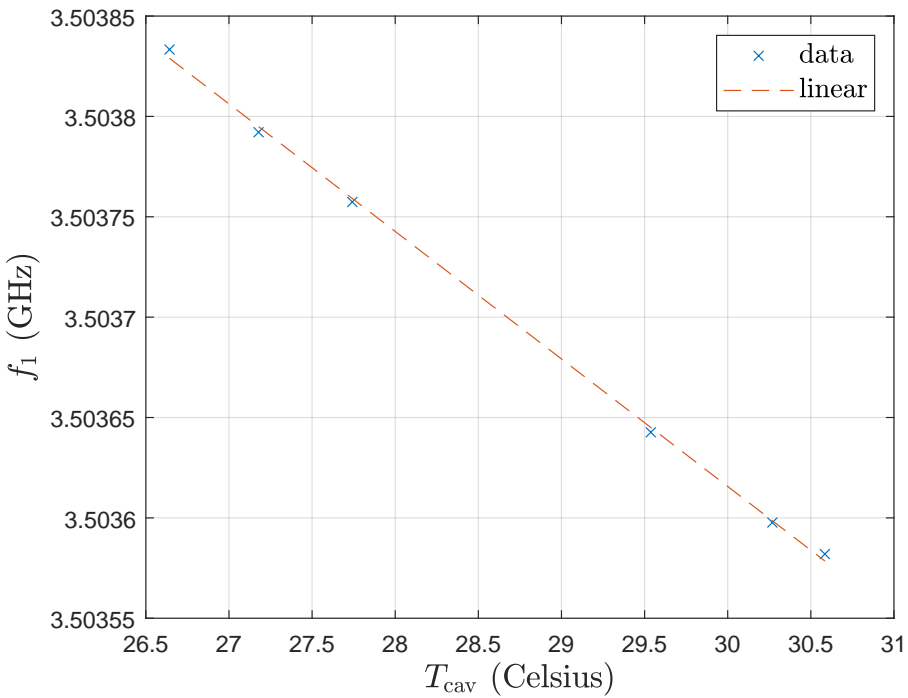


Figure 9.11: Resonance frequency with continuous argon discharge f_1 as a function of the average cavity temperature T_{cav} measured during the MCRS experiments. The measured resonance frequency for each temperature are indicated by the blue crosses. The linear fit is depicted by the dashed red line.

9.6.5 Theoretical analysis of collision frequency

The electron-neutral momentum transfer cross section σ_m has been obtained from the LXCat database for both argon and oxygen [56]. The dependence of σ_m on the (directed) electron energy ϵ can be seen from the panels (a) in Fig. 9.12 and 9.13. Based on the momentum transfer cross section $\sigma_m(\epsilon)$, the momentum transfer collision frequency for electron-neutral collisions can be calculated as follows:

$$\nu_m = n_g \sigma_m(\epsilon) v_e, \quad (9.19)$$

where n_g denotes the neutral gas density (equals $2.5 \times 10^{25} \text{ m}^{-3}$ at atmospheric pressure), and $v_e = \sqrt{\frac{2e\epsilon}{m_e}}$ the electron velocity. The momentum transfer collision frequency ν_m is shown in the panels (b) of Fig. 9.12 for argon, and Fig. 9.13 for oxygen.

It should be noted that such momentum transfer collisions have been measured using a directed electron beam onto a neutral gas target, where the neutral gas particles are essentially at rest. Hence, this means that we need to integrate over the electron energy distribution $F(\epsilon)$ when a plasma or gas discharge is considered. This idea is captured in the definition of the effective collision frequency, which—assuming a Maxwellian distribution function—can be defined as follows [28]:

$$\nu_{\text{eff}} = \frac{\int_0^\infty \epsilon^{3/2} \frac{\nu_m(\epsilon)}{\nu_m^2(\epsilon) + \omega^2} \frac{dF(\epsilon)}{d\epsilon} d\epsilon}{\int_0^\infty \epsilon^{3/2} \frac{1}{\nu_m^2(\epsilon) + \omega^2} \frac{dF(\epsilon)}{d\epsilon} d\epsilon}. \quad (9.20)$$

Here, the energy distribution function is denoted by $F(\epsilon)$, and $\omega (= 2\pi f)$ describes the angular microwave frequency. The effective collision frequency is depicted in the panels (c) of Fig. 9.12 and 9.13, for electron-argon and electron-oxygen collisions, respectively.

With regard to the discussion, the following values have been evaluated numerically in the program to facilitate the analysis. Please note that room temperature $T = 300 \text{ K}$ equals $T = 0.026 \text{ eV}$, and that the number density of argon in the spatial afterglow is significantly higher than oxygen density.

The electron-argon effective collision frequency $\nu_{\text{eff}} \approx 36 \text{ GHz}$ at $\bar{\epsilon} = 0.025 \text{ eV}$ and $\nu_{\text{eff}} \approx 28 \text{ GHz}$ at $\bar{\epsilon} = 0.032 \text{ eV}$. However, there is a second intersection point where $\nu_{\text{eff}} \approx 30 \text{ GHz}$ at $\bar{\epsilon} = 0.398 \text{ eV}$. This is due to the Ramsauer minimum in the momentum transfer cross section for elastic electron-argon collisions, where the minimum occurs around $\epsilon = 0.25 \text{ eV}$. The electron-O₂ effective collision frequency $\nu_{\text{eff}} \approx 35 \text{ GHz}$ at $\bar{\epsilon} = 0.025 \text{ eV}$ and $\nu_{\text{eff}} \approx 41 \text{ GHz}$ at $\bar{\epsilon} = 0.032 \text{ eV}$.

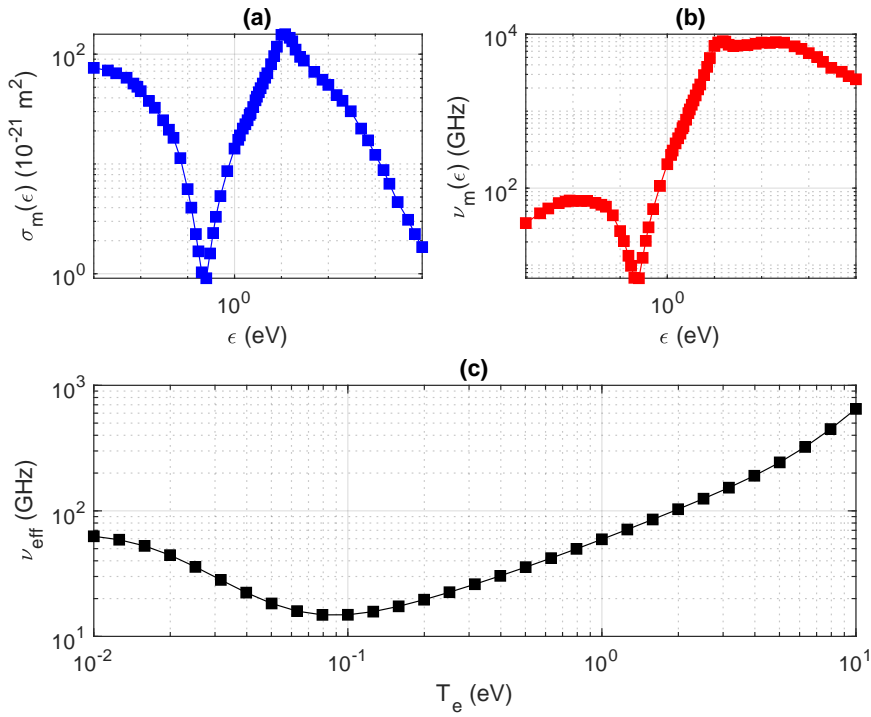


Figure 9.12: Theoretical analysis of effective collision frequency for momentum transfer collisions between electrons and argon. (a) The momentum transfer cross section $\sigma_m^{e-\text{Ar}}$ for collisions between electrons and argon is shown as a function of the electron energy ϵ . (b) The momentum transfer collision frequency $\nu_m^{e-\text{Ar}}$, calculated using Eqn. (9.19), is depicted as a function of electron energy ϵ . (c) The theoretical calculation of the effective collision frequency $\nu_{\text{eff}}^{e-\text{Ar}}$ for electron-argon collisions as a function of the mean electron energy $\bar{\epsilon}$.

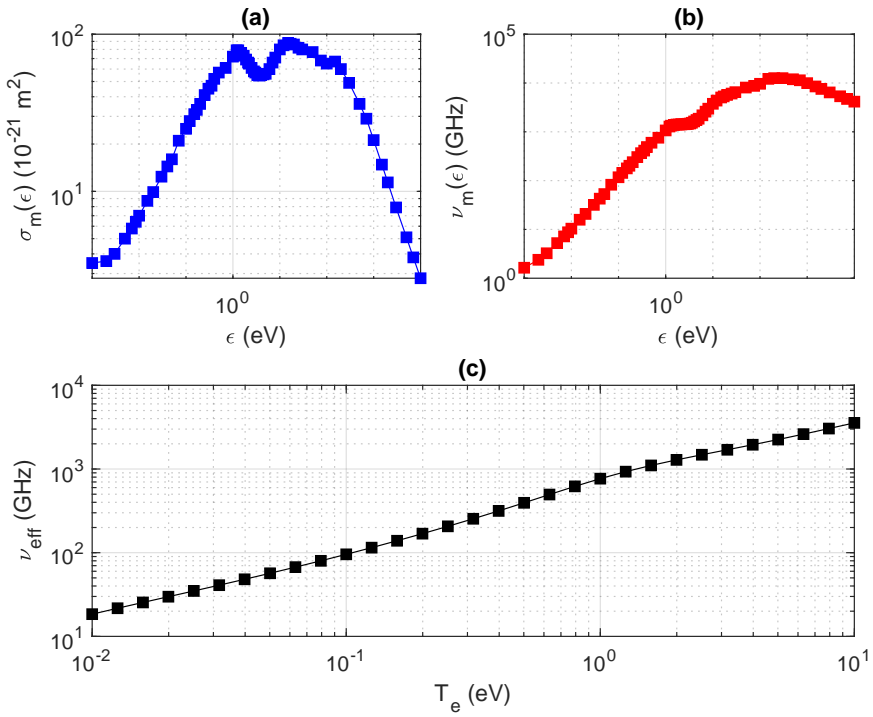


Figure 9.13: Theoretical analysis of effective collision frequency for momentum transfer collisions between electrons and molecular oxygen. (a) The momentum transfer cross section $\sigma_m^{e-O_2}$ for collisions between electrons and molecular oxygen is shown as a function of the electron energy ϵ . (b) The momentum transfer collision frequency $\nu_m^{e-O_2}$, calculated using Eqn.(9.19), is depicted as a function of electron energy ϵ . (c) The theoretical calculation of the effective collision frequency $\nu_{\text{eff}}^{e-O_2}$ for electron-molecular oxygen collisions as a function of the mean electron energy $\bar{\epsilon}$.

9.6.6 Timescale of first-order reaction

The timescale for a first-order reaction follows from the solution of the first-order differential equation, which describes the rate of change of the (photodetached) electron density:

$$\frac{dn_e}{dt} = -k_i n_r n_e \quad (9.21)$$

where i indicates the type of reaction (reaction Ri in Section 9.4.2), k_i represents the corresponding reaction rate coefficient, n_e denotes the electron density, and n_r describes the density of the reacting species, i.e. atomic or molecular species that react with the electrons. This differential equation has the following solution,

$$n_e(t) = n_e^0 \exp\left(-\frac{t}{k_i n_r}\right), \quad (9.22)$$

with n_e^0 the initial electron density, from which the timescale of electron loss can be defined as:

$$\tau_i = \frac{1}{k_i n_r}. \quad (9.23)$$

9.7 Bibliography

- [1] Ulrich Kogelschatz. Dielectric-barrier Discharges : Their History, Discharge Physics, and Industrial Applications. *Plasma Chemistry and Plasma Processing*, 23(1):1–46, 2003.
- [2] A Schutze, J Y Jeong, S E Babayan, Jaeyoung Park, Gary S Selwyn, and Robert F Hicks. The atmospheric-pressure plasma jet: a review and comparison to other plasma sources. *IEEE Transactions on Plasma Science*, 26(6):1685–1694, 1998.
- [3] M. G. Kong, G. Kroesen, G. Morfill, T. Nosenko, T. Shimizu, J. Van Dijk, and J. L. Zimmermann. Plasma medicine: An introductory review. *New Journal of Physics*, 11:115012, 2009.
- [4] J. Ehlbeck, U. Schnabel, M. Polak, J. Winter, Th Von Woedtke, R. Brandenburg, T. Von Dem Hagen, and K. D. Weltmann. Low temperature atmospheric pressure plasma sources for microbial decontamination. *Journal of Physics D: Applied Physics*, 44(1):013002, 2010.
- [5] Mounir Laroussi. Low temperature plasma-based sterilization: Overview and state-of-the-art. *Plasma Processes and Polymers*, 2(5):391–400, 2005.
- [6] Davide Mariotti, Thierry Belmonte, Jan Benedikt, Tamilselvan Velusamy, Gunisha Jain, and Vladimir Švrček. Low-Temperature Atmospheric Pressure Plasma Processes for "Green" Third Generation Photovoltaics. *Plasma Processes and Polymers*, 13(1):70–90, 2016.
- [7] Fabio Palumbo, Chiara Lo Porto, Francesco Fracassi, and Pietro Favia. Atmospheric pressure plasma deposition of TiO₂: A review. *Coatings*, 10(5):440, 2020.
- [8] Davide Mariotti and R. Mohan Sankaran. Microplasmas for nanomaterials synthesis. *Journal of Physics D: Applied Physics*, 43(32):323001, 2010.
- [9] K. Ostrikov and A. B. Murphy. Plasma-aided nanofabrication: Where is the cutting edge? *Journal of Physics D: Applied Physics*, 40(8):2223–2241, 2007.
- [10] K. Ostrikov, E. C. Neyts, and M. Meyyappan. Plasma nanoscience: From nano-solids in plasmas to nano-plasmas in solids. *Advances in Physics*, 62(2):113–224, 2013.
- [11] Hyun Ha Kim. Nonthermal plasma processing for air-pollution control: A historical review, current issues, and future prospects. *Plasma Processes and Polymers*, 1(2):91–110, 2004.
- [12] Alyen Abahazem, Hasna Guedah, Nofel Merbahi, Mohamed Yousfi, Olivier Eichwald, and Ahmed Ihlal. Energy injected in multi-tip pulsed corona discharge reactor in air at atmospheric pressure for pollution control. *Materials Today: Proceedings*, 2(9):4694–4700, 2015.

- [13] Agata Giardina, Milko Schiorlin, Ester Marotta, and Cristina Paradisi. Atmospheric Pressure Non-thermal Plasma for Air Purification: Ions and Ionic Reactions Induced by dc+ Corona Discharges in Air Contaminated with Acetone and Methanol. *Plasma Chemistry and Plasma Processing*, 40(4):1091–1107, 2020.
- [14] F. Thevenet, L. Sivachandiran, O. Guaitella, C. Barakat, and A. Rousseau. Plasma-catalyst coupling for volatile organic compound removal and indoor air treatment: A review. *Journal of Physics D: Applied Physics*, 47(22):224011, 2014.
- [15] A. Fridman, A. Chirokov, and A. Gutsol. Non-thermal atmospheric pressure discharges. *Journal of Physics D: Applied Physics*, 38(2):R1–R24, 2005.
- [16] Stefano Perni, Gilbert Shama, J. L. Hobman, P. A. Lund, C. J. Kershaw, G. A. Hidalgo-Arroyo, C. W. Penn, X. T. Deng, J. L. Walsh, and M. G. Kong. Probing bactericidal mechanisms induced by cold atmospheric plasmas with *Escherichia coli* mutants. *Applied Physics Letters*, 90(7):10–13, 2007.
- [17] M. Laroussi and F. Leipold. Evaluation of the roles of reactive species, heat, and UV radiation in the inactivation of bacterial cells by air plasmas at atmospheric pressure. *International Journal of Mass Spectrometry*, 233(1-3):81–86, 2004.
- [18] Eleazar Gonzalez, Michael D. Barankin, Peter C. Guschl, and Robert F. Hicks. Surface activation of poly(methyl methacrylate) via remote atmospheric pressure plasma. *Plasma Processes and Polymers*, 7(6):482–493, 2010.
- [19] K. Sekimoto and M. Takayama. Dependence of negative ion formation on inhomogeneous electric field strength in atmospheric pressure negative corona discharge. *European Physical Journal D*, 50(3):297–305, 2008.
- [20] K. Niemi, V. Schulz-Von Der Gathen, and H. F. Döbele. Absolute atomic oxygen density measurements by two-photon absorption laser-induced fluorescence spectroscopy in an RF-excited atmospheric pressure plasma jet. *Plasma Sources Science and Technology*, 14(2):375–386, 2005.
- [21] K. Niemi, J. Waskoenig, N. Sadeghi, T. Gans, and D. O’Connell. The role of helium metastable states in radio-frequency driven helium-oxygen atmospheric pressure plasma jets: Measurement and numerical simulation. *Plasma Sources Science and Technology*, 20:055005, 2011.
- [22] Jochen Waskoenig, Kari Niemi, Nikolas Knake, Lucy Marie Graham, Stephan Reuter, Volker Schulz-Von Der Gathen, and Timo Gans. Diagnostic-based modeling on a micro-scale atmospheric-pressure plasma jet. *Pure and Applied Chemistry*, 82(6):1209–1222, 2010.
- [23] Peter Bruggeman, Felipe Iza, Daniël Lauwers, and Yolanda Aranda Gonzalvo. Mass spectrometry study of positive and negative ions in a capacitively coupled atmospheric pressure RF excited glow discharge in He–water mixtures. *Journal of Physics D: Applied Physics*, 43(1):012003, 2010.

-
- [24] P. A.C. Beijer, A. Sobota, E. M. Van Veldhuizen, and G. M.W. Kroesen. Multiplying probe for accurate power measurements on an RF driven atmospheric pressure plasma jet applied to the COST reference microplasma jet. *Journal of Physics D: Applied Physics*, 49:104001, 2016.
- [25] John C. Slater. Microwave Electronics. *Reviews of Modern Physics*, 18(4):441–512, 1946.
- [26] Manfred A. Biondi. Measurement of the electron density in ionized gases by microwave techniques. *Review of Scientific Instruments*, 22(7):500–502, 1951.
- [27] R. F. Harrington. *Time-Harmonic Electromagnetic Fields*. Wiley-IEEE Press, New York, 2001.
- [28] Marc van der Schans, Bart Platier, Peter Koelman, Ferdi van de Wetering, Jan Van Dijk, Job Beckers, Sander Nijdam, and Wilbert IJzerman. Decay of the electron density and the electron collision frequency between successive discharges of a pulsed plasma jet in N₂. *Plasma Sources Science and Technology*, 28(3):035020, 2019.
- [29] B. Platier, T.J.A. Staps, M. van der Schans, W.L. IJzerman, and J. Beckers. Resonant microwaves probing the spatial afterglow of an RF plasma jet. *Applied Physics Letters*, 115:254103, 2019.
- [30] B. Platier, T. J.A. Staps, C. C.J.M. Hak, J. Beckers, and W. L. IJzerman. Resonant microwaves probing acoustic waves from an RF plasma jet. *Plasma Sources Science and Technology*, 29:045024, 2020.
- [31] Nicolas Balcon, G. J.M. Hagelaar, and J. P. Boeuf. Numerical model of an argon atmospheric pressure RF discharge. *IEEE Transactions on Plasma Science*, 36(5 SUPPL. 4):2782–2787, 2008.
- [32] M. Moravej, X. Yang, G. R. Nowling, J. P. Chang, R. F. Hicks, and S. E. Babayan. Physics of high-pressure helium and argon radio-frequency plasmas. *Journal of Applied Physics*, 96(12):7011–7017, 2004.
- [33] G. Nayak, M. Simeni Simeni, J. Rosato, N. Sadeghi, and P. J. Bruggeman. Characterization of an RF-driven argon plasma at atmospheric pressure using broadband absorption and optical emission spectroscopy. *Journal of Applied Physics*, 128(24):1–17, 2020.
- [34] W. Van Gaens and A. Bogaerts. Erratum: Kinetic modelling for an atmospheric pressure argon plasma jet in humid air (J. Phys. D: Appl. Phys. 46 (2013) 275201). *Journal of Physics D: Applied Physics*, 47(7), 2014.
- [35] Jie Pan, Zhenyu Tan, Yadi Liu, Guangsheng Pan, and Xiaolong Wang. Effects of oxygen concentration on atmospheric-pressure pulsed dielectric barrier discharges in argon/oxygen mixture. *Physics of Plasmas*, 22(9):1–8, 2015.

- [36] Sanghoo Park, Wonho Choe, and Holak Kim. Electron heating in rf capacitive discharges at atmospheric-to-subatmospheric pressures. *Scientific Reports*, 8(1):1–7, 2018.
- [37] Ganyoung Park, Hyunwoo Lee, Gyoocheon Kim, and Jae Koo Lee. Global model of He/O₂ and Ar/O₂ atmospheric pressure glow discharges. *Plasma Processes and Polymers*, 5(6):569–576, 2008.
- [38] B. Breizman, G. Stupakov, and G. Vekstein. Diffusion regime of electron-electron collisions in weakly ionized plasmas. *Physics of Plasmas*, 28:030701, 2021.
- [39] Lewis M. Branscomb, David S. Burch, Stephen J. Smith, and Sydney Geltman. Photodetachment Cross Section and the Electron Affinity of Atomic Oxygen. *Physical Review*, 111(2):504–513, 1958.
- [40] L. M. Branscomb, S. J. Smith, and G. Tisone. Oxygen metastable atom production through photodetachment. *The Journal of Chemical Physics*, 43(8):2906–2907, 1965.
- [41] Matthieu Génévriez, Kevin M. Dunseath, Mariko Terao-Dunseath, Alan Hibbert, Arnaud Dochain, Raphaël Marion, and Xavier Urbain. Absolute total, partial, and differential cross sections for photodetachment of O. *Physical Review A*, 98(3):1–14, 2018.
- [42] H.T. Jackson and W.R. Garrett. Theoretical photodetachment cross section for the negative atomic oxygen ion. Technical report, National Aeronautics and Space Administration, Huntsville, Alabama, 1965.
- [43] L. C. Lee and G. P. Smith. Photodissociation and photodetachment of molecular negative ions. VI. Ions in O₂/CH₄/H₂O mixtures from 3500 to 8600 Å. *The Journal of Chemical Physics*, 70(4):1727–1735, 1979.
- [44] P. Lin and R. R. Lucchese. Studies of angular distributions and cross sections for photodetachment from the oxygen molecular anion. *Journal of Chemical Physics*, 114(21):9350–9360, 2001.
- [45] Matthieu Génévriez and Xavier Urbain. Animated-beam measurement of the photodetachment cross section of H. *Physical Review A - Atomic, Molecular, and Optical Physics*, 91(3):1–6, 2015.
- [46] P. Hlavenka, R. Otto, S. Trippel, J. Mikosch, M. Weidemüller, and R. Wester. Absolute photodetachment cross section measurements of the O- and OH- anion. *The Journal of Chemical Physics*, 130:061105, 2009.
- [47] W. Van Gaens and A. Bogaerts. Corrigendum: Kinetic modelling for an atmospheric pressure argon plasma jet in humid air (2013 J. Phys. D: Appl. Phys. 46 275201). *Journal of Physics D: Applied Physics*, 47:079502, 2014.
- [48] Bram Van Gessel, Ronny Brandenburg, and Peter Bruggeman. Electron properties and air mixing in radio frequency driven argon plasma jets at atmospheric pressure. *Applied Physics Letters*, 103(6):6–9, 2013.

-
- [49] A. V. Phelps. Laboratory studies of electron attachment and detachment processes of aeronomic interest. *Canadian Journal of Chemistry*, 47(10):1783–1793, 1969.
- [50] L. Frommhold. Über verzögerte Elektronen in Elektronenlawinen, insbesondere in Sauerstoff und Luft, durch Bildung und Zerfall negativer Ionen (O⁻). *Fortschritte der Physik*, 12:597, 1964.
- [51] Eldon E. Ferguson. Ionospheric Ion-Molecule Reaction Rates. *Reviews of Geophysics*, 5(3):305–327, 1967.
- [52] F C Fehsenfeld, D L Albritton, J A Burt, and H I Schiff. Associative-detachment reactions of O⁻ and O₂⁻ by O₂. *Canadian Journal of Chemistry*, 47:1793–1795, 1969.
- [53] R. J. Freiberg and L. A. Weaver. Microwave investigation of the transition from ambipolar to free diffusion in afterglow plasmas. *Physical Review*, 170(1):336–341, 1968.
- [54] B. Platier, R. Limpens, A. C. Lassise, T. J.A. Staps, M. A.W. Van Nindhuijs, K. A. Daamen, O. J. Luiten, W. L. Ijzerman, and J. Beckers. Transition from ambipolar to free diffusion in an EUV-induced argon plasma. *Applied Physics Letters*, 116(10), 2020.
- [55] R. Limpens, B. Platier, A. C. Lassise, T. J.A. Staps, M. A.W. Van Nindhuijs, O. J. Luiten, and J. Beckers. Influence of a magnetic field on an extreme ultraviolet photon-induced plasma afterglow. *Journal of Physics D: Applied Physics*, 54:435205, 2021.
- [56] LXcat Database. Dutton database for electron diffusion coefficient in argon, 2021.
- [57] Manfred A. Biondi. *Principles of Laser Plasmas*. Wiley, Chichester, Sussex, UK, 1976.
- [58] Fumihiko Kannari, Minoru Obara, and Tomoo Fujioka. An advanced kinetic model of electron-beam-excited KrF lasers including the vibrational relaxation in KrF*(B) and collisional mixing of KrF*(B,C). *Journal of Applied Physics*, 57(9):4309–4322, 1985.
- [59] I. A. Kossyi, A. Yu Kostinsky, A. A. Matveyev, and V. P. Silakov. Kinetic scheme of the non-equilibrium discharge in nitrogen-oxygen mixtures. *Plasma Sources Science and Technology*, 1(3):207–220, 1992.
- [60] Manfred A. Biondi and Sanborn C. Brown. Measurements of Ambipolar Diffusion in Helium. *Physical Review*, 75(11):1700–1705, 1949.
- [61] Bart Platier, Tim Staps, Peter Koelman, Marc van der Schans, Job Beckers, and Wilbert IJzerman. Probing collisional plasmas with MCRS: Opportunities and challenges. *Applied Sciences (Switzerland)*, 10(12):4331, 2020.

Conclusion

This chapter presents the conclusions derived from the results obtained throughout Chapter 4 to 9, and a reflection on the research questions as defined in Chapter 1.

10.1 General conclusions

The preliminary studies in Chapter 4 and 7, conducted chronologically before the experiments using dust-forming discharges, led to two important conclusions regarding the feasibility of using microwave cavity resonance spectroscopy (MCRS) for monitoring the dust formation process in dust-forming discharges.

- An important step in the interpretation of MCRS experiments is based on the assumption of a homogeneous medium, which does not necessarily need to fill the whole cavity volume. In general, gas discharges produced by, for instance, radio-frequency power or high-energy photons do not comply with this assumption. In Chapter 4, it is shown that the shape of the electron density profile contributes to a correction of about a factor ~ 2 to the absolute electron density values obtained from MCRS experiments on a pristine argon RF discharge. However, it was concluded that MCRS nevertheless constitutes a feasible technique for studying low pressure dust-forming plasmas considering the current capabilities of present-day numerical and experimental techniques.
- In Chapter 7, microwave cavity resonance spectroscopy was proven as a feasible technique to determine the electron dynamics in the spatial afterglow of an atmospheric pressure plasma jet. Before this experimental study, MCRS had been applied at atmospheric pressure only once to streamer discharges propagating through ambient air (generated by high-voltage pulses). It was shown that the electron density and the effective collision frequency of electrons originating from the discharge bulk could be measured by MCRS during the phases of plasma

ignition, steady state plasma operation, and plasma decay after termination of the RF power.

10.2 Research question I

The first research question considered the way in which dust grains affect the properties of gas discharges produced in gas mixtures containing an organosilicon compound, which was defined in Chapter 1 as:

Research question I: how do dust grains affect the plasma properties in organosilicon-containing gas discharges?

This effect was studied by determining the electron dynamics (electron density and effective collision frequency) in gas discharges containing hexamethyldisiloxane (HMDSO). The electron dynamics were probed using microwave cavity resonance spectroscopy (MCRS) in a time-resolved fashion under low and under atmospheric pressure conditions.

Under low pressure conditions, discharges were produced in a mixture of argon and HMDSO in order to study the effect of dust formation, of which the results are explained in Chapter 5. This showed that the effect of HMDSO-based dust formation on the electron density is very similar to that of other reactive mixtures such as acetylene, methane, and silane, although the timescales corresponding to the various growth phases differ quantitatively. The effective collision frequency, however, was not probed in such dust-forming discharges before, and revealed that dust formation has a strong effect on the collision frequency of electrons with neutral gas species. It was found that the effective collision frequency was significantly greater than the electron plasma frequency, which raised doubts about the collisionless assumption of the electron current towards the dust grain. Although the electron current is likely not affected to a severe extent under the conditions of the experiment, the presence of dust grains induces a surge of the electron temperature combined with (possibly) changes to the electron energy distribution function. In conclusion, under low pressure conditions, the formation of dust has a significant impact on:

- the electron density, which follows a steep decline during the coagulation phase, and attains minimum values during the accretion phase due to the depletion of electrons,
- and the effective collision frequency (electron-neutral collisions) which exceeds the plasma frequency during the accretion phase, indicating the surge of the mean electron energy and/or combined with changes to the electron energy distribution.

Under atmospheric pressure conditions, the spatial afterglow of a gas discharge produced in a mixture of helium and HMDSO was probed using MCRS, of which the

results have been stated in Chapter 8. By contrast to the low pressure experiments, it was observed that the electron density and effective collision frequency are not significantly affected by the presence of dust grains. This observation is substantiated by the (theoretically) expected number of electrons permanently confined to the surface of the dust grains, which was estimated to be much lower than the free electron density during the time period that the gas discharge was actively produced. However, doubts were raised about the validity of using Fuchs' charging theory during the decay period of the electrons. In conclusion, it was shown that MCRS provided a feasible method to probe the effect of HMDSO addition on the electron dynamics in the afterglow of a dust-forming atmospheric pressure discharge which revealed that:

- the electron density is higher with HMDSO added compared to pristine discharges, which is most probably due to the lower ionization potential of HMDSO compared to that of the carrier gas,
- the electron decay takes longer with HMDSO, which is most probably due to the presence of negative ions,
- and the presence of dust grains does not affect the electron density and effective collision frequency to a detectable extent.

10.3 Research question II

The second research question was concerned with the validity of the theoretical framework for dust charging, defined as follows in Chapter 1:

Research question II: how well does the theoretical framework predict the charge of nanometer-sized dust grains immersed in a low pressure plasma?

The dust charge was experimentally determined using laser-induced photodetachment to liberate electrons from charged dust grains immersed in a low pressure discharge, of which the results have been discussed in Chapter 6. First, the dust grains were formed in an Ar/HMDSO discharge, by temporarily adding the HMDSO vapor, under conditions comparable to those used in the experiments described in Chapter 5. Second, the dust grains were confined in an argon-only discharge, which confined the dust grains in the same volume for subsequent photodetachment experiments. It was found that this procedure led to the stable confinement of the dust cloud for about 20 min, after which the dusty plasma departed from a stable configuration.

Using MCRS, while the dust cloud was stable, the photodetached electron density was determined in a time-resolved fashion, which demonstrated their release into the discharge and subsequent reattachment to dust grains. The experiment resulted directly in the dust charge density, i.e. the product of the dust density and the average

surface charge, inside the laser perturbed volume. A range of values for the average dust charge was derived using additional experiments to obtain the dust density by means of laser light extinction. The theoretical predictions of the dust charge and the charging timescale, based on the orbital-motion-limited theory, showed good agreement, respectively, with the lower bound of the experimental range of the dust charge and the decay time of the photodetached electron density. In conclusion, laser-induced photodetachment experiments demonstrated that:

- the combination of ultraviolet laser pulses and MCRS provides a valuable technique for experimental determination of the dust charge density,
- and the technique can be used independently of dusty plasma phenomena such as dust density waves that form the basis for other experimental charge detection methods.

10.4 Research question III

The third research question focused on the behavior of negative ions in the spatial afterglow of an atmospheric pressure discharge, stated as follows in Chapter 1:

Research question III: how do negative ions behave in the spatial afterglow of atmospheric pressure plasmas?

Negative ions can be relevant for the (de)charging of dust grains in the spatial afterglow, in addition to the ions and electrons. Moreover, the negative ions could become more important further downstream of the discharge, because the electron density diminishes more quickly than the ion density does.

In Chapter 9, the first step towards the effect of negative ions on dust (de)charging is taken by determining the behavior of negative ions produced in the spatial afterglow of an atmospheric pressure argon discharge interacting with an argon-oxygen gas mixture at atmospheric pressure. The experimental technique was based on laser-induced photodetachment in combination with microwave cavity resonance spectroscopy, which allowed to determine the electron density and effective collision frequency of electrons liberated from negative ions.

Based on the interpretation of the experimental data, it was found that the addition of oxygen, an electronegative gas, resulted in the production of mainly negative atomic oxygen ions, O^- . The subsequent loss of the photodetached electrons proceeded most probably through the dissociative attachment of the photodetached electrons with molecular oxygen neutrals: $e + O_2 \rightarrow O^- + O$. This conclusion was based on the outcome of a timescale analysis. The (local) negative ion density $n_i^- \sim 1 \times 10^{18} \text{ m}^{-3}$ was found to exceed the (electric-field-weighted volume-averaged) free electron density produced by the discharge in the spatial afterglow $n_e \sim 1 \times 10^{17} \text{ m}^{-3}$, which strengthens the hypothesis that negative ions can constitute a relevant current towards dust grains.

Outlook and recommendations

This chapter is concerned with an outlook for further research in Section 11.1, based on the obtained results in this thesis. Thereafter, Section 11.2 comprises a set of recommendations for the development of ultrafine particle (UFP) sensing devices, which provides the link between the research results and the engineering challenges encountered during the development of UFP sensing devices.

11.1 Outlook for future research

The outlook is split into three parts: future experiments, applications, and fundamental challenges.

With technically feasible developments, the current low pressure experimental setup could be used to study the dust growth process in more detail, and the surface charge of dust grains with high accuracy.

- The dust charge density could be studied under a wide range of ion collisionality regime in the low pressure system. Dust charge density measurements with the current low pressure setup could be performed at different neutral gas pressure. For pristine discharges, the experimental setup can be used to generate discharges up to ~ 1 mbar. If dust-forming discharges can be done at higher pressure, the collision-enhanced regime for dust charging can be explored experimentally. Otherwise, it may be feasible to grow a dust cloud under a specific condition, and vary the pressure and conditions afterwards.
- Measurements of the average dust charge can be obtained with smaller uncertainty. The development of a dust density and size measurement technique would be useful to decrease the uncertainty in the determination of the dust density. For instance, Mie ellipsometry is a feasible technique to monitor these dust properties during dust growth. Combined with laser-induced

photodetachment and MCRS as shown in this thesis, this would result in the development of an in-situ dust charge diagnostic with much higher accuracy.

- The effective collision frequency measurements could be conducted at different neutral gas pressures using the current low pressure experimental setup. The effect of electron-neutral collisions is more pronounced at higher neutral gas density. However, to conduct a systematic study on the effective collision frequency, it is necessary to investigate the microwave spectral response due to resonances caused cable and feedthrough characteristics in the microwave frequency range. It was found that the effective collision frequency was more difficult to obtain for plasma conditions resulting in a spectral position of the resonant mode overlapping with other resonances.

Related to applications, it would be interesting to study the dust charge and growth process in the spatial afterglow of the atmospheric pressure system with respect to the following aspects.

- Manipulation of the dust charge in the spatial afterglow can be done by the application of bias electrodes. Several studies have shown that a bias voltage downstream of the discharge bulk affects the electron and ion losses. In turn, this affects the currents towards the dust grains traveling the afterglow. By extracting the ions from the afterglow, the dust charge is less neutralized and may remain negative. In such case, the dust charge measurement using laser-induced photodetachment may be a feasible method for dust charge determination at atmospheric pressure.
- Measurement of the positive dust charge in the spatial afterglow directly inhibits neutralization and charge reversal. Current techniques are based on extraction of charged dust grains and subsequent measurement using, e.g., differential mobility analyzers (DMA) and condensation particle counters (CPC). Sampling charged dust grains at various locations in the spatial afterglow avoids neutralization or reversal of the charge due to interaction with positive and negative ions. This could be done, for example, by sampling charged dust grains by a differential pumping system with an orifice located in the afterglow.
- In-situ measurement of the dust size and density in the atmospheric pressure system. The growth process of dust grains at atmospheric pressure has been studied by deposition or extraction of dust grains, but the measurement of the size and density in-situ in the spatial afterglow or plasma bulk would be useful to avoid processes such as aggregation after transport, and accumulation and/or clustering at the deposition surface. Additionally, the measurement of the density, size and charge in-situ would greatly assist the interpretation of the dust charge measurements, and their accuracy.
- The link between discharge conditions and dust properties could be studied extensively. It would be interesting to explore systematically a broader range of discharge conditions such as the gas flow rate, the RF power, or the addition of an electronegative gas (e.g.oxygen). This would provide more insight in the

effect of the gas residence time in the discharge on the dust size and density. Moreover, the effect of discharge conditions on the plasma chemistry could be useful information to understand the composition of dust grains generated for various purposes.

From a fundamental perspective, the charging currents induced by an atmospheric pressure discharge represent an interesting model system for the collisional ion current regimes. In addition, it has been observed that dust grains can be studied for long periods of time in the atmospheric pressure vessel.

- The atmospheric pressure plasma bulk represents a situation similar to the low pressure bulk, with much smaller mean free path lengths, but similar temperatures of the charged plasma species. This means that it potentially serves as the higher pressure variant of low pressure dusty plasmas. Laser-induced photodetachment could be applied axially through the discharge tube in combination with a microwave cavity surrounding the bulk plasma. This would require a redesign of the plasma reactor with an RF and ground electrode surrounding the tube.
- The transition of the dust charge governed by the currents in the plasma bulk towards the ion-rich region downstream would be interesting to study experimentally. In the spatial transition region, the theory breaks down because the electron density becomes much lower than the ion density, and the situation tends towards the one described by Fuchs' theory. This situation resembles the effect of electron depletion at low pressure, where the electron density is lower than the ion density and quasi-neutrality is violated.
- The aggregation of dust grains was observed experimentally in the far spatial afterglow. It has been observed that dust grains can be confined inside vortices in the atmospheric pressure discharge vessel due to the gas flows (with and without microwave cavity). It appeared from camera images that many layers of dust (visualized by a laser sheet) were confined to these vortices. This could be a useful method to study aggregation of dust grains formed in the discharge at atmospheric pressure for times during which the electron and ion density have decayed significantly. In such cases, the conditions resemble that of the ambient atmosphere in which there are very few electrons and ions.

11.2 Recommendations for applications

There are several recommendations for ultrafine particle sensing (UFPS) devices:

- Different type of discharge. In the original design of the UFPS, a corona discharge is applied to generate a gas discharge from which the ions are actively extracted. However, it was found that a direct-current discharge is not practical in case a layer of contamination is formed which requires an increase of the ignition voltage up to impractical values. In case of alternating-current discharges, the electric fields are able to penetrate the dielectric layer.

- Contamination. Also in the atmospheric pressure plasma reactor used in this thesis, severe contamination of the electrodes was observed in case HMDSO or oxygen was added to the discharge gas. The presented atmospheric pressure experimental setup could be used to study the deposition rate of hexamethyldisiloxane (HMDSO) on the electrode. The HMDSO vapor density can be set to the concentration found in applications (e.g., in vehicles with significant amounts of silicon-containing materials).
- Combination of the precipitation and sensing section. By application of an electric field, the smallest grains are precipitated first in the precipitation section, while the largest dust grains proceed to the sensing section. This reduces the transport time, and likely increases the left-over charge.
- Reduction of charge neutralization and/or reversal. The mean free path of the species could be increased by reducing the neutral gas pressure. By injecting the dust and ambient air into vacuum, measurements can be done at reduced pressure with slower electron decay. On the other hand, a bias electrode could be added to the design to manipulate the dust charge. This leads to longer maintenance of the dust charge, and a larger signal-to-noise ratio.

Summary

Complex and dusty plasmas comprise a significant amount of the visible matter in the universe. Such plasmas are important for the formation of planets in distant galaxies and the interaction of extraterrestrial dust particles with molecules in the interstellar medium. Also, the formation and charging of nanoparticles by plasmas is increasingly important in high-tech industrial systems. Examples of such high-tech industrial systems are lithography machines, glass-fiber production chambers and ultrafine particle sensors. This thesis was motivated by the latter example, in which the size and concentration of nanoparticles follows from measuring how an atmospheric pressure plasma charges these nanoparticles. The scientific challenge presented by the development of these ultrafine particle sensing devices is threefold:

- Predicting accurately the (de-)charging of nanoscale dust particles coming in contact with plasma.
- Understanding the processes leading to electrode contamination by material deposition due to the atmospheric pressure plasma.
- Dealing with fluctuations in atmospheric conditions—such as humidity, molecular and particulate contamination, and temperature—that heavily affect the plasma parameters and the charging behavior induced on nanoscale particles.

In this work, low-temperature plasmas containing dust particles were studied under low pressure and atmospheric pressure conditions in order to increase the understanding of their formation and the interaction with the plasma in which they are embedded.

This project targeted the development of methods to measure the surface charge of nanoscale particles. The main concept is based on laser-induced photodetachment of elementary charges residing on the dust particles that can be measured using microwave cavity resonance spectroscopy (MCRS). Similar to negative ions, the interaction of photons created by an intense laser pulse have the ability to detach electrons from negatively charged dust grains. The free electron density can be measured using the

MCRS technique similar to how this method is generally used to measure the electron density generated by a gas discharge.

To this end, the project first focused on the development of the MCRS technique with respect to its validity to study non-uniform plasmas at low pressure and its application at atmospheric pressure where the collision frequency of electrons with neutrals largely exceeds the plasma frequency. The MCRS technique is based on the detuning of a resonant mode of a microwave cavity due to the number density of free electrons and the frequency with which they collide elastically with neutrals. The presence of the electrons results in changes of the resonance frequency and full-width-at-half-maximum of the resonant mode excited in the cavity, from which the electron density and effective collision frequency can be derived. It was shown that MCRS possesses the necessary accuracy to determine the free electron density in low pressure discharges with a non-uniform electron density profile, and the free electron density and effective (electron-neutral) collision frequency in the spatial afterglow of a plasma jet.

Second, the project focused on the formation of dust grains in low and atmospheric pressure discharges by the addition of hexamethyldisiloxane (HMDSO) to the discharge gas. It was found that the effective collision frequency during dust formation at low pressure is significant with respect to the electron plasma frequency, which may have important consequences for the collisionality of electrons and for the overall charging mechanism of dust particles. At atmospheric pressure, it was found that dust charging has a negligible effect on the electron density and effective collision frequency in the spatial plasma afterglow, which is in contrast to the observed depletion of electrons during dust formation in the low pressure HMDSO-containing discharges.

Third, laser-induced photodetachment in concert with MCRS was used to probe charged nanoparticles confined in a low pressure discharge, and negative ions produced in the spatial plasma afterglow at atmospheric pressure. The dust charge was measured in a low pressure argon-only discharge, and compared to theoretical predictions using the same conditions. At atmospheric pressure, the dominant negative ion species was determined to be O^- by analyzing the temporal behavior obtained from the time-resolved MCRS measurements.

In conclusion, the most important results obtained from the low and atmospheric pressure experiments have shown that electron-neutral collisions need to be included in the OML theory, that laser-induced photodetachment in combination with MCRS provides an excellent method for measuring the dust charge density under low pressure conditions, and that the same technique at atmospheric pressure constitutes an indispensable method for the detection of negative ions in the spatial afterglow. This provides an excellent starting point for future research to conduct experimental studies on nanodust charging and further critical assessments of the theoretical framework for plasma-based charging of nanoparticles. Owing to these developments, future research could be focused on studying the charging of nanoscale particulate matter at atmospheric pressure by combining laser-induced photodetachment with MCRS, and studies on the effect of negative ions on the (de)charging of nanoparticles in the spatial plasma afterglow at atmospheric pressure.

Acknowledgments

Without the collaborative efforts and help of the people involved, directly or indirectly, the work presented in this thesis would not have seen the light of day. In this section, I want to express my gratitude to those people, for their contributions, the lively discussions, and their patience.

First of all, I want to express my deepest gratitude to Job Beckers and Gerrit Kroesen—my first and second promotor, respectively—for granting me the opportunity to pursue a doctoral candidacy in their field of expertise: complex and dusty plasmas. Job, as a master student in Mechanical Engineering and Nuclear Fusion, I developed a background in fusion plasmas, but there was still a deep dive into the field of low-temperature plasmas and dusty plasmas in particular, and a risk for the one taking me aboard. At the first day we met, we directly dove into a discussion concerning scientific and engineering matters, almost forgetting that I came for questions regarding one of your master courses. Looking back at the (almost) five years that passed, I must say that the amount of enthusiasm with which we have been discussing such matters has only been increasing, and I don't think that will be lost in the future for the both of us. During periods of ever-increasing chaos, about half-way of my PhD, you took the time for me so that we could sit back, and lay out a new strategy. I have experienced you as an amazing supervisor that is well equipped with all skills necessary. You have provided me with all the freedom I could imagine, but your continued enthusiasm and optimism were vital to the end result. Your eye on novelty and scientific relevance has contributed greatly to my prolonged development as a scientist, and even a physicist, for which I am sincerely grateful. Gerrit, during our six (or so)-weekly discussions, we had interesting conversations on the topics that were most difficult for me to grasp or solve at that moment. Specifically targeting those topics, you were always sharp and to-the-point providing me with references of a thesis or paper published some tens of years ago that already had discussed the problem. In the midst of the most difficult period of my PhD, you were there together with Job to set up the new direction. Thank you, both, for your support, I am glad that I chose to do a PhD under your guidance.

To my doctorate committee, Uwe Kortshagen, Adriana Creatore, and Eva Kovačević, I want to express my gratitude for serving as the opposition and taking your time to scour this dissertation. I hope you enjoyed reading it. Eva, thank you for the opportunity to visit you in Orleans. I enjoyed spending time with you and Johannes, and I still think that the comparison of our microwave diagnostics is a great idea.

Talking about contributions, many aspects of this thesis have originated from the collaboration with Bart Platier. Bart, you are a co-author on almost of all of the contributions listed in this thesis, and I enjoyed (most of the time) working on every one of them together. After the fire at Prodrive—the most chaotic moment during my PhD—I took the risk to collaborate with you, not knowing what to expect. It turned out to be a great decision, for both of us according to your own words as well, leading to many contributions to the field. Most of my knowledge and practical experience with MCRS I heard from you first. Thank you for that, and for making daily struggles much more pleasant with your non-exhaustive list of (im)practical jokes.

The second person with whom I collaborated intensively is Tim Donders, thank you. Especially, during the final year of my PhD, it has been a life saver to collaborate with you both in the laboratory as well as during the writing of publications and chapters. The pace with which you got to the bottom of the setup was very impressive, and I hope you will hold on to that pace while working on your own topics with the setups.

Thirdly, I want to thank the other contributors for their time, patience and effort. Marvin van de Ketterij, I enjoyed working in the laboratory together (although it was not that much due to the pandemic) and appreciated the novel ideas with which you came up more than once. You have delivered a very nice thesis, and your contribution to one of the chapters/papers is surely recognized! Martijn van Ruijendaal, you have surprised me more than once with your goal-oriented and efficient problem solving skills. Specifically, I am grateful for the code you wrote to interpret the camera images for Abel inversion. I did not see often the pace and sharpness with which you are able to dive into the physics, although it is a good quality for a PhD candidate. In addition, I also want to thank other students that I supervised, of which the work did not end up in this thesis: Roeland, Stefan, Daan, Sjoerd, Judith, Isabella, Thomas, Mark, and Thijs.

My office mates, without you it would not have been possible to enjoy the time spent. This one is addressed to you all: Patrick, Boy, Marlous, Siebe, Shahriar, Zahra, Saman, Dimitry, Federico. Although I spent a lot of time at Prodrive during the first years, I have increasingly come to understand that a lively atmosphere at the work place is an important prerequisite for doing the actual work. In particular, I want to thank Patrick, Boy and Marlous for taking me on-board for the many lunch walks, many more coffee breaks, and our outside-of-the-office hours. In addition, with respect to those that have left some time ago, I want to thank my former colleague Dirk Trienekens. Dirk, as my Prodrive supervisor during the first two years, I have learned a great deal from your scientific and industrial skills.

Regarding the design and engineering of the setups, I want to thank several people that have contributed greatly. First, Ab, Pieter, Eddie, Jurgen from our group, thank you for the joyful coffee breaks, your practical insights, and all the time in the lab

spent to get things up and running. Ginny and Henk, from the Cascade workshop, thank you for your continuous effort in the creation of many components from the setup. Paul, Meindert, Paul, Nico, Gerrit, Simon, Dave, thank you for all your help in the creation and design of the plasma jet, the power probe, the laser enclosures, and all other components. Your effort contributed greatly to operation and safety of the setups. Without all of your help, the experimental setups would not have come to existence at all.

Furthermore, I want to thank Anita, the cornerstone of our research group, and Beatriz, the SEM-expert. Anita, you have always been the go-to person for any matter. And of course, not to forget, thank you for the reminders to fill in the hourly registration form! Beatriz, thank you for the speed course on scanning electron microscopy and energy-dispersive X-ray measurements.

Finally, I want to thank my friends and family for their interest and continuous support, during good and bad times. In particular, Daan and Jelle, I am grateful for you being my paranymphs and taking on the practical matters in preparation of my defense ceremony. However, most of all, I want to thank the fundamental person in my life, my wife Gaby, for your everlasting support, and for our beautiful daughter, Faye.

Scientific contributions

11.3 Journal publications

- T.J.A. Staps, T.J.M. Donders, B. Platier, and J. Beckers, *Laser-induced photodetachment of negative oxygen ions in the spatial afterglow of an atmospheric pressure plasma jet*, submitted for publication.
- T.J.A. Staps, T.J.M. Donders, B. Platier, and J. Beckers, *In-situ measurement of dust charge density in nanodusty plasma*, Journal of Physics D: Applied Physics, 2021, DOI: 10.1088/1361-6463/ac3581.
- T.J.A. Staps, M.I. van de Ketterij, B. Platier, and J. Beckers, *The underexposed effect of elastic electron collisions in dusty plasmas*, Communications Physics 4, 2021, 231.
- R. Limpens, B. Platier, A.C. Lassise, T.J.A. Staps, M.A.W. van Ninhuijs, O.J. Luiten, and J. Beckers, *Influence of a magnetic field on an extreme ultraviolet photon-induced plasma afterglow*, Journal of Physics D: Applied Physics 54, 10 August 2021, 435205.
- T.J.A. Staps, B. Platier, D. Mihailova, P. Meijaard, and J. Beckers, *Numerical profile correction of microwave cavity resonance spectroscopy measurements of the electron density in low-pressure discharges*, Review of Scientific Instruments 92, 2 September 2021, 093504.
- P. Meijaard, T.J.A. Staps, and J. Beckers, *Step-wise excitation for the determination of the resonance frequency of a microparticle confined in a low pressure plasma*, Physics of Plasmas 28, 2 August 2021, 083502. Correction: Physics of Plasmas 28, 099901 (2021).
- B. Platier, R. Limpens, A.C. Lassise, T.T.J. Oosterholt, M.A.W. van Ninhuijs, K.A. Daamen, T.J.A. Staps, M. Zangrando, O.J. Luiten, W.L. IJzerman, and J.

Beckers, *Magnetic field-enhanced beam monitor for ionizing radiation*, Review of Scientific Instruments 91, 9 June 2020, 063503.

- B. Platier, T.J.A. Staps, P.M.J. Koelman, M. van der Schans, J. Beckers, and W.L. IJzerman, *Probing Collisional Plasmas with MCRS: Opportunities and Challenges*, Applied Sciences 10, 12, 24 June 2020, 4331.
- B. Platier, T.J.A. Staps, C.C.J.M. Hak, J. Beckers, and W.L. IJzerman, *Resonant microwaves probing acoustic waves from an RF plasma jet*, Plasma Sources Science and Technology 29, 17 April 2020, 045024.
- B. Platier, R. Limpens, A.C. Lassise, T.J.A. Staps, M.A.W. van Nindhuijs, K.A. Daamen, O.J. Luiten, W.L. IJzerman, and J. Beckers, *Transition from ambipolar to free diffusion in an EUV-induced argon plasma*, Applied Physics Letters 116, 9 March 2020, 103703.
- B. Platier, T.J.A. Staps, M. van der Schans, W.L. IJzerman, and J. Beckers, *Resonant microwaves probing the spatial afterglow of an RF plasma jet*, Applied Physics Letters 115, 18 December 2019, 254103.

11.4 Oral contributions

- T.J.A. Staps, T.J.M. Donders, B. Platier, and J. Beckers, *Laser-induced release of electrons from dust grains confined in low-pressure dusty plasma*, European Physical Society, 47th Conference on Plasma Physics, 2021.
- T.J.A. Staps, *The importance of future nanoparticle sensors for human health*, Young Speakers Contest, Van der Waals Symposium, 2019.
- T.J.A. Staps, B. Platier, P. Meijaard, J. Berndt, E. Kovacevic, and J. Beckers, *Measuring plasma parameters: comparison of microwave interferometry and microwave cavity resonance spectroscopy*, Presented at: 22nd Euregional Workshop on the Exploration of Low Temperature Plasma Physics (WELTPP), Kerkrade, The Netherlands, 2019.

11.5 Poster contributions

- T.J.A. Staps, B. Platier, P. Meijaard, J. Berndt, E. Kovacevic, and J. Beckers, *Measuring plasma parameters: comparison of microwave-based diagnostics in detail*, Presented at: 22nd Euregional Workshop on the Exploration of Low Temperature Plasma Physics (WELTPP), Kerkrade, The Netherlands, 2019.
- T.J.A. Staps, B. Platier, and J. Beckers, *Obtaining the electron density in a rf-driven plasma jet at atmospheric pressure using microwave cavity resonance spectroscopy*, Presented at: 31th NNV-Symposium on Plasma Physics and Radiation Technology, Lunteren, The Netherlands, 2019.

- T.J.A. Staps, G.M.W. Kroesen, and J. Beckers, *Measuring surface charge on nanoparticles using FT-IR spectroscopy*, Presented at: 21th Euregional Workshop on the Exploration of Low Temperature Plasma Physics (WELTPP), Kerkrade, The Netherlands, 2018.
- T.J.A. Staps, D.J.M. Trienekens, and J. Beckers, *A novel particle injector to study (nano)dusty plasma*, Presented at: 3rd International Conference on Atmospheric Dust, Bari, Italy, 2018.
- T.J.A. Staps, D.J.M. Trienekens, and J. Beckers, *A novel particle injector to study dusty plasma at the nanoscale*, Presented at: 30th NNV-Symposium on Plasma Physics and Radiation Technology, Lunteren, The Netherlands, 2018.

Curriculum Vitae

Timmy Jacobus Adrianus Staps

Tilburg, the Netherlands

Born on 27 September 1991.

Experience

2017 - 2021 | Doctoral Candidate (full-time)

Eindhoven University of Technology, Eindhoven, the Netherlands

PhD candidate in the research group of Elementary Processes in Gas Discharges (EPG), department of Applied Physics, Eindhoven University of Technology, in collaboration with Prodrive Technologies B.V. The main focus of the project resulted in this dissertation, titled: *Towards experimental characterization of nanoparticle charging in plasmas*.

2016 - 2017 | Master Graduate

DIFFER, Eindhoven, the Netherlands

Dutch Institute for Fundamental Energy Research. Double degree-master graduation project (fusion and control systems) on the development of a feedback control strategy (backstepping) for the (non-linear) L-H confinement transition in fusion plasma.

2015 - 2016 | Teaching Assistant

Eindhoven University of Technology, Eindhoven, the Netherlands

Supervising groups of Bachelor students during design-based learning courses: Combustion Engine, Robotic Arm, and Engineering design.

2012 - 2014 | Bachelor Graduate and Mechanical Engineer (volunteer)

University Racing Eindhoven, Eindhoven, the Netherlands

Bachelor graduation project on the development, realization, and implementation of a motor controller for the full-electric race car. After six months graduation project,

design and realization of the complete thermal management system for the URE07 and URE08 on voluntary basis.

2012 - 2017 | Mechanical Engineer (part-time)

Prodrive Technologies B.V., Son, the Netherlands

Engineering of high-tech systems in a variety of projects such as the control system for a scanning electron microscope and the development of a PM_{2.5} particle sensor.

Education

2014 - 2017 | Master of Science in Mechanical Engineering

Eindhoven University of Technology, Eindhoven, the Netherlands

Specialization in Control System Technology track, department of Mechanical Engineering, Eindhoven University of Technology. Double degree with Science and Technology of Nuclear Fusion.

2013 - 2017 | Master of Science in Science and Technology of Nuclear Fusion

Eindhoven University of Technology, Eindhoven, the Netherlands

Master program of Science and Technology of Nuclear Fusion, department of Applied Physics, Eindhoven University of Technology. Double degree with Mechanical Engineering.

2009 - 2012 | Bachelor of Science in Mechanical Engineering

Eindhoven University of Technology, Eindhoven, the Netherlands

Specialization in Automotive Technology, and graduation project (in 2012) at University Racing Eindhoven (URE) in collaboration with the Thermal and Fluids Engineering group (TFE, department of Mechanical Engineering, Eindhoven University of Technology) and Prodrive Technologies B.V.

2001 - 2007 | VWO (secondary education)

St.-Odulphyslyceum, Tilburg, the Netherlands

Preliminary scientific education in Economics and Society, and Nature and Technology.